SLAC-R-974

Measurement of Hadronic Event Shapes and Jet Substructure in Proton-Proton Collisions at 7.0 TEV Center-Of-Mass Energy with the Atlas Detector at The Large Hadron Collider

By David W. Miller

SLAC National Accelerator Laboratory, Stanford University, Stanford CA 94309

Work funded in part by DOE Contract DE-AC02-76SF00515

MEASUREMENT OF HADRONIC EVENT SHAPES AND JET SUBSTRUCTURE IN PROTON-PROTON COLLISIONS AT 7.0 TEV CENTER-OF-MASS ENERGY WITH THE ATLAS DETECTOR AT THE LARGE HADRON COLLIDER

A DISSERTATION
SUBMITTED TO THE DEPARTMENT OF PHYSICS
AND THE COMMITTEE ON GRADUATE STUDIES
OF STANFORD UNIVERSITY
IN PARTIAL FULFILLMENT OF THE REQUIREMENTS
FOR THE DEGREE OF
DOCTOR OF PHILOSOPHY

David W. Miller

June 2011

I certify that I have read this dissertation and that, in my opinion, it is fully adequate in scope and quality as a dissertation for the degree of Doctor of Philosophy.

(Su Dong) Principal Adviser

I certify that I have read this dissertation and that, in my opinion, it is fully adequate in scope and quality as a dissertation for the degree of Doctor of Philosophy.

(John Jaros)

I certify that I have read this dissertation and that, in my opinion, it is fully adequate in scope and quality as a dissertation for the degree of Doctor of Philosophy.

(Michael Peskin)

Approved for the University Committee on Graduate Studies

Abstract

This thesis presents the first measurement of 6 hadronic event shapes in proton-proton collisions at a center-of-mass energy of $\sqrt{s} = 7$ TeV using the ATLAS detector at the Large Hadron Collider. Results are presented at the particle-level, permitting comparisons to multiple Monte Carlo event generator tools. Numerous tools and techniques that enable detailed analysis of the hadronic final state at high luminosity are described. The approaches presented utilize the dual strengths of the ATLAS calorimeter and tracking systems to provide high resolution and robust measurements of the hadronic jets that constitute both a background and a signal throughout ATLAS physics analyses. The study of the hadronic final state is then extended to jet substructure, where the energy flow and topology within individual jets is studied at the detector level and techniques for estimating systematic uncertainties for such measurements are commissioned in the first data. These first substructure measurements in ATLAS include the jet mass and sub-jet multiplicity as well as those concerned with multi-body hadronic decays and color flow within jets. Finally, the first boosted hadronic object observed at the LHC – the decay of the top quark to a single jet – is presented.

Preface

The Large Hadron Collider (LHC) is the largest machine ever built by humankind and is designed to accelerate protons to the highest energies ever produced on Earth. This fact alone merits respect and awe of the infinite creativity and willingness of humans to believe that they can achieve the impossible in order to understand the unknowable. The possibility to study the properties of the interactions that such a machine produces is truly a once in a lifetime opportunity.

The work constituted by this thesis represents an endeavor to understand the way that quarks and gluons – the *partons* that were at one time only a theoretical "convenience" for Richard Feynman, Murray Gell-Mann and George Zweig – evolve to form experimental signatures in our detectors, the jets of the so-called hadronic final state. But the LHC is a unique machine, producing a complex environment in which these signatures are manifested. As a result, techniques must be developed to tease out the interesting physics buried within a complex *milieu* created by the enormous energy and intensity of the LHC. This thesis is at least in part devoted to describing those tools, some of which have since come to be used in analyses measuring the top quark, the W boson, and searches for new physics throughout ATLAS.

An attempt is made to draw a connection among the many studies performed throughout the initial phases of the ATLAS experiment. Critical efforts during the commissioning of the detector, the first acquisition of $\sqrt{s} = 900$ GeV and then $\sqrt{s} =$ 7 TeV data, and the full-fledged analysis of the full 2010 dataset, are all tied together by a common thread: the ability to utilize the largest and most advance instruments ever built in a coherent manner to understand the highest energy collisions of the smallest components of the universe, as yet known to humankind.

The timing of the silicon pixel detector at the heart of ATLAS, the geometric or topological representation of signals in the electromagnetic calorimeter, the use of ferrite cores wrapped around low voltage power supply wires in the hadronic calorimeter, the need to subtract the background due to multiple proton collisions from jets measured in that same calorimeter; these all form seemingly disparate pieces of the experimental enterprise, but are each necessary for every single plot in this thesis.

"We shall neither fail nor falter; we shall not weaken or tire
...give us the tools and we will finish the job."
– Winston Churchill

"In God we trust; all others must bring data."
– W. Edwards Deming

Acknowledgements

I would like to thank my mother and my father for always pushing me to endeavor towards that which I believe in and intrigues me (had they done otherwise, I'd be running into burning buildings at the moment). I would like to thank my advisors (all of them) for allowing me the freedom to pursue that which I felt most compelling within ATLAS, while simultaneously providing the guidance and insight that helped me to choose what might be the most worthwhile paths. My ATLAS colleagues, while not always maintaining a strict time limit on their presentations, nonetheless created an environment in which lively debates about deep scientific questions could take place, and were always ready and willing to answer (and write) emails. Much of the technical expertise – if I may be so bold as to say I have any at all – that I garnered throughout the years in ATLAS is due to Zach Marshall and David Lopez Mateos and their enormous competence, scientific prowess, and most of all patience. I would like to especially acknowledge the confidence and trust that Tancredi Carli and Peter Loch had in me and their constant striving to understand just *exactly* how the ATLAS detector is working to measure these complex, strange objects we call *jets*. Steve Ellis, whether he knows it or not, provided continuous guidance and an atmosphere of deep collaboration for the work on jet substructure, without which I never would have become so involved in the subject in the first place. I would of course like to thank Andrea Banfi, Gavin Salam and Giulia Zanderighi for their enormous help and guidance in the analysis of hadronic events shapes.

Contents

Chapter 1

Introduction

The Standard Model of particle physics has emerged over the last half century as a predictive and accurate description of the structure of the fundamental forces of nature, at least up to the scale of the weak interactions. Since the prediction of the existence of the Z boson by Sheldon Glashow – based simply on the convergence of electromagnetic and weak interaction Lagrangians [1] – the Standard Model has proven to provide a *nearly* complete picture of the particles that compose the known universe and how they interact with one another. However, we know that this model is *not* complete. We have not yet discovered the Higgs boson [2, 3, 4, 5], supposed to be responsible for the breaking of the electroweak symmetry that Glashow predicted [6]. There is no known particle candidate for the dark matter, the substance observed to form nearly one third of the energy-density of the universe [7, 8, 9, 10, 11]. There is currently no substantial evidence for a fundamental difference between matter and anti-matter, and so the vast preponderance of the former remains a mystery [12, 13, 14, 15, 16, 17, 18, 19].

The Large Hadron Collider (LHC) was built in order to answer these questions. The as yet undiscovered facets of nature that may provide those answers have remained hidden from all other experiments seeking to uncover them. Both the energy frontier exposed by the LHC and new techniques and approaches for asking the right questions will be necessary to extract the signatures of any new physics from the background of that which we already know. Much of this knowledge has been gained

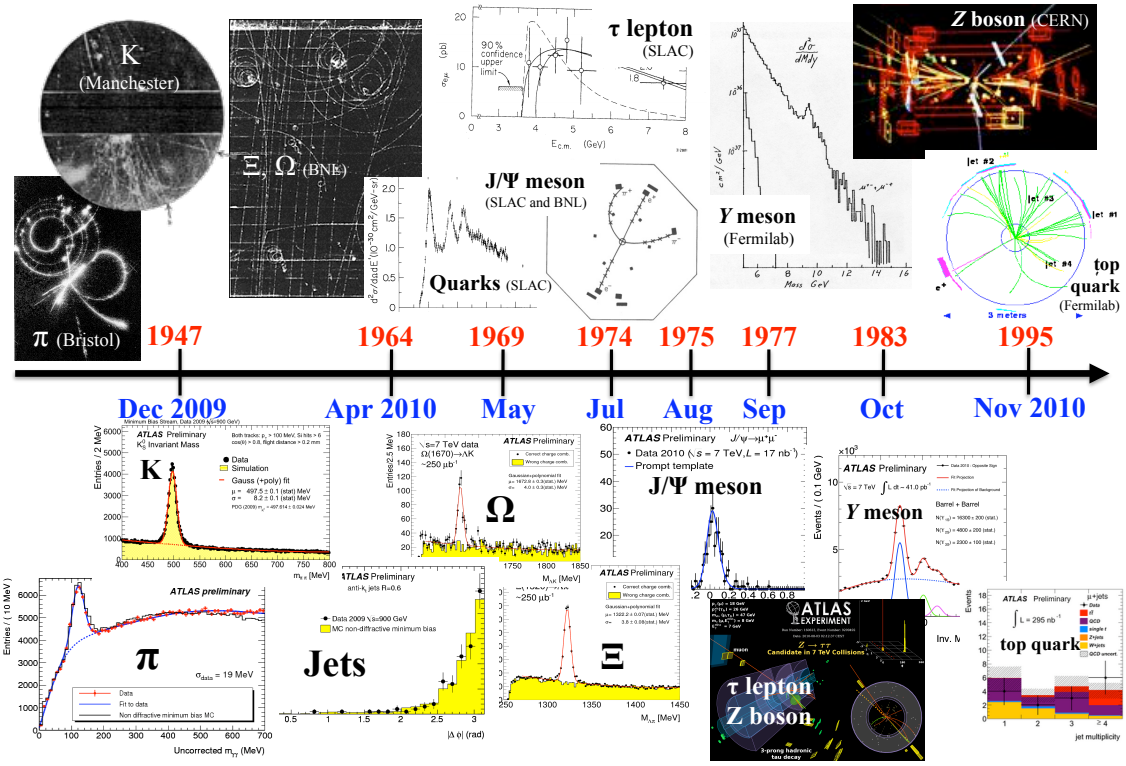

Figure 1.1: (top) Selected timeline of achievements of the Standard Model of particle physics, and their experimental verification or discovery. (bottom) "Re-discovery" of the Standard Model of particle physics by the ATLAS experiment during the first run of the Large Hadron Collider (LHC) in 2009 and 2010.

through the extensive experience at past colliders such as SPEAR at SLAC [20, 21], the PETRA storage ring at DESY [22, 23], the Stanford Linear Collider (SLC) at SLAC [24, 25], the $Sp\bar{p}S$ [26, 27], PEP-II at SLAC [28, 29], the Large Electron-Positron (LEP) collider at CERN [30, 31, 32, 33], and the Tevatron collider at Fermilab [34, 35, 36]. For a comparison of these machines and their design parameters see [37].

In order to answer these deep questions about nature, a thorough understanding of the processes which can mask signatures of new phenomena must be gained. To this end, one of the primary goals of the initial physics program at the LHC is to establish – to "re-discover" – the Standard Model of particle physics. Only then might we hope to extract these signatures, those that have remained hidden for so long. Quantum chromodynamics (QCD) – the theory within the Standard Model that describes the interactions of quarks and gluons [38, 39, 40, 41, 42, 43, 44, 45] – underlies the most frequently observed events in the collision of two protons. QCD is thus one of the most crucial theories to understand in this new energy regime and with this new apparatus, the ATLAS detector. Figure 1.1 attempts to depict that, over the course of just one year, the ATLAS collaboration has systematically "re-discovered" the Standard Model at the Large Hadron Collider, covering achievements that previously required nearly a half century to realize.

Perhaps the most striking feature of the strong dynamics of QCD is the experimental determination that quarks cannot exist in isolation, a phenomenon referred to as confinement [41, 46, 47]. Consequently, the experimental signatures of quarks and gluons are not the quarks and gluons themselves, but so-called jets. Jets are the clusters of collimated particles that form as quarks separate from one another and form stable particles called hadrons. Jets – the study of their structure, substructure and the hadronic final state which they comprise – will be the central focus of this thesis. We will see that a thorough understanding of these objects is crucial for nearly all physics goals at the Large Hadron Collider, and that jets themselves provide a window into the strong dynamics of QCD at a new energy scale and a means to discovering new physics. Particular emphasis will be given to the techniques developed to perform precision physics in the high luminosity environment at the LHC.

Chapter 2 describes the theory of the strong interactions, with significant attention given to those aspects that are important for the theoretical understanding of jet properties and the hadronic final state with which we are concerned in this thesis. The LHC itself is described in Chapter 3, including a detailed description of the interaction region, which is crucial for understanding the experimental challenges addressed in Chapter 6. Chapter 4 describes the ATLAS detector systems, the trigger design and strategy for selecting events to be saved for analysis, and the data quality and conditions experienced during 2010. Chapter 5 describes the hadronic final state and the details of jet reconstruction, calibration and analysis that are relevant to the results presented in Chapters 7 and 8. Chapter 6 describes the experimental hurdle of multiple proton-proton interactions (collectively referred to as "pile-up") that must be overcome at the LHC, both presently and in the future. Finally, Chapter 7 presents the analysis of event shapes, correlations measured between final state hadrons that describe the energy flow within the event. Chapter 8 extends these studies by presenting some of the first measurements of jet substructure, the detailed analysis of the energy flow within a single jet itself.

Chapter 2

The theory of the strong interactions

Quantum chromodynamics (QCD) – the theory of the strong interactions – provides the theoretical framework for describing the properties and interactions of the particles that comprise the familiar protons and neutrons: quarks, and their associated force carriers, the gluons. Far from being a fundamental building block of nature, the proton is a composite particle, a bound state hadron that is merely nature's most stable version of two up quarks and one down quark[1]. That one can speak of such particles – the constituent quarks and gluons – is a triumph of QCD that has only emerged in the last half century and that we will discuss in detail in Section 2.1.

Like quantum electrodynamics (QED), QCD is a renormalizable gauge field theory and thus shares many of the characteristics of QED. Several important differences abound, though. QCD is, in many ways, a much richer theory [49]. QCD is represented by the non-Abelian symmetry group $SU(3)$ [47]. In this representation, the gluon is the gauge field – the QCD analog of the QED photon. Like electric charge in QED, QCD introduces its own "charge," or quantum number, referred to as color. However, the gluon is not a charge-neutral force carrier like the photon; the gluon in fact carries both color and *anti*-color charges (anti-color being the analog of negative

[1]The fact that the proton itself *is* stable, up to lifetimes on the order of 10^{33} years [48], is yet still a postulate based on the fact that we have not seen otherwise.

charge in QED). Gluons form an octet in color $SU(3)$ and due to its non-Abelian nature, the gluon gauge fields also exhibit self-couplings that allow for self-interactions. Such self-interactions significantly alter the gluon field dynamics in comparison to the more familiar photon field, which does not exhibit such couplings.

It is instructive to write down the Yang-Mills Lagrangian formulation of a generic non-Abelian gauge theory – the simplest QCD Lagrangian – and to analyze each term in order to establish the mathematical underpinning of the the theory's most important features. This Lagrangian can be written as

$$\mathcal{L} = \overline{\psi}(i\gamma^{\mu}\mathcal{D}_{\mu} - m)\psi - \frac{1}{4}F_{\mu\nu}F^{\mu\nu}, \tag{2.1}$$

where the first term, the fermion mass term, describes the basic equations of motion of the quarks, and the second term results in the self-interaction of the gluon vector fields [50]. This equation has only been written for only a single quark flavor, $\psi_j \rightarrow \psi$, and a single gauge field , $F^a_{\mu\nu} \rightarrow F_{\mu\nu}$ (of which there are three and eight, respectively). The ψ represent the fermion doublets, the quarks, and $\gamma^{\mu}\mathcal{D}_{\mu}$ is the covariant derivative.

Through experiments conducted during the mid 20^{th} century [40, 51], indications emerged that the $SU(3)$ formulation could naturally accommodate the full multiplet structure observed in terms of the fundamental representation of $SU(3)$. This representation, however, required the existence undiscovered new particles, the quarks themselves. These particles eventually became the constituents of the proton that Feynman had referred to as "partons" [52] in trying to describe the observations made in deep inelastic scattering experiments. This complex structure within QCD has persisted throughout the remainder of the 20^{th} century and gives rise to the rich phenomenology of the theory and jets in particular, the subject of this thesis.

2.1 The parton model of QCD

The development of QCD into a unique theory of the strong interactions did not start from the Lagrangian of Eq. 2.1, but rather from the experimental proliferation

of particle species found primarily in bubble chamber target experiments [53, 54]. These observations prompted Gell-Mann and Zweig to suggest that perhaps these particles were themselves composed of constituent fermions, the quarks [51, 55]. In order explain the full spectrum of hadronic states observed in terms of the higher dimension group, $SU(3)$, three quark *flavors* were required, up (u), down (d) and strange (s), each carrying fractional charge (2/3, -1/3 and -1/3, respectively). As Zweig stated:

> The 27-dimensional representation which occurs naturally in the Eightfold Way and which does not seems to be used by nature is suggestively absent [in $SU(3)$]. The only difficulty is that now the baryons seem to have baryon number 3. This we get around by assigning baryon number 1/3 to each member of the basic triplet....It is quite possible that aces [quarks] are completely fictitious, merely providing a convenient way of expressing a symmetry not present in the Eightfold Way. On the other hand, as we shall see, an experimental search for aces [quarks] would definitely seem worthwhile.

In this way, the proton could be described as a bound state of uud and the neutron as a bound state of udd. The fly in the ointment of this model, however, was the existence of the Δ^{++} baryon, which has angular momentum $J_3 = \frac{3}{2}$ and a charge of $+2$. That this configuration requires all three u quarks to have identical spin quantum numbers and seems to violate the fundamental assumption of an anti-symmetric fermion state necessitated an extension to the simple parton model of Gell-Mann and Zweig: color. Color is an extra quantum number denoted by R, G, B and is assigned to both quarks and gluons, where the latter comprise an octet of color $SU(3)$ while the former combine to form colorless hadrons.

Among the most fundamental quantities within QCD, in addition to the strong coupling strength, α_{S}, are the couplings of the quarks and gluons to each other. These interactions are commonly parameterized by the color factors C_F and C_A, which describe the relative probability of the quark-gluon and gluon-gluon couplings, respectively. Figure 2.1 shows the combined fit from LEP data to the preferred values

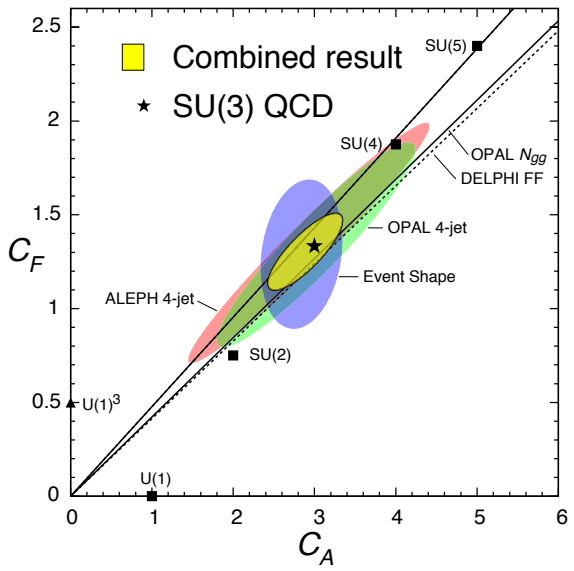

Figure 2.1: Constraints on color factors from multiple experiments [38], adapted from [30]. The combination of measurements results in a fit that supports the values $C_F = 4/3$ and $C_A = 3$.

of both C_F (4/3) and C_A (3) [30, 38]. Crucial to these fits were the measurements of the hadronic event shapes by the JADE collaboration at multiple center-of-mass energies [56, 57].

A consequence of the partonic nature of QCD is that a hadron like the proton is actually a complex composite object. A "core" set of valence quarks and gluons, as well as a sea of quarks that flit in and out of existence as the proton travels along comprise each proton. A proton's momentum is thus shared among these constituent partons. The distribution of the momentum fraction, x, carried by each parton expressed as a probability to find a particular parton with a given x. This formulation allows one to describe the structure of the proton at a very fundamental level and is termed the proton distribution function (PDF). In fact, the experiments described above discovered these features of hadrons via the scattering of other particles, primarily leptons, within the protons. The momentum transfer, Q^2, between the probe particles and the target hadron is analogous to the distance scale within the hadron being measured.

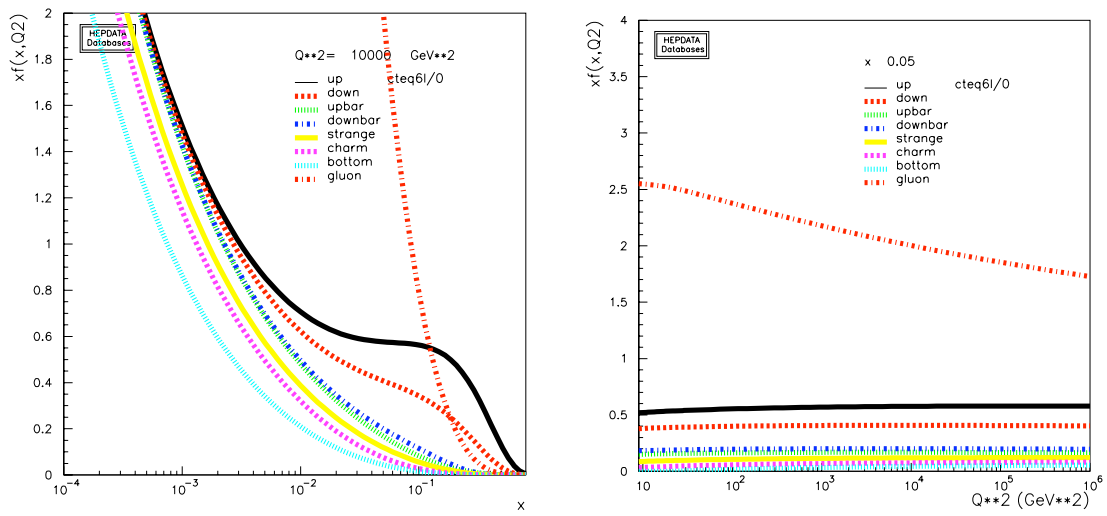

Figure 2.2: Parton distribution functions from the CTEQ Fitting Group version 6l [62] (a) as a function of the momentum fraction x and (b) as a function of Q^2 for a fixed momentum fraction $x = 0.05$.

Measurements of deep inelastic lepton-hadron scattering provided some of the first indications of the presence of quarks. Those measurements also became one of the primary methods by which to measure the PDF of protons [58, 59, 60, 61]. Tevatron measurements at 1.96 TeV were then combined with these measurements to refine the accuracy of the result through the use of additional Q^2 measurement points [62, 63]. In the case of Ref. [62], for example, the gluon PDF in particular was updated to match the inclusive cross-section measurement of jets (see Section 2.2). Figure 2.2 shows the PDF obtained from the CTEQ Fitting Group version 6l [62] as a function of both the momentum fraction x and as a function of Q^2 for a fixed momentum fraction $x = 0.05$. The dramatic scaling of the gluon PDF as a function of Q^2, as well as the choice to use pp instead of $p\overline{p}$ collisions at the LHC, is the source of the oft-heard phrase "the Tevatron is a quark collider and the LHC is a gluon collider."

A comparison of the cross-sections for several physics processes of interest is shown in Figure 2.3. It quickly becomes clear why the LHC has been constructed to operate at a center-of-mass energy of $\sqrt{s} = 14$ TeV; the cross-section for new physics processes such as Higgs production rises quickly with $\sqrt{s}$. It is also clear, however, that the

cross-sections for many processes of the Standard Model also rise quickly, the largest of which is the production of jets with large transverse energy.

2.2 Jet physics and phenomenology

Due to "infrared slavery" [6] – or its more commonly known name "confinement" – quarks do not exist in isolation, but rather hadronize to form stable color-singlet hadrons. Consequently, the experimental signatures of quarks and gluons are the final state hadrons into which they eventually coalesce. The bundle of particles produced tends to travel collinearly with the direction of the initiator quark or gluon. The result is a "spray" of hadrons entering the detector in place of the original parton; these clusters of objects are what we define as jets, and which we discuss in much more detail in Sections 2.2.1- 2.2.2.

Evidence for jet production was first observed in e^+e^- collisions at the SPEAR storage ring at SLAC in 1975 [20] using inclusive hadronic event shapes to demonstrate the presence of jets. Evidence for similar processes at a hadron collider required another 7 years for a suitable experimental apparatus to develop [26, 64]. The evidence came in the form of $2 \to 2$ processes, or so-called "di-jet" events such as the one shown in Figure 2.4 from the UA2 experiment at the CERN $Sp\bar{p}S$ collider. Such a seemingly simple event represents some the most fundamental processes within the Standard Model – that of the coupling of quarks to gluons and of gluons to each other. These events provide a probe of the very smallest distance scales attainable in modern physics and could potentially even contain sources of new physics hidden beneath the enormous cross-section.

The richness of QCD results in a much more diverse set of phenomena than merely the production of quark pairs. Soft and collinear divergences result in a high probability for both quarks and gluons to emit gluons, and gluons themselves can decay into two quarks. This showering effect gives rise to a "parton-level" jet prior to the formation of any hadrons. The resulting parton then showers and undergoes hadronization, as described above, resulting in the jets observed in the detector. In addition, it is possible to consider $N > 2$ partons participating in the initial and final states of the

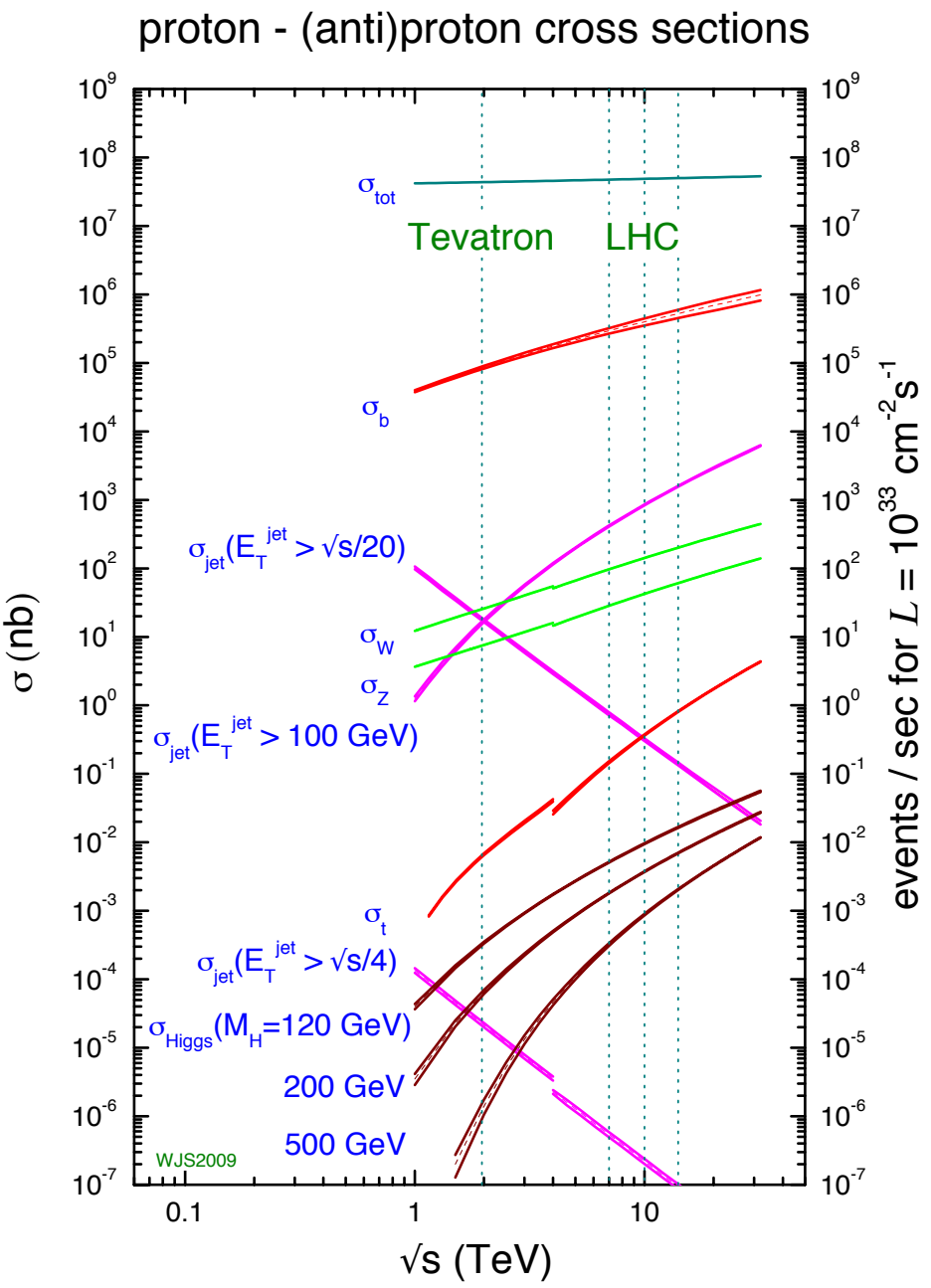

Figure 2.3: Cross-sections for various processes as a function of the center-of-mass energy.

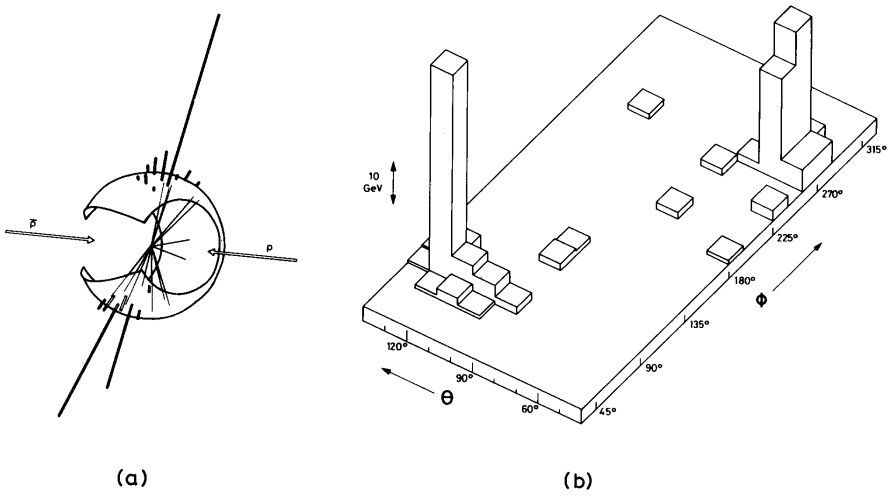

Figure 2.4: First evidence for hadronic jet production in the UA2 experiment in 1982 [26]. (a) Charged tracks pointing to the inner face of the central calorimeter of the UA2 detector are shown together with calorimeter cell energies (indicated by heavy lines with lengths proportional to cell energies). (b) The cell energy distribution as a function of polar angle θ and azimuthal angle ϕ.

process of interest, so called $2 \to n$ processes. In the latter case the computational complexity increases dramatically.

2.2.1 Monte Carlo tools, the parton shower, and underlying event

Cross-section predictions for jet production are obtained using either direct perturbative calculation of the cross-section matrix elements in powers of the strong coupling constant, α_S, or a comparison with a Monte Carlo (MC) sampling of the phase-space available for gluon emission with some suitable approximations. The former approach is performed at a fixed-order in α_S for each relevant partonic subprocess, with leading-order (LO) and next-to-leading order (NLO) calculations available for many processes. Simulation programs implementing the latter approach use LO perturbative calculations of matrix elements for $2 \to 2$ processes and rely on the parton shower to produce the equivalent of multi-parton final states. Matrix element MC programs

include ALPGEN [65], COMPHEP [66], MADGRAPH [67] and others [68, 69, 70, 71]. In the analysis presented here, we utilize ALPGEN 2.13 with exact matrix element calculations up to $n \leq 6$ partons and interfaced to HERWIG 6.510 [72] to provide the parton shower and hadronization model and with JIMMY 4.31 [73] for the underlying event model. Comparisons are made to the predictions from the MC programs PYTHIA 6.423 [74] with the Perugia 2010 tune [75] and HERWIG++ 2.4 [76], where these are used both for the simulation of the hard $2 \to 2$ process as well as for the parton shower, underlying event, and hadronization models. Very good summaries of the tools available for the LHC era are provided in Refs. [77, 78, 79].

Both MC and direct calculation methods must account for and correctly model the showering of partons prior to forming stable, detectable hadrons due to the non-Abelian nature of QCD, in turn due to the self-interaction term in the gluon field strength in Eq. 2.1. This fact allows both quarks *and* gluons to radiate additional gluons, and for gluons to form quark-antiquark ($q\bar{q}$) pairs along their path to hadronization. The cross-section for these emissions, however, is infinite at low k_t where the transverse momentum of the outgoing gluon with respect to the direction of the initial quark is small. This occurs when the gluon is either soft (an "infrared" divergence) or nearly collinear (a "collinear" divergence) with the original quark direction. Different MC programs control the coherence of these emissions by ordering successive emissions by scales related to their transverse momenta or angle with respect to the parton direction. PYTHIA 6.423 and HERWIG++ provide shower models which are p_T^2-ordered and angular-ordered, respectively, in the analyses presented in Chapters 7 and 8.

Infinities that arise as a result of the soft, collinear divergences in QCD often present an obstacle to precise calculations because of large logarithms that appear. These will be discussed in more detail below. The MC approach adopts a model for the probability and mode by which partons shower and hadronize and then utilize well motivated approximations to form predictions for the outcome . Another approach is to form an *effective* theory [80, 81, 82] that reduces the degrees of freedom involved in the system such that one can factorize the *calculation of* the hard, soft, and collinear components [83, 84, 85, 86, 87, 88, 89, 90, 91]. Such a soft, collinear effective

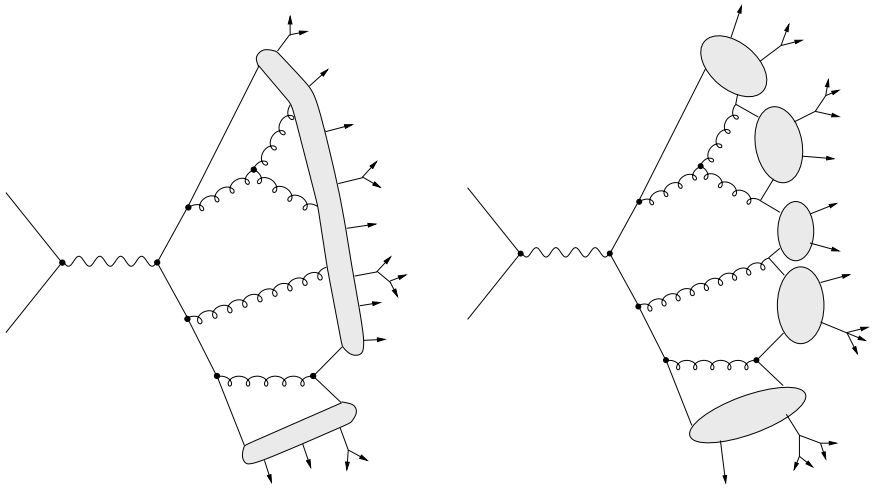

Figure 2.5: Most common phenomenological models for describing the parton shower in Monte Carlo simulations include (a) the string model, or the "Lund model" as implemented in the PYTHIA leading order Monte Carlo program and (b) the cluster fragmentation model as in the Herwig event generator.

theory (SCET) allows for an analytical prediction for processes that are otherwise only tractable using approximate models within MC programs. For the analyses presented here, multiple MC programs are used to compare to the data as they are much more ubiquitous in terms of their availability for a wide range of observables. The latter SCET methods have begun to reach fruition for hadron colliders in recent years [92, 93] and offer a fertile testing ground for our understanding of QCD from first principles. The results presented in this thesis are in part aimed at providing experimental results that might be useful to compare to these calculations in the future.

The two leading models to approximate the non-perturbative process of hadronization utilize string formation (Pythia) and clusterization (Herwig) of the final state partons. These models effectively to map partons onto stable hadrons as shown schematically in Figure 2.5. These hadrons are then what are used as input to the detector simulation.

Implicit in this entire discussion is the concept of *factorization* [83]. Factorization

refers to the set of theorems that allows one to calculate the cross-section for, say, jet production without reference to the complex processes of hadronization and parton shower evolution that were described above. Effectively, this permits the systematic separation of short and long distance behavior, thereby decoupling the phenomena which are perturbatively calculable from those which are not. This concept is exemplified by the structure of the cross-section for $pp \to X$. Following a common form (such as that used in Ref. [94]), the parton distributions are written as f, the cross-section for the process being considered is $\hat{\sigma}$, and the various scales of the problem are written as μ

$$\sigma_{pp' \to X}(\mu_{\mathrm{F}}, \mu_{\mathrm{R}}) = \int dx_1 dx_2 \; f_q(x_1, \mu_{\mathrm{F}}) \, f_{q'}(x_2, \mu_{\mathrm{F}}) \, \hat{\sigma}(x_1 x_2 Q^2, \alpha_{\mathrm{S}}(\mu_{\mathrm{R}}^2), \mu_{\mathrm{F}}, \mu_{\mathrm{R}}) \; . \quad (2.2)$$

Two scales enter the problem: the factorization scale, μ_{F}, and the renormalization scale, μ_{R}. The latter is the scale at which the natural divergences in the cross-sections are canceled by counter-terms in the Lagrangian [95, 96]. On the other hand, μ_{F} describes the scale at which the proton is being probed and thus also the scale at which the PDF of quarks and gluons participating in the scattering represented by Eq. 2.2 is evaluated. Often, these scales are identified with one another and written as $\mu_{\mathrm{F}} = \mu_{\mathrm{R}} = \mu$. Both scales will appear in ratios within the cross-section integral and thus as logarithms when expanded order-by-order in perturbation theory.

The presence of logarithms due to multiple scales is most apparent in the example of the dependence of α_{S} on μ_{R} and Λ_{QCD}, the ultraviolet cutoff scale used in QCD [97]. The "running of α_{S}," or the evolution of the coupling strength as the scale of the hard interaction is varied, is written at leading order as

$$\alpha_{\mathrm{S}}(\mu^2) = \frac{4\pi}{b \ln(\mu^2 / \Lambda_{\mathrm{QCD}}^2)} \, , \quad (2.3)$$

where the b coefficient originates in the renormalization group equation from which this result derives and is negative for QCD. This implies that when evolving to a lower scale, the resulting coupling strength increases. Eq. 2.3 reveals the order of magnitude of the scale at which α_{S} becomes large enough to destroy the assumption

that perturbative expansion is valid: $\Lambda_{\rm QCD} \approx 200$ MeV for $\mu \approx M_Z$, the mass of the Z boson.

Fundamentally, Eq. 2.3 represents an ultraviolet divergence that results in a scaling logarithm in the process of renormalization. Infrared divergences like those due to soft gluon emission result in similar *collinear* logarithms of the form $\alpha_{\rm S}^n \ln^{2n}(p_{\rm T}/m)$ and $\alpha_{\rm S}^n \ln^{2n-1}(p_{\rm T}/m)$. We will see the former in the discussion of jet mass in Section 2.3. One convention [98] is to refer to these terms as "leading logarithmic" (LL) and "next-to-leading logarithmic" (NLL), respectively. These terms may be exponentiated, leading to a sum of ratios of the relevant scales (here, $p_{\rm T}/m$) to all orders.

2.2.2 Jet algorithms

The ability to consistently define a jet as a single well-defined object is integral to the experimental measurements and to the theoretical predictions to which these data will be compared. Partons, hadrons, calorimeter clusters, even charged particles tracks may all be – and will be – used as input to the jet algorithm. At any stage of the evolution from initial state partons to final state hadrons to detector-level energy depositions we must be able to define and identify jets. Ideally, one jet $\longleftrightarrow$ one parton, but this is not necessarily well-defined in perturbation theory. In practice, it is also more complicated. One parton may form multiple experimentally observed jets (or vice-versa) due to the parton shower evolution, for example. In comparing data to expectations from theory and MC programs, one must be aware that the definition used to measure jets is exactly that, *a definition*. We must be consistent in the choice – for example, it is necessary to compare detector-level jets formed by calorimeter clusters with parton-level jets from a MC using the exact same definition – but that choice may differ depending on the physics goals towards which we aim.

Traditionally, jet algorithms have fallen into two general categories corresponding to the underlying approaches to defining a jet: "cone-like" and recombination algorithms. Cone-like algorithms are based on the collinear nature of gluon radiation and the parton shower described above; the decay products of and emissions from

an initial state quark will tend to form a cone of particles in the rapidity-azimuth ($y-\phi$) plane as they propagate outwards. This cone is equivalent to a cylinder in ($y-\phi-p_{\mathrm{T}}$) space. It is therefore natural to imagine that a cone of a suitable radius will capture these decay products and allow for some-level of representation of the final state particle(s) into which the initial quark hadronized. The design of cone-like algorithms attempts to maximize the amount of energy present in a stable cone of fixed radius. A crucial difficulty in the majority of implementations of this type of algorithm is the tendency to be sensitive to the details of soft or collinear radiation, which results in deep complications when attempting to perform NLO calculations of cross-sections [97].

Recombination-type algorithms, on the other hand, are specifically designed to be be well-behaved in the presence of soft (infrared) and collinear gluon emission. Such good behavior is referred to as being infrared and collinear (IRC) "safe." They are thus usable for calculations to any order in perturbation theory. The term recombination is used since they attempt to follow the parton shower branchings which become progressively softer as the shower evolves. The resulting jet can be thought of as as the final stage of this process and the algorithm is the device used to retrace the tree of sequential branchings. Recombination algorithms operate by successively combining pairs of particles using a distance metric, d_{ij}. At hadron colliders, for every pair of particles this metric is compared to a so-called "beam distance," d_{iB}, and only when d_{ij} is smaller than d_{iB} is the particle pair combined[2] and considered for subsequent clustering steps. The motivation for this approach is intimately related to the discussion of the parton shower evolution above: the soft, collinear divergences inherent in QCD suggest that the most likely gluon emission is at low k_t. For a pp or $p\overline{p}$ collision, the fact that one of the incoming partons may continue along the beam necessitates that the additional d_{iB} metric be included in order to account for this possibility.

[2]In all cases described here, the combination of two particles is always performed via a four-momentum sum, the so-called "E-scheme" recombination. In the case of single calorimeter cells, the four-momentum mass is set to zero, whereas for truth particles and track-jets the true particle mass or the pion mass is used, respectively (see Chapter 5 for details). Other approaches are possible, but this yields the most generically appropriate recombinations and is used throughout.

The three recombination algorithms that we will consider are natural extensions of the original k_t algorithm developed for the analysis of multi-jet events at e^+e^- colliders [22, 23, 99]. This algorithm was subsequently extended for use at hadron colliders by utilizing a metric that is invariant under longitudinal Lorentz boosts [100, 101]. It is instructive to compare both the original algorithm from the JADE collaboration as well as the ultimate definition of the modern k_t algorithm in order to identify relevant features of the algorithm.

The JADE recombination algorithm

1. Utilize the particle distance metric between particles i and j defined by

$$d_{ij} = \frac{2E_iE_j(1-\cos\theta_{ij})}{Q^2} \tag{2.4}$$

   where Q is the total energy in the event, E_i is the energy of particle i and θ_{ij} the angle between particles i and j.

2. Compute the minimum d_{ij}, $d_{\text{min}} = \min(d_{ij})$ among all particles.

3. For some threshold y_{cut}, if $d_{\text{min}} < y_{\text{cut}}$ then combine particles i and j and repeat from step 1.

4. If $d_{\text{min}} > y_{\text{cut}}$, then identify the remaining particles as the final jets.

The structure of this formulation will persist into the modern sequential recombination, but one feature is worth noting with this original definition. The jet multiplicity depends on the value of y_{cut}, as a lower value will result in more soft or collinear emissions surviving as jets. As noted in Ref. [102], this results in the number of jets being controlled by a single parameter instead of the two parameters (energy and angle) of cone algorithms. This is thus the first definition of an "event shape" that we encounter, and it is directly related to the design jet algorithm itself. The threshold y_{cut} marks the transition between two-jet events and three-jet event, wherein a small $y_{23} = d_{i=2,j=3}$ indicates a "two-jet-like" event and a large y_{23} indicates a multi-jet event. This can easily be seen by taking the limit of a nearly perfect di-jet event

compared to a so-called "Mercedes-like" event wherein three jets are spherically distributed in the event in both energy and momentum (i.e. angle). In the former case, $\theta_{23} \to 0$ and y_{23} vanishes so that any soft radiation should be combined with particles 1 and 2. In the latter case, $\theta_{12} = \theta_{23} = \theta_{13} = 2\pi/3$ and the numerator becomes $E_2 E_3$. When considering how the threshold to be considered a three-jet event plays a role, we take $Q^2 = (E_1 + E_2 + E_3)^2 = 9E^2$ and find that y_{cut} has the allowed values $0 < y_{\text{cut}} < 1/3$. In the case where Q^2 is defined using only the two leading jets, the allowed range is $0 < y_{\text{cut}} < 1/4$. This latter definition will be used in Chapter 7.

For a jet algorithm at a hadron collider, the definition of d_{ij} must account for the fact that partons scatter in a rest frame other than that of the center-of-mass of the colliding protons, unlike at an e^+e^- collider. In particular, the notion of the beam distance is added in order to render the algorithm frame-independent. A distance scale, $\Delta R = \sqrt{\Delta y^2 + \Delta\phi^2}$, is introduced to define the typical radius for a jet, effectively replacing y_{cut}. In this case, the particle distance metric becomes

$$d_{ij} = \min\left(p_{ti}^2, p_{tj}^2\right) \frac{\Delta R_{ij}^2}{R^2}. \tag{2.5}$$

In this case the beam distance metric is simply $d_{iB} = p_{ti}^2$ such that when no particle j is found such that $\Delta R_{ij} < R$, then i is promoted to the status of a jet. The formulation of the modern inclusive k_t algorithm is formulated as follows.

The inclusive and longitudinally invariant k_t algorithm

1. Utilize the particle distance metric d_{ij} defined by Eq. 2.5.
2. Compute the minimum d_{ij}, $d_{\text{min}} = \min(d_{ij})$, among all particles.
3. If $d_{\text{min}} < d_{iB}, d_{jB}$, where $d_{iB} = p_{ti}^2$, then combine particles i and j and repeat from step 1.
4. If $d_{ij} > d_{iB}$, then identify i as a jet and remove it from the list.
5. Continue until all particles are considered jets or have been clustered with other particles.

Two features render the k_t algorithm complex to utilize in the busy environment of a hadron collider. The first is that the definition of the distance metric in Eq. 2.5 results in the clustering of soft particles first. This has the potential to introduce complications when the detector noise or energy density fluctuations are large. The second feature is that particles with $\Delta R_{ij} > R$ can still be clustered within the jet, resulting in irregularly shaped jets. This is a problem when, for example, an irregularly shaped jet happens to extend into poorly instrumented detector regions. These issues will be discussed in more detail in the context of the ATLAS experiment itself in Chapter 5 using the full detector simulation.

The prescription given above may also be generalized beyond the k_t algorithm itself. The two most notable examples are the Cambridge-Aachen algorithm [103], or C/A, and the anti-k_t algorithm [104, 105], so named because of the inverted power law in the particle distance metric, d_{ij}. The particle distance metrics, d_{ij}, used by each of the three algorithms are shown in Table 2.1 along with the beam distance metric. The C/A algorithm relies solely on angular ordering of emissions in order to reconstruct the shower by omitting the transverse momentum scales from d_{ij} altogether. Going a step further, the anti-k_t algorithm effectively removes any sensitivity to the internal structure of the parton shower by clustering the hardest emissions first. The result is a much more experimentally tractable jet algorithm that has several benefits in the context of high-luminosity hadron collisions. For these reasons, both ATLAS and CMS have chosen the anti-k_t algorithm as the default jet algorithm for use in physics analysis [106]. One such example is illustrated in Figure 2.6 which shows the highest mass central dijet event (at the end of October 2010). Finally, an even more general prescription can be defined that encompasses all three of the algorithms described here and is provided in Table 2.1 as well. All of these algorithms, and many more, are implemented in the FastJet [107] software package that has effectively revolutionized jet physics at hadron colliders.

Algorithm	Particle distance (d_{ij})	Beam distance (d_{iB})
k_t ($a = +1$)	$\min\left(p_{ti}^2, p_{tj}^2\right) \dfrac{\Delta R_{ij}^2}{R^2}$	p_{ti}^2
C/A ($a = 0$)	$\dfrac{\Delta R_{ij}^2}{R^2}$	1
anti-k_t ($a = -1$)	$\min\left(p_{ti}^{-2}, p_{tj}^{-2}\right) \dfrac{\Delta R_{ij}^2}{R^2}$	p_{ti}^{-2}
Generic	$\min\left(p_{ti}^{2a}, p_{tj}^{2a}\right) \dfrac{\Delta R_{ij}^2}{R^2}$	p_{ti}^{2a}

Table 2.1: Summary of sequential recombination jet algorithms used at the LHC and the associated distance metrics. Each of these algorithms can be recast into the generic form shown in the bottom row with the power law parameter a defining the behavior of the algorithm.

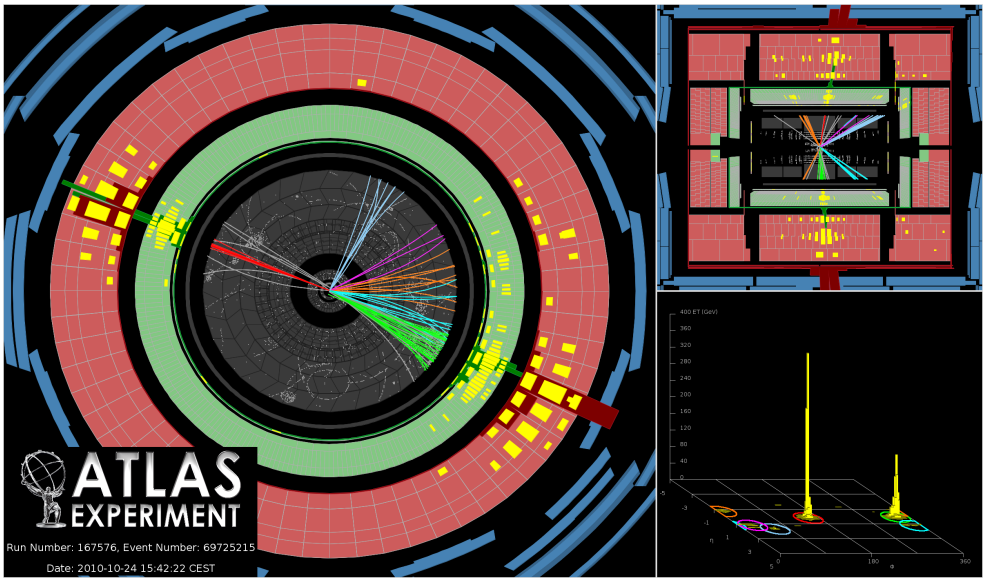

Figure 2.6: A di-jet event collected with the ATLAS detector clustered with the anti-k_t, $R = 0.6$ algorithm. The highest mass central dijet event and the highest-p_{T} jet collected by the end of October 2010, the event contains two central high-p_{T} jets that together have an invariant mass of 2.6 TeV and the highest p_{T} jet has $p_{\mathrm{T}} = 1.3$ TeV.

2.3 Hadronic event shapes and jet substructure

The hadronic final state may be explored in terms of the structure and shape of the hadronic energy flow – the "event shape" – as well as within the structure of the jets themselves. Both approaches seek to identify patterns and topological features that distinguish certain classes of events or individual objects, whether in the interest of describing perturbative QCD accurately or in the search for new physics.

Event shapes represent a generic class of observables that seek to describe the patterns, correlations, and origins of the energy flow throughout an event. These observables have had a long and fruitful history, having been used to observe gluon emission [108], measure the strong coupling constant α_S [33, 57, 109, 110], to constrain color factors for quark and gluon couplings [111], to test asymptotic freedom, to assess the accuracy of leading order and next-to-leading order MC generators [112, 113], and to search for physics beyond the Standard Model (BSM) [114].

The majority of event shapes are designed to distinguish between $2 \to 2$ and $2 \to n$ processes that have large contributions from gluon emission and soft, collinear divergences. To this end, we construct observables that vanish in the limit of a pure $2 \to 2$ process, and approach one for democratically distributed energy within a multi-jet event. In other words, these measurements attempt to determine the degree to which a particular event is *not like* a di-jet event. Perturbatively calculable predictions must account for all of the possible emissions within an event and therefore utilize all particles present in the event. Experimental measurements are necessarily restricted to a subset of this phase space insofar as real detectors must always implement energy thresholds and are never 100% hermetic.

Hadronic event shapes can offer several advantages over the explicit cross-section calculations for inclusive single and multi-jet production. One may define event shapes as normalized ratios of hadronic final state components, thus reducing the sensitivity to experimental uncertainties. Various choices can lead to enhanced or suppressed sensitivity to different components of the fundamental physical processes involved, such as underlying event, the parton shower, choice of renormalization and factorization scale, and so on. A full treatment of event shapes must go beyond fixed-order

calculations, however, due to the explicit inclusion of soft gluon emission.

In this analysis we consider six event shapes that are crucially tied to both the multi-jet nature of the event as well as the later consideration of jet substructure and have a strong history in the literature: the third jet resolution parameter, y_{23}, the sphericity and transverse sphericity, S^{pheri} and $S_{\perp}^{pheri}$ [115], the aplanarity, A, and the event thrust and its minor component, $\tau_{\perp}$ and $T_{m,\perp}$ [116, 117, 118]. The first observable, y_{23}, is directly related to the JADE recombination algorithm described in Section 2.2.2 and Eq. 2.4. y_{23} represents the threshold at which the event transitions from a di-jet event into a multi-jet (specifically three-jet) event and is here defined as:

$$y_{23} = \frac{d_{23}}{Q^2} \tag{2.6}$$

$$\text{where} \quad d_{23} = p_{T,3}^2 \tag{2.7}$$

$$\text{and} \quad Q^2 = (p_{T,1} + p_{T,2})^2, \tag{2.8}$$

and the $p_{T,i}$ are the transverse momenta of the i^{th} jets in the event, ordered by p_{T}. The sphericity, transverse sphericity, and aplanarity all embody more global information about the full momentum tensor of the event via its eigenvalues λ_1, λ_2 and λ_3:

$$M_{\alpha\beta} = \frac{\sum_i p_\alpha^i p_\beta^i}{\sum_i (p^i)^2} \tag{2.9}$$

where the sum runs over all particles, calorimeter energy clusters, or jets used in the measurement and $\alpha, \beta = 1, 2, 3$ are the x, y, and z components of the momenta. The eigenvalues satisfy the relations $0 \leq \lambda_3 \leq \lambda_2 \leq \lambda_1$ and $\lambda_1 + \lambda_2 + \lambda_3 = 0$. These can be combined to define the S^{pheri}, $S_{\perp}^{pheri}$, and A:

$$S^{pheri} \equiv \frac{3}{2}(\lambda_2 + \lambda_3), \tag{2.10}$$

$$S_{\perp}^{pheri} \equiv \frac{2\lambda_2}{\lambda_1 + \lambda_2}, \tag{2.11}$$

$$A \equiv \frac{3}{2}\lambda_3. \tag{2.12}$$

In this case, the sphericity (Eq. 2.10) and transverse sphericity (Eq. 2.11) measure the total transverse momentum with respect to the event axis which is defined by the four-momenta used for the event shape measurement. The aplanarity (Eq. 2.12) measures the amount of transverse momentum *out of* this plane. The transverse thrust, $T_\perp$, and its minor component, $T_{m,\perp}$, attempt to define explicitly a thrust axis for the event that maximizes the total transverse momentum of the event. These quantities are written as

$$T_\perp \equiv \max_{\hat{n}_\perp} \frac{\sum_i |\vec{q}_{\perp i} \cdot \hat{n}_\perp|}{\sum_i q_{\perp i}} \tag{2.13}$$

$$\tau_\perp \equiv 1 - T_\perp \tag{2.14}$$

$$T_{m,\perp} \equiv \frac{\sum_i |\vec{q}_{\perp i} \times \hat{n}_\perp|}{\sum_i q_{\perp i}}, \tag{2.15}$$

where $T_\perp$ is translated into $\tau_\perp$ in order to maintain a common event shape definition in which a large value indicates a departure from a two-body system. The unit vector $\hat{n}_\perp$ defines the thrust axis of the event. The *event plane* is defined by $\hat{n}_\perp$ and the beam and allows for a measurement of $T_{m,\perp}$. $T_{m,\perp}$ quantifies the sum of all transverse momenta $\vec{q}_{\perp i}$ *out of the event plane*, where the sum again runs over each particle, cluster, or jet i considered in the final state.

Figure 2.7 shows the predictions from various calculational tools and Monte Carlo generators. The matched NLO+NLL calculation including a full evaluation of the μ_R and μ_F scale uncertainties is compared to that using only a symmetric variation in which $\mu_R = \mu_F = \mu$. The deviation is very small, indicating that the three-jet resolution is relatively insensitive to the variation of these scales.

The NLO+NLL calculations shown in Figure 2.7 are compared to MC events generated using HERWIG 6.5 (green dashed line), PYTHIA 6.4 virtuality ordered shower (solid black line) and the PYTHIA 6.4 p_T ordered shower (magenta dotted line). In order to compute the event shapes where the logarithms from soft, collinear emissions are resummed and accounted for, a functional form for the observable's dependence on the momentum of a single soft emission, k, collinear to one of the hard "Born" partons ("legs") in the event is required. This parameterization is denoted by $V(\{\tilde{p}\}, k)$, which stands for any event shape that is perturbatively calculable and resummable.

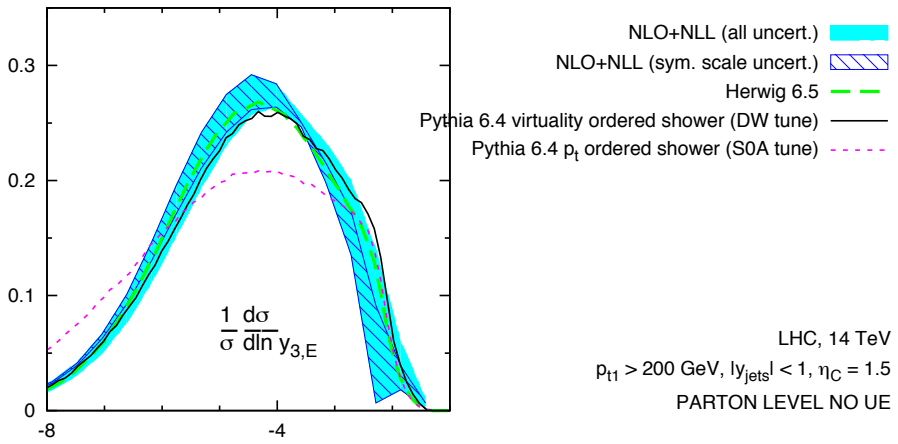

Figure 2.7: NLO+NLL predictions for the y_{23} event shape compared among various calculational tools and Monte Carlo generators. The matched NLO+NLL calculation including a full variation of the renormalization, μ_{R}, and factorization, μ_{F}, scales (filled blue) is compared to that using only symmetric variations (dark blue hatched). Comparisons are made with respect to MC events generated using HERWIG 6.5 (green dashed line), PYTHIA 6.4 virtuality ordered shower (solid black line) and the PYTHIA 6.4 p_{T} ordered shower (magenta dotted line) [119].

This can be written as

$$V(\{\tilde{p}\},k) = d_\ell \left(\frac{k_t^{(\ell)}}{Q}\right)^{a_\ell} e^{-b_\ell \eta^{(\ell)}}\, g_\ell(\phi)\,, \tag{2.16}$$

where the $\{\tilde{p}\}$ represent the Born momenta and k is the soft collinear emission. The terms $k_t^{(\ell)}$ and $\eta^{(\ell)}$ are the transverse momentum and rapidity, respectively, measured with respect to each Born parton or leg denoted by ℓ. Here, ϕ is an event-level quantity representing the azimuthal angle of each emission with respect to a the event plane, although for some specific observables (such as the three-jet resolution parameter) this is irrelevant. The function $g(\phi)$ represents the event shape's dependence on multiple soft, collinear emissions and can be any function for which $\int d\phi \ln g(\phi)$ is well defined. Lastly, Q is a hard scale of the event which we will take to be the sum of the momenta of the two hardest jets in the event, $Q = (p_{t,j1} + p_{t,j2})$. In fact, this choice has the possibility to introduce large variations in the higher order corrections,

as discussed at length in Ref. [120] and highlighted in Figure 2.8 for di-jet events. However, our choice of this form for Q is shown to reduce the enhancement of these so-called "K-factors"[120].

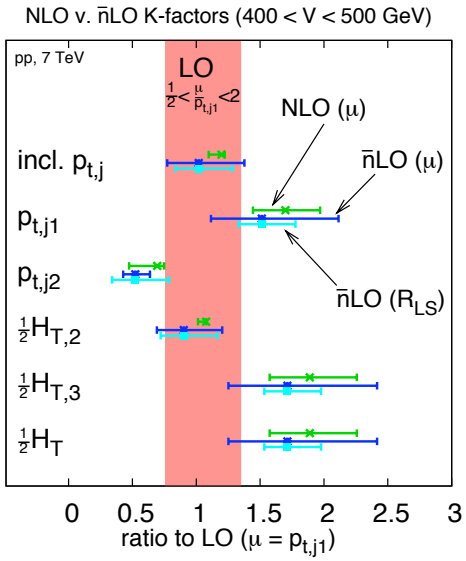

Figure 2.8: NLO and $\bar{\nu}$LO K-factors for the $400 < V < 500$ GeV bin for each choice of variable V among the following: the inclusive jet spectrum, the p_t distribution of the hardest ($p_{t,j1}$) and second hardest ($p_{t,j2}$) jets, (half) the effective mass of the two hardest jets ($H_{T,2}$), three hardest jets ($H_{T,3}$) and of all jets above 40 GeV (H_T). The NLO and $\bar{\nu}$LO (μ) error bars correspond to the uncertainty due to simultaneous renormalisation and factorisation scale variation by a factor of two around a central value $\mu = p_{t,j1}$. The $\bar{\nu}$LO ($R_{\rm LS}$) width shows the uncertainty from a variation of $R_{\rm LS}$ in the range $0.5 < R_{\rm LS} < 1.5$ [120].

The generic concept of event shapes is useful for classifying events and the energy flow on a global scale. In searches for new physics one often would like a prescription for the identification of individual objects that might be the signature of new particles or their decay products. For example, the decay products of a boosted heavy quark or boson might be reconstructed as a single jet; an ability to select these jets allows for the study of their properties. This is the realm of *jet substructure* in which the detailed internal structure of jets is used as a probe of both QCD and new physics. The primary aim of approaches that fall under this growing discipline is to utilize the jet as more than simply a "surrogate for individual short distance partons" [121] and

to probe its internal structure for information about the physics of parton showers, leading log resummation, and even new physics.

A wide array of tools and techniques has developed rapidly in recent years [122, 121, 123, 124, 125, 126, 127, 128, 129, 130, 131, 132] and some of these have already been tested in LHC data [133, 134]. The analysis of $H \to b\bar{b}$ presented in Ref. [122] by Butterworth, Davison, Rubin, and Salam (BDRS) is widely credited with jump starting these activities. However, the legacy of jet substructure stretches back nearly 20 years to Michael H. Seymour's Ph.D. thesis work [135]:

> The W-finder used in study utilizes [the ΔR_{jj} cut] by running a jet finder twice, once with cone sizes of $\Delta R = 0.75$ and $\Delta R = 0.25$, and then demands a big jet containing two small jets, with $|m_{jj} - m_W| < 10$ GeV.

This approach of "peeking" inside of the jet with a well defined algorithm to see if there is structure representative of heavy objects persists into the 20$^{\text{th}}$ century.

Among the diverse set of tools that has become available in recent years, the common thread linking each of them is their reliance on the use of modern jet algorithms such as those described in Section 2.2.2. The sequential recombination algorithms allow for parsing of the parton shower tree using both angular and transverse momentum scales in a very natural and well-defined manner. Both the k_t and C/A algorithms allow one to trace the parton shower backwards from the jet through each successive splitting (or recombination when viewed from the perspective of the showering parton). At each point, the angular and momentum scales of the two recombined branchings can be compared to each other as well as to the "parent" jet. Due to the structure of QCD, the distribution of these scales is expected to peak in the soft and collinear region. This is contrasted with that expected from heavy particle decays which will exhibit structure characteristic of the mass scales involved, for example as in the case of a top quark decay at high boost.

Figure 2.9 shows two jets that originate from completely different physics processes: the first is the result of a boosted hadronic top quark decay ($\bar{t} \to W^- \bar{b} \to q\bar{q}\bar{b}$) whose decay products are collimated into a single jet, whereas the second example is a similarly high-mass jet (157 GeV) but instead initiated by final state gluon emission.

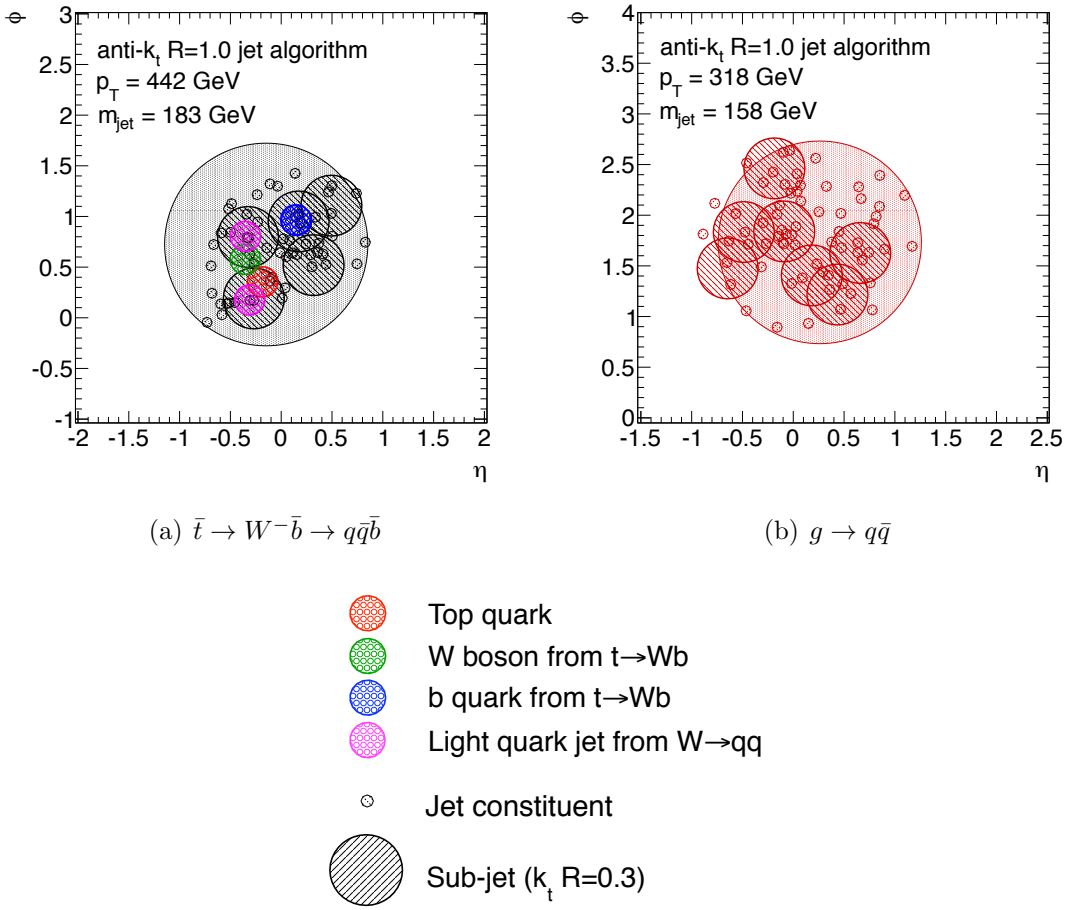

(a) $\bar{t} \to W^- \bar{b} \to q\bar{q}\bar{b}$ (b) $g \to q\bar{q}$

Figure 2.9: Single high mass ($m^{\text{jet}} \sim 150 - 200$ GeV), high transverse momentum ($p_{\text{T}}^{\text{jet}} > 300\ GeV$) jets from (a) boosted hadronic top quark decay ($p_T^t = 337$ GeV) and (b) a gluon splitting to two light quark jets (q). In the case of the top quark the substructure of the jet, including both the subjets and the application of the jet filtering algorithm, aid in discriminating this jet from the background.

In this particular case, several distinguishing characteristics can be determined using the techniques of jet substructure which aim to characterize such internal jet energy flow.

Jet Mass The jet mass itself can be used to discriminate at a high-level between jets initiated by a massive object and those that are the result of successive branchings of the parton shower. As discussed above, massive jets formed by the latter are expected to be dominated by wide-angle emissions and which are difficult to predict due to the presence of large logarithms [136]. One approach is to approximate a "jet function" which aims to quantify the probability for a jet with a given p_{T} to acquire a mass between m^{jet} and $m^{\mathrm{jet}} + \delta m^{\mathrm{jet}}$. The eikonal approximation introduced in Ref. [136] permits an approximate jet function, $J^{(eik),c}(m^{\mathrm{jet}}, p_{\mathrm{T}}, R)$, to be written as

$$J^{(eik),c}(m^{\mathrm{jet}}, p_{\mathrm{T}}, R) \simeq \alpha_{\mathrm{S}}(p_{\mathrm{T}}) \frac{4\, C_c}{\pi m^{\mathrm{jet}}} \log\left(\frac{R\, p_{\mathrm{T}}}{m^{\mathrm{jet}}}\right). \tag{2.17}$$

In Eq. 2.17, $\alpha_{\mathrm{S}}(p_{\mathrm{T}})$ is the strong coupling constant, c represents the flavour of the parton which initiated the jet and C_c represents the quark and gluon color factors, C_F and C_A, respectively, and R is the characteristic jet radius. This approximation breaks down in the low m^{jet} regime for which NLO predictions are overwhelmed by non-perturbative effects. The three most salient features of this approximation are the logarithmic decay of the probability to observe high mass jets arising purely from QCD effects, the increased probability to see high mass jets initiated from a gluon as opposed to a quark, and the dependence on R and p_{T}. Large radii jets at high p_{T} are thus expected, naturally, to exhibit higher mass scales. This feature will come into play in Chapter 8 where the competing effects of detector-related experimental issues will be brought to bear on the measurement of high mass jets.

Subjet multiplicity and topology By using successive recombination algorithms such as those described in Section 2.2.2, it is straightforward to define a "subjet algorithm" in which the structure of the constituents of a given jet are parsed using either the original algorithm or a new one at a fixed distance parameter. This concept was initially suggested in the context of e^+e^- and DIS experiments [137, 138, 139] in

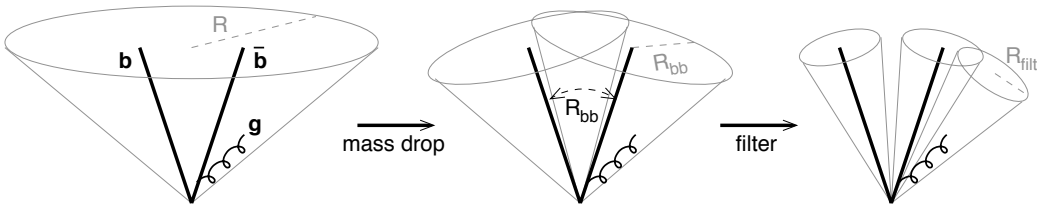

Figure 2.10: Jet filtering using the C/A algorithm as defined in Ref [122]. subjets are defined by de-clustering the C/A algorithm and then evaluating the relative masses of the subjets compared to the parent jet. As a final step, the three hardest identified subjets are recombined to define the resulting "filtered" jet.

order to quantify the jet multiplicity at various kinematic scales in order to facilitate comparisons with theory. Subsequent to the development of a longitudinally invariant $k_\perp$ algorithm [100, 101], a similar but slightly different approach was also used at hadron colliders [140, 141, 142].

In addition to fixed distance parameter subjets, it is also possible to "unfold" the jet algorithm, or to undo the last recombination step in a successive recombination algorithm. In fact, any number of de-clustering steps may be used in order to reverse the action of the jet algorithm. This approach is used in several jet grooming procedures [122, 123, 124, 126] in order both to identify the primary features of the parton shower and perturbative QCD as well as to improve the signal to background ratio for specific searches for new physics. This method has been demonstrated to work well to search for the Higgs boson decays to two b-quarks, $H \to b\bar{b}$ [122].

The so-called BDRS method of jet grooming uses the C/A algorithm (see Section 2.2.2). Subjets are then defined by de-clustering the C/A algorithm and evaluating the relative masses of the subjets compared to the parent jet. As a final step, the three hardest identified subjets are recombined to define the resulting "filtered" jet. Each step of this procedure is described below, with Figure 2.10 describing this schematically for a single jet meant to be representative of the manner in which the technique is used in Ref. [122].

1. Undo the last clustering step of J to get two subjets $j1$ and $j2$ ordered such that $m_{j1} > m_{j2}$. If J cannot be unclustered (i.e. it is a single particle) or $\Delta R_{j1,j2} < 0.3$ then it is not a suitable candidate, so stop.

2. If the splitting has $m_{j1}/m^{\text{jet}} < \mu$ (large drop in mass) and $y_2 > y_{2\text{cut}}$ (fairly symmetric) then go to step 4.

3. Otherwise redefine $J = j1$ and go back to step 1.

4. Recluster the constituents of J with the Cambridge-Aachen algorithm with an R-parameter of $R_{\text{filt}} = \min(0.3, \Delta R_{j1,j2})$ finding n new subjets j_1, $j_2 \ldots j_n$.

5. Redefine $J^{\text{filt}} \equiv \sum_{i=1}^{\min(n,3)} j_i$.

The algorithm defines $y_2 = \frac{\min(p_{T,j1}^2, p_{T,j2}^2)}{(m^{\text{jet}})^2} \Delta R_{j1,j2}$ and $\Delta R_{j1,j2} = \sqrt{\delta y_{j1,j2}^2 + \delta \phi_{j1,j2}^2}$. The selection placed on the "mass drop" is $\mu = 0.67$ and the symmetry between the two subjets is required to be $y_2 > y_{2\text{cut}} = 0.09$. The commissioning of this algorithm in data will be explored in detail in Chapter 8.

The utility of such jet grooming techniques have been thoroughly documented [143, 144] for their ability to improve the mass resolution of jets from heavy particle decays and to remove energy contributions unrelated to the hard partons (see Chapter 8 for demonstrations of this in the ATLAS data). Figure 2.11 from Ref. [144] exemplifies the use of jet grooming techniques such as filtering. While a full and complete breakdown of the other techniques appearing in Figure 2.11 is outside the scope of this thesis, each approach is designed to achieve an enhancement in the signal obtained from boosted objects decaying to jets while reducing the fake rate for QCD jets to appear in the signal region of such selections.

It is also possible to extend the use of individual subjets in conjunction with more traditional jet shape variables. Using these tools, an inclusive jet shape based on the substructure topology of a single jet, "N-subjettiness" [130] has been defined. This observable seeks to measure the extent to which a given jet is likely to be composed of N subjets by first identifying a set of subjets and then comparing the energy flow in the jet to the direction of these subjets. The observable, τ_N is calculated as

$$\tau_N^{(\beta)} = \frac{1}{d_0} \sum_k p_{T,k} \min \left\{ (\Delta R_{1,k})^\beta, (\Delta R_{2,k})^\beta, \cdots, (\Delta R_{N,k})^\beta \right\}. \tag{2.18}$$

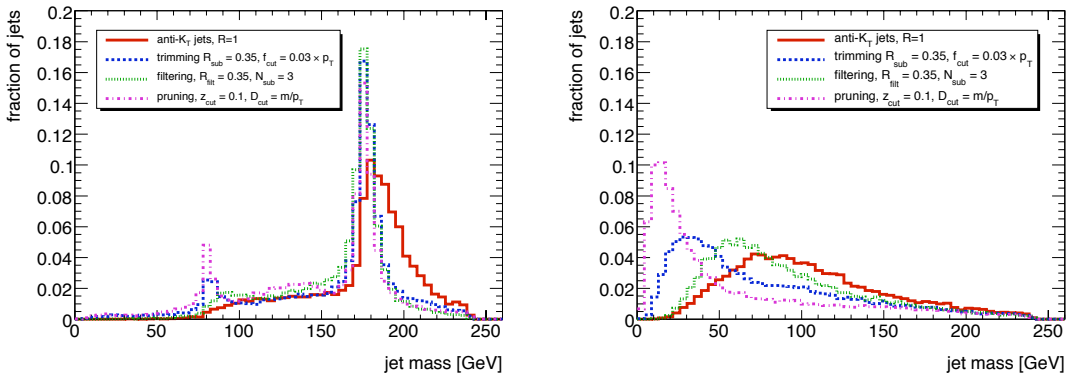

(a) $t\bar{t}$, 500–600 GeV

(b) QCD dijets, 500–600 GeV

Figure 2.11: Jet invariant mass m^{jet} for (left) $t\bar{t}$ and (right) dijet events for three grooming methods. Each groomed analysis begins withanti-k_t, $R = 1.0$ jets. The red curve represents these jets without grooming. The distributions correspond to $t\bar{t}$ and QCD dijet samples with parton-level p_{T} of 500–600 GeV.

The sum runs over the k constituent particles in a given jet where $p_{T,k}$ are their transverse momenta, and $\Delta R_{j1,k} = \sqrt{\delta y_{j1,k}^2 + \delta\phi_{j1,k}^2}$ is the distance in $\Delta y \times \Delta\phi$ between a candidate subjet $j1$ and a constituent particle k. An exponential weight β may optionally be applied to the angular distance computed between the subjets and the jet constituents. The normalization factor is defined by

$$d_0 = \sum_k p_{T,k} \left(R_0\right)^{\beta}, \tag{2.19}$$

where R_0 is the characteristic jet radius used in the original jet clustering algorithm. The parton level studies of the performance of this observable for hadronic W boson and top quark decays indicate that *ratios* of τ_N exhibit the most disrimination power between signal and background. Two ratios, $\frac{\tau_2}{\tau_1}$ and $\frac{\tau_3}{\tau_2}$ are defined as

$$\tau_{nm} = \frac{\tau_n}{\tau_m} \tag{2.20}$$

with $n = m + 1$ in order to differentiate between states with a high probability to be composed of only a single subjet as compared to two, and so on. I will focus on

evaluating the modeling and usage of these ratios in Chapter 8.

Color flow Jet substructure techniques also extend beyond the identification of hard objects within a jet and into the event itself. This "event-shape-meets-jet-shape" regime is explored in an effort to profit from the vastly different physics processes that give rise to massive QCD jets as compared to massive jets from the decays of boosted massive particles. Planar flow, angularity [125], jet pull [127], and dipolarity [145] are just a few such quantities that each aim to provide a description of the color flow, or energy correlations due to color connections between initial and final state partons, as well as to the decay products of massive particles. For example, the production of two b-quarks is possible both from electroweak production of a Higgs boson – a color singlet – as well as QCD production of a gluon that splits to two b's – a color octet. The radiation pattern of these processes are expected to exhibit marked differences that might be measurable using the concept of color flow.

In the studies presented in Chapter 8, detector level measurements of dipolarity, $\mathcal{D}_{mn}$, are presented. This quantity, like jet pull, is intended to measure the color "connectedness" of the final state. Whereas pull is a p_{T}-weighted vector in $y-\phi$ space that is intended to point towards the color-connected partner (or to the beam, in the case of generic QCD radiation in a di-jet system), the dipolarity attempts to consider the radiation pattern of the jet system in consideration in its entirety.

The definition of $\mathcal{D}$ once again uses the concept of subjets in order to define reference points within a jet. For a jet, J, with two subjets, $j1$ and $j2$, located at (η_{j1}, ϕ_{j1}) and (η_{j2}, ϕ_{j2}) the distribution of jet constituents i around the line segment $\ell_{j1,j2}$ connecting the two subjets defines $\mathcal{D}$. In this case, R_i is the Euclidean distance in $\eta-\phi$ between the jet constituent at (η_i, ϕ_i) and $\ell_{j1,j2}$. Dipolarity is then calculated for this two-subjet system as the p_{T}-weighted sum

$$\mathcal{D} \equiv \frac{1}{R^2_{j1,j2}} \sum_{i \in J} \frac{p_{Ti}}{p_{T_J}} R_i^2, \tag{2.21}$$

where $R^2_{j1,j2} \equiv (\eta_{j1} - \eta_{j2})^2 + (\phi_{j1} - \phi_{j2})^2$. This definition may also be extended beyond the study performed in Ref. [145] in the case of three-body decays where

three subjets are measured by defining $\mathcal{D}$ with respect the third subjet as well. This results in $\mathcal{D}_{12}$, $\mathcal{D}_{13}$, and $\mathcal{D}_{23}$, defined just as in Eq. 2.21, except by redefining $R_{j1,j2}$ and $\ell_{j1,j2}$ appropriately.

Finally, it has been shown that the combination of many different approaches to defining substructure can increase the potential to distinguish the many classes of hadronic jets expected to be produced at the Large Hadron Collider [129, 144].

Chapter 3

The Large Hadron Collider

The Large Hadron Collider (LHC) is a proton-proton (pp) synchrotron located in the previous Large Electron Positron (LEP) collider tunnel at CERN approximately 100 m underground. As of 2010, it is the largest scientific instrument ever constructed and the source of the highest energy collisions ever produced by mankind[1]. Perhaps more impressive than its breathtaking proportions is the fact that the LHC machine is a precision instrument capable of delivering pp collisions millions of times per second in a volume whose dimensions are similar to that of a human hair. Both the precision and the power delivered by the LHC make very real the new possibilities for the discovery of as yet unknown components of our universe. The detectors that hope to see evidence for these features – themselves representative of superlatives such as the largest superconducting magnet system ever built (ATLAS, see Chapter 4) and heaviest particle detector system (CMS) – are the windows into the sub-subatomic world that the LHC creates trillions of times per year.

[1] Of course, Nature is able to produce collisions between ultra high-energy cosmic rays and the upper atmosphere more than 7 orders of magnitude more energetic – 10^{20} eV compared to 10^{13} eV – right here on Earth. However, these happen at a rate of less than once per year within the Pierre Auger Observatory [146] making them much less useful for studying processes which are themselves rare.

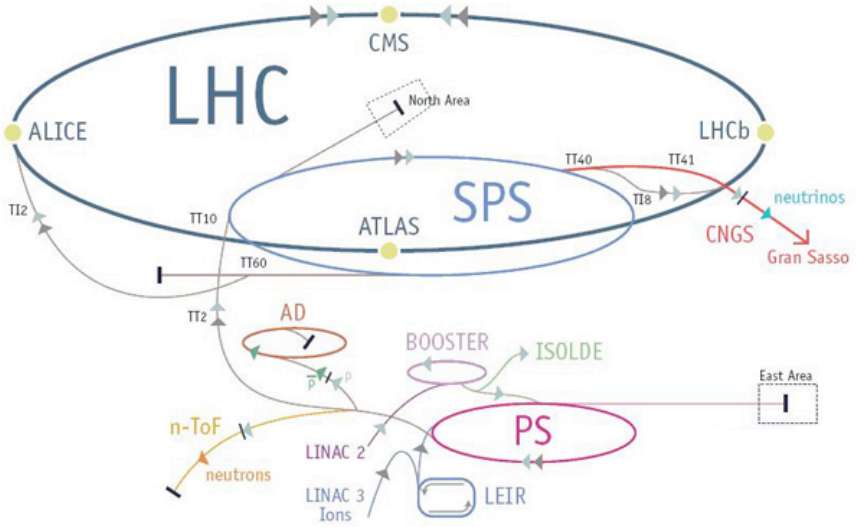

Figure 3.1: The CERN accelerator complex.

3.1 Machine design and early LHC Operation

The LHC is only the final stage in an accelerator complex consisting of several intermediate accelerators. This chain is shown graphically in Figure 3.1 and consists of the following components, with the proton energy at extraction from each stage also specified: Linac 2 (50 MeV) – Proton Synchrotron Booster (PSB, or "Booster"; 1.4 GeV) – Proton Synchrotron (PS; 25 GeV) – Super Proton Synchrotron (SPS; 450 GeV) – LHC (0.45 - 14 TeV). Each stage leaves an imprint on the resulting beam structure and stability. A coherent operation of each system must be maintained in order for the final high-energy proton beam to be of sufficient quality to provide stable collisions for physics in the detectors.

The experiments tasked with analyzing the collisions produced by the LHC are distributed around the 27 km ring at the various interaction points or IPs. The all-purpose detectors ATLAS [147] and CMS [148] are situated at IP1 and IP5, respectively. Specialized detectors of the ALICE [149] and LHCb [150] experiments are located a IP2 and IP8, respectively. Perhaps the most crucial aspect of the machine system for physics is the quality and characterization of the interaction point

within each experiment, as this is where the resulting luminosity is ultimately established. The definition of the "geometric" luminosity in terms of the overlap of the two colliding beams is given as

$$\mathcal{L}_0 = n_c \, f_{\text{rev}} \, \frac{N_1 N_2}{4\pi \, \sigma_x^* \, \sigma_y^*}. \tag{3.1}$$

Written this way, f_{rev} is the revolution frequency of the proton bunches in the beam, n_c is the number of colliding bunch pairs, N_b ($b = 1, 2$) is the number of protons per bunch in beam b, and $\sigma_{x,y}^*$ are the transverse IP beam sizes. The $\sigma_{x,y}^*$ are not to be confused with the size of the resulting interaction, or "luminous," region which represents the spatial distribution of the pp interactions. This distribution is characterized by a position $(\overline{x}_{\mathcal{L}}, \overline{y}_{\mathcal{L}}, \overline{z}_{\mathcal{L}})$, a size $(\sigma_{x\mathcal{L}}, \sigma_{y\mathcal{L}}, \sigma_{z\mathcal{L}})$, and two tilt angles $(\overline{x}'_{\mathcal{L}}, \overline{y}'_{\mathcal{L}})$. A full description of the parameterization of this distribution is reserved for Appendix A.2.

The LHC design calls for round, symmetric proton beams at the LHC interaction points. The normalized transverse emittances, $\epsilon_{N\,x,y}$, and the β-functions at each IP, $\beta_{x,y}^*$, characterize these properties of the beams and the resulting luminous region. Values for $\epsilon_{N\,x,y}$ and $\beta_{x,y}^*$ in 2010, among others, are compared to design specification and summarized in Table 3.1. These parameters define the sizes and shapes of the individual LHC beams at the interaction point and are thus integral to the optimization of the luminosity delivered to each experiment. The expression for the individual transverse beam sizes σ_{ib} ($i = x, y$ and $b = 1, 2$) in terms of these quantities is given in Eq. A.1 as

$$\sigma_{ib} = \sqrt{\epsilon_{ib} \beta_{ib}}. \tag{3.2}$$

Although $\epsilon_{N\,x,y}$ and $\beta_{x,y}^*$ are not directly measurable at the IP they can be inferred from synchrotron-light or wire-scanner beam-profile measurements elsewhere in the LHC ring, provided the lattice functions are known with sufficient accuracy. The resulting transverse luminous size, or transverse size of the "beam spot", is directly determined from the sizes of each of the individual beams. The vertical luminous

size, or vertical *beam spot width*, is given by

$$\sigma_{y\mathcal{L}} = \left(\frac{1}{{\sigma_{y1}}^2} + \frac{1}{{\sigma_{y2}}^2} \right)^{-1/2} , \tag{3.3}$$

with an equivalent expression for the horizontal luminous size $\sigma_{x\mathcal{L}}$. More details on the definitions used here can be found in Appendix A. The experimental characterization of the luminous region constituted a significant undertaking in the first data and is one of the tools for measuring the absolute luminosity of the LHC and in reducing the systematic error on its value [151].

The potential for multiple pp interactions in a single bunch-crossing also increases with increasing luminosity for a given bunch structure configuration (such as the number of filled bunch positions, n_c) and bunch charge, N_b. For a given average number of pp collisions, $\langle N_{pp} \rangle$, the average expected number of inelastic collisions is referred to as $\langle \mu \rangle$, whereas the number of resulting primary vertices is often written as $\langle N_{\mathrm{PV}} \rangle$ (see Section 3.3 and Chapter 6). $\langle N_{\mathrm{PV}} \rangle$ is typically smaller than $\langle \mu \rangle$ and $\langle N_{pp} \rangle$ as the observed interactions are dominated by non-single diffractive collisions where both protons break-up. Table 3.1 also lists the expected $\langle N_{pp} \rangle$ for 2010 compared to the LHC design.

The LHC produced pp collisions for the first time with the full ATLAS and CMS detectors recording data in December 2009 at the SPS extraction energy of 450 GeV per beam. During this period, bunch intensities were limited by machine-protection considerations to 1.5×10^{10} protons, with typically 4 bunches in each beam out of which two bunch pairs were colliding in ATLAS [152]. The larger energy stored in the 3.5 TeV beams limited the early 2010 collisions to bunch intensities of $\sim 1 \times 10^{10}$ protons, with 2 (3) bunches in each beam of which 1 (2) pair(s) collided in ATLAS. At these reduced intensities, the injected transverse and longitudinal emittances were often a factor of two smaller than nominal, providing some margin for mismatch and blowup in the not-yet-fully-optimized LHC rings. The β-functions were measured and corrected back to the nominal values to an average accuracy of $\pm 20\,\%$. All $\sqrt{s} = 900$ GeV data, and early $\sqrt{s} = 7$ TeV data, were logged with $\beta^* = 11$ m at IP1, whereas the majority of data recorded in 2010 at $\sqrt{s} = 7$ TeV were logged with

Machine parameter	$\sqrt{s} = 900$ GeV	$\sqrt{s} = 7$ TeV	$\sqrt{s} = 14$ TeV (design)
f_{rev} [Hz]	11245	11245	11245
n_c	1 - 9	1 - 368	2808
N_b (10^{10} p/bunch)	1.5	1 - 11	11.5
$\epsilon_{N\,x,y}$ [μm-rad]	2 - 4	1.5 - 10	3.75
$\beta^*_{x,y}$ [m]	11	11 - 2	0.55
$\sigma^*_{x,y}$ [μm]	280	100 - 40	16.6
σ_z [mm]	65	35 - 60	75
$\mathcal{L}$ [cm^{-2}s^{-1}]	1 - 3 $\times 10^{26}$	$10^{27} - 2 \times 10^{32}$	1.0 $\times 10^{34}$
$\langle N_{pp} \rangle$	$\ll 1$	1-5	25

Table 3.1: Typical parameters at the ATLAS IP during 2010 LHC operation, and design parameters at the nominal energy. f_{rev} is the revolution frequency, n_c is the number of colliding bunch pairs, N_b ($b = 1, 2$) is the number of protons per bunch in beam b, $\epsilon_{N\,x,y}$ are the normalized transverse emittances, $\beta^*_{x,y}$ are the β-functions at the ATLAS IP, $\sigma^*_{x,y}$ are the transverse IP beam sizes, σ_z is the bunch length, $\mathcal{L}$ is the luminosity and $\langle N_{pp} \rangle$ is the expected average number of pp interactions per bunch crossing.

$\beta^* = 3.5$ m with a brief period during phase 1 (see below) with $\beta^* = 2$ m. The very small number of bunches allowed the beams to be brought into collision at IP1 with zero (or negligible) crossing angle. Luminosity scans were used to optimize the transverse overlap between the two colliding beams so as to measure the geometrical luminosity.

Two of the first tasks undertaken when first attempting to collide the LHC beams at $\sqrt{s} = 900$ GeV were to verify that the beams were indeed colliding and to optimize the interaction point position within ATLAS. The procedure used to conduct these tests is called "RF cogging" in reference to the radio frequency controlled arrangement of bunches. The location of the colliding proton pair is shifted sequentially among the available RF positions in order to adjust the collision point with respect to the nominal interaction point.

On Monday, November 23$^{\text{rd}}$, the beams were brought into collision and an RF cogging shift of 900 ps was performed [153] and measured by electrostatic beam pickups [154]. This cogging shift corresponds to an expected longitudinal shift in the

interaction point of $\Delta z^{\text{expected}} = 134.9 \pm 0.7$ mm, according to the BPTX which has a timing precision of approximately 50 ps. The charged track longitudinal impact parameter with respect to the nominal origin (z_0) was measured before and after the beam position shift, in order to confirm that collisions were indeed occurring and that the collision point was centered. Indeed, as shown in Figure 3.2, the observed shift of $\Delta z^{\text{observed}} = 140.7 \pm 10.5$ mm, both confirmed the presence of pp collisions by demonstrating that a timing shift of the expected proton bunch positions within the detector resulted in the expected shift of the charged particles emitted transverse to the beam line. This fact verified that the observed charged particle tracks were the result of pp collisions and that the collision point was well-positioned within 3 cm of the nominal detector origin.

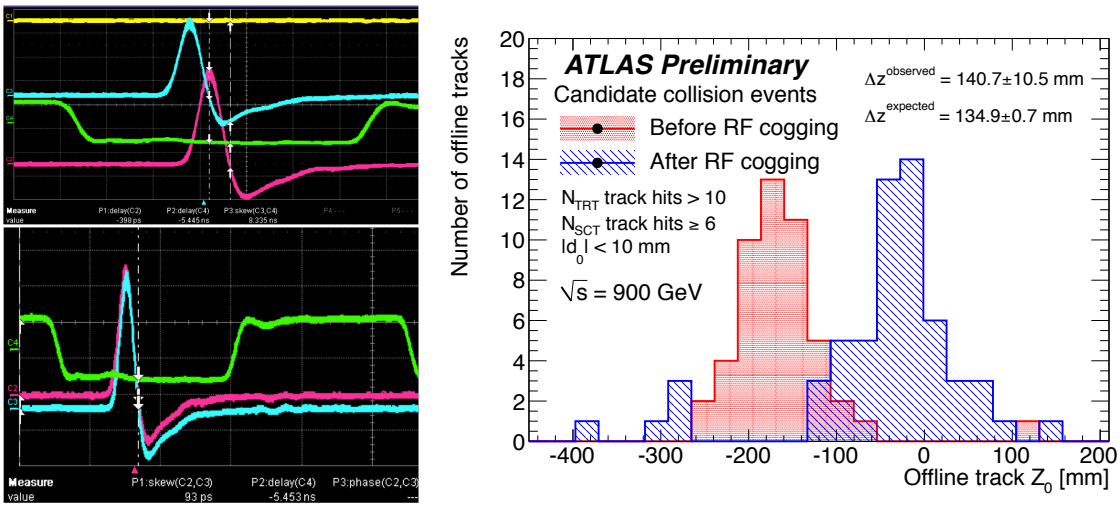

(a) (b)

Figure 3.2: Measurements conducted during the RF cogging procedure for the first collisions of the LHC. (a) Phase relationship of beam 1 (blue) to beam 2 (red/magenta) before (top) and after (bottom) the RF cogging. (b) Measured shift in the longitudinal impact parameter with respect to the nominal origin before (blue) and after (red) RF cogging of the LHC. An expected shift of $\Delta z^{\text{expected}} = 134.9 \pm 0.7$ mm is measured via the BPTX phase difference and is to be compared with the observed shift of $\Delta z^{\text{observed}} = 140.7 \pm 10.5$ mm, thus confirming the presence of pp collisions.

Following the winter shutdown for maintenance, operations resumed in early Spring 2010 with the first collisions at 3.5 TeV per beam, or $\sqrt{s} = 7$ TeV, achieved on March 30, 2010. The LHC operational status reported in this section covers the 2010 running period through the end of pp operations in November 2010. The IP parameters typical of this period, as well as the corresponding design values [155], are both described. Table 3.1 summarizes this information and Figure 3.3 shows the entire LHC ring at its nominal operational temperature of 1.9 K in the days preceding the first high energy collisions.

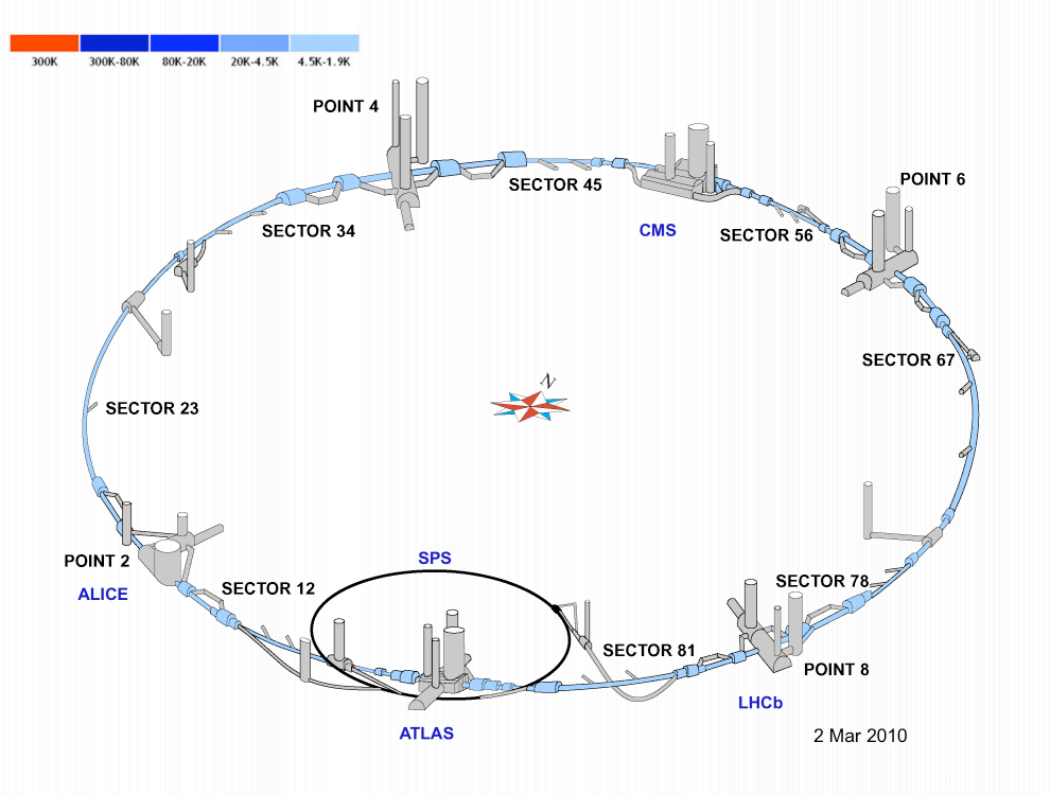

Figure 3.3: The LHC accelerator ring at it nominal operational temperature of 1.9 K. The sectors into which the LHC is divided and the various experimental halls ("interaction points", IPs, or "Points") are also shown.

The 2010 run can be divided into three phases [156]:

- **Phase 1:** Commissioning the individual beam energy to 3.5 TeV and first collisions at $\sqrt{s} = 7$ TeV. During this period the beam optics at IP1 were

squeezed to $\beta^*_{x,y} = 2$ m (the value of the β-function at the interaction point) and the number of low intensity bunches ($N_b = 10^{10}$ p) proton bunches was increased from $n_c = 2$ to $n_c = 13$. The peak instantaneous luminosity range increased from approximately $\mathcal{L} = 10^{27}$ cm^{-2}s^{-1} to $\mathcal{L} = 2 \times 10^{29}$ cm^{-2}s^{-1}.

- **Phase 2:** Due to the success of Phase 1, $\beta^*_{x,y}$ was increased to 3.5 m in order for improved beam protection and stability while dramatically increasing the bunch intensity to $N_b = 10^{11}$ p. The number of bunches in the machine was also increased from $n_c = 3$ to $n_c = 50$ during this phase. The peak instantaneous luminosity range increased from approximately $\mathcal{L} = 2 \times 10^{29}$ cm^{-2}s^{-1} to $\mathcal{L} = 10^{31}$ cm^{-2}s^{-1}.

- **Phase 3:** Finally, the machine operators commissioned the use of bunch trains, allowing for groups of eight proton bunches separated by 150 ns to be injected collectively. This allowed the total number of bunches to reach $n_c = 368$ in Phase 3. Consequently, the peak instantaneous luminosity achieved was $\mathcal{L} = 2 \times 10^{32}$ cm^{-2}s^{-1}, comparable to the Tevatron luminosity after many years of operation.

3.2 Interaction region

This section briefly describes the interaction region at IP1 (ATLAS) and parameters relevant to the discussion of pile-up and the study of hadronic final states. A more complete description can be found in Refs. [151, 157].

The pp phase space and luminous region at IP1 is studied by following and adapting a methodology developed at CESR [158], the Tevatron [159] and PEP-II [160]. Charged-particle tracks emerging from pp collisions, recorded during early LHC operation (Section 3.1) in 2009 and 2010 by the ATLAS detector, are reconstructed and combined to form event vertices. The three-dimensional distribution of these vertices reflects that of the luminosity and its parametrization is therefore dubbed the luminous ellipsoid. The size and shape of the ellipsoid plays a significant role in the delivered luminosity of the accelerator and hence also in the amount of pile-up

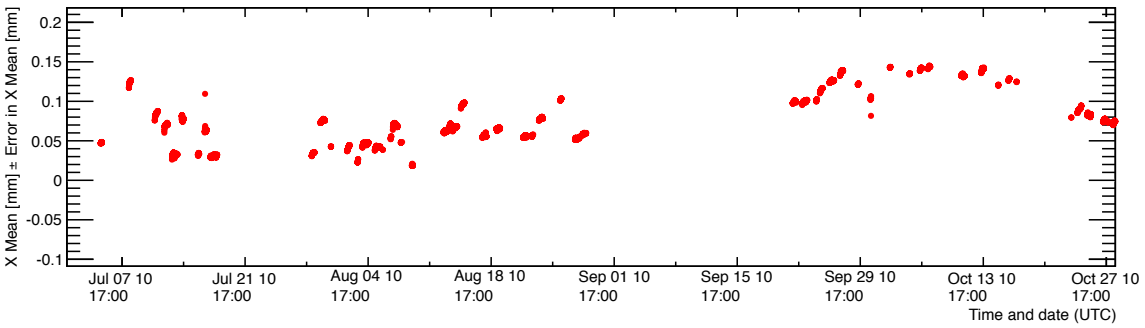

Figure 3.4: Timeline of the transverse horizontal position of the luminous region as measured by this online system throughout most of 2010.

obtained. A smaller transverse size – such as that obtained when $\beta^*_{x,y}$ was decreased for the first time in May 2010 – implies a higher number of pp collisions per bunch crossing. The coordinates of its *luminous centroid* determine, in the ATLAS system, the position of the average collision point. The orientation of the luminous ellipsoid in the horizontal (x-z) and vertical (y-z) planes is determined by the angles and relative transverse sizes of the two beams at the IP. Lastly, the transverse and longitudinal dimensions of the luminous region, quantified in terms of the RMS *luminous sizes*, are simply related to the corresponding IP sizes of the two beams as defined by Eq. A.7.

These observables are continuously reconstructed and monitored online in the ATLAS High-Level Trigger and communicated to the LHC control system every few minutes. Figure 3.4 shows a timeline of the transverse horizontal position as measured by this online system throughout most of 2010. The high-precision offline measurement of the luminous-centroid positions and of the transverse luminous sizes is used to enhance the accuracy of the absolute luminosity calibration by beam-separation scans, as well as to provide, under the beam conditions at the time of these scans, a direct measurement of the transverse IP sizes of the two beams separately (see Appendix A).

3.3 Luminosity and pile-up

The delivered luminosity of the LHC is measured using a variety of methods and by several LHC experiments, including ATLAS. The simplest definition of the machine luminosity is given by Eq. 3.1 and depends very intuitively on the number of protons in each colliding bunch and on the transverse size of the luminous region. In order to measure the luminosity, Simon van der Meer developed a method that first allowed for the luminosity of the ISR to be measured [161]. These beam-separation scans – or "van der Meer (vdM) scans" as they have come to be called – are routinely used at most high-energy particle colliders and provide a simple method for calibrating the absolute luminosity by measuring simultaneously the collision rate and the fundamental accelerator parameters that determine the luminosity. The bunch charges N_1, N_2 are measured by beam-current transformers; the transverse convolved beam sizes which depend directly on σ_{ib} (Eq. A.1) are determined by scanning one beam across the other, first horizontally and then vertically, and recording the relative collision rate as a function of the two-beam separation. Using this method, the ATLAS collaboration has determined that the uncertainty on its luminosity measurement is $\delta\mathcal{L} = \pm 3.4\%$. For a full discussion of the systematic errors evaluated in determining the uncertainty see Appendix A for a description and measurement of the first vdM scan and Appendix D and Ref. [162] for a complete description of the methods used to determine the luminosity calibration.

The influence of several distinct periods of machine configuration and detector operation are present in the first 40 pb^{-1} of data collected by ATLAS. As the LHC commissioning progressed through the three phases described in Section 3.1, changes in the beam optics and proton bunch parameters resulted in clear changes in the delivered luminosity of the machine. Due to the cross-section for interaction and the total number of protons per bunch, the possibility to observe multiple pp interactions per bunch crossing increases proportionally. This phenomenon is collectively referred to as "pile-up" but can really occur in two distinct forms. The first form is the presence of multiple extraneous (to the interaction of interest) pp collisions in the same bunch crossing and this is referred to as "in-time" pile-up. The second form

of pile-up is a purely instrumental effect due to electronic integration times within the detector. Certain detector components are actually sensitive to multiple bunch crossings due to the long electronic signals generated in response to energy depositions or charge collection. One or more pp collisions in a bunch-crossing *different* from that which produced the collision of interest can therefore affect the measurement. This latter form of pile-up is referred to as "out-of-time" and will become important as the LHC bunch spacing is decreased from many hundreds of nanoseconds to only a few tens of nanoseconds. This effect is discussed in more detail in Chapter 4, in particular as it relates to the calorimeter energy measurements of jets (Section 4.2).

As suggested in Table 3.1 the very first data were essentially devoid of pile-up until the optics of the accelerator beam (specifically $\beta^*_{x,y}$) were changed in order to decrease the transverse size of the beam and increase the luminosity [152]. This change alone raised the fraction of events with at least two observed interactions from less than 2% to between 8-10% (May-June), with the peak number of interactions shown in Figure 3.5. The experimental signature of this fact is obtained via the number of reconstructed primary vertices, or N_{PV} (see Chapter 6). Further significant change occurred when the number of protons in each proton bunch (ppb, or the bunch intensity) was increased from approximately $N_b = 5 - 9 \times 10^{10}$ to $N_b = 1.15 \times 10^{11}$ ppb. Since the number of pp collisions per crossing is proportional to the square of the bunch intensity, via Eq. 3.1, the fraction of events with pile-up was increased to more than 50% for runs between June and September. Finally, continued beam intensity enhancement slowly raised the average number of interactions per crossing to more than $\langle N_{\mathrm{PV}} \rangle = 3$ by the end of the pp run in November 2010.

In order to achieve the final peak luminosity of $\mathcal{L} = 2 \times 10^{32}$ cm^{-2}s^{-1} in 2010, the total number of bunches was increased to $n_c = 368$. To reduce beam-beam interactions and to aid in filling the accelerator, a "bunch-train" scheme was adopted in which groups of proton bunches are injected into the LHC with a fixed inter-bunch spacing, or τ_{bunch}. The minimum spacing used in 2010 was limited to $\tau_{\mathrm{bunch}} = 150$ ns, whereas the operational design of the machine is $\tau_{\mathrm{bunch}} = 25$ ns. As the bunch spacing is decreased towards its nominal value, the second form of pile-up due to out-of-time collisions becomes relevant.

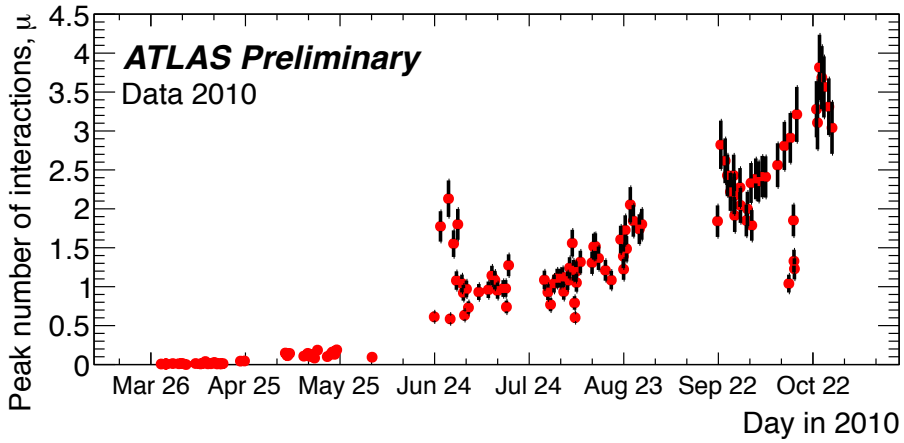

Figure 3.5: The peak number of interactions per pp collision within a two-minute period ("luminosity block") as measured by the ATLAS luminosity detectors [151]. In order to calculate the equivalent mean number of interactions, an inelastic cross-section of $\sigma_{\text{inel}} = 71.5$ mb is assumed. The error bars represent an 11% systematic uncertainty on the luminosity determination.

The bunch structure itself is governed by both the operational capacity of the machine and the design of the accelerator chain leading up to and including the LHC. Issues such as machine protection against high total beam currents and beam-beam effects must be balanced against luminosity goals. The nominal bunch structure of the LHC when operating at its current design capacity is shown in Figure 3.6. This nominal bunch structure configuration contains four different structures – patterns of filled bunches and empty bunches – worth noting:

1. Filled bunch trains of 72 bunches each, with bunches equally spaced by $\tau_{\text{bunch}} = 25$ ns.

2. Groups of two, three and four bunch trains separated by trains of empty bunches $\tau_{\text{bunch}} = 200$ ns in duration (8 bunches). These are present due to the requirements of the SPS injection kicker.

3. Ensembles of these bunch train groups (each of two, three and four bunch trains) separated by even longer trains of empty bunches $\tau_{\text{bunch}} = 950$ ns in duration

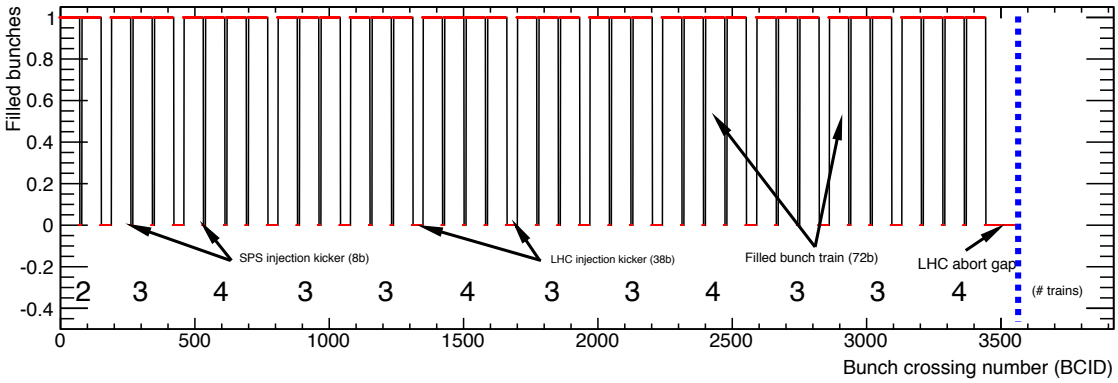

Figure 3.6: The nominal bunch train structure at the LHC. The "3-3-4" structure is a consequence of the SPS and LHC injection kicker gaps and the minimum possible bunch spacing of $\tau_{\text{bunch}} = 25$ ns. For 2010 running, bunch trains consisting of 8 consecutive bunches spaced by $\tau_{\text{bunch}} = 150$ ns were utilized for 20 pb^{-1} of the total 40 pb^{-1} collected.

(38 bunches). These are present due to the requirements of the LHC injection kicker.

In contrast, the 2010 data taking period used bunch trains consisting of 8 consecutive bunches spaced by $\tau_{\text{bunch}} = 150$ ns. The factor of 1.5 difference in the total bunch train length compared to the design is due to a constraint on the accelerator filling procedure in 2010. The same number of bunches per PS batch (in this case, 8) was forced to be the same throughout the whole filling process [156]. Nonetheless, this configuration was utilized for 20 pb^{-1} of the total 40 pb^{-1} collected during 2010.

Chapter 4

The ATLAS Detector System

The design and operational parameters of the LHC clearly present an enormous challenge for any detector system to perform precise and accurate measurements of the products of the *pp* collisions. The ATLAS detector is one of two multi-purpose particle detectors designed to not only survive this harsh environment, but in fact to carry out high precision physics measurements within it. Although the design is primarily driven by the scientific goals of the experiment, the ability to achieve those goals is inextricably linked with the understanding of the detector itself.

The ATLAS detector is shown in Figure 4.1 and is centered on Interaction Point 1 (IP1) at the LHC [147], with the companion multi-purpose experiment CMS (Compact Muon Solenoid) [148] located at nearly the opposite side of the accelerator at IP5. ATLAS is perhaps best characterized by its tremendous size: 44 m in length, 25 meters in height, containing over *300 thousand kilometers* of cables, and weighing nearly 7000 tons altogether. The ATLAS and CMS designs are both driven by the physics requirements of the experiment and generally adopt that of a cylindrical, nearly hermetic system that measures the energy and momentum of particles produced in the *pp* collisions through a variety of methods. ATLAS has adopted a traditional construction, with 3 primary detection systems layered radially upon each other: a central inner tracking detector surrounded by a 2 T solenoidal magnetic field for charged particle identification and position and momentum measurement (Section 4.1), a calorimeter system for energy measurements of both charged and neutral

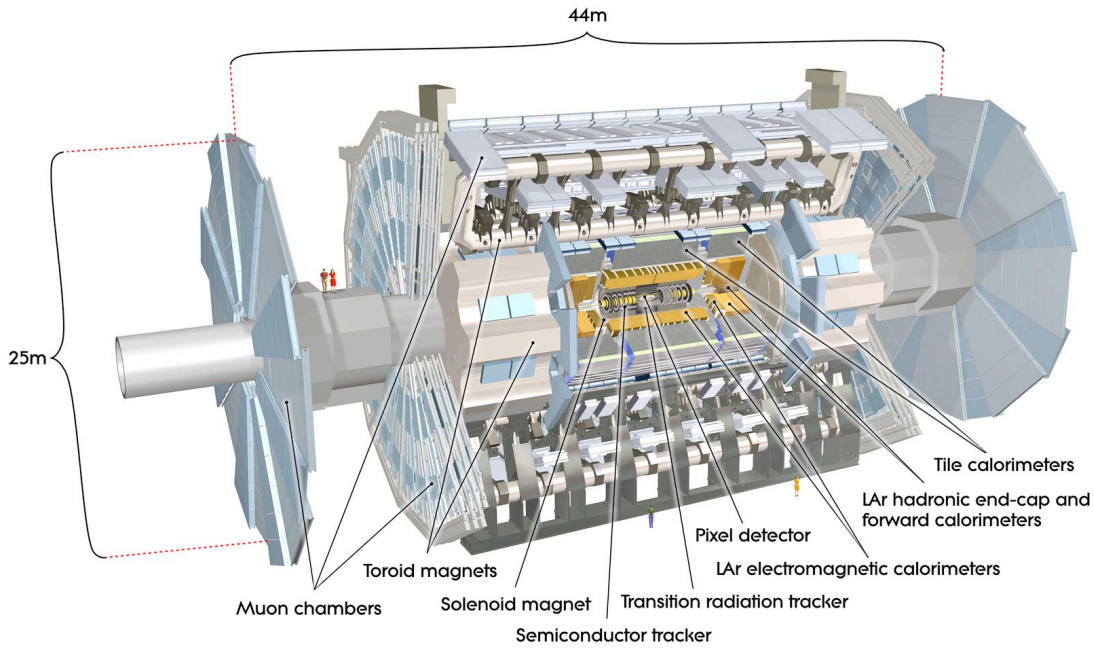

Figure 4.1: The ATLAS detector

particles (Section 4.2), and a muon system located within a large air-core toroidal magnetic field to measure the position and momentum of muons produced in the collision or the decays of heavy particles (Section 4.3).

The magnet systems that comprise ATLAS, which also include a pair of large end-cap toroidal magnets, do as much to influence the overall design and size of the ATLAS detector as do the particle detector systems themselves. The extensive magnet system provides the magnetic field responsible for bending the trajectory of charged particles such that their momentum can be measured via the radius of curvature of the tracks left within the detector systems. This is achieved primarily via a long moment arm, approximately equal to the radius of the detector and consisting in several layers in order to obtain a precise measurement of the trajectory.

To meet the extremely high demands that the LHC luminosity places on the speed with which ATLAS must record data, a dedicated trigger and data acquisition (TDAQ) system is used. This system communicates with the front-end electronics,

facilitates the use of both simple and complex pattern recognition algorithms in order to accept or reject events for offline storage, and provides a framework within which to organize the flow of recorded data and to monitor its quality. An offline data storage and monitoring system complements the online TDAQ system by allowing for the execution of more time-consuming monitoring checks and to provide comparisons over long periods of time. Once selected and written to disk, the offline data processing and monitoring system ensures that the data are reconstructed, that detector conditions changes are taken into account, and that systematic examination of these data pinpoints peculiarities and flags low-quality data for further scrutiny or rejection from analysis.

The ATLAS reference system is a Cartesian right-handed coordinate system, with nominal collision point at the origin. The anti-clockwise beam direction defines the positive z-axis, with the x-axis pointing to the center of the LHC ring. The pseudorapidity is defined as $\eta = -\ln(\tan(\theta/2))$, where the polar angle θ is taken with respect to the positive z direction. The rapidity is defined as $y = 0.5 \times \ln[(E + p_z)/(E - p_z)]$, where E denotes the energy and p_z is the component of the momentum along the beam direction. In the limit of massless particles, $y = \eta$, and both are invariant under Lorentz boosts along the beam axis (z), which is important since the initiator quarks have relative momenta within the proton, as described in Section 2.1.

4.1 Inner tracking system

The central tracking system shown in Figure 4.2 is referred to as the Inner Detector (ID) and is responsible for the position and momentum measurement of charged particles emanating from the primary pp interactions. The overall acceptance in pseudorapidity is $|\eta| < 2.5$ for particles coming from the nominal LHC interaction region, with full coverage in ϕ. The track reconstruction efficiency ranges from 78% at $p_{\mathrm{T}}^{\mathrm{track}} = 500$ MeV to more than 85% above 10 GeV, averaged across the full η coverage [163]. The transverse momentum resolution of $\sigma_{p_{\mathrm{T}}}/p_{\mathrm{T}} = 0.05\%\ p_{\mathrm{T}}\ GeV\ \oplus\ 1\%$ and a transverse impact parameter resolution of 10 μm for high momentum particles in the central η region [147] are primarily achieved through the use of multiple

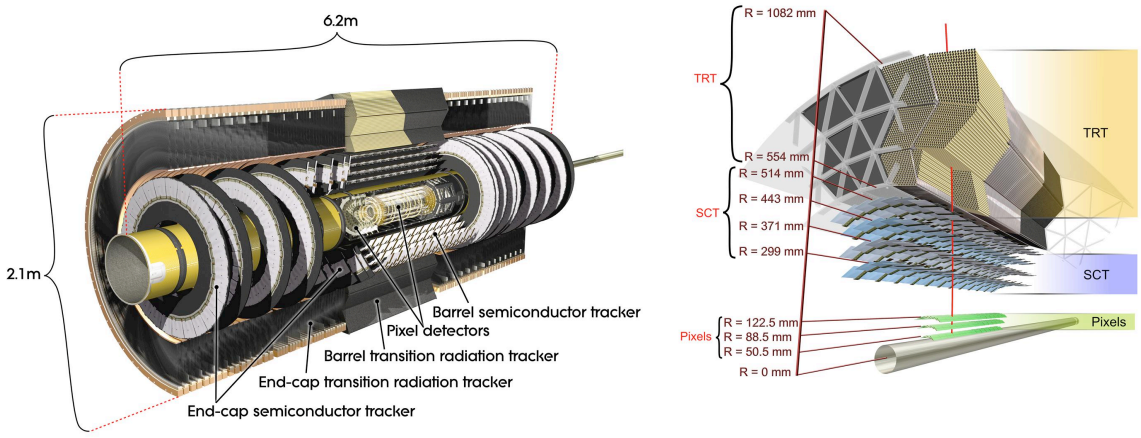

(a) (b)

Figure 4.2: The ATLAS Inner Detector

high precision subsystems within the ID: the Pixel Detector (Pixel), the SemiConductor Tracker (SCT) and the Transition Radiation Tracker (TRT). These are briefly described below.

4.1.1 Silicon pixel detector

The innermost part of the ATLAS detector [147] is the silicon pixel detector. This device consists of three concentric barrel layers, the innermost one – termed the "*b*-layer" due to its role in identifying *b*-quarks initiated jets – is located at 5 cm from the interaction region (see Figure 4.2(a)). Three additional disks at each endcap result in a total of over 80 million silicon pixels. Each layer or disk is instrumented with so-called "modules" that form the basic unit of data acquisition, with 1744 in total. Each module covers an active area of 16.4 mm×60.8 mm and contains 47,232 pixels, primarily 50 μm $\times$ 400 μm in size. The direction of the shorter pitch corresponds to the high precision position measurement in the $R-\phi$ plane. A module is read out by 16 radiation-hard front-end chips [164] bump-bonded to the sensor. Hits in a pixel are only collected if the signal exceeds a tunable threshold. This leads to the concept of occupancy which describes the fraction of the entire detector that is read out at

any given moment. Typical occupancies of the pixel detector at $\mathcal{L} = 10^{32}$ cm^{-2}s^{-1} are approximately $10^{-5} - 10^{-4}$. This concept will return when discussing the issues specifically due to the high luminosity environment at the LHC in Chapter 6.

In order to reach the physics goals laid out by ATLAS, both vertex and track reconstruction require that the Pixel Detector maintain a hit detection efficiency greater than 98% [165]. At the design luminosity of $\mathcal{L} = 10^{34}$ cm^{-2}s^{-1}, the fluence of particles through the b-layer will reach the equivalent of 10^{14}cm^{-2} 1 MeV neutrons, or 160 kGy/year[1]. At such high rates and fluences, both the radiation hardness of the detector and the synchronization and timing performance of the readout electronics are crucial for the optimal performance of the detector. Due to the large number of channels, the readout window for the full detector was optimized [166] for large bunch spacings and then reduced in steps throughout 2009 and 2010 until it was finally restricted to a single 25 ns bunch crossing (BC). This restriction is necessary because there is a fixed bandwidth allocated to read out the 80 million channels and the fewer individual pixels that are incorporated into each event the more events can be saved.

4.1.2 Silicon strip sensor tracker

The silicon strip sensor tracker (SCT) adds four additional concentric double layers of silicon micro-strips in the barrel, nine disks on each side that make up the endcaps, and contains 6.3 million channels. This arrangement provides typically eight strip measurements (four space-points) along the charged particle track. The SCT layers are located at radii from 29.9 cm to 56.0 cm. In a fashion similar to that of the Pixel, the SCT readout is organized among 4088 modules of silicon-strip devices that arrange the strips parallel to the solenoid field and beam axis. The spacing of the strips is an approximately constant pitch of 80 μm in the barrel, while in the endcaps the strip direction is radial and of variable pitch. The strips are read out by radiation-hard front-end readout chips [167], with each chip containing 128 channels for a the total of $\sim$6.3 million readout channels.

[1]For comparison, 1-10 Gy is a lethal dose for humans.

The signal readout of the SCT is again similar to that of the Pixel insofar as only a binary threshold is used in order to maintain a low readout occupancy. A hit is registered only if the pulse height in a channel exceeds a preset threshold, normally corresponding to a charge of 1 fC. The charge measured in the strip is then recorded into a memory buffer that is itself only read out and used for tracking if a trigger is received signaling that the event should be considered in more detail, typically originating in either the calorimeter or the muon system.

4.1.3 Transition radiation tracker

The transition radiation tracker (TRT) surrounds the silicon detectors and is comprised of up to 76 layers of longitudinal straw tubes in the barrel and 160 radial straw planes in each endcap. The sensitive volume covers radial distances from 563 mm to 1066 mm. The detector consists of 298,304 proportional drift tubes (straws), 4 mm in diameter, read out by 350,848 channels of electronics. The tubes in the barrel region are arranged in three cylindrical layers and 32 ϕ sectors; they have split anodes and are read out from each side [168]. The tubes in the endcap region are radially oriented and arranged in eighteen wheel-like modular structures [169]. In the central pseudorapidity region, 52,544 axially oriented straw tubes with split anodes are arranged in 96 modules (three cylindrical layers and 32 ϕ sectors). They are read out from each side in the TRT barrel [168]. In each of the TRT endcaps [169], extending from a rapidity of $|\eta| \approx 1$ to $|\eta| \approx 2$ on each side of the barrel, there are 122,880 radially oriented straws organized in eighteen wheel-like modular structures. The TRT straw layout is designed so that charged particles with transverse momentum $p_{\mathrm{T}} > 0.5$ GeV and with pseudorapidity $|\eta| < 2.0$ cross typically 30 straws. The TRT provides electron identification via transition radiation from polypropylene fibers (barrel) or foils (endcaps) interleaved between the straws. The much higher energy of the transition radiation photons (~ 6 keV compared with the few hundred eV deposited by an ionizing particle) is sensed by a second, high threshold, discriminator in the radiation-hard front-end electronics [170].

4.2 Calorimeter system

The measurement of the energy and topology of particles emerging from the interaction region is a crucial component of this thesis. Thus, I will focus on the calorimeter system responsible for that task with some detail.

The ATLAS calorimeter system is a non-compensating sampling calorimeter built of multiple sub-detector systems with several different designs spanning the pseudo-rapidity range up to $|\eta| < 4.9$. "Non-compensation" refers to the fact that some energy released in the nuclear collisions between high energy particles from the interaction and the detector material is lost to nuclear recoils and dissociation that is not captured in the active readout. The sampling term refers to the design approach that utilizes alternating layers of absorber and active readout, relying on ionization or scintillation light proportional to the energy loss of the particle in the medium. Both electromagnetic and hadronic energy measurements require the multiple subsystem designs in order to maximize both sensitivity and resolution throughout the detector while coping with the high radiation environment, particularly in the forward region.

The measurements described in this thesis are predominantly carried out by the Liquid Argon (LAr) barrel electromagnetic (EM) calorimeter, the Tile hadronic (HAD) calorimeter and the LAr hadronic end-cap (HEC) calorimeter. Their operation and design is of crucial importance to the results. An overview of the entire calorimeter system is given in Figure 4.3, showing the four primary systems involved in ATLAS calorimetry: the LAr electromagnetic barrel (EMB) and end-cap calorimeters (EMEC), the HAD barrel and extended barrel calorimeters, the HEC, and the forward calorimeter (FCAL).

The barrel LAr and Tile calorimeters constitute the central calorimeter, where the former extends to $|\eta| < 1.475$ and the larger radius Tile calorimeter extends to $|\eta| < 1.7$. The LAr EMB and EMEC are each housed within their own cryostat – three in total – which is also shared with the HEC and FCAL calorimeters on each end. Liquid argon was chosen for the EM calorimeter and for the more forward hadronic calorimeters due to its radiation hardness and speed. The steel and plastic scintillating tile design for the barrel HAD calorimeter was motivated by robustness

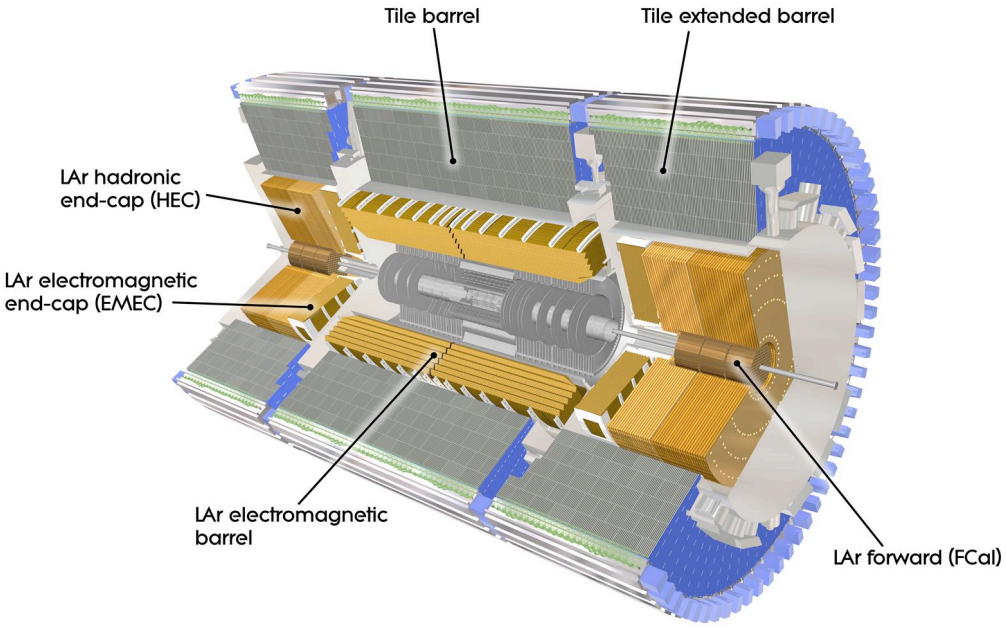

Figure 4.3: The ATLAS calorimeter system

and the energy resolution provided by its 9.7 λ depth at $\eta = 0$. The relatively lower cost of course facilitated the deeper calorimeter design and thus the choice of this technology.

It is very important to note that each calorimeter is segmented both laterally and longitudinally. This fact yields a high granularity EM calorimeter that maximizes the accuracy with which electrons and photons can be reconstructed. It also provides detailed information on the transverse and longitudinal shower shapes of hadronic jets. For many applications it is desirable to construct a geometrical grouping of these cells into $\Delta\eta \times \Delta\phi = 0.1 \times 0.1$ projective towers that approximately point back to the nominal LHC interaction region at the center of the detector. A schematic representation of this grouping is shown in Figure 4.4 for the Tile calorimeter cells, which themselves are described in more detail below. The design features relevant to the measurements described in subsequent chapters are presented in greater detail in Sections 4.2.1 and 4.2.2.

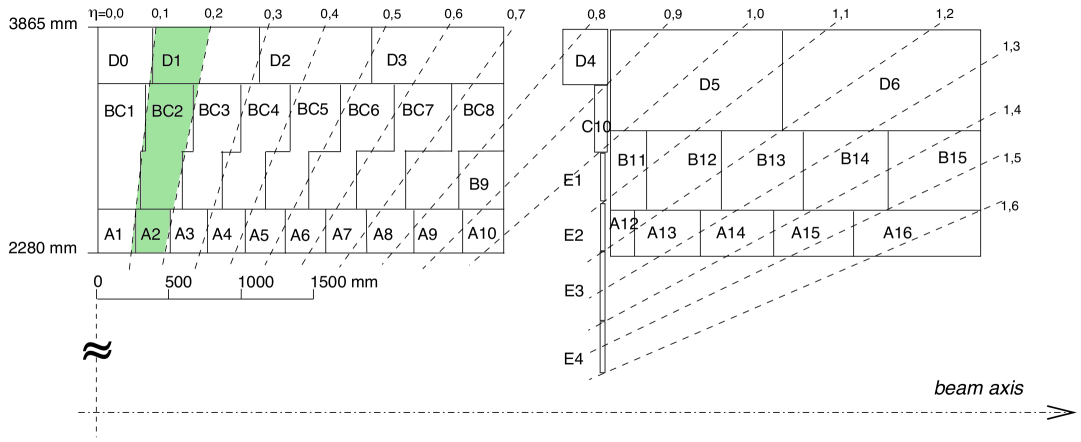

Figure 4.4: Projective calorimeter towers with $\Delta\eta \times \Delta\phi = 0.1 \times 0.1$ shown schematically using only the Tile calorimeter cells. The projective nature of this geometric grouping of cells is clear as the towers point towards the nominal interaction region at the center of the ATLAS detector and the physical size of towers becomes smaller at higher η.

4.2.1 Liquid argon EM calorimetry

The hallmark of the ATLAS electromagnetic calorimeter is the accordion geometry design, shown in Figure 4.5. This design was chosen to ensure high azimuthal uniformity, a regular liquid argon ionization gap, and a constant sampling fraction within a given detector region. Stainless-steel-clad Pb absorber plates and honeycomb spacers form the ionization gap for the liquid argon active medium. In the barrel ($|\eta| < 0.8$) the thickness of the lead absorber plates is 1.53 mm. Beyond $|\eta| > 0.8$, the thickness is 1.13 mm, thereby limiting the decrease in sampling fraction at high pseudorapidity. Figure 4.5 highlights how this geometry is divided among cells, or individual readout elements of varying size that are finely segmented both laterally and longitudinally. Such fine segmentation – $\Delta\eta \times \Delta\phi = 0.025 \times 0.025$ in the primary layer of the EMB, for example – permits a detailed mapping of both EM and hadronic showers in the calorimeter, allowing for studies of the internal structure of hadronic jets and partially giving rise to the high resolution measurements of their energy, described in Chapter 5. Furthermore, the total thickness of a module is at least 22 radiation lengths

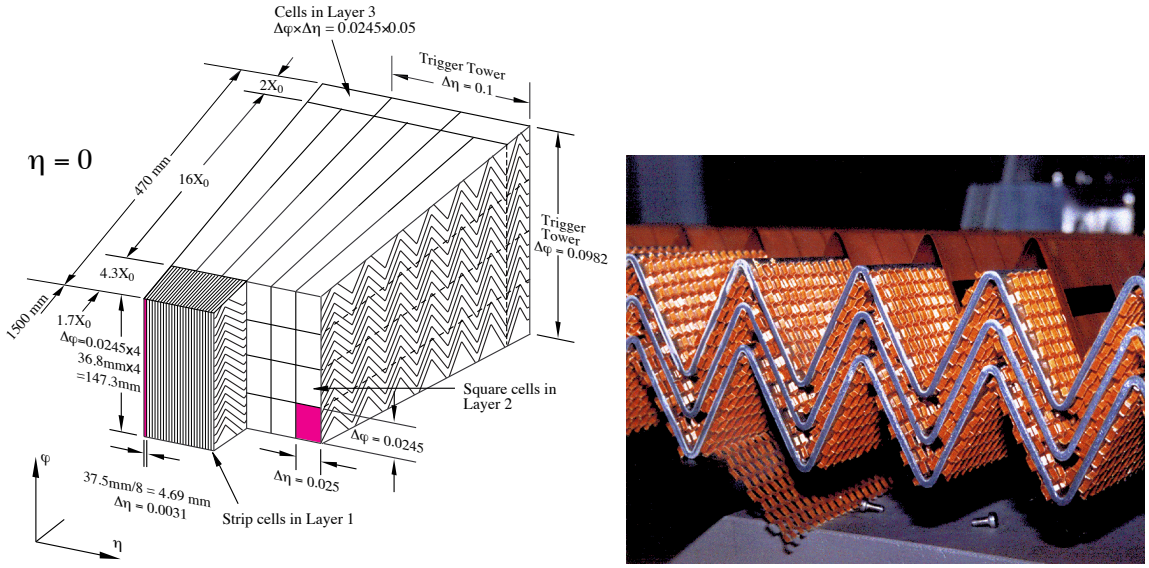

(a) (b)

Figure 4.5: (a) Cross-section of the LAr barrel calorimeter showing the presampler and layers 1-3 which exhibit the accordion sampling and readout geometry. (b) An image of the accordion readout and sampling design showing the honeycomb electrode spacers that form the ionization gap.

(X_0), increasing from 22 X_0 to 30 X_0 between $|\eta| = 0$ and $|\eta| = 0.8$ and from 24 X_0 to 33 X_0 between $|\eta| = 0.8$ and $|\eta| = 1.3$, providing excellent coverage even at very high energies.

The signal readout chain for the LAr calorimeter – indeed, for all of the calorimeter systems – is divided into a fast analog readout for the trigger system (see Section 4.4) and a slower digital readout used for more refined trigger decisions and the offline reconstruction. However, regardless of readout path, the signal is initiated within the active LAr medium.

When a charged particle enters a cell it ionizes the LAr and the resulting charge is collected on the readout electrodes via a high voltage bias placed across the medium (the ionization gap). Photons are detected via the production of electron-position pairs (e^+e^-) which subsequently produce an ionization signal, while hadronic particles will begin to shower within the dense Pb absorber. Shaping electronics induce a bipolar pulse shape in the resulting ionization signal. This shape is characterized by

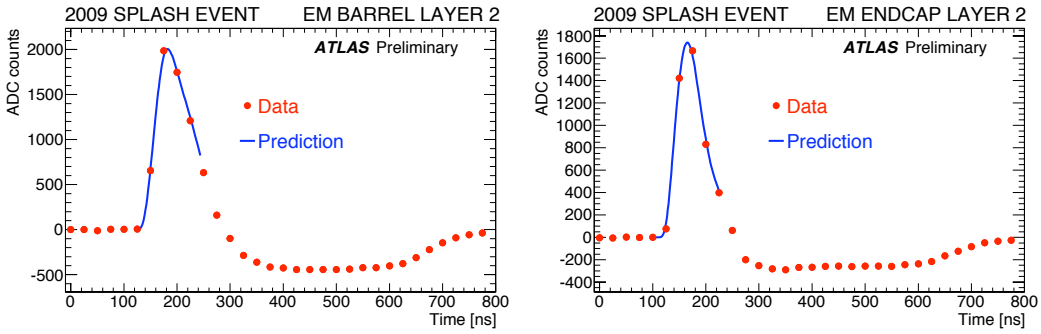

(a) (b)

Figure 4.6: Predicted and measured pulse shapes during the first LHC beam splashes for the(a) LAr barrel (EMB) and (b) the LAr electromagnetic end-cap (EMEC). The time between consecutive samplings of the signal is 25 ns.

having both a positive and a negative component, which renders the integral of the signal exactly equal to zero.

The performance of the shaping electronics is critical for a correct energy calibration of the detector since the energy is primarily determined from the peak height of the pulse. Pulse shapes from the EMB and EMEC regions are shown in Figure 4.6 where the bipolar shape is clearly visible. In each calorimeter region, the overall pulse shape and duration are optimized to approximately cancel a constant injection of energy into the detector. The motivation for this approach is to effectively redefine the baseline of the energy measurement. In the high luminosity environment of the LHC, this reduces the sensitivity to the background from multiple pp interactions *on average*. This approach is in fact used for all LAr calorimeters (EMB, EMEC, HEC and FCAL), although each region is optimized independently for a nominal LHC bunch spacing of 25 ns, the LAr pulse shape peaking time, and integration length [171]. Tests using both cosmic rays [172] and initial collisions (Figure 4.6) indicate that the predicted pulse shapes match the measured pulse shapes to a very high precision. In Chapter 6 it will be shown that this feature of the LAr calorimeter must be taken into account when defining the energy calibration for hadronic jets.

The end-cap calorimeters are enclosed within separate cryostats at each end and contain both the EMEC and the HEC ($1.375 < |\eta| < 3.2$ and $1.5 < |\eta| < 3.2$,

respectively). The EMEC uses the same accordion geometry as the EMB, whereas the granularity is typically slightly larger than in the barrel. The geometrical arrangement of layers is also different due to the fact that it must be oriented vertically within the cryostat. Radially arranged "wheels" are thus used with Pb absorber plates 1.7 mm thick for $|\eta| < 2.5$ and 2.2 mm thick for $|\eta| > 2.5$.

4.2.2 Hadronic calorimetry

The barrel hadronic calorimeter system, the Tile calorimeter, is most notable for its depth of 7.4 radiation lengths (λ) over nearly 2 m. Modularity in both construction and readout geometry is achieved by arranging the entire detector in 64 wedge-like modules, each spanning $\Delta\phi \sim 0.1$. A schematic of the module design is presented in Figure 4.7. These modules are instrumented independently and installed in the underground cavern and and then connected to off-detector electronics and services (e.g. water cooling). The active readout utilizes individual plastic scintillating tiles, surrounded by steel absorber and connected by wavelength shifting fibers to photomultiplier tubes (PMTs), as depicted in Figure 4.7(a). The scintillating tiles are 3 mm thick, from from 97 mm to 187 mm in radial length, from 200 mm to 400 mm in azimuthal length, and surrounded by approximately 5 mm of steel absorber. By arranging the PMT mapping to groups of scintillator tiles, 3 radial sampling layers (longitudinal with respect to the interaction region) are formed, each approximately 1.5, 4.1 and 1.8 λ thick at $\eta = 0$. The first two layers span $\Delta\eta = 0.1$, while the last layer is twice as large with $\Delta\eta = 0.2$.

The HEC uses the LAr active readout design due to the higher radiation tolerance required for the forward regions. The liquid argon itself is recycled and so is less susceptible to radiation damage over time. On the other hand, the plastic scintillating tiles in the barrel are expected to degrade at higher luminosity. Although housed in the same cryostat as the accordion geometry EMEC, the HEC implements a flat-plate design with copper as the absorber material.

The FCAL implements the novel electrode structure shown also in Figure 4.7 to cope with the extremely high particle flux experienced in the far forward region

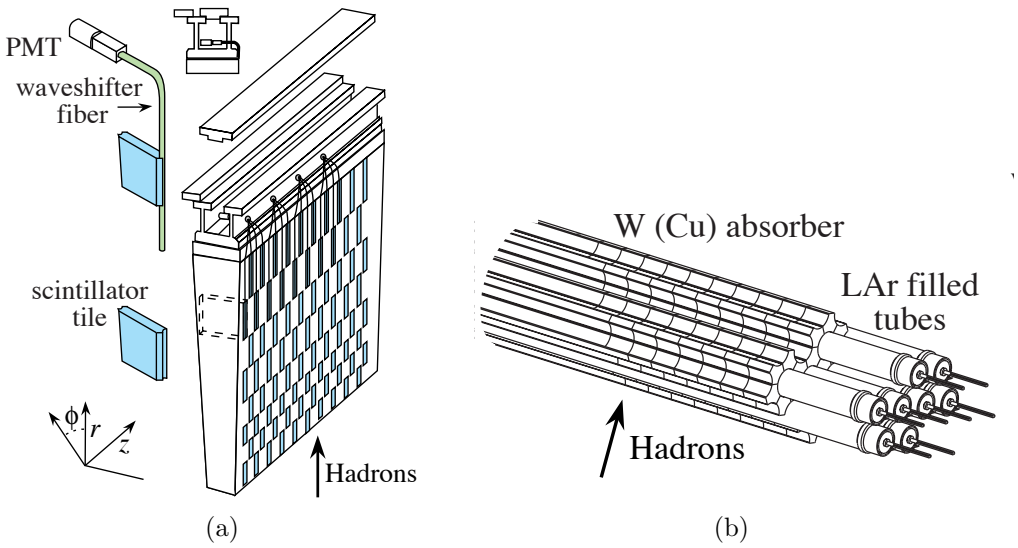

Figure 4.7: (a) A single module of the hadronic Tile calorimeter showing the scintillating plastic tiles, the wavelength shifting fibers and the PMTs used to collect the scintillation light. (b) Schematic of a group of FCAL readout cells depicting the grouping into LAr filled tubes with tungsten and copper absorber that is able to withstand the high radiation dose received in the forward region.

($3.1 < |\eta| < 4.9$). The LAr ionization readout is achieved with thin annular gaps formed by tubes containing the LAr active medium in a W or Cu absorber matrix, which are filled with anode rods of slightly smaller radius. The ionization gap in this detector is maintained by helically-wound radiation hard plastic fibre (PEEK). As with the other calorimeter subsystems, the FCAL is divided into three layers arranged along the beam in z. The first layer is designed for electromagnetic energy deposition and contains a Cu absorber matrix yielding 27.6 X_0 over 45 cm, whereas the latter two are designated for forward hadronic energy measurements and contain a W absorber matrix providing a hadronic absorption length 3.68 λ (3.60 λ) for the second (third) FCAL modules.

4.2.3 Calorimeter calibration

The baseline EM energy scale of the calorimeters is the result of the calibration of the electronics signal to the energy deposited in the calorimeter by electromagnetic

showers. This calibration is established using test-beam measurements of electrons in the EMB [173, 174, 175, 176, 177] and EMEC calorimeters [178, 179]. The hadronic calorimeters are calibrated using muons in test-beam experiments [177, 180] and those muons produced by cosmic-rays in-situ [181]. The invariant mass of the Z boson in $Z \to ee$ events measured in-situ in the 2010 pp collisions is then used to adjust the calibration derived from test-beams and cosmic muons[2].

4.3 Muon spectrometer system

The muon system gives the ATLAS detector its overall shape and imposing nature, as depicted in Figure 4.8. Four primary subsystems comprise the integrated muon spectrometer: monitored drift tubes (MDT), cathode strip chambers (CSC), resistive plate chambers (RPC) and thin gap chambers (TGC). The MDT and CSC subsystems are primarily designed for precision measurements of muon tracks, with the MDT system providing coverage for the more central region ($|\eta| < 2.7$, with full coverage only in $|\eta| < 2.0$), whereas the CSC is located in the more forward region ($2.0 < |\eta| < 2.7$) due to its ability to cope with higher background rates [182]. The RPC and TGC muon subsystems are designed to provide fast, robust readout for use in the trigger and data acquisition system (Section 4.4).

Studies of the muon reconstruction efficiency and tracking performance of the spectrometer were carried out using cosmic ray data collected in 2008 and 2009 [182]. These measurements demonstrate an integrated reconstruction efficiency of approximately 94% when including the poorly instrumented region near $\eta \sim 0$, or more than 97% when excluding this gap region. Muon tracks within the central barrel region of $|\eta| < 1.1$ were measured to have a transverse momentum resolution consistent with expectations from MC studies, and described by the following relationship

$$\frac{\sigma_{p_{\mathrm{T}}}}{p_{\mathrm{T}}} = \frac{(0.29 \pm 0.03)\ \ \mathrm{GeV}}{p_{\mathrm{T}}} \oplus (0.043 \pm 0.002) \oplus (4.1 \pm 0.4) \times 10^{-4}\ \mathrm{GeV}^{-1} \times p_{\mathrm{T}}, \quad (4.1)$$

[2]This additional calibration has been applied to the electromagnetic barrel, electromagnetic endcap and to the full forward calorimeter.

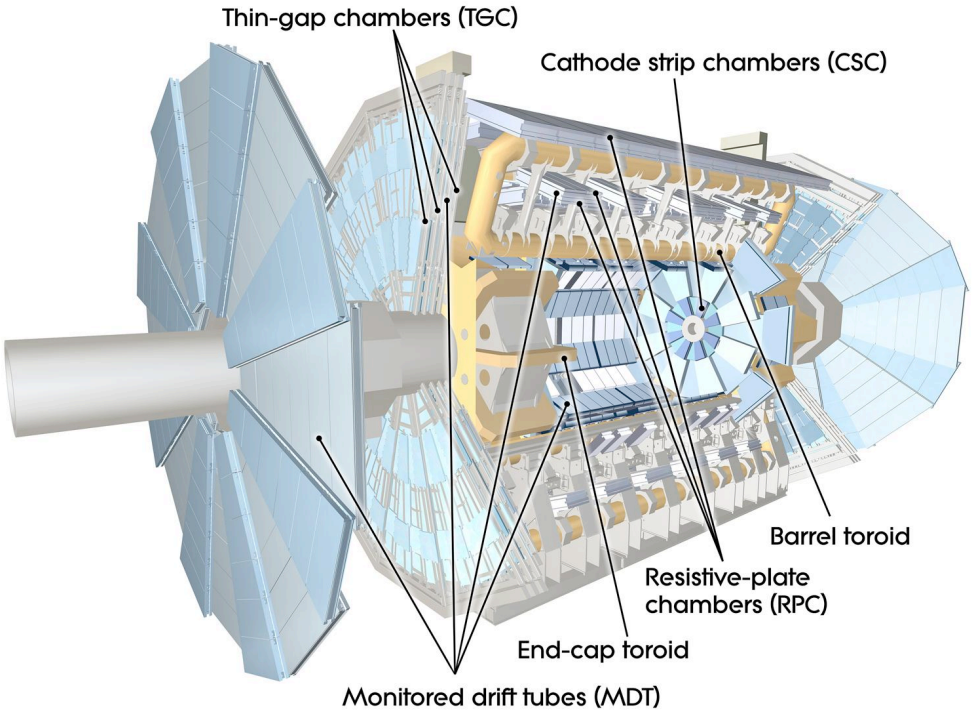

Figure 4.8: The ATLAS muon system

where the uncertainties represent only the (dominant) systematic uncertainties due to the curve fitting method. The first term in Eq. 4.1 represents the uncertainty in the energy loss of the muon as it traverses the detector and is thus inversely proportional to the muon transverse momentum. The second term is a constant term due to the multiple scattering uncertainty. The third term is proportional to the muon transverse momentum and represents the intrinsic resolution of the track fit due to measurement error. Since it becomes increasingly difficult to measure the curvature of a nearly straight (i.e. infinitely high momentum) track, this error dominates at high p_{T}.

4.4 Trigger and data acquisition system

The data provided by the calorimeter and muon systems provide the criteria by which events are selected or rejected every 4.5 μs by the first level of the ATLAS trigger

Monitored drift tubes	**MDT**
- Coverage	$\|\eta\| < 2.7$ (innermost layer: $\|\eta\| < 2.0$)
- Number of chambers	1088 (1150)
- Number of channels	339 000 (354 000)
- Function	Precision tracking
Cathode strip chambers	**CSC**
- Coverage	$2.0 < \|\eta\| < 2.7$
- Number of chambers	32
- Number of channels	31 000
- Function	Precision tracking
Resistive plate chambers	**RPC**
- Coverage	$\|\eta\| < 1.05$
- Number of chambers	544 (606)
- Number of channels	359 000 (373 000)
- Function	Triggering, second coordinate
Thin gap chambers	**TGC**
- Coverage	$1.05 < \|\eta\| < 2.7$ (2.4 for triggering)
- Number of chambers	3588
- Number of channels	318 000
- Function	Triggering, second coordinate

Table 4.1: Primary design parameters of the ATLAS muon spectrometer subsystems.

system [183, 184, 185]. This system is responsible for the online event selection which is performed in three stages: the Level 1 (L1), Level 2 (L2) and Event Filter (EF) stages. L1 utilizes information from only the calorimeter and muon systems using only simple hardware based algorithms to accept or reject events within a 4.5 μs time window after the collision. L2 and EF are collectively referred to as the High Level Trigger (HLT) and are based on software algorithms running on large farms of commercial processors. L2 is the first stage of the ATLAS data acquisition system that has access to data from the Inner Detector and is capable of doing partial reconstruction of events at combined rates of up to 75 kHz. This high rate environment, achieved by the massive parallelism of the processor farm, results in a tightly constrained budget for the processable data volume as well as for the CPU time available to the algorithms (a few tens of milliseconds altogether). This challenge, characteristic of the online environment, leads to algorithms that are optimized for speed and robustness rather than for maximum resolution or reconstruction efficiency.

The analyses presented in Chapters 7 and 8 rely primarily on the hardware-based L1 calorimeter trigger. At this level coarse calorimeter information is available in the form of jet elements with $\Delta\eta \times \Delta\phi = 0.2 \times 0.2$ for $|\eta| < 3.2$. Jets are reconstructed using a square sliding window algorithm. In addition to coarse jets, the total transverse energy, or $\sum E_T$, is also measured at L1. Muon segments reconstructed by the muon spectrometer are also used as input to the L1 trigger. The region of the detector corresponding to the location where the L1 thresholds were passed – so called "regions of interest" – are then delivered to the L2 software algorithms.

The particular place of the L2 trigger in the data acquisition chain and its capability to reconstruct tracks and vertices online provide the unique capability of reconstructing regions of the detector with the full granularity of the readout. Results may thus be monitored and delivered in quasi-real time, i.e. with minimal latency, with the added advantage of the high statistics of the early trigger stage, including events that are subsequently rejected from the data logging and thus not available for offline analysis.

The next and last stage in the trigger chain is the EF, which receives events that have been selected by the L2 "region of interest" triggers and processes the entire event with the full detector granularity instead of only a restricted region. Offline jet and tracking algorithms can thus be run at this stage, as the required latency is about three seconds.

By restricting the event data written to disk – a procedure referred to as partial event building – a large fraction of events rejected at L2 can actually be saved and can be made available offline for dedicated calibration and bias studies. Partial event building is used by the beam line characterization described in Section 3.2 by saving events used for online vertex finding for high precision offline analysis. This is primarily achieved by saving only the Inner Detector space point information, thereby reducing the data volume by more than a factor of ten due to exclusion of the LAr calorimeter. The monitoring infrastructure of the HLT supports the real-time accumulation of histograms, and their aggregation across the farm, so that parameters can be extracted from cumulative distributions that contain events from all processor nodes. Beam parameters determined from those live histograms are transmitted

online to the LHC and are also available to be fed back into the HLT itself for use by its own trigger algorithms that depend on the precise knowledge of the luminous region (such as b-jet tagging).

4.5 Data quality and conditions in 2010

Events selected by the trigger are divided into a number of inclusive streams (i.e. a given event may occur in several streams). There are currently five physics streams, an express stream containing a subset of events corresponding to a rate of about 10 Hz, and several calibration streams with partial event data. Reconstruction of the express and calibration streams starts at the Tier-0 computing farm as quickly as possible after recording the data. The so-called "bulk reconstruction" of the remaining stream is delayed in order to assess data quality and allow for the determination of updated conditions (including updated luminous-region parameters) on the express stream, and typically starts within 36 hours after a run is closed.

Compared to the processing possible at the trigger level, the expanded time frame of the offline reconstruction allows for a more refined reconstruction of tracks, vertices and luminous-region parameters. Tracks can be reconstructed down to a minimum $p_{\mathrm{T}}^{\mathrm{track}} > 150$ MeV. Vertices are fitted using an iterative algorithm, and an unbinned maximum likelihood fit is used to subtract the vertexing resolution from the observed distribution of primary vertices in order to determine the luminous size. In addition to the prompt reconstruction at the Tier-0 computing farms, periodic reprocessing of the offline data is performed at the Tier-1 computing centers with updated detector conditions and with the latest validated version of the ATLAS offline software.

In 2010, the detector conditions allowed for a very high data quality efficiency, as described in detail in Table 4.5 for each of the ATLAS sub-detectors. The table shows the luminosity weighted relatIve fractIon of good quality data delivered by the various ATLAS subsystems during LHC fills with stable beams in pp collisions at $\sqrt{s} = 7$ TeV. The startup time for the tracking detectors following the LHC operators' indication of safe beams is omitted. The data collected between March 30$^{\mathrm{th}}$ and October 31$^{\mathrm{st}}$ corresponds to a recorded integrated luminosity of 45 pb^{-1}. The 2.0%

Detector Data Quality		
Tracking Detectors	Pixel	99.1%
	SCT	99.9%
	SCT	100%
Calorimeters	LAr EM	90.7%
	LAr HAD	96.6%
	LAr FWD	97.8%
	Tile	100%
Muon Detectors	MDT	99.9%
	CSC	96.2%
	RPC	99.8%
	TGC	99.8%

Table 4.2: Luminosity weighted relatIve fractIon of good quality data delivered by the various ATLAS subsystems during LHC fills with stable beams in pp collisions at $\sqrt{s} = 7$ TeV. The startup time for the tracking detectors following the LHC operators' indication of safe beams is omitted. The data collected between March 30$^{\text{th}}$ and October 31$^{\text{st}}$ corresponds to a recorded integrated luminosity of 45 pb^{-1}.

inefficiency due to ID startup, as well as the 4.4% data acquisition inefficiency, are not included in Table 4.5, but are accounted for in the ATLAS data taking efficiency. The inefficiencies in the LAr calorimeter are mostly due to isolated HV trips and noise bursts. These have been recovered in the 2011 data taking period.

Chapter 5

The hadronic final state in ATLAS

The hadronic final state represents the ensemble of stable particles observed in an event that results from the showering and decay specifically of colored particles. Since it is a hadron collider, the LHC preferentially produces such colored final states via the collision of two constituent quarks or gluons within the incoming protons. New physics models that contain colored objects or which couple to the Standard Model (SM) quarks and gluons might thus be observed within the larger class of hadronic final states. Furthermore, the presence of initial and final state radiation as well as multiple simultaneous pp collisions, necessitates a thorough understanding of the reconstruction of and physics contained within the hadronic final state.

This chapter describes in detail the methods by which jets are reconstructed and the choice of the particular jet algorithm used for standard multi-jet final states. Characteristics of the hadronic final state that will be important for assessing both the precision and the accuracy of the measurement of hadronic event shapes and the substructure of individual jets are also described.

5.1 Inputs to jet reconstruction

‘

The first choice that the experimentalist must make upon constructing a detector and establishing its correct operation is what will be the *signal* that he will use

to measure the hadronic final state. This choice can impact various aspects of the final measurement in terms of experimental tractability or sensitivity to systematic uncertainties. However, the underlying physics is the same and at least part of this choice must be guided by consideration of the ease with which that physics can be measured accurately and precisely.

As described in Chapter 4, the ATLAS detector has a multitude of signal possibilities available among the various detector systems present. The calorimeters themselves have cell sizes granular enough to permit a variety of inputs to algorithms meant to define the presence of hadronic jets.

Four primary inputs to jet reconstruction are considered in ATLAS and in this thesis. These are each depicted pictorially in Figure 5.1[1]. Two types of geometric calorimeter signal, one defined with and one defined without a dynamic form of noise suppression, as well as one utilizing charged particle tracks from the inner tracking detectors. In each case, as described in Section 2.2.2, the calorimeter inputs to the jet reconstruction are combined as massless four-momentum objects in order to form the final four-momentum of the jet which allows for a well-defined single-jet mass [186]. In the case of track-jets described below, the track four-momentum is constructed assuming the π meson mass for each track.

Standard calorimeter towers Perhaps the most naive approach is to combine cells into the projective towers described in Chapter 4 without any further manipulation or form of noise suppression. This approach has been used at previous collider detectors [187, 188] but introduces a complication: Any jet algorithm definition must cope with the possibility that fluctuations in the noise will create input objects with negative energies. For a jet definition using the four-momentum recombination scheme – as is used in ATLAS – a valid four-momentum must be defined for each input object, which implies that some manipulation of the energy must be performed. Due to the large fluctuations in the measured energy inherent in a non-compensating calorimeter, it is possible that an entire tower obtains a negative energy. Ad hoc schemes are thus necessary in order to define a valid four-momentum for such towers,

[1]Representations of input types courtesy of K. Perez.

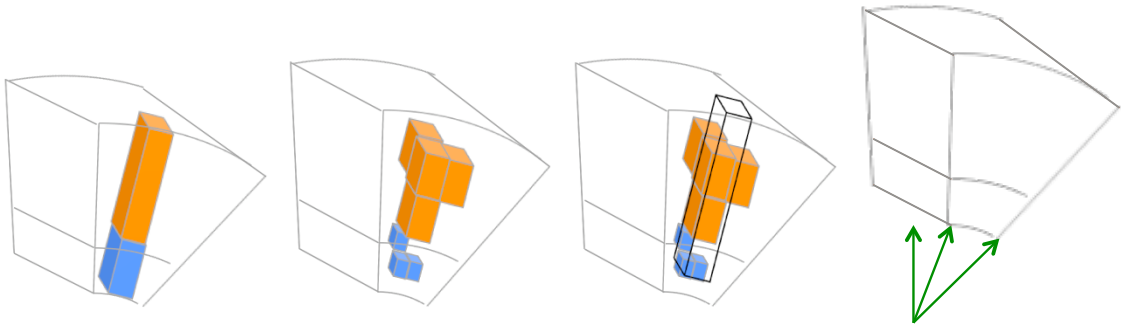

(a) Towers (b) Clusters (c) Topo-towers (d) Tracks

Figure 5.1: Types of input to jet reconstruction considered. (a) Non-noise-suppressed towers constructed from a geometric grid in $\eta - \phi$ coordinates, (b) three-dimensional noise-suppressed calorimeter clusters constructed using topological clustering and a splitting and merging algorithm, (c) noise-suppressed towers constructed using the two-dimensional tower grid with cells selected by the topological clustering, and (d) charged particle tracks reconstructed using the inner tracking detectors.

for example by successively recombining the negative energy tower with nearby towers until a total positive energy "proto-tower" is achieved. The results below indicate that this is not a viable option in the high luminosity environment at the LHC. A new approach, adopted in response to the studies presented here, uses a so-callled "ghost" scheme that resets a negative energy object to have $E = 0$ but maintains a record of the total sum of negative energy. The resulting jet is rescaled by the total negative energy clustered inside of it. However, this approach is not widely used, primarily because of the success of noise-suppressed tower and clusters.

Topological clusters Topological energy clusters represent dynamically formed three-dimensional objects seeded by a calorimeter cell with $|E_{\text{cell}}| > 4\sigma_{\text{cell}}$ above the noise [189]. Here, σ_{cell} refers to the RMS of the energy distribution for random events and is dependent on both the sampling layer in which the cell resides and the position along the calorimeter in η. Neighbor cells with $|E_{\text{cell}}| > 2\sigma_{\text{cell}}$ are then added to the cluster, increasing the size of the cluster until no nearest-neighbor cell has an energy above $2\sigma_{\text{cell}}$ of the noise. In a final step, all nearest-neighbor cells surrounding the

clustered cells are added to the cluster, as this was shown to improve energy resolution in single pion test beam studies. These clusters can then be split or merged depending on local maxima or minima within the clusters. Negative energy clusters are rejected entirely from the jet reconstruction. The design of these clusters is to follow the calorimeter shower development in an intuitive way and to accurately reflect the shower shape in the detector. One potential issue, especially for substructure measurements, is the dynamic growth of clusters, which needs to be monitored carefully to be sure that systematic effects do not arise in very energetic, complex jet internal topologies.

Noise-suppressed towers Noise-suppressed towers are constructed on the standard fixed geometrical grid of $\Delta\eta \times \Delta\phi = 0.1 \times 0.1$. However, in this case the energy in each tower is computed using only cells that have been selected using topological clustering. Therefore, the same noise suppression is used in both cases. For this reason, we will refer to noise-suppressed towers as "topo-towers" when comparing their performance with that of standard towers described above. Since all inputs are required to have an energy above 0 as dictated by the four-momentum recombination scheme, slight differences with respect to topological clusters can be observed in low energy jets. These differences occur when cells in a single positive energy cluster populate multiple geometrical towers, some of which may then have small negative energies due to individual negative energy cells that were present within the single cluster.

Charged particle tracks In a departure from the purely calorimetric perspective of hadronic jets, the use of charged particle tracks as the input to jet reconstruction provides an alternative view of the jet itself that yields several complementary features. The four-momentum of each track is defined using the momentum measurement provided by the ID track reconstruction and the assumption of the pion mass. Analogous to the noise-suppression applied to calorimeter cells, tracks may be preselected using track quality criteria such as the total number of silicon hits on the track, the χ^2 of the track fit, and so on. Furthermore, tracks yield additional

information that is not available for purely calorimeter-based jets, in particular, the production vertex. The z coordinate of the track impact parameter defines a third position dimension for the jet, so to speak, in addition to η and ϕ. As will be shown in Chapter 6 this has significant advantages.

As described in Appendix C, until this work only the 3-dimensional topological clustering method applied any form noise suppression in order to select cells with significant energy content compared to the expected noise. Based on the results obtained herein, ATLAS adopted the noise-suppressed tower definition as the default approach to using the geometrical tower grid as the input to tower-jet reconstruction. Topological clustering remains the primary approach to jet reconstruction, however, due to the promising technique of local cluster calibration (see Section 5.3) and certain technical features of the core software which are optimized for the calorimeter cluster objects. We shall see in Chapter 8 that the benefit extends to the complex analysis of the jet internal structure as well.

5.2 Jet algorithms

The choice of jet algorithm for the default reconstruction is governed by many factors: the sensitivity to noise, the efficiency and purity of the resulting jets, the sensitivity to additional close-by jets, and so on. Each of these factors were considered in Ref. [106], with the final decision to use anti-k_t as the default jet algorithm in ATLAS. The decision considered as many as 14 different figures of merit, including the performance of the jet algorithms at high luminosity.

In this section, the effects of multiple simultaneous interactions on the reconstruction of jets in ATLAS are briefly described for various jet algorithms. This is one of the primary factors influencing the choice of jet algorithm in ATLAS due to the expected high level of pile-up at the LHC. This discussion will provide crucial insight into the final analysis using the first year data, in which a significant amount of pile-up is already present.

Algorithms which are known to contain infrared and collinear sensitivities such

Jet algorithm	Distance parameter (R)	Split-merge parameter ($f_{S/M}$)
ATLAS cone	0.4 and 0.7	0.50
SIS-cone	0.4 and 0.7	0.50
k_t	0.4 and 0.6	N/A
anti-k_t	0.4 and 0.6	N/A

Table 5.1: Jet algorithm parameters used for pile-up studies. A split-merge fraction $f_{S/M} = 0.50$ is used for SIS-cone jets in order to compare to the same split-merge parameter being used by the ATLAS cone algorithm.

as the original ATLAS cone algorithm are the most susceptible to such effects. It is crucial to consider such effects when evaluating the performance of jet algorithms in the LHC environment because of the unprecedented expectation of nearly 25 simultaneous collisions per bunch crossing at nominal luminosity, as well as significant pile-up is the very first data recorded at $\sqrt{s} = 7$ TeV.

Monte Carlo samples of inclusive two-jet events are passed through the ATLAS detector simulation without additional pp interactions overlaid and compared directly to the same processes where pile-up has been included at the level of $\langle N_{pp} \rangle = 4.6$. Here, $\langle N_{pp} \rangle$ refers to the Poisson average number of independent pp interactions in addition to the hard-scattering collision. The nominal LHC bunch spacing of 25 ns is used so as to isolate pile-up effects from those related to non-optimal bunch spacing effects (see Chapter 6 for more details). The simulated hard-scattering considered here corresponds to hard-scattering processes with $35 < \hat{p}_T < 70$ GeV for the so-called $J2$ sample and $560 < \hat{p}_T < 1120$ GeV for the $J6$ sample. The simulated physics process (QCD di-jet production) is *precisely* the same for each pair of samples with and without pile-up.

The various non-standard jet algorithms used for this study and the parameter settings used for each are listed in Table 5.1. Note that in particular, a split-merge parameter of $f_{S/M} = 0.50$ is used for SIS-cone jets in order to compare to the same split-merge parameter being used by the ATLAS cone algorithm. This setting is known to be non-optimal in several non-pile-up studies but was chosen here to be consistent with the ATLAS cone algorithm.

Note that one important systematic effect in the use of any jet algorithm is the

choice of algorithm parameters. In the case of the cone algorithms, the need to tune the split/merge parameter, $f_{S/M}$, may add to the systematic error for analyses that are sensitive to the use or rejection of close-by jets. For such cases, the effect of splitting and merging jets has measurable consequences on observable quantities.

The variety of ATLAS input constituent types described in Section 5.1 has a direct influence on the choice of default jet algorithm used for physics analysis. The three calorimeter-based input constituent types described above – both non-noise-suppressed and noise-suppressed calorimeter towers and topological clusters – are used to compare the performance of these jet algorithms under various luminosity conditions. The jet constituents are uncalibrated; that is, the energy scale of the constituent is at the EM scale of the detector. Ideally, the choice of jet algorithm should be robust with respect to the input constituent type, assuming that each input reflects the energy depositions of the constituent particles accurately. In practice, these input constituents exhibit differences in their correlation to the truth input particle spectrum and do influence the jet reconstruction. Furthermore, in the case of calorimeter towers, the introduction of noise suppression can significantly reduce the sensitivity to pile-up compared to towers used without noise-suppression.

One measure of the sensitivity to pile-up in the context of the input constituent choice is the total number of constituents that are clustered together by the jet algorithm. Differences in the multiplicity spectrum are expected for different input choices since this defines the granularity of objects to be considered as jet constituents by the jet algorithm. However, as shown in Table 5.2, algorithms can exhibit different behavior in events with and without pile-up for different inputs to the jet finder algorithms. The ratio of the mean and RMS of the number of constituents is used as a figure of merit in this study. A large change in the mean number of constituents signifies that the jet content is changing significantly due to the additional soft interactions present in the event from pile-up. Increases in the RMS of the constituent multiplicity implies that the introduction of pile-up leads to less predictable jets in a given event due to larger fluctuations in the jet content.

anti-k_t jets are shown to be the most stable after the introduction of pile-up when using non-noise-suppressed inputs. This behavior is expected since the design of

Jet algorithm	clusters		towers		topo-towers	
	$\frac{\langle N\rangle_{\mathrm{pu}}}{\langle N\rangle}$	$\frac{RMS_{\mathrm{pu}}}{RMS}$	$\frac{\langle N\rangle_{\mathrm{pu}}}{\langle N\rangle}$	$\frac{RMS_{\mathrm{pu}}}{RMS}$	$\frac{\langle N\rangle_{\mathrm{pu}}}{\langle N\rangle}$	$\frac{RMS_{\mathrm{pu}}}{RMS}$
ATLAS cone ($R = 0.4$)	1.43	1.55	0.73	0.62	1.07	1.50
ATLAS cone ($R = 0.7$)	1.69	1.83	0.85	0.95	–	–
SIS-cone ($R = 0.4$)	1.49	1.99	1.40	1.97	1.01	2.43
SIS-cone ($R = 0.7$)	1.80	2.23	1.13	1.42	–	–
k_t ($R = 0.4$)	1.18	1.04	0.79	0.84	0.92	0.87
k_t ($R = 0.7$)	1.24	1.01	0.73	0.79	–	–
anti-k_t ($R = 0.4$)	1.26	1.07	0.95	1.12	1.00	0.88
anti-k_t ($R = 0.7$)	1.42	1.01	0.99	1.20	–	–

Table 5.2: Ratio for both the mean number of jet constituents and RMS of the multiplicity distribution in events with pile-up compared to events without pile-up. Both the ATLAS cone and the SIS-cone algorithms show large increases in the number of topo-cluster and topo-tower jet constituents and the RMS of the distributions in events with pile-up. The anti-k_t algorithm shows a notable stable RMS in all cases, suggesting that the expected jet content is quite robust against both the input constituent type and pile-up.

the algorithm is to cluster the hardest particles first, and to then form a relatively rigid cone of radius R around that constituent, but in an IRC safe manner. Both recombination type algorithms are stable with respect to pile-up when constructed from topological clusters, although the constituent multiplicity is observed to increase. Importantly, the RMS of the multiplicity distribution is very stable for both k_t and anti-k_t. Interestingly, the ATLAS cone and the k_t algorithms both show a *decrease* in the mean number of constituents when pile-up is added and the jet is constructed from non-noise-suppressed towers. This phenomenon is due to a "nibbling" of the jets by nearby low-p_{T} jets that arise due to the inherent sensitivity to soft activity of non-noise-suppressed towers.

The constituent multiplicity spectrum for each algorithm and distance parameter (narrow, $R = 0.4$ and wide, $R = 0.7$) using topological clusters as input is shown in Figure 5.2. The stability of the anti-k_t and k_t algorithms for both narrow and wide cone radii is quite visible.

The k_t and anti-k_t algorithms are consistently more well behaved in both the

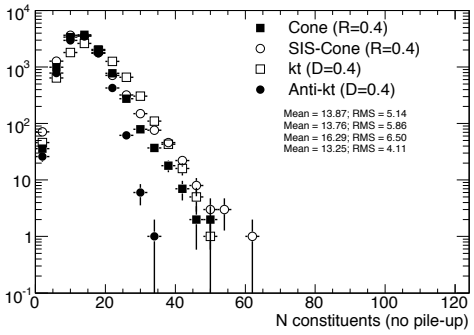

(a) Narrow cone sizes without pile-up

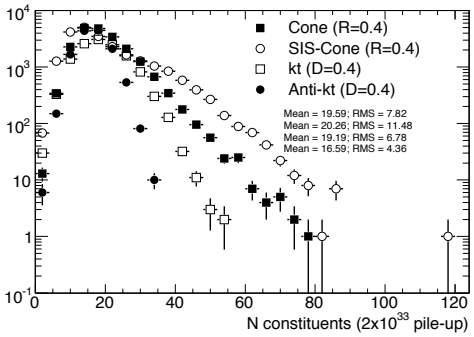

(b) Narrow cone sizes with pile-up

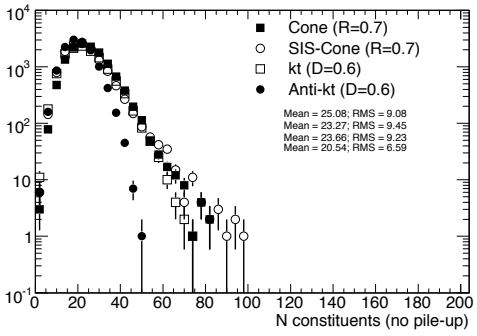

(c) Wide cone sizes without pile-up

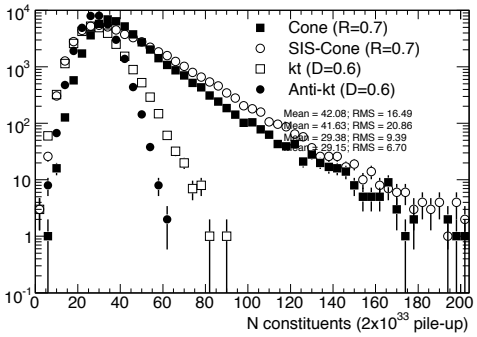

(d) Wide cone sizes with pile-up

Figure 5.2: Constituent multiplicity for both narrow ($R = 0.4$) topo-cluster jets without pile-up (a) and with pile-up (b) and for wide ($R = 0.7$ and $R = 0.6$) topo-cluster jets without pile-up (c) and with pile-up (d). For both jet radii, the k_t and anti-k_t jet algorithms show much less sensitivity to pile-up through the number of topo-clusters included in the jet for events with pile-up.

mean number of constituents and the RMS of the distributions in events with pile-up. k_t exhibits the interesting feature that the number of tower constituents seems to *decrease* with the addition of pile-up, suggesting that the priority for low-p_T clustering is creating jets which are then not included in the leading jets of the event, thus reducing the number of input constituents available for clustering the higher-p_T jets in the event. A similar effect is present for the ATLAS cone algorithm. Both the ATLAS cone and the SIS-cone algorithms show large increases in the number of topo-cluster and topo-tower jet constituents and the RMS of the distributions in events with pile-up. The anti-k_t algorithm shows a notably stable RMS in all cases, suggesting that the expected jet content is quite robust against both the input constituent type and pile-up.

To highlight the sensitivity to the jet input, a single low p_T event ($p_{T,1}^{\text{true}} = 35$ GeV) is chosen and the leading reconstructed jets in the event above $p_T^{\text{reco}} = 20$ GeV are drawn in the $\eta \times \phi$ plane along with their constituents in Figure 5.3. All four jet algorithms considered in this study are shown with each of the three possible jet inputs considered here. Both the ATLAS cone and SIS-cone algorithms change significantly depending on which type of constituent is used and if that constituent has noise suppression applied. The clustering algorithms, k_t and anti-k_t, both provide a consistent picture for this event regardless of the constituent type.

5.3 Jet identification and calibration

As described in Chapter 4.2.3, the baseline calibration of the calorimeters only corrects the energy measured in the detector to the EM energy scale. In order to compensate for the difference between the energy measurement of purely EM objects (such as electrons and photons) and the energy of a hadronic jet, an additional jet calibration procedure must be applied to convert the EM scale of the ATLAS calorimeters to the hadronic scale. The procedure used for the 2010 data utilizes simple energy and η-dependent calibration scheme (referred to as EM+JES calibration) that is primarily based on Monte Carlo simulation with some direct in-situ measurements and is supported by in-situ tests of the resulting jet energy scale.

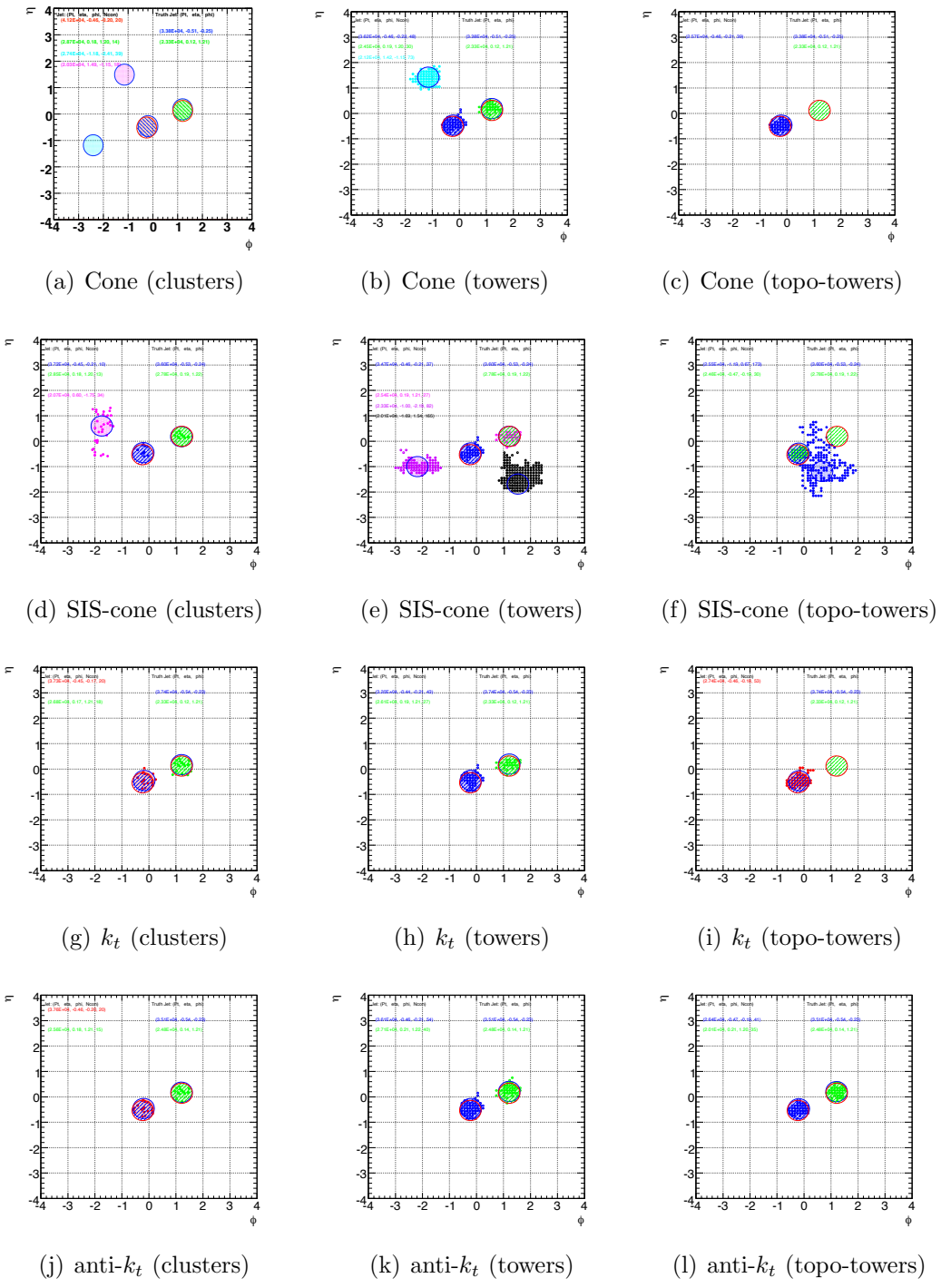

(a) Cone (clusters) (b) Cone (towers) (c) Cone (topo-towers)

(d) SIS-cone (clusters) (e) SIS-cone (towers) (f) SIS-cone (topo-towers)

(g) k_t (clusters) (h) k_t (towers) (i) k_t (topo-towers)

(j) anti-k_t (clusters) (k) anti-k_t (towers) (l) anti-k_t (topo-towers)

Figure 5.3: Event displays for each jet algorithm (small radius only, $R = 0.4$) and each input constituent type, (left) topological clusters, (middle) towers without noise suppression (calo-towers) and (right) towers with noise suppressions (topo-towers). k_t and anti-k_t are shown to be the most stable with respect to input constituent type.

The jet calibration is intended to correct for several detector effects that affect the jet energy measurement:

- partial measurement of the energy deposited by hadrons (calorimeter non-compensation),
- energy losses in inactive regions of the detector (dead material),
- energy deposits from particles not contained in the calorimeter (leakage),
- energy deposits of particles inside the truth jet that are not included in the reconstructed jet (out-of-cone),
- signal losses in calorimeter clustering and jet reconstruction.

The EM+JES calibration scheme consists of three principal steps:

1. for events with pile-up, the average additional energy due to additional *pp* collisions is subtracted from the energy measured in the calorimeters using correction constants extracted from an in-situ measurement (this is discussed in Chapter 6 in more detail),
2. the position of the jet is corrected such that the jet direction points to the primary vertex of the interaction instead of the geometrical centre of ATLAS detector,
3. the jet energy and position as reconstructed in the calorimeters are corrected using constants derived from the comparison of the kinematics of reconstructed jets and corresponding truth jets in Monte Carlo.

In the second step, the jet direction is corrected for the difference between the default ATLAS detector origin and the actual position of the primary *pp* interaction. In the case of multiple such interactions, the primary vertex with the highest associated sum of track transverse momenta squared, $\max\left(\sum p_{T,\text{track}}^2\right)$, is used. The kinematics of each topo-cluster is recalculated using the vector from the primary vertex to the

topo-cluster centroid as its direction. The raw jet four-momentum is thereafter redefined as the vector sum of the topo-cluster four-momenta. This correction improves the angular resolution, resulting in a small improvement (<1%) in the jet p_T response. The jet energy is unaffected.

In the last step, the calibration is derived in terms of the energy response of the jet, or the ratio of the reconstructed jet energy to that of a jet constructed from stable truth particles in the Monte Carlo simulation. This response, written as

$$\mathcal{R} = E_{\text{reco}}/E_{\text{truth}} \tag{5.1}$$

may be defined at any energy scale. To compute this quantity, reconstructed jets must be matched to isolated truth jets in the Monte Carlo within $\Delta R < 0.3$. The isolation requirement is applied in order to factorize the effects due to close-by jets from those due to purely detector effects such as dead material and non-compensation. The isolation criterion requires that no other jet with a $p_T > 7$ GeV be within $\Delta R < 2.5R$, where R is the distance parameter of the jet algorithm. The EM scale energy response ($\mathcal{R}^{\text{EM}} = E^{\text{EM}}_{\text{calo}}/E_{\text{truth}}$) is binned in truth jet energy E_{truth} and the calorimeter jet detector η, or η_{det}, which refers to the pseudorapidity of the original reconstructed jet before the origin correction. The reason for this is both that the origin correction is a component of the calibration that is applied independent of the energy calibration, and that the detector-level kinematics are the subject of the correction and so η_{det} is the appropriate quantity to use in order to account for detector non-uniformity, for example. The EM scale response for multiple energy ranges and as a function of η_{det} is shown in Figure 5.4.

Following the measurement of the distribution of EM scale response, $\mathcal{R}^{\text{EM}}$, for an ensemble of jets the peak position of a Gaussian fit to the distribution is used to extract $\left\langle \mathcal{R}^{\text{EM}} \right\rangle$ in each $(E_{\text{truth}}, \eta_{\text{det}})$-bin. A function $\mathcal{F}_{\text{calib},k}(E^{\text{EM}}_{\text{calo}})$ is then defined for each η_{det}-bin k that describes the response as a function of the uncalibrated jet energy. $\mathcal{F}_{\text{calib},k}(E^{\text{EM}}_{\text{calo}})$ is parameterised as:

$$\mathcal{F}_{\text{calib},k}(E^{\text{EM}}_{\text{calo}}) = \sum_{i=0}^{N_{\text{max}}} a_i \left(\ln E^{\text{EM}}_{\text{calo}}\right)^i, \tag{5.2}$$

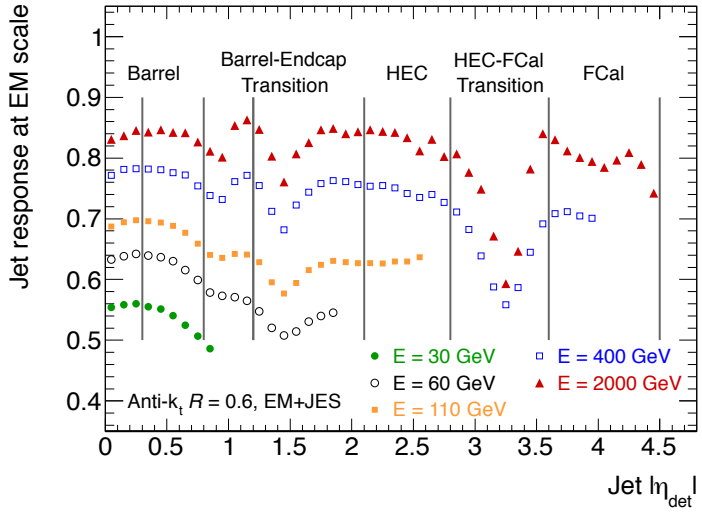

Figure 5.4: Simulated jet energy response at the electromagnetic scale as a function of EM+JES calibrated jet energy $E_{\text{calo}}^{\text{EM+JES}}$ and detector pseudorapidity η_{det}. Also shown are the η-intervals used to evaluate the JES uncertainty (see Table 5.3). The inverse of the response shown in each bin is equal to the average jet energy scale correction (and therefore equal to $\mathcal{F}_{\text{calib}}$).

where a_i are free parameters, and N_{max} is chosen between 1 and 6 depending on the goodness of the fit. The final jet energy scale correction that relates the measured calorimeter jet energy scale to the hadronic scale is then defined as $1/\mathcal{F}_{\text{calib},k}(E_{\text{calo}}^{\text{EM}})$ in the following:

$$E_{\text{calo}}^{\text{EM+JES}} = \frac{E_{\text{calo}}^{\text{EM}}}{\mathcal{F}_{\text{calib}}(E_{\text{calo}}^{\text{EM}})|_{\eta_{\text{det}}}}, \tag{5.3}$$

where $\mathcal{F}_{\text{calib}}(E_{\text{calo}}^{\text{EM}})|_{\eta_{\text{det}}}$ is $\mathcal{F}_{\text{calib},k}(E_{\text{calo}}^{\text{EM}})$ for the relevant η_{det}-bin k.

The average jet energy scale correction $\left\langle 1/\mathcal{F}_{\text{calib},k}(E_{\text{calo}}^{\text{EM}})\right\rangle$ is shown as a function of calibrated jet transverse momentum $p_{\text{T}}^{\text{jet}}$ for three jet η-intervals in Figure 5.5.

For many physics analyses, the uncertainty on the JES constitutes the dominant systematic uncertainty because of its tendency to shift jets in and out of analysis selections due to the steeply falling jet p_{T} spectrum. The uncertainty on the above derived JES is determined primarily by six factors: varying the physics models for hadronization and parameters of the Monte Carlo generators, evaluating the baseline calorimeter response to single particles, comparing multiple models for the detector

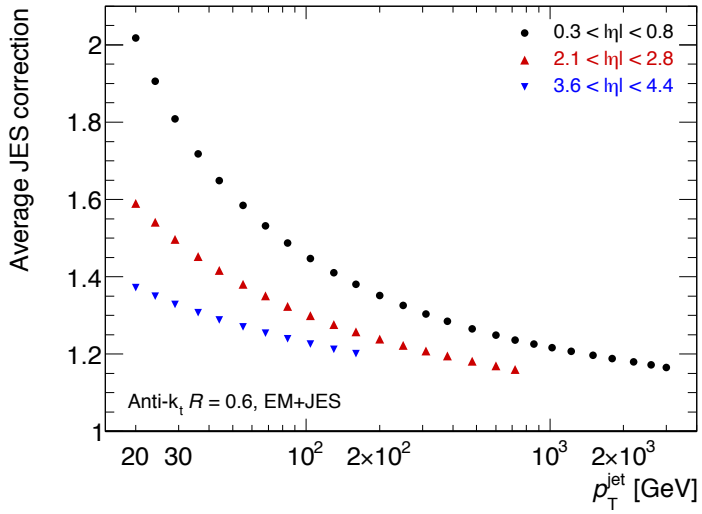

Figure 5.5: Average jet energy scale correction as a function of calibrated jet transverse momentum for three representative η-intervals. The correction is only shown over the accessible kinematic range, i.e. values for jets above the kinematic limit are not shown.

simulation of hadronic showers, assessing the calibration scales as a function of pseudorapidity, and by adjusting the JES calibration method itself. In addition to these tests, in-situ tests of the JES using direct γ-jet balance, multi-jet balance, and track-jets indicate that the uncertainties presented in Figure 5.6 accurately reflect the true uncertainties in the JES.

The final JES uncertainty, after taking in account the six factors briefly described above, is determined from the maximum deviation in response observed with respect to the response in the nominal sample (which does not include pile-up). Figures 5.6 and 5.7 show the final fractional jet energy scale systematic uncertainty and its individual contributions as a function of jet $p_{\mathrm{T}}^{\mathrm{jet}}$ for three selected η regions. These results are also summarized in Table 5.3. For the more forward region shown in Figure 5.7, the dominant component at low p_{T} is the η-intercalibration. This is a procedure that uses direct di-jet balance measurements in two-jet events to measure the *relative* energy scale of jets in the more forward regions compared to jets in a reference region. The technique exploits the fact that these jets are expected to have equal p_{T} due to transverse momentum conservation. This feature is not the case for jet mass,

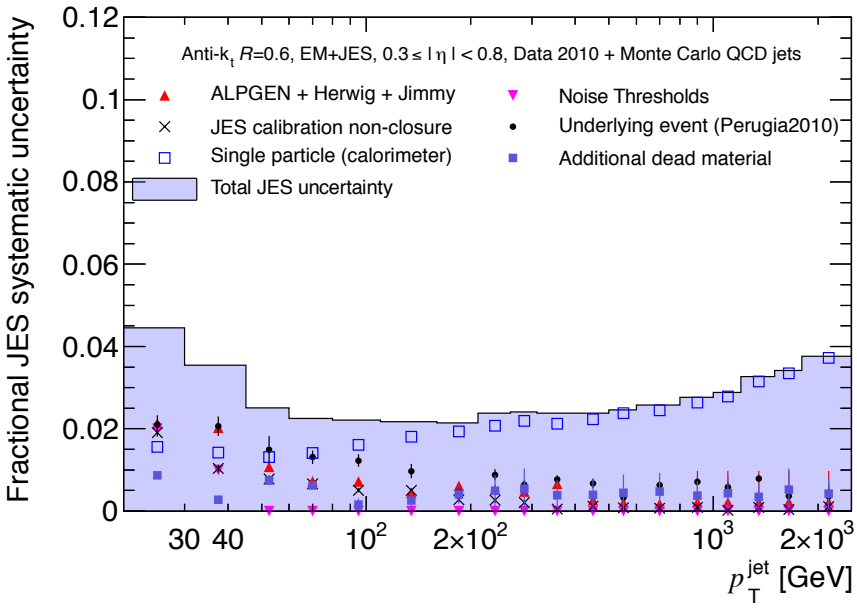

Figure 5.6: Fractional jet energy scale systematic uncertainty as a function of $p_{\mathrm{T}}^{\mathrm{jet}}$ for jets in the pseudorapidity region $0.3 < |\eta| < 0.8$ in the calorimeter barrel. The total uncertainty is shown as the solid light blue area. The individual sources are also shown, with uncertainties from the fitting procedure if applicable.

for example, which complicates the calibrations and validation. This is discussed in Chapter 8. The p_{T} balance is measured via the asymmetry $\mathcal{A}$, defined as

$$\mathcal{A} = \frac{p_{\mathrm{T}}^{probe} - p_{\mathrm{T}}^{ref}}{p_{\mathrm{T}}^{\mathrm{avg}}}, \tag{5.4}$$

where $p_{\mathrm{T}}^{\mathrm{avg}} = (p_{\mathrm{T}}^{probe} + p_{\mathrm{T}}^{ref})/2$. The reference region is chosen to be the central region of the barrel, $|\eta| < 0.8$. $\mathcal{A}$ is then used to measure the η-intercalibration factor c of the probe jet, or its response relative to the reference jet $1/c$, using the relation

$$\frac{p_{\mathrm{T}}^{probe}}{p_{\mathrm{T}}^{ref}} = \frac{2+\mathcal{A}}{2-\mathcal{A}} = 1/c. \tag{5.5}$$

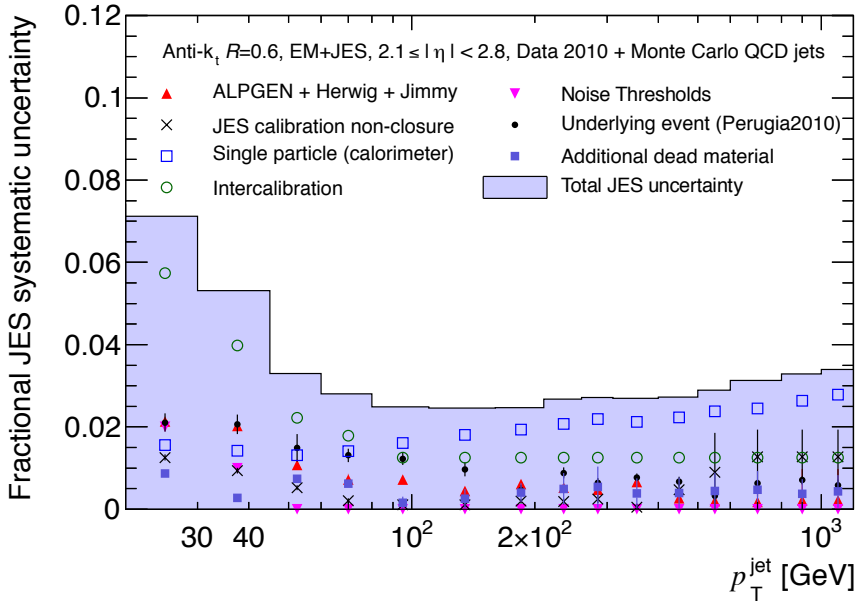

Figure 5.7: Fractional jet energy scale systematic uncertainty as a function of $p_{\mathrm{T}}^{\mathrm{jet}}$ for jets in the pseudorapidity region $2.1 < |\eta|| < 2.8$. The JES uncertainty in the endcap region is extrapolated from the barrel uncertainty, with the uncertainty contribution from the η-intercalibration between central and endcap jets in data and Monte Carlo added in quadrature. The total uncertainty is shown as the solid light blue area. The individual sources are also shown, with uncertainties from the fitting procedure if applicable.

η **region**	**Maximum fractional JES Uncertainty**		
	p_T^{jet} **=20 GeV**	p_T^{jet} **=200 GeV**	p_T^{jet} **=1.5 TeV**
$0 < \|\eta\| < 0.3$	4.6%	2.3%	3.1%
$0.3 < \|\eta\| < 0.8$	4.5%	2.2%	3.3%
$0.8 < \|\eta\| < 1.2$	4.5%	2.4%	3.4%
$1.2 < \|\eta\| < 2.1$	5.5%	2.5%	3.5%
$2.1 < \|\eta\| < 2.8$	7.1%	2.5%	
$2.8 < \|\eta\| < 3.2$	8.5%	3.0%	
$3.2 < \|\eta\| < 3.6$	8.7%	3.0%	
$3.6 < \|\eta\| < 4.5$	12.6%	2.9%	

Table 5.3: Summary of the maximum EM+JES jet energy scale systematic uncertainties for different $p_{\mathrm{T}}^{\mathrm{jet}}$ and η regions from Monte Carlo-based study for anti-k_t jets with $R = 0.6$.

5.4 Jet properties at $\sqrt{s} = 7$ TeV

In this section, we present studies of the objects used for jet finding and calibration (towers and clusters). These observations are extended to include charged particle distributions within jets in anticipation of the detailed jet internal structure analysis in Chapter 8. Finally, the transverse structure of jets is measured using both calorimeter-based objects and tracks. These measurements are used to study the presence of both physics and detector effects in the jet reconstruction and global jet properties. Results describing the jet properties observed in proton-proton collisions at a center-of-mass energy of 900 GeV are shown in Ref. [190]. More details may also be found in Ref. [186].

Jet Constituent Properties

A good understanding of jet reconstruction requires the characterization of the inputs to jet reconstruction inside the jets they form. This section presents distributions of the multiplicity of the constituents inside jets. Comparisons of these distributions between Monte Carlo simulations and data without pile-up aid in determining how well the generated particle spectra and the detector simulation describe the formation of the constituent objects in the context of a jet. Comparisons are made to Pythia 6.421, which is used for both even generation and the parton shower and hadronization models using the ATLAS MC09 tune [191]. This is a slightly older version of the Pythia tuning available in ATLAS as compared to that used for the analyses presented in Chapter 7 and 8.

Figure 5.8 shows the number of topological clusters and noise-suppressed towers inside jets built of these constituents, as well as the variation as a function of y^{jet}. Since towers have a size of $\Delta\eta \times \Delta\phi = 0.1 \times 0.1$, the maximum number of constituents expected in these jets, from a purely geometrical argument, is $N_{\text{towers}} \approx 113$ (assuming a perfect jet cone with radius $R = 0.6$). The distribution shows that jets contain many fewer towers when noise suppression is applied, with a mean of $\langle N_{\text{towers}} \rangle \approx 44$ for central jets ($|y^{\text{jet}}| < 0.3$, Fig. 5.8) . The mean number of topological clusters per jet is roughly one quarter of the mean number of towers, $\langle N_{\text{clusters}} \rangle \approx 13$, for central

jets. The smaller number of topological clusters is expected, given that the clustering algorithm attempts to incorporate the hadronic shower of one particle in one cluster.

For both input constituent types, the overall shape of the multiplicity distribution is well described by the Monte Carlo simulation. However, in both cases, a shift is observed in the comparison leading to a 6.4% (4.0%) deficiency in the Monte Carlo simulation for towers (clusters). This shift is common to the observations that will be made with tracks, jet widths, jet shapes, and jet masses and points to a real physical difference between the soft internal structure of jets in data and in the MC.

This disagreement implies also that topological clusters are slightly larger in the data than in the Monte Carlo simulation, since the noise-suppressed towers merely reflect the number of cells used to build topological clusters. The difference has been shown to be due to an excess of low-energy towers, which is consistent with the transverse jet structure results indicating that jets are slightly wider in the data than in the Monte Carlo simulation. Repeating this analysis with tracks implies that this discrepancy is a combination of an underestimation of the soft underlying event as well as of the hard jet structure.

The discrepancy between data and Monte Carlo simulation is larger for topological clusters in the transition region between the barrel and end-cap calorimeters (Figure 5.8(d)), whereas the difference is roughly constant for jets built from towers (Figure 5.8(c)). The difference in the trend of the multiplicity distributions at high y^{jet}– where the tower multiplicity per jet increases yet the cluster multiplicity decreases – is another feature of the difference in definition of these inputs. Since the towers follow a projective geometrical definition, the physical size of each tower changes with y, while the topological cluster definition follows the shower development. In the forward region, hadronic showers are large with respect to the tower size. As a result, it is more difficult to separate showers from individual particles in the forward regions of the detector.

Properties of Tracks in Jets

The Inner Detector (ID) provides precise measurements of the momentum of charged particles emerging from the pp collisions which in turn yield information regarding

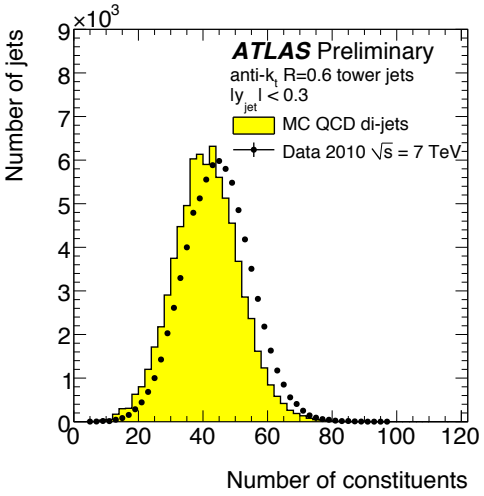

(a) Number of towers per jet

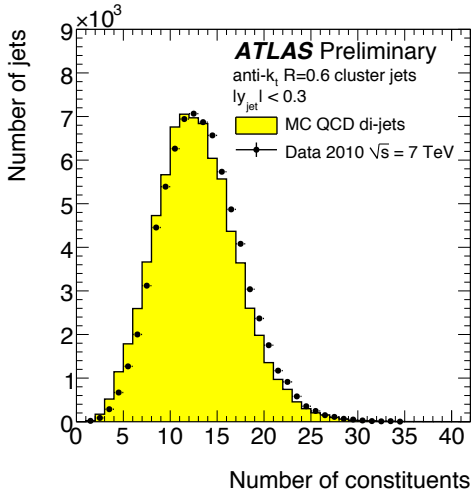

(b) Number of clusters per jet

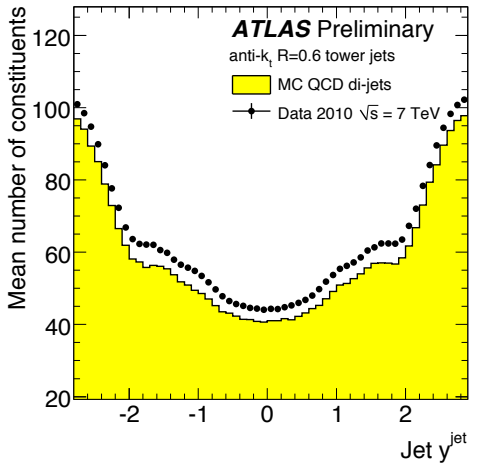

(c) Number of towers vs. y^{jet}

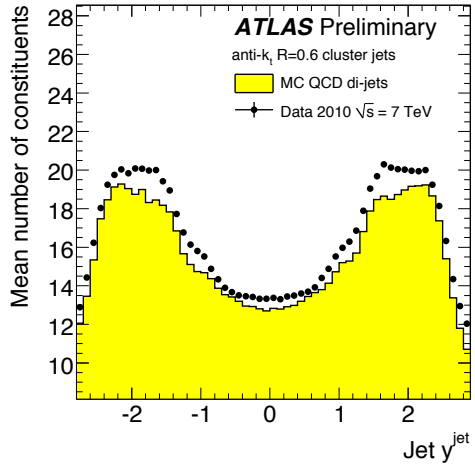

(d) Number of clusters vs. y^{jet}

Figure 5.8: Number of constituents (top) in jets built with noise-suppressed towers (left) and topological clusters (right), compared between data and Monte Carlo simulation for central jets ($|y^{\mathrm{jet}}| < 0.3$). The variation of the constituent multiplicity as a function of y^{jet} is also shown (bottom).

the fraction of neutral and charged energy contained in the jet and the internal jet structure. Measurements of the track multiplicity in jets, N_{track}, and its correlation with $p_{\text{T}}^{\text{jet}}$ using the simple $\Delta R < 0.6$ matching criterion are presented, where the matching is performed using the track coordinates at the point of closest approach to the production vertex without extrapolating them to the surface of the calorimeter. The total scalar sum of track momenta associated with a jet, $\sum p_{\text{T}}^{\text{track}}$, can be used to provide further details on the calorimeter response to jets. The ratio of $\sum p_{\text{T}}^{\text{track}}$ to $p_{\text{T}}^{\text{jet}}$, referred to as f_{track}, can be used after the jet calibration in order to improve the jet energy resolution, as demonstrated in Monte Carlo simulations [183] but this has not been fully implemented in the data yet.

In this section, jets are selected with $|y^{\text{jet}}| < 1.9$, to account for the ID coverage ($|\eta^{\text{track}}| < 2.5$) and the requirement that tracks be contained within a cone of radius $R = 0.6$ around the jet axis. For all distributions, the Monte Carlo simulations have been normalized to the number of jets present in the data. Jets are also required to have transverse momenta within the range $20 < p_{\text{T}}^{\text{jet}} < 300$ GeV so that any uncertainties related to tracking efficiency in higher p_{T} jets do not impact these studies.

Figure 5.9 shows the measured number of tracks inside jets and Figure 5.10 the variation of N_{track} with $p_{\text{T}}^{\text{jet}}$, in each case for jets built from topological clusters and repeated for tracks with $p_{\text{T}}^{\text{track}} > 0.5$ GeV and 1 GeV. The measurements are nearly identical for jets built from noise-suppressed towers, and are thus omitted for brevity. The track multiplicity is peaked at $N_{\text{track}} = 4$ ($N_{\text{track}} = 3$) with a mean of $\langle N_{\text{track}} \rangle = 5.0$ ($\langle N_{\text{track}} \rangle = 3.5$) for $p_{\text{T}}^{\text{track}} > 0.5$ GeV ($p_{\text{T}}^{\text{track}} > 1$ GeV). As expected, $\langle N_{\text{track}} \rangle$ increases with increasing $p_{\text{T}}^{\text{jet}}$.

The measurements indicate that the Monte Carlo simulation underestimates the number of tracks in a jet by roughly 5% across a large range in $p_{\text{T}}^{\text{jet}}$ in the case of the 0.5 GeV $p_{\text{T}}^{\text{track}}$ selection. This discrepancy is greatly reduced by increasing the track selection to 1 GeV. Even when restricting the measurement to the very central region of the calorimeter ($|y^{\text{jet}}| < 0.3$) the discrepancy at low-$p_{\text{T}}^{\text{track}}$ remains. As will be shown in Chapter 8, this is one of several indications of potentially imperfect tuning of the Monte Carlo simulation in terms of the internal jet structure. Other

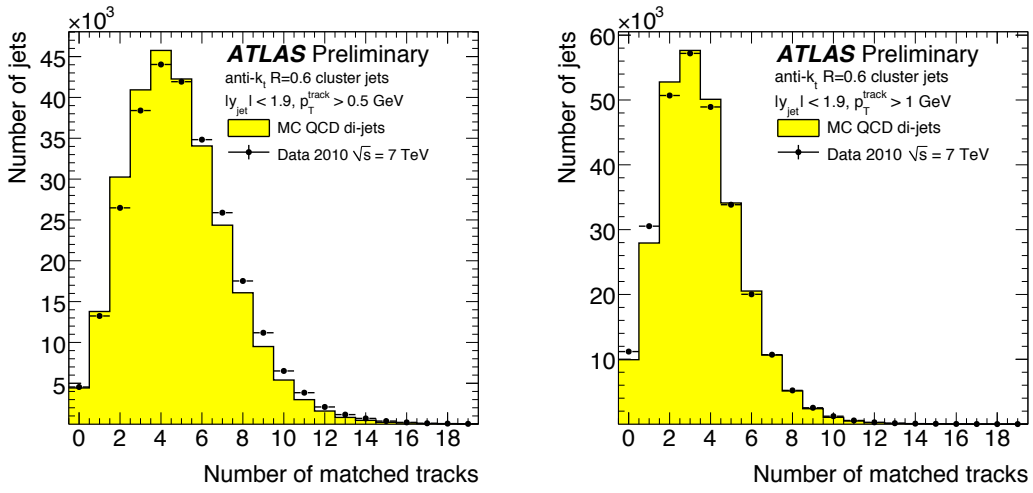

(a) Track multiplicity ($p_{\mathrm{T}}^{\mathrm{track}} > 0.5$ GeV) (b) Track multiplicity ($p_{\mathrm{T}}^{\mathrm{track}} > 1$ GeV)

Figure 5.9: Distribution of the number of charged tracks (N_{track}) matched to the calorimeter jet for both (a) the nominal $p_{\mathrm{T}}^{\mathrm{track}} > 0.5$ GeV requirement and (b) an increased $p_{\mathrm{T}}^{\mathrm{track}} > 1$ GeV selection.

studies [192] indicate that the detector simulation models well properties of tracks in jets while the fragmentation function and underlying event used by the Monte Carlo generator may require further tuning [193].

The measured f_{track} distribution is shown in Figure 5.11 for jets built from topological clusters and indicates a 3-4% higher mean value predicted from the Monte Carlo simulation compared to the data for the inclusive y selection (the same effect is seen for noise-suppressed tower jets). When restricting the jets to be within $|y^{\mathrm{jet}}| < 0.3$ or above $p_{\mathrm{T}}^{\mathrm{jet}} > 30$ GeV (or both) this difference vanishes, suggesting that the discrepancy is primarily localized in the low-p_{T} range and slightly more forward directions. This difference is approximately within the total jet-energy scale uncertainty [194].

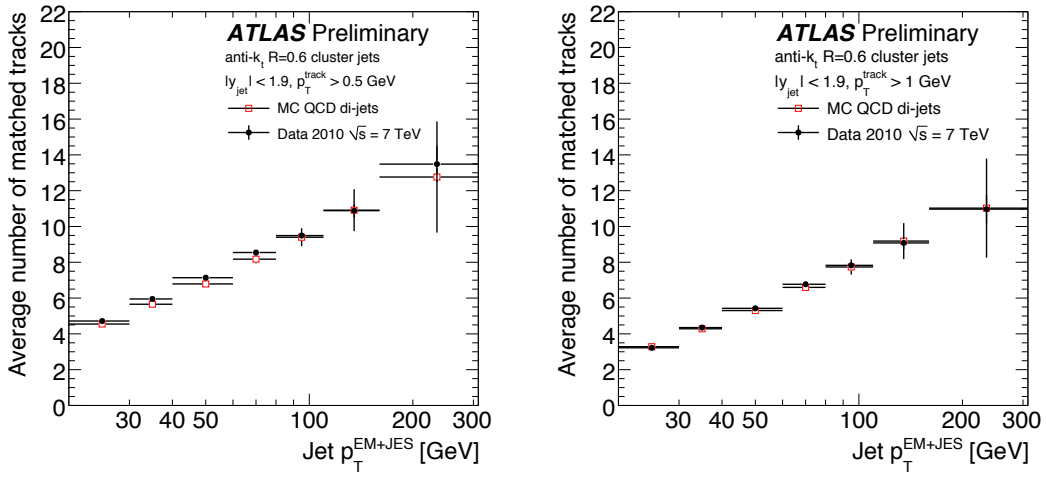

(a) N_{track} vs. $p_{\text{T}}^{\text{jet}}$ ($p_{\text{T}}^{\text{track}} > 0.5$ GeV) (b) N_{track} vs. $p_{\text{T}}^{\text{jet}}$ ($p_{\text{T}}^{\text{track}} > 1$ GeV)

Figure 5.10: Correlation of the number of charged tracks (N_{track}) matched to the calorimeter jet with $p_{\text{T}}^{\text{jet}}$ for both (a) the nominal $p_{\text{T}}^{\text{track}} > 0.5$ GeV requirement and (b) an increased $p_{\text{T}}^{\text{track}} > 1$ GeV selection.

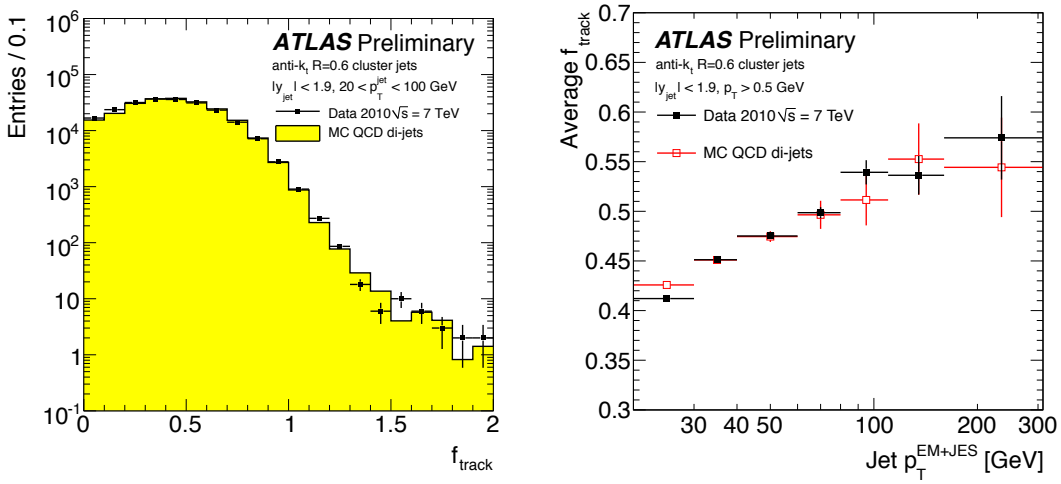

(a) Charged fraction (f_{track}) (b) Dependence of f_{track} on $p_{\text{T}}^{\text{jet}}$

Figure 5.11: (a) Distribution of the charged particle fraction, f_{track}, for calorimeters jets built from topological clusters and (b) its correlation with $p_{\text{T}}^{\text{jet}}$. The same trends are observed for noise-suppressed tower jets.

Transverse Jet Profile

The transverse profile of the jet can be characterized in terms of the jet width, w^{jet}, defined as the first moment of the transverse energy with respect to the jet axix,

$$w^{\text{jet}} = \sum_{\text{constituents}} (r^i \times E_T^i) / \sum_{\text{constituents}} E_T^i, \text{where} \quad (5.6)$$

$$r^i = \sqrt{(\phi^i - \phi^{\text{jet}})^2 + (\eta^i - \eta^{\text{jet}})^2}, \quad (5.7)$$

where E_T^i is the transverse energy of the jet constituent (tower or cluster), and the sum runs over all constituents comprising the jet. This observable is also highly correlated to the mass of the jet. Figure 5.12 shows the measured jet width distribution for an inclusive selection of jets built from topological clusters within $|y| < 2.8$ and $p_{\text{T}}^{\text{jet}} > 20$ GeV. Although the spread of the width distribution is well described, a clear shift in the mean width of approximately 10% is observed. The dependence of the width on $p_{\text{T}}^{\text{jet}}$ indicates that this shift is not simply an artifact of low-p_{T} threshold effects but rather suggests that the jets themselves are wider in data than in Monte Carlo simulation, with the jets in data being roughly 10% wider over the full $p_{\text{T}}^{\text{jet}}$ range. Requiring that the measured jets are well isolated from other jets ($\Delta R > 1.5$) does not change this conclusion. The jet width and charged track multiplicity can then be used as a means to build templates for quark and gluon composition within multijet samples [195].

An alternative approach to measuring the transverse profile is to use the angular separation of the two highest $p_{\text{T}}^{\text{track}}$ tracks inside jets. This has the advantage of effectively removing any dependence on the shower development within the calorimeter and focuses on the hard component of the jet fragmentation before even reaching the calorimeter and the bulk of the dead material (the cryostat). The angular separation between the two hardest tracks in each jet, $\Delta R(\text{trk}_1, \text{trk}_2)$, is shown in Figure 5.13 for topological cluster jets in the region $|y^{\text{jet}}| < 1.9$. The data again favor slightly wider track separation than predicted from the Monte Carlo simulation, and the shape is significantly broader in the data. When measured as a function of $p_{\text{T}}^{\text{jet}}$, the same tendency is again observed: even at moderate jet momenta in the range

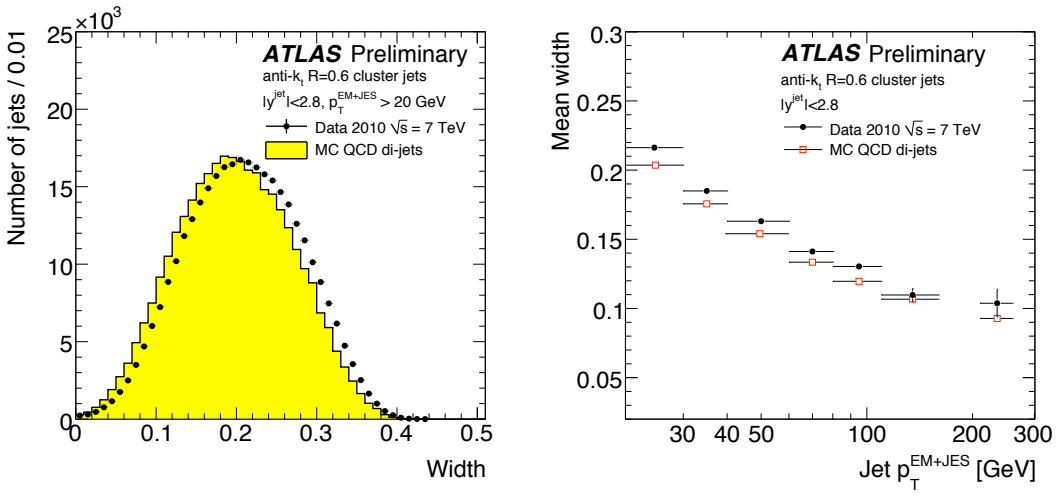

(a) Jet width (b) Jet width vs $p_{\mathrm{T}}^{\mathrm{jet}}$

Figure 5.12: Jet width distribution (see Eq. 5.6) for jets built from topological clusters within $|y^{\mathrm{jet}}| < 2.8$ (a) for all jets with $p_{\mathrm{T}}^{EM+JES} > 20$ GeV and (b) as a function of p_{T}^{EM+JES}.

$80 < p_{\mathrm{T}}^{\mathrm{jet}} < 100$ GeV, the data still indicate a wider average $\Delta R(\mathrm{trk}_1, \mathrm{trk}_2)$ than seen in the Monte Carlo simulation. This suggests that improvements in the description of both soft processes and the hard jet fragmentation are needed, as well as potential improvements in the jet-energy scale calibration. These generic features will also be present in the measurements of jet mass in Chapter 8.

Jet reconstruction

In order to understand the purity with which calorimeter jets can be found and reconstructed in the data, track-jets constructed from charged particle tracks only are used as a reference. Reconstruction purity is then defined as the fraction of calorimeter jets that can be matched to a reconstructed track-jet within a radius of $\Delta R < 0.3$ for jets with a nominal radius of $R = 0.6$. In this case, both calorimeter jets and track-jets are reconstructed with the same nominal jet radius. This definition of purity is shown as a function of calorimeter jet p_{T} and η in Figure 5.14.

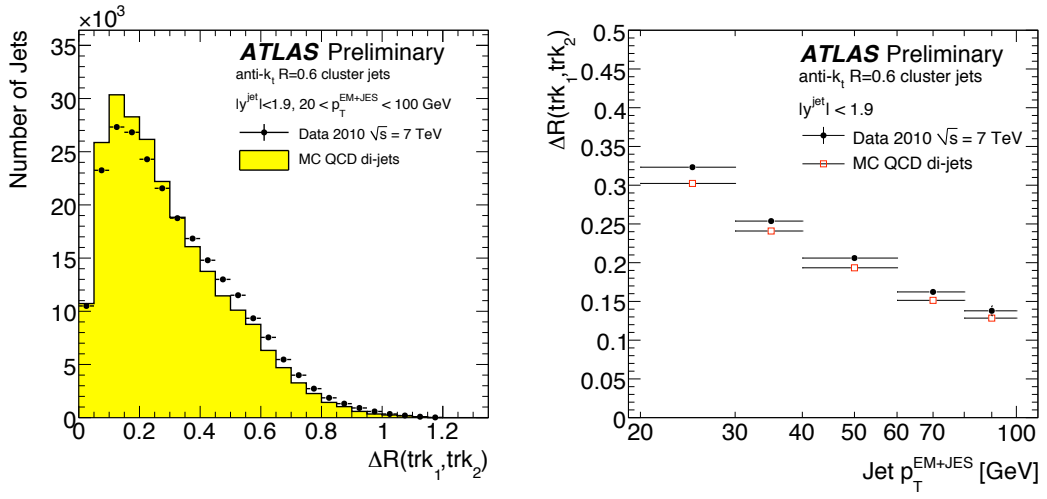

(a) $\Delta R(\mathrm{trk}_1, \mathrm{trk}_2)$ of the two hardest tracks in jets

(b) Dependence of $\Delta R(\mathrm{trk}_1, \mathrm{trk}_2)$ with $p_{\mathrm{T}}^{\mathrm{jet}}$

Figure 5.13: The angular spread of the two hardest tracks inside jets for (a) an inclusive selection of jets within $|y^{\mathrm{jet}}| < 1.9$ and (b) as a function of $p_{\mathrm{T}}^{\mathrm{jet}}$.

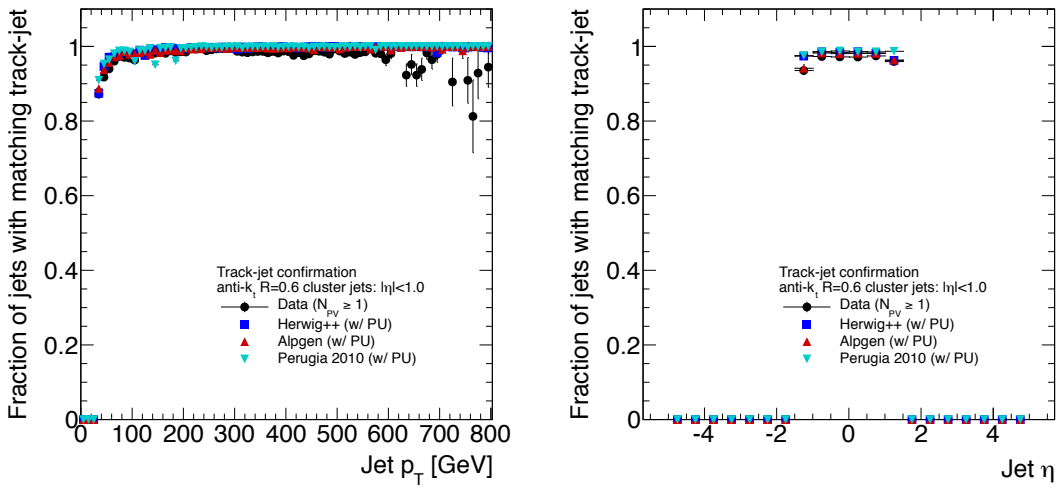

(a) (b)

Figure 5.14: Calorimeter jet reconstruction purity measured with respect to reconstructed track-jets (left) as a function of the reconstructed jet p_{T} and (right) η, where the latter is integrated above $p_{\mathrm{T}} = 30$ GeV .

Chapter 6

Jet physics at high luminosity

In addition to the already complex environment produced at a hadron collider, both the initial physics program of the LHC as well as the ultimate luminosities expected will contain events with multiple simultaneous proton-proton interactions, or pile-up [196]. Figure 6.1 depicts the numerous components typically present in a given pp bunch crossing at the LHC. These additional soft collisions are uncorrelated with the hard-scattering process that typically triggers the event and therefore present a background of soft diffuse radiation that not only offsets the energy measurement of jets but will impact jet shape and structure measurements as well. Furthermore, hard-scattering events may contain jets from these additional interactions, introducing challenges for jet identification, missing transverse energy reconstruction and jet counting. A single di-jet event with and without additional interactions overlaid is shown in Figure 6.2 and demonstrates the many ways in which pile-up affects the picture obtained of the reconstructed event. It is essential that physics analyses involving jet measurements (and most analyses do) be able to disentangle or correct for the pile-up background. Methods to reduce or even eliminate these effects will be essential for jet multiplicity and energy scale measurements and enable precision physics at high luminosities.

In-situ methods to correct jets for effects due to pile-up interactions are presented. The *relative* effect of additional pp interactions on the jet energy is compared to events with only a single hard-scattering using two independent approaches: a

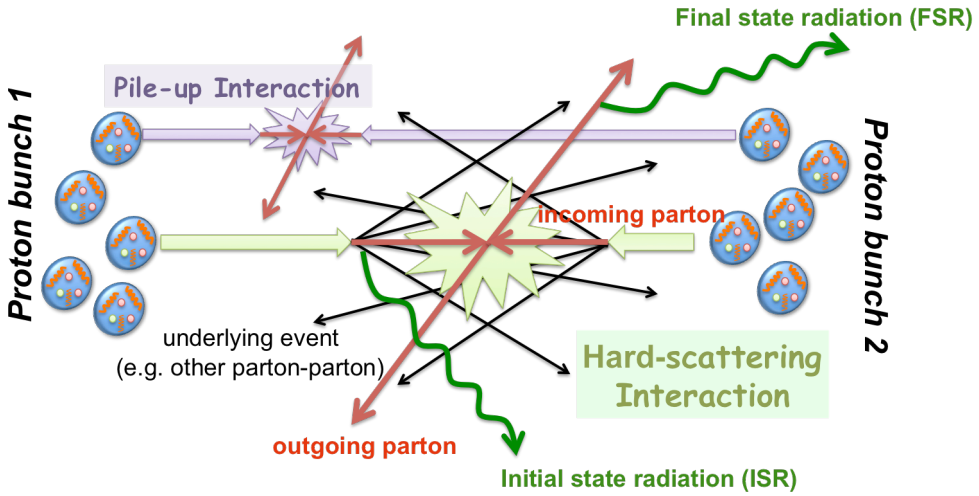

Figure 6.1: Schematic depiction of relevant processes present in pp collisions at the LHC.

purely calorimeter-based (specifically, tower-based) technique, where the uncorrected energy density is measured for each additional observed interaction, and a so-called track-jet technique. The latter method makes use of jets constructed using charged particle tracks originating from only the identified hard-scattering to provide a reference against which to compare calorimeter-jets, which are affected by pile-up. Both techniques utilize relative measurements of the transverse jet energy ($E_{\mathrm{T}}^{\mathrm{jet}}$) in order to estimate the offset due to pile-up, and therefore do not correct for the underlying event by construction.

The ATLAS tracking system (the Inner Detector, or ID) provides a very precise tool for understanding the structure of calorimeter jets and for mitigating the pile-up background. Charged particle jet constituents that leave tracks in the ID provide 3-dimensional information (z in addition to η and ϕ) on the jet origin and direction as a result of the vertexing provided by the tracks. The typical vertexing resolution in z is $\mathcal{O}(100\ \mu\mathrm{m})$ compared to $\mathcal{O}(10\ \mu\mathrm{m})$ which is obtained using photon reconstruction using only the calorimeter information. The combination of tracking and calorimetry can therefore greatly enhance the identification and selection of hadronic jets from primary interactions that do typically have associated charged tracks.

Using this information, a discriminant is defined for each jet with respect to each

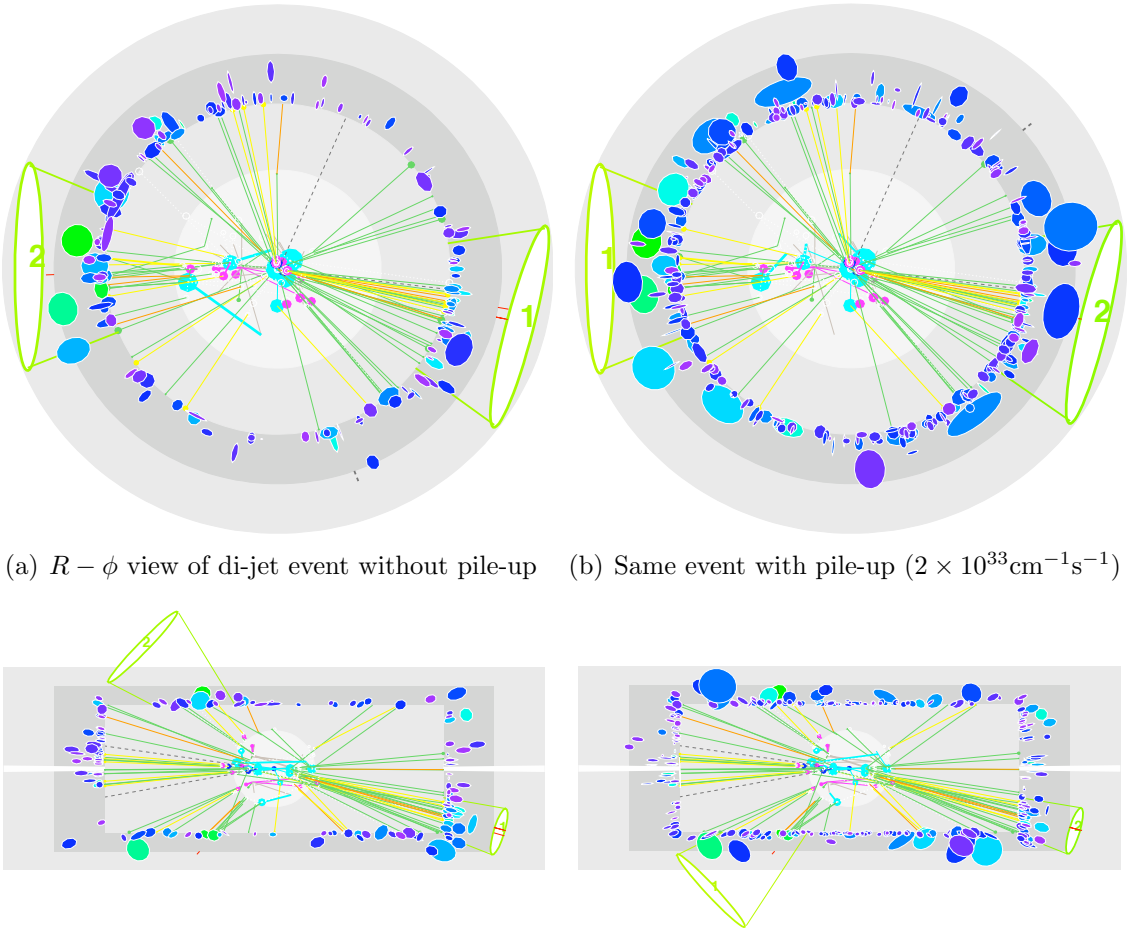

(a) $R-\phi$ view of di-jet event without pile-up (b) Same event with pile-up ($2 \times 10^{33}\text{cm}^{-1}\text{s}^{-1}$)

(c) $R-Z$ view of di-jet event without pile-up (d) Same event with pile-up ($2 \times 10^{33}\text{cm}^{-1}\text{s}^{-1}$)

Figure 6.2: Event display of a single simulated QCD di-jet event with and without accompanying pile-up. Jets are displayed as cones and only those with $p_T > 45$ GeV are shown. The overall jet multiplicity for jets with $p_T > 10$ GeV doubles when pile-up is included. The second-leading jet (labeled 2) becomes the first-leading (labeled 1) jet due to a 20% increase in the reconstructed p_T in the case of pile-up, and the jet axis shifts slightly in both η and ϕ. The apparent "flip" in the event display of the sub-leading jet on the left is misleading and is due to the inherent limitation of a 2D projection; a shift is induced, but it is modest. The multiplicity of energy clusters in the calorimeter (indicated by the colored ellipsoids) increases dramatically.

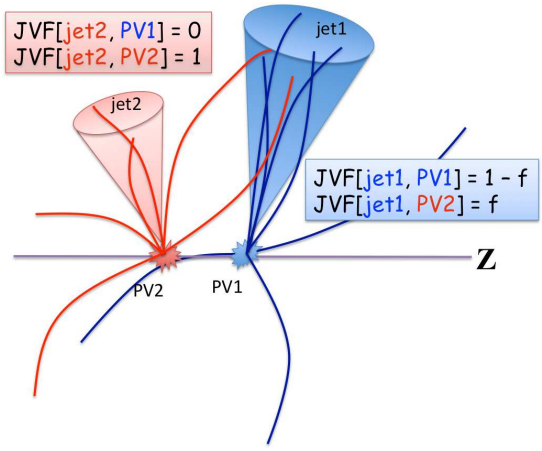

Figure 6.3: Schematic representation of the jet-to-vertex association provided by the jet-vertex fraction (JVF) discriminant corresponding to the fraction of the charged particle transverse momentum in a jet originating from each reconstructed primary vertex in the event.

identified primary vertex (PV) in the event using tracks as the proxy to the interaction region. Once the hard-scattering PV is selected, the jet-vertex fraction (JVF) may be be used to select jets having a high likelihood of originating in that vertex, as described schematically in Figure 6.3.

The benefit of JVF is twofold; it allows for the suppression of jets originating from additional soft interactions, but it also provides a tool to remove the diffuse soft contributions to jets from pile-up on a jet-by-jet basis. By identifying the origin of charged particle tracks pointing towards a jet we can quantify the extent to which the jet energy is augmented by pile-up and correct for it.

Identifying the jet origin allows for the suppression of pile-up jet backgrounds without raising the nominal jet p_T threshold. In addition, we introduce a new method for correcting jet energy contributions due to pile-up on a jet-by-jet basis using the charged particle content of a jet and its origins. Such corrections may prove essential when simple jet selection requirements severely reduce the total number of jets from the hard-scattering at higher luminosities.

Section 6.1 introduces the methodology and concept of the offset correction and and Sections 6.2 and 6.3 detail its derivation and performance in the first LHC data.

Section 6.4 presents the very first look at a dynamic pile-up energy correction proposed by Salam et al [197] and which has the potential to extend the possibility of correcting jets for the impact of pile-up to non-standard jet algorithms. Finally, Section 6.5 describes the jet-vertex association algorithm and the derivation of jet energy corrections in detail. The performance of the algorithm and jet energy corrections in the ATLAS simulation with pile-up are presented, and a data-driven determination of the pile-up jet-energy corrections is discussed.

6.1 Jet energy offset correction

The jet energy scale baseline offset correction aims to correct for energy offsets due to pile-up by subtracting the additional contributions on average. This is particularly important for jet calibration techniques that aim to improve the jet energy resolution, as they should not depend on uncorrelated hadronic activity. As Figure 6.4 depicts, the average energy measured in the calorimeter increases for each additional primary vertex measured in the event even at the relatively low simulated luminosity of $\mathcal{L} = 10^{32}$ cm^{-2}s^{-1} ($\langle N_{\mathrm{PV}} \rangle = 4.1$) and large inter-proton bunch spacing of 450 ns. The energy distribution also exhibits some structure as a function of η. Each of these effects must be taken into account when attempting to correct for the presence of multiple interactions.

The strategy adopted for the application of the offset correction can be written as

$$E_T^{\mathrm{corrected}} = E_T^{\mathrm{uncorrected}} - \mathcal{O}(\eta, N_{\mathrm{PV}}, \tau_{\mathrm{bunch}}, \mathcal{L}), \tag{6.1}$$

where $\mathcal{O}(\eta, N_{\mathrm{PV}}, \tau_{\mathrm{bunch}}, \mathcal{L})$ is derived as a function of η, due to the underlying differential particle spectrum and the variation in the calorimeter geometry. The number of reconstructed primary vertices, N_{PV}, serves as the event-by-event metric with which to estimate the amount of pile-up, and thus the response of the calorimeter. τ_{bunch} is the spacing between consecutive colliding proton bunches, which may affect the response of the calorimeter at high luminosity. Both τ_{bunch} and $\mathcal{L}$ are explicitly considered due to the possibility of pile-up from previous pp bunch crossings which may

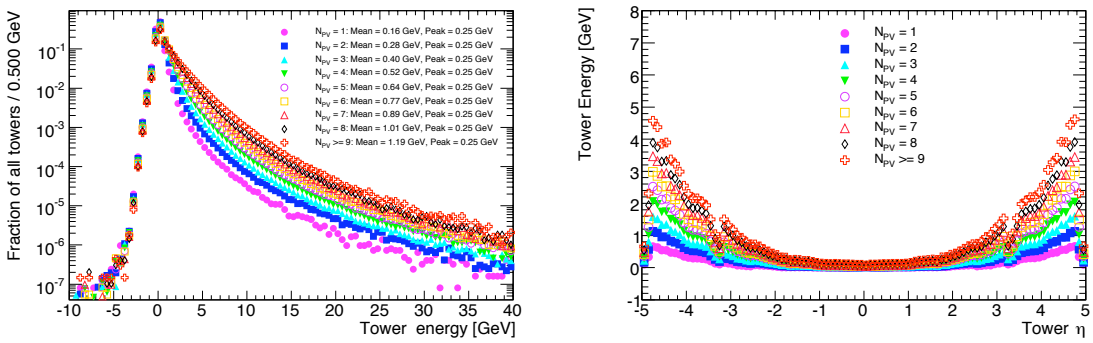

(a) MC tower energy

(b) MC tower $\langle E \rangle$ vs. η

Figure 6.4: (a) Raw tower energy distributions in the MC (no noise suppression applied) for various reconstructed vertex multiplicities (N_{PV}) and (b) the mean tower energy as a function of η and N_{PV} for events simulated at $\mathcal{L} = 10^{32}$ cm^{-2}s^{-1} ($\langle N_{\mathrm{PV}} \rangle$ =4.1) and a large 450 ns bunch spacing. Each tower forms a $\Delta\eta \times \Delta\phi = 0.1 \times 0.1$ grid element, thus providing the energy density measurement needed for the offset correction.

change as the total number of bunches increases ($\mathcal{L}$) or as the bunch spacing between the bunches (τ_{bunch}) is decreased. Although this study does not investigate the impact of various τ_{bunch} on the offset in the data (MC studies are presented in Appendix C), it will be an important consideration for the 2011-2012 LHC run as the number of bunches is increased and the spacing between consecutive bunches is reduced. The correction shown in Eq. 6.1 is assumed to be independent of the jet energy, as contributions due to pile-up are uncorrelated with the pp collision which produces the jet of interest. This assumption will be tested. In the tower-based and track-jet approaches, a reference class of events is defined by a given number of interactions, $N_{\mathrm{PV}}^{\mathrm{ref}}$, such that the offset correction is written as

$$\mathcal{O}(\eta, N_{\mathrm{PV}}) = \langle E_T^{\mathrm{measured}}(\eta, N_{\mathrm{PV}}) \rangle - \langle E_T^{\mathrm{reference}}(\eta, N_{\mathrm{PV}}^{\mathrm{ref}}) \rangle, \tag{6.2}$$

where the brackets denote a statistical average over events with a given N_{PV} and the dependence on $\mathcal{L}$ and τ_{bunch} has been omitted for brevity. For the 2010 data, events with only a single reconstructed primary interaction are used as the reference class of events, such that $N_{\mathrm{PV}}^{\mathrm{ref}} = 1$.

The primary approach to correcting for pile-up in jets is based upon the average energy deposited in the calorimeter towers for each additional primary vertex, N_{PV}, as a function of η. This so-called tower-based method provides an energy density grid upon which the correction is based. The correction for each jet is proportional to the number of towers in the jet, as this provides a clear geometric definition for the application of the correction; a jet "area" that facilitates the subtraction of the event-average energy density measured with calorimeter towers. For jets built directly from dynamically-sized topological clusters, for which no clear geometric definition is available, a model is used that describes the *average* area of a jet in terms of the equivalent number of constituent towers. In this way, the correction can be extended to jet algorithms whose input are not calorimeter towers. This is discussed in Section 6.4.

The average multiplicity of noise-suppressed towers in jets provides information on both the jet composition and on the extent to which that composition may be augmented by the presence of pile-up. Previous studies have shown, as in Figure 5.8 [186], that slight discrepancies exist even in this very simple measure of jet composition. It is therefore crucial that any correction that relies on such properties be derived *in-situ*. In the case of the offset correction, the mean constituent tower multiplicity allows for the extrapolation of a correction based on a per-tower energy deposition to jets that are not built from towers (e.g. topological cluster jets).

Figure 6.5 depicts the average noise-suppressed constituent tower multiplicity for an inclusive jet selection. The shape of the constituent tower multiplicity distribution is governed by the change in physical size of towers for a constant size in pseudorapidity, as well as by differences in the noise spectrum for the various calorimeters and sampling regions. This distribution is used to translate the tower-level offset into a jet-level offset. The known p_{T} and N_{PV} dependencies – shown in Figures 6.5 and 6.6 – are neglected here, and will result in a slight systematic uncertainty in the application of the jet-level offset correction. As a result of these studies, ATLAS has adopted a tower-based measure of the jet area for topo-cluster jets that allows a more precise application of the offset and alleviates the systematic uncertainty due to these dependencies. Consequently, this piece of the resulting systematic uncertainty

is eliminated for 2011.

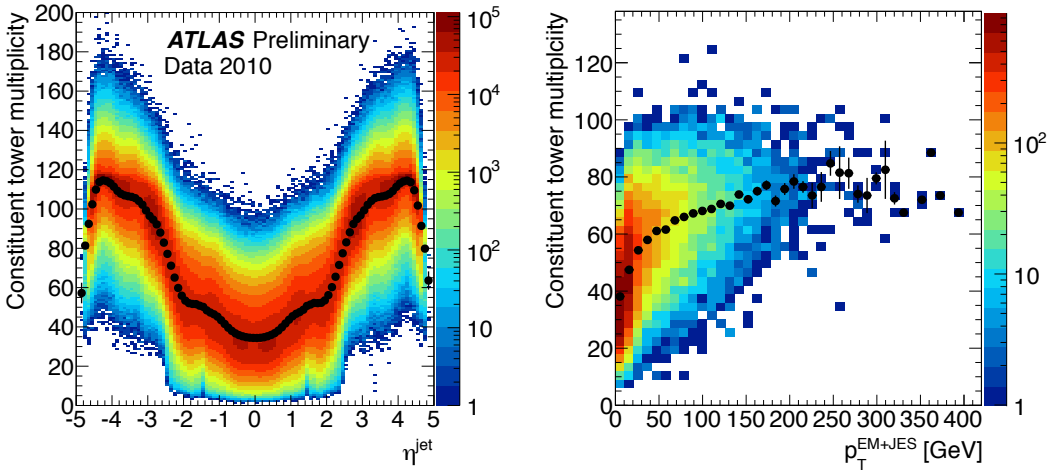

(a) (b)

Figure 6.5: (a) The calorimeter tower multiplicity as a function of pseudorapidity for anti-k_t jets with $R = 0.6$ for the inclusive jet spectrum above $p_{\mathrm{T}}^{EM+JES} > 7$ GeV. The full distribution is shown for each η bin, as well as the mean multiplicity in each bin (black circles). (b) The variation of the tower multiplicity as a function of p_{T}^{EM+JES}, showing the increase in the jet plateau

The foundation of the offset correction is the measurement of the additional transverse energy contributed to a tower for each additional observed interaction in the event. By measuring the tower energy distribution for events with $N_{\mathrm{PV}} = 1, 2, ...N$ and comparing the energy density measured in the calorimeter with a reference class of events (here, $N_{\mathrm{PV}}^{\mathrm{ref}} = 1$), we explicitly derive the tower-based offset as shown in Figure 6.7(a). The offset is then defined as

$$\mathcal{O}_{\mathrm{tower-based}}(\eta, N_{\mathrm{PV}}) = \langle E_T^{\mathrm{tower}}(\eta, N_{\mathrm{PV}})\rangle - \langle E_T^{\mathrm{tower}}(\eta, N_{\mathrm{PV}}^{\mathrm{ref}})\rangle, \tag{6.3}$$

where again the brackets denote a statistical average over events with a given N_{PV} and the implicit dependence on $\mathcal{L}$ and τ_{bunch} has been omitted. For higher luminosities, or accelerator configurations which contain closely spaced pp collisions, it may be necessary to use values $N_{\mathrm{PV}}^{\mathrm{ref}} > 1$ to account for a different calorimeter response.

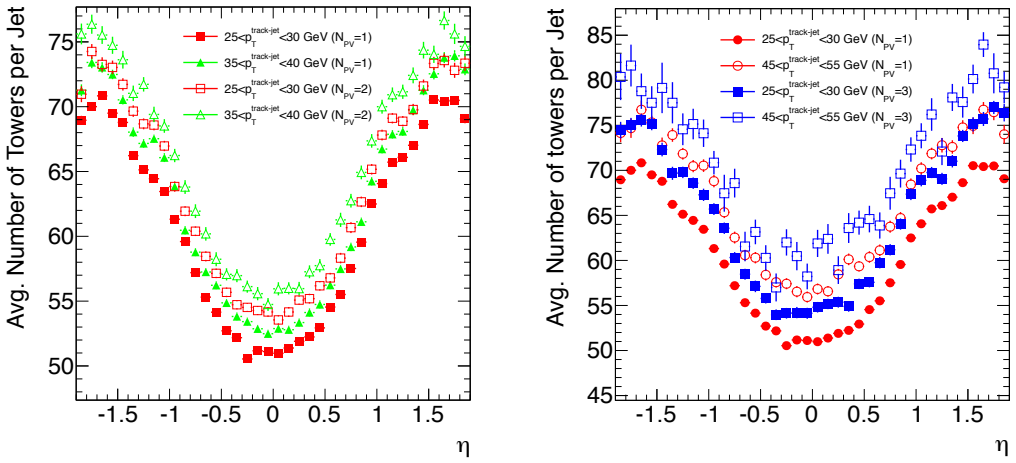

(a) (b)

Figure 6.6: Variation in the tower multiplicity for two different $p_T^{\text{track-jet}}$ bins and vertex multiplicities. Events with $N_{\text{PV}} = 1$ are shown in the solid points on the left and in the circles on the right.

The *tower-level* offset can be extrapolated to a *jet-level* offset by assuming the average tower multiplicity per jet, given by Figure 6.5. Using this information, we can translate the tower-based offset measurement to an average jet-level offset, which is written as

$$\mathcal{O}_{\text{jet|tower}}(\eta, N_{\text{PV}}) = \mathcal{O}_{\text{tower-based}}(\eta, N_{\text{PV}}) \times \langle N^{\text{jet}}_{\text{towers}} \rangle. \tag{6.4}$$

The jet-level offset is shown for $R = 0.6$ in Figure 6.7(b). In this way, the tower-based offset correction can be applied to cluster-jets. The uncertainty associated with this extrapolation is not negligible, but will be shown to be smaller than the impact of pile-up for 2010 data.

The dependence of the tower energy distribution on the trigger used to select the event to be analyzed is observed to have a maximum uncertainty of approximately 25%, on average, on the measured energy density. This was determined by comparing the measured energy density in events with calorimeter triggers, as used here, with events triggered via the minimum bias trigger scintillators. We will see, however,

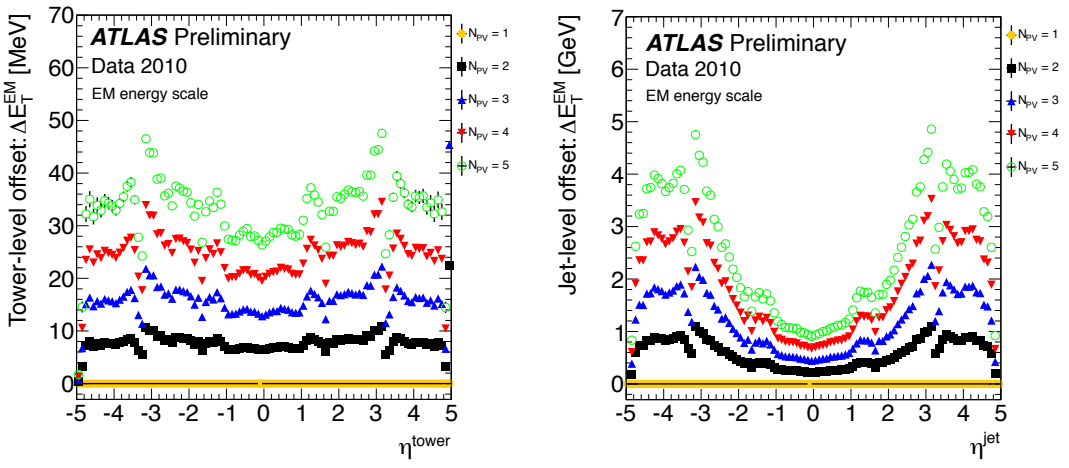

(a) (b)

Figure 6.7: (a) Tower-level offset at the electromagnetic (EM) scale and the (b) jet-level offset at the electromagnetic (EM) scale, each shown as a function of pseudorapidty and the number of reconstructed primary vertices.

that this variation is constrained by the final closure tests shown in Section 6.3, and is taken into account in the systematic uncertainties via the overall variation in these tests.

6.2 Track-jet-based validation and offset correction

The track-jet approach utilizes jets constructed of charged particles, originating only from the hard-scatter interaction, in order to provide a stable reference against which to compare calorimeter-jets. The method consists of matching track-jets to calorimeter-jets and measuring the variation of the calorimeter $E_{\mathrm{T}}^{\mathrm{jet}}$ as a function of the number of observed primary vertices, N_{PV}. It is therefore possible to both validate the tower-based offset correction (tower-level and jet-level) as well as to directly estimate the pile-up energy contribution to jets. As this method is only applicable to jets within the tracker acceptance, it serves primarily as a cross-check for the tower-based

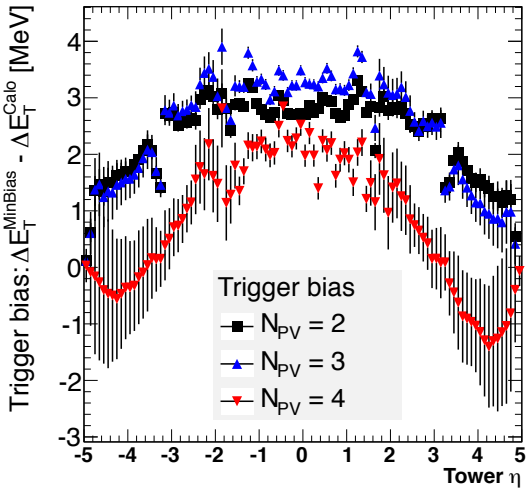

Figure 6.8: Bias in the tower-level offset correction due to the choice of trigger stream.

method discussed above. It can also be used, however, to derive a dedicated offset correction that can be applied to jets at energy scales other than the electromagnetic energy scale.

The technique consists of matching track-jets within a small $p_T^{\mathrm{track-jet}}$ range with calorimeter-jets and subsequently measuring the average calorimeter jet E_{T} versus N_{PV}. The matching criteria used for jets with $R = 0.6$ is

$$\Delta R(\mathrm{jet}, \mathrm{track} - \mathrm{jet}) < 0.4, \tag{6.5}$$

where $\Delta R = \sqrt{\Delta\eta^2 + \Delta\phi^2}$, and 5 GeV bins in $p_T^{\mathrm{track-jet}}$ are used. The offset is calculated as

$$\mathcal{O}_{\mathrm{track-jet}} = \langle E_{\mathrm{T}}^{\mathrm{jet}}(N_{\mathrm{PV}}|p_T^{\mathrm{track-jet}})\rangle - \langle E_{\mathrm{T}}^{\mathrm{jet}}(N_{\mathrm{PV}}^{\mathrm{ref}}|p_T^{\mathrm{track-jet}})\rangle. \tag{6.6}$$

For the purposes of the present study $N_{\mathrm{PV}}^{\mathrm{ref}} = 1$, but this may be extended to $N_{\mathrm{PV}}^{\mathrm{ref}} > 1$ for higher luminosity, short bunch-spacing operation in 2011-2012. Studying the variation of the offset as a function of the $p_T^{\mathrm{track-jet}}$ range helps to establish the systematic uncertainty of the method. In addition, this approach has the advantage that it can

be derived with the large di-jet sample available in the first data.

Using the method described above, the transverse energy of the calorimeter jet is measured in six $p_T^{\text{track-jet}}$ ranges as a function of N_{PV}. Jets constructed from both noise-suppressed towers and topological clusters are used at both the EM and EM+JES energy scales.

Figure 6.9 displays the impact of pile-up on tower and topo-cluster jets at the EM scale, using the most probable value of a Landau distribution convoluted with a Gaussian fit to the $E_{\text{T}}^{\text{jet}}$ distribution (referred to as "Landau+Gauss") for each range of $p_T^{\text{track-jet}}$. In almost every case, a consistent offset of approximately $\mathcal{O} = 0.5$ GeV per vertex is found for $|\eta| < 1.9$, and no systematic trend of the offset as a function of $p_T^{\text{track-jet}}$ is observed, supporting the hypothesis that the offset correction is independent of $E_{\text{T}}^{\text{jet}}$. Typical errors for this differential offset are 20-50 MeV per vertex, as shown in Table 6.1 in Section 6.3. A similar estimate of the jet-level offset using track-jets is performed at the EM+JES scale.

Figure 6.10 provides a summary of each of these results, presented in the form of the actual jet-level offset correction as a function of N_{PV} derived with respect to $N_{\text{PV}}^{\text{ref}} = 1$. The errors shown are statistical only. As expected, the magnitude of the offset is higher after calibration (Figures 6.10(c) and 6.10(d)), and the difference corresponds to the average jet energy scale correction received for jets with $p_{\text{T}}^{\text{jet}} > 40$ GeV [194, 198].

This track-jet approach offers the possibility to directly compute the offset correction, as shown in Figure 6.10. The variation of the offset among the various ranges of $p_T^{\text{track-jet}}$ indicates a systematic uncertainty on the correction of approximately $\delta(\mathcal{O}_{\text{track-jet}}^{\text{EM}}) < 100$ MeV per additional vertex at the EM scale and $\delta(\mathcal{O}_{\text{track-jet}}^{\text{EM+JES}}) < 200$ MeV per additional vertex at the EM+JES scale. Even when using this maximal EM scale systematic uncertainty, the application of the offset correction represents an improvement of a factor of five over the systematic bias associated with pile-up effects on the jet transverse momentum.

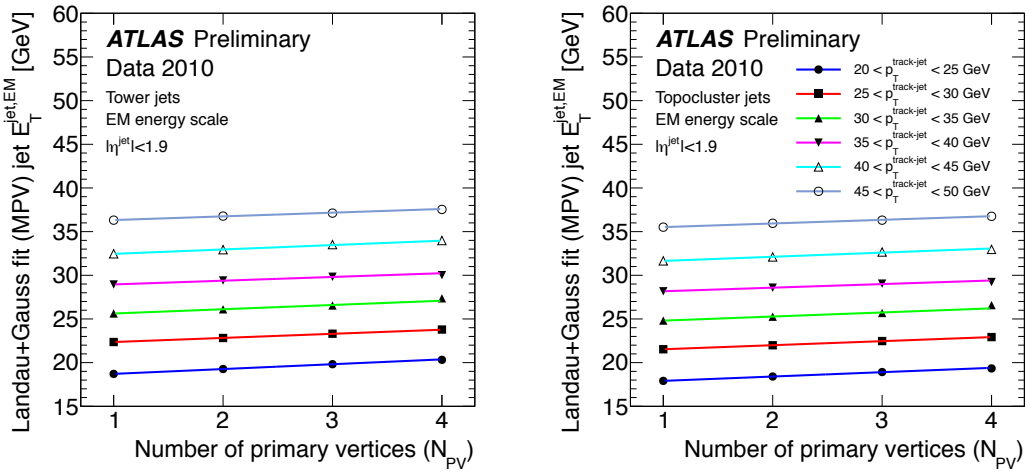

(a) Tower jets (EM scale, Landau+Gauss fit) (b) Topo-cluster jets (EM scale, Landau+Gauss fit)

Figure 6.9: Measurements of the impact of pile-up on the calorimeter $p_{\mathrm{T}}^{\mathrm{jet,EM}}$ for jets constructed with (a) noise-suppressed towers and (b) topological clusters, as a function of the number of interactions in the event. Both jet types exhibit a slope of approximately 0.5 GeV per vertex. The track jets used for comparison are limited to $|\eta| < 1.9$.

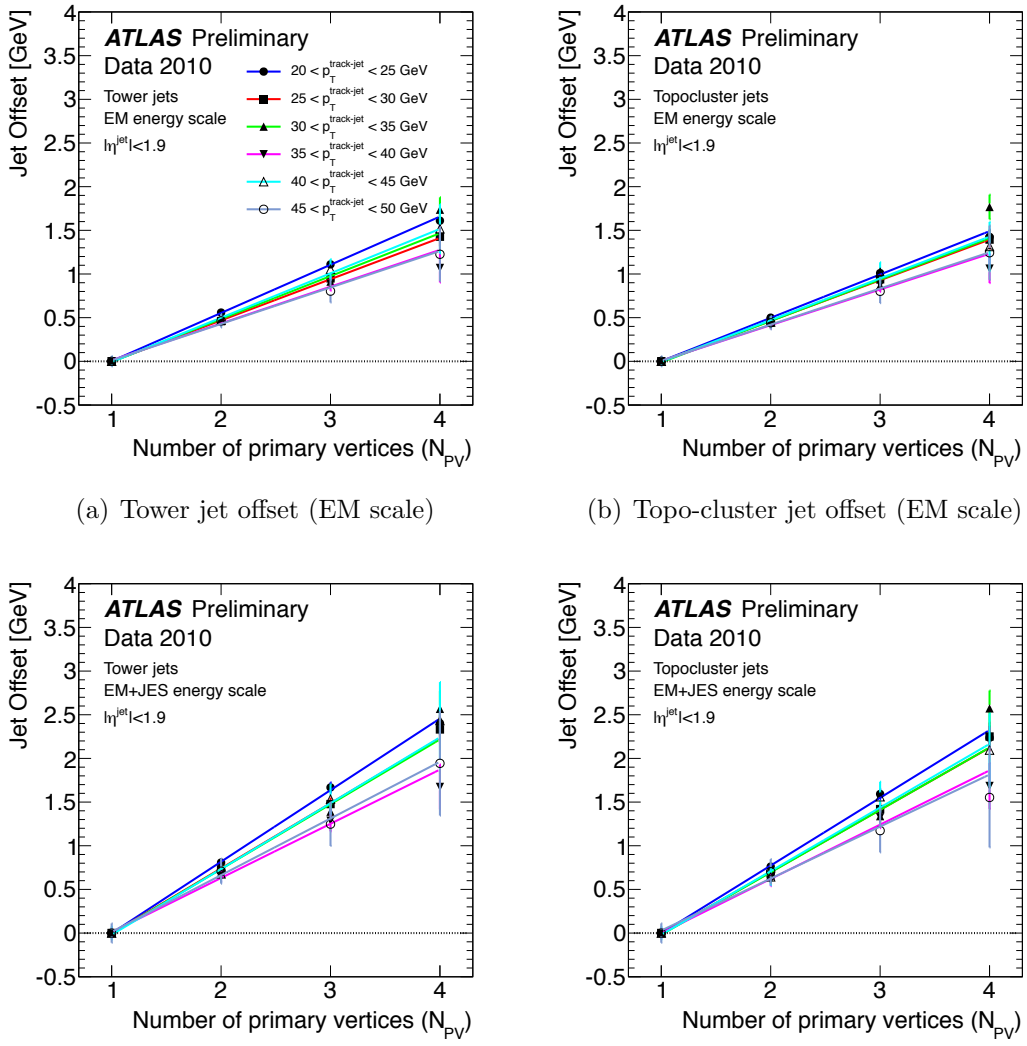

(a) Tower jet offset (EM scale)

(b) Topo-cluster jet offset (EM scale)

(c) Tower jet offset (EM+JES scale)

(d) Topo-cluster jet offset (EM+JES scale)

Figure 6.10: Direct measurements of jet-level offset as a function of the number of interactions in the event for several ranges in $p_T^{\text{track-jet}}$. The track-jet offset is derived for (a) tower jets at the EM scale (b) topo-cluster jets at the EM scale (c) tower jets at the EM+JES scale and (d) topo-cluster jets at the EM+JES scale. Errors shown are statistical only.

6.3 Results of the tower-based offset correction

In this section, the results of closure tests of the tower-based offset correction, which apply the track-jet method to the corrected $p_{\mathrm{T}}^{\mathrm{jet}}$, are reported. In addition, the wide applicability of the tower-based offset correction is demonstrated by applying it to measurements of the differential jet shapes in events with two or three observed interactions.

The application of the offset correction shows reasonable closure at the tower-level and a slight under-correction at the jet-level, when evaluated using the most probable value of the corrected $E_{\mathrm{T}}^{\mathrm{jet}}$ distribution. Figure 6.11(a) shows the tower-level correction applied to tower jets at the EM scale, as a function of the reconstructed vertex multiplicity. Figures 6.11(b) and Figure 6.11(c) show the jet-level correction applied to both tower jets and topo-cluster jets, respectively. The tower-level correction exhibits a closure consistent with zero variation as a function of N_{PV} (zero slope in $E_{\mathrm{T}}^{\mathrm{jet}}$ vs. N_{PV}). However, the use of the jet-level offset correction slightly under-corrects for the effect of pile-up for jets constructed from *both* towers and topo-clusters.

The implication of this observation is two-fold:

- There are no significant differences in the ability to obtain closure when applying the tower-based offset correction to jets built from topological clusters.
- There is a systematic underestimation of the tower multiplicity in jets due to both the assumed $E_{\mathrm{T}}^{\mathrm{jet}}$ spectrum and the effect of pile-up.

Based on the latter observation, ATLAS has adopted a tower-based measure of the jet area for topo-cluster jets that allows a more precise application of the offset and alleviates the systematic uncertainty due to these dependencies[1]. Recent tests suggest that this piece of the resulting systematic uncertainty is eliminated for 2011.

The systematic uncertainties on the offset correction are estimated from the variation of the tower-multiplicity, trigger selection, the variation of the offset derived from the track-jet method (Section 6.2), and finally from the result of the closure

[1]This has been implemented in the ATLAS jet software as the `NumTowers JetMoment`

Track-jet p_{T} ($p_T^{\mathrm{track-jet}}$)	Tower jets [GeV/vertex]		Topo-cluster jets [GeV/vertex]	
	Before	After	Before	After
20 - 25 GeV	0.55 ± 0.02	0.06 ± 0.02	0.50 ± 0.02	0.19 ± 0.02
25 - 30 GeV	0.47 ± 0.02	0.00 ± 0.02	0.47 ± 0.02	0.16 ± 0.02
30 - 35 GeV	0.49 ± 0.03	0.01 ± 0.03	0.47 ± 0.03	0.17 ± 0.03
35 - 40 GeV	0.42 ± 0.03	-0.08 ± 0.03	0.41 ± 0.03	0.12 ± 0.03
40 - 45 GeV	0.51 ± 0.05	0.01 ± 0.05	0.48 ± 0.05	0.18 ± 0.05
45 - 50 GeV	0.42 ± 0.06	-0.07 ± 0.06	0.41 ± 0.06	0.12 ± 0.06
Average	0.48 ± 0.02	-0.01 ± 0.02	0.46 ± 0.02	0.16 ± 0.02

Table 6.1: Variation of the calorimeter $E_{\mathrm{T}}^{\mathrm{jet}}$ with pile-up. Slopes are given in GeV/vertex for each pile-up vertex in the event, and represent the slope of the jet offset before and after the tower-based offset correction. Both tower-level and jet-level corrections are shown, applied to tower jets and topo-cluster jets, respectively.

test. Each systematic uncertainty is summarized in Table 6.2 and expressed as a percentage of the average offset correction, shown in Table 6.1.

For the tower-level offset correction, in which the towers themselves are corrected within the jet, the quadrature sum of each systematic uncertainty is significantly larger than the closure test indicates. We therefore adopt the larger of the two individual uncertainties, or $\delta(\mathcal{O}^{\mathrm{tower-level}}) = 100$ MeV per vertex for the tower-level correction[2]. The resulting total uncertainty is a factor of five smaller than the bias attributable to pile-up ($\mathcal{O} \approx 500$ MeV per vertex) even while using a very conservative systematic uncertainty.

It is important to note that the jet-level offset correction receives an additional uncertainty due to the average tower multiplicity approximation. This contribution is estimated to introduce a 20% variation in the constituent multiplicity by comparing jets in events with $N_{\mathrm{PV}} = 1-3$ and for the five highest $p_T^{\mathrm{track-jet}}$ bins, which translates directly into a 20% uncertainty on the jet-level offset. The resulting systematic uncertainty on jets corrected by the jet-level offset correction (topological cluster jets) is estimated to be $\delta(\mathcal{O}^{\mathrm{jet-level}}) \approx 160$ MeV per vertex, a factor of three smaller than the bias due to pile-up.

[2]Using twice the RMS of the variation in the closure test yields the same value

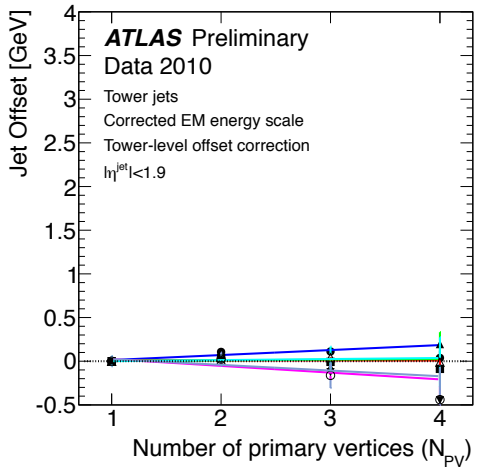

(a) Tower jets with EM scale tower-based correction

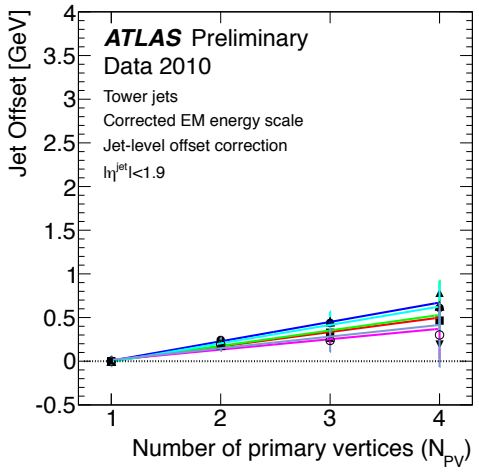

(b) Tower jets with EM scale jet-level correction

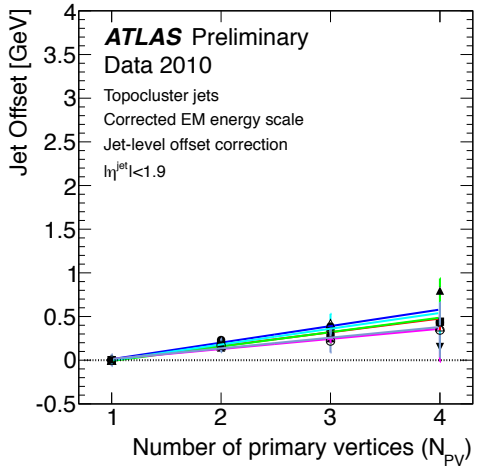

(c) Topo-cluster jets with EM scale jet-level correction

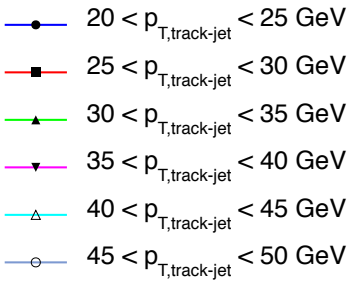

(d)

Figure 6.11: Closure tests of the offset correction using the fitted (Landau+Gauss fits) $E_{\mathrm{T}}^{\mathrm{jet}}$ most probable value (MPV) for various track-jet $p_T^{\mathrm{track-jet}}$ bins for (a) tower jets corrected with tower-based offset correction, (b) tower jets corrected with the jet-level offset correction and (c) topo-cluster jets corrected with the jet-level offset correction. The axis ranges are identical to Figure 6.10 for ease of comparison.

Systematic	Tower-level	Jet-level	Comments
Tower multiplicity variation	–	20%	$p_T^{\text{track-jet}}$, N_{PV}
Trigger selection	16%	16%	MinBias vs. calo
$p_T^{\text{track-jet}}$ variation	21%	22%	$\delta\mathcal{O}$ ≈100 MeV/vertex
Total (quadrature sum)	26%	34%	Assumed uncorrelated
Result from closure test	2%	35%	Determined from average

Table 6.2: Summary of systematics associated with the offset correction for both the tower-level offset and the jet-level offset correction variants. The uncertainty is expressed as a percentage of the average offset correction, shown in Table 6.1.

Finally, in order to assess the applicability of the tower-based offset outside of the narrow context of jet response, the correction is applied to the measurement of the differential jet shape for $R = 0.6$ tower jets, as described in [199, 200].

The jet shape variable used, $\rho^a(r)$, is defined as:

$$\rho^a(r) = \frac{1}{\pi\left[(r+\delta r/2)^2 - (r-\delta r/2)^2\right]} \times \left\langle \frac{p_T\left(r-\frac{\delta r}{2}, r+\frac{\delta r}{2}\right)}{p_T(0,0.7)} \right\rangle \tag{6.7}$$

where the brackets denote an average over all jets, $p_T(a,b)$ is the sum of the p_T of all noise-suppressed towers with an opening angle $a < \Delta R < b$ with respect to the jet axis, and $\delta r = 0.1$. This definition differs from the canonical jet shape variable $\rho(r)$ [201] in two important ways. First, by normalizing to area, the variable measures a normalized energy density. Therefore, $\rho^a(r)$ will asymptote far from the jet axis. The level of the asymptote is related to the energy density in the calorimeter and is measurably higher in events with pile-up. Second, all noise-suppressed towers (not just the constituents of the jet) are included in the definition. This allows an examination of energy outside of the jet cone, in some sense measuring "energy flow" around the jet axis. This is the first encounter of the study of jet internal structure and the impact that pile-up can have in distorting this structure.

Figure 6.12 depicts $\rho^a(r)$ at detector level with and without the tower-based offset correction applied to each individual tower, and for events with more than one reconstructed vertex. In events with 2 (3) reconstructed vertices, differences in this

particular jet shape variable of up to 35% (70%) just outside the jet ($r > 0.6$) and 20% (40%) near the nominal jet radius are observed. The bulk of the shape ($0.1 < r < 0.6$) is restored to that observed in events with only a single interaction, as well as both the core ($r < 0.1$) and the periphery ($r > 0.6$) of the jet.

The results demonstrate that the tower-based offset correction can be applied on a fine scale granularity and is applicable both inside and *near* jets. The possibilities for correcting the jet shape in both direct QCD physics measurements and for searches for beyond the Standard Model physics using jet substructure are very promising.

6.4 Jet-area pile-up subtraction in the first LHC data

The simple technique described in Sections 6.1- 6.3 offers a baseline approach to correcting jets for the impact of pile-up on the average jet energy scale. However, in order to provide detailed measurements of the jet substructure at even higher luminosity, it is important that the evaluation of the correction take into account more detailed *jet-by-jet* information regarding its susceptibility to pile-up. The method described here is aimed at using an event-by-event-determined p_T density to correct each jet's p_{T} proportional to its area, where the area is determined dynamically for each jet. It was originally suggested and studied by Cacciari and Salam [105].

The jet area method is predicated on the idea that a jet's propensity to include additional soft energy from the underlying event and pile-up is proportional to the jet's area in $\eta-\phi$ space. By properly accounting for the variation of the background energy density throughout the event, a subtraction procedure can be formulated similar to that used for the above described average offset correction.

The basic procedure is as follows:

1. Find all of the jets in the event with no minimum p_T cut. This step is typically done with a k_t algorithm of size $R = 0.5$ to cluster low-p_T showering effectively.

2. Distribute a uniform grid of infinitely soft "ghost" particles into the event. The number of these particles that are clustered into the jet defines the area of the

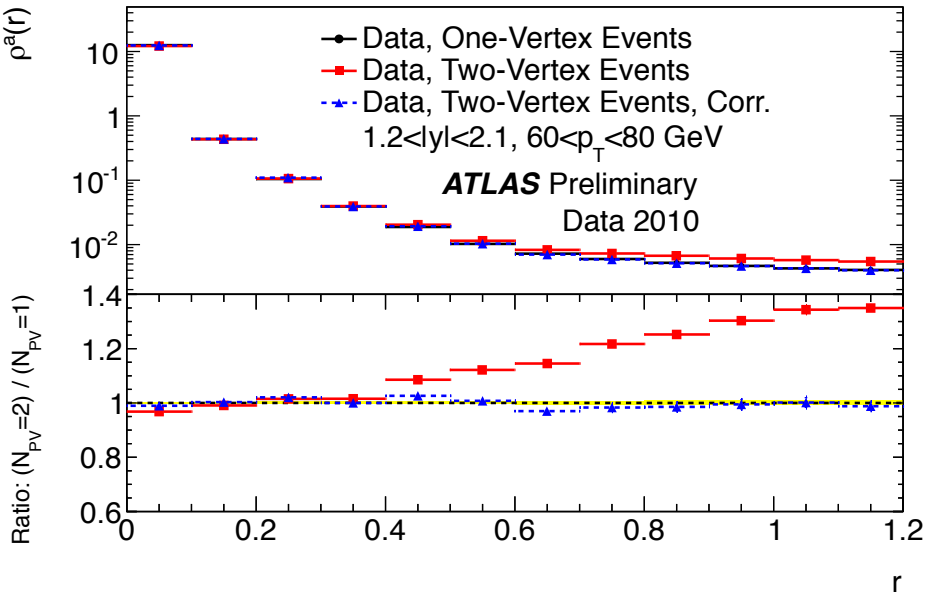

(a) Comparison of $N_{\mathrm{PV}} = 1$ and 2 ($1.2 < |y^{\mathrm{jet}}| < 2.1$)

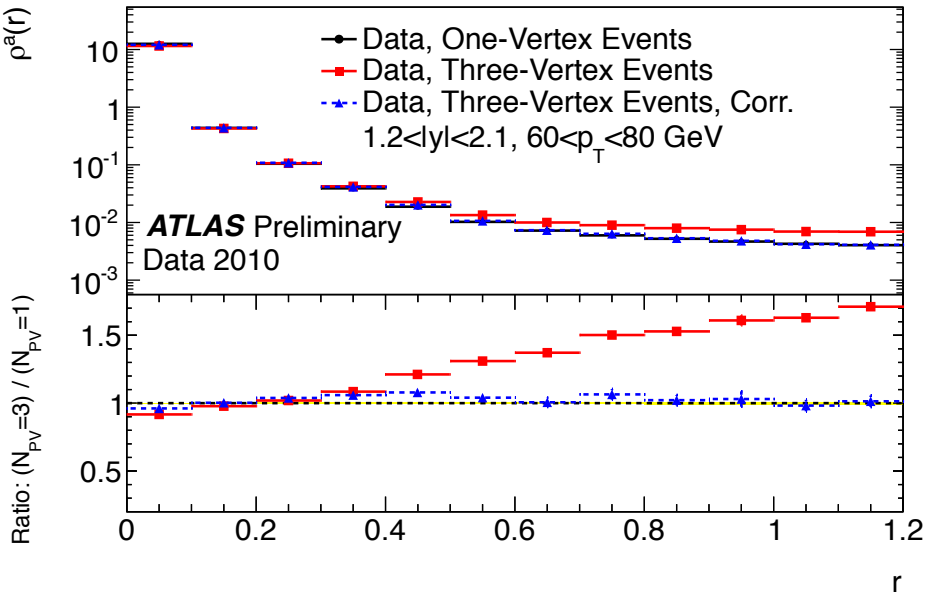

(b) Comparison of $N_{\mathrm{PV}} = 1$ and 3 ($1.2 < |y^{\mathrm{jet}}| < 2.1$)

Figure 6.12: Measured sum p_{T} in annuli around the jet axis, divided by the total p_{T} around the jet, and normalized by the area of each annulus. Events are selected with more than one reconstructed vertex. The shapes of jets in the rapidity range $1.2 < |y^{\mathrm{jet}}| < 2.1$ are compared, before and after the offset corrections, in events with (a) one and two vertices, and (b) one and three vertices. The corrected distribution is also shown (blue triangles).

jet.

3. Alternatively, one may calculate the area of these jets by dividing the $\eta - \phi$ plane into Voronoi cells and determining the area of each cell using the above defines ghost particles.

4. Determine the p_T density of all jets in the event by evaluating the total p_{T} in each Voronoi cell, calculated as $\sum(p_{\mathrm{T}}/\mathrm{cell})/(\mathrm{area\ of\ each\ cell})$, where the sum runs over all constituents of the jet.

5. Select the **median** p_T density ρ as the event p_T density.

6. Find the area for the jets to be corrected. (Area description can be algorithm dependent)

7. Subtract from each signal jet the jet area-based offset, or the event p_T density ρ multiplied by the jet's area.

This method can be altered by splitting the correction into separate eta bins which reflect regions over which the p_T density is relatively constant. Caution must be taken, though, since this may introduce a dispersion in the measured values of ρ due to the finite sampling region over which is it measured. This method is entirely data-based, and only requires calorimeter information. It requires no knowledge of the beam conditions. Possible drawbacks to this method include the computational requirements of accurate jet area determination. The choice of area description has been studied and can be optimized for performance.

Figure 6.13 shows the first measurement of this approach in the 2010 data using the ghost particle approach. The resulting energy density is referred to as the "ghost energy density". In this case, the $k_\perp$ algorithm is used to compute both the event density and the jet area for jets found using the anti-k_t, $R = 0.6$ algorithm. Since the anti-k_t algorithm tends to form stable uniform cones (in the absence of close-by jets), the natural choice of jet area definition is approximately a constant for a given R parameter. That is why the comparison in Figure 6.13 is made to the jet area determined with the k_t algorithm. The result indicates that although the energy density

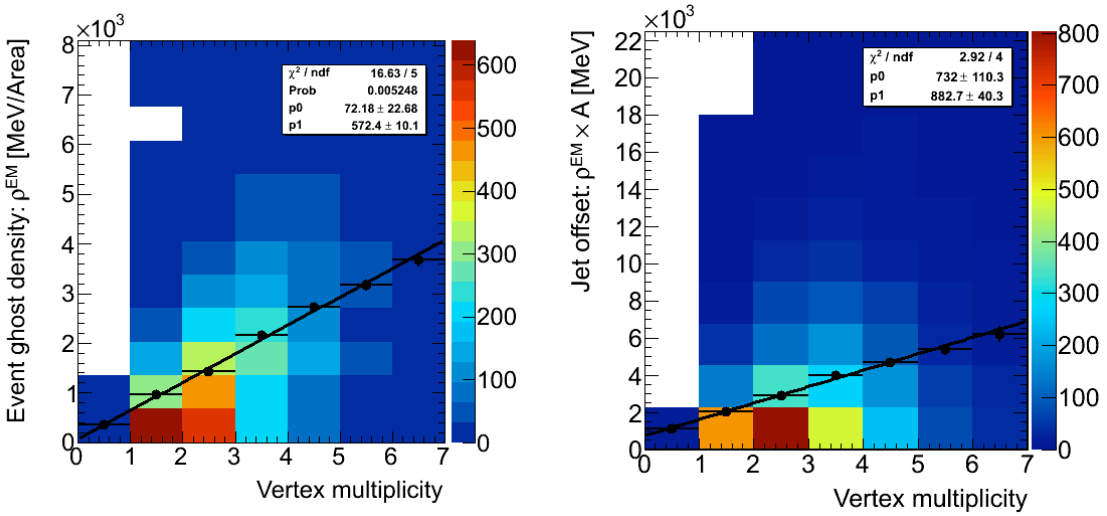

(a) Ghost energy density

(b) Jet area offset

Figure 6.13: (a) Event energy density measured via the ghost area method. (b) Jet offset computed using the event density measured with ghost area method and the measurement of the jet area.

scales very linearly with N_{PV}, the resulting correction obtained as a function of N_{PV} is larger than that measured by the baseline offset correction described above. The optimal choice of area definition and systematics for this correction will be explored in the 2011-2012 data.

6.5 Jet-vertex association

The jet-vertex association algorithm uses tracks which pass simple kinematic and quality selection criteria in order to associate jets to individual primary vertices. In this way, the contribution of pile-up to jets may be pinpointed using the precision tracking and vertexing system available in ATLAS.

Tracks are first selected and then matched to jets via the simple angular matching criterion $\Delta R(\mathrm{jet}, \mathrm{track}) \leq 0.4$, where the track parameters are determined at the point of closest approach to the beam line, itself determined from the beam spot measurements. We then calculate the fraction of the total track transverse momentum

matched to each jet that originates from each primary vertex (PV). Following the jet-track selection for each jet, no further tracks are considered by the algorithm.

The resulting discriminant is termed the jet-vertex fraction and is defined for each jet with respect to each PV. JVF represents the fraction of each jet's matched transverse track-momentum contributed by each vertex. More specifically, it is the ratio of the sum p_T^{track} of all matched-tracks from a given vertex to the total jet-matched track p_T from all vertices. Formally, for a single jet i the JVF with respect to vertex j in the event is written as

$$JVF(\text{jet}_i, \text{vtx}_j) = \frac{\sum_k p_T(\text{trk}_k^{\text{jet}_i}, \text{vtx}_j)}{\sum_n \sum_l p_T(\text{trk}_l^{\text{jet}_i}, \text{vtx}_n)}. \tag{6.8}$$

Unless otherwise stated, JVF will be defined with respect to the selected hard-scatter vertex (equivalently, $JVF(\text{jet}_i, 0)$), chosen using the the default $\max(\sum p_T^2)$ criterion [183]. Calorimeter jets which fall outside of the fiducial tracking region of approximately $|\eta| > 2.0$ (taking into account the finite angular extent of the jet) or which have not been matched to tracks are assigned a $JVF = -1$. The limitation to the inner tracker volume is an inherent limitation of this method.

The distribution of JVF for di-jet events with $p_T^{\text{jet}} \geq 20$ GeV and a simulated luminosity of 10^{32} cm^{-2}s^{-1} ($\langle N_{\text{pile-up}} \rangle$=4.1) is shown in Fig. 6.14. Three distinct components are labeled in the figure in addition to the peak at $JVF = 1$ for which no pile-up contribution is observed. The component at $JVF = -1$ corresponds to jets without matched tracks and is comprised primarily of low p_{T} or neutral-dominated jets which do not have at least 2 matched tracks passing track selection. The second component consists of jets with $JVF = 0$ for which the matched tracks did not point back to the selected hard-scatter vertex, but to an additional pile-up vertex. These jets typically have low transverse momentum and are distributed in η according to the minimum bias particle spectrum, with significant populations even in the central region. For the study shown here, with a large $\tau_{\text{bunch}} = 450$ ns, this component has no impact due to jets from previous crossings. For short bunch spacings, a small impact is expected from jets in previous crossings. This is due to the fact that the Pixel detector will eventually each readout only a single bunch crossing whereas

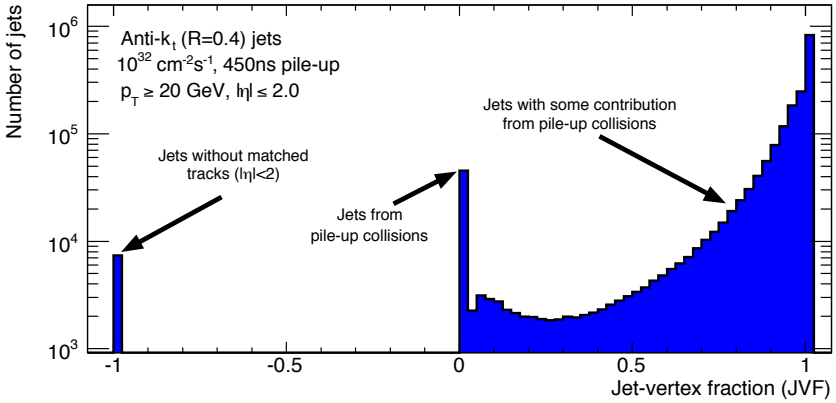

Figure 6.14: (Simulation) Reconstructed jet-vertex fraction (JVF) with respect to the selected primary vertex for all jets passing the kinematic selection criteria and with $p_T^{\text{jet}} \geq 20$ GeV. Three distinct regions of the distribution represent (1) hard-scatter jets with some contribution from pile-up collisions ($0.50 \leq JVF \leq 1.0$), (2) jets originating in pile-up collisions ($JVF = 0.0$), and (3) jets without matched tracks but which are well within the fiducial region of the tracker ($JVF = -1$, with $|\eta| \leq 2.0$).

the calorimeter is still sensitive to multiple crossings. The "valley" present in this distribution represents the range in which hard-scattering jets impacted by pile-up transitions to a mixture of fake jets, induced by the busy environment, and jets produced by pile-up interactions.

The third component is the distribution of jets below $JVF = 1$. It is this population – those which have some fraction (typically between 50-90%) of matched track momentum from vertices other than the selected hard-scatter vertex – that require the most consideration. Jets with significant (25-50%) pile-up contamination will severely distort important observables for many physics analyses, and may need to be rejected altogether. Jets with only minor, but still measurable, contributions from pile-up may still exhibit energy scale offsets and angular shifts that will need to be dealt with directly for each analysis. Finally, the majority of jets fall into the peak of the distribution at $JVF = 1$ which corresponds to jets which have *all* of their matched transverse track momentum originating in the selected primary hard-scattering vertex. It is crucial to recover as large a fraction of pile-up contaminated jets as possible

while efficiently discarding the remainder; JVF is a tool with precisely this goal.

The ability to accurately discriminate between jets from pile-up and hard-scattering interactions is important for the many measurements dependent on the jet multiplicity spectrum, both as signal and as background. By utilizing tracking information to identify the jet origin in the interaction region, we can effectively reject jets which are predominantly formed from additional pile-up interactions in the intense LHC collisions.

In Fig. 6.15 we show both the discrimination power when using JVF as a selection tool as well as the achieved rejection against jets originating in pile-up interactions as a function of the efficiency for retaining hard-scatter jets. Even with the very low p_T^{reco} threshold of 20 GeV, a factor of 90 rejection against pile-up jets for a hard-scatter jet selection efficiency of 98% is achievable. For transverse momentum thresholds above 25 GeV, this rejection factor quickly rises above 100.

Physics analyses must be insensitive to contributions to jet multiplicity from pile-up as these are entirely uncorrelated with the hard-scattering process of interest. The JVF discriminant allows for suppression of these jets, thus ensuring the required insensitivity. We demonstrate that a flat jet multiplicity distribution is recovered when jets with tracking information are required to have $|JVF| \geq 0.50$ compared to that with no selection applied, as seen in Fig. 6.16 where only very central ($|\eta^{\text{jet}}| \leq 2.0$) jets are considered. Furthermore, by selecting events with exactly $N_{PV} = 8$, Fig. 6.16(b) shows that not only do we improve the mean jet multiplicity, but we also recover the shape of the true jet multiplicity spectrum. The excellent agreement indicates that the JVF selection removes the high-end tail of the multiplicity distribution induced by pile-up while maintaining the true shape of the spectrum, which indeed is a much stronger statement.

We have also extended the study to include various other physics processes, such as $t\bar{t}$, $t\bar{t}$+jets, and $H \to \gamma\gamma$. The ability to recover a uniform jet multiplicity distributions as a function of the in-time pile-up holds true in each case considered. These results highlight the general applicability of the method and the importance of incorporating a jet-vertex selection algorithm in analyses which utilize jet counting to measure

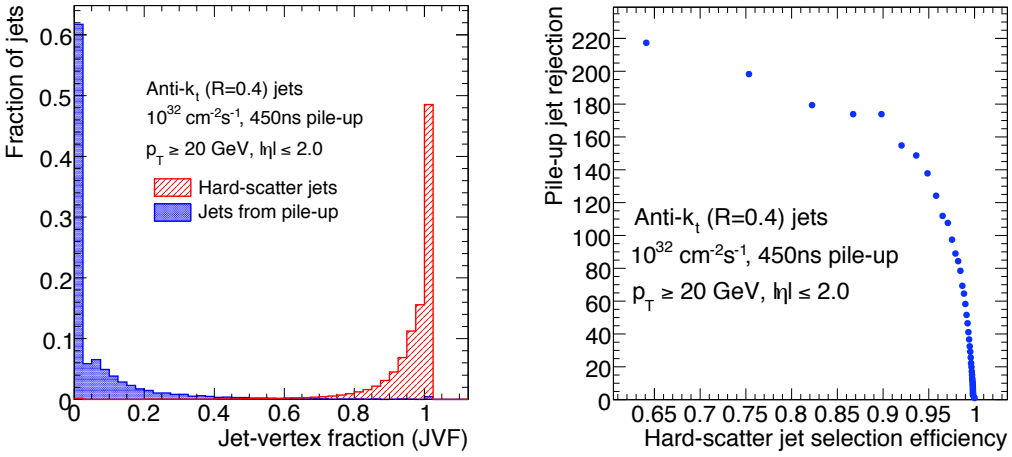

(a) Hard-scatter and pile-up jet discrimination

(b) Pile-up jet rejection vs. hard-scatter jet efficiency

Figure 6.15: (a) The JVF separation between jets originating from the hard-scatter and pile-up jets, those arising solely from the presence of additional interactions. (b) The rejection factor against pile-up jets as function of the efficiency for retaining jets from the hard-scatter. Using JVF directly as a discriminating variable between jets originating in the hard-scattering interaction and those from additional minimum bias pile-up provides clear separation between the two classes of jets even for a nominal p_T requirement of 20 GeV, yielding a factor of 90 rejection against pile-up jets for a hard-scatter jet efficiency of 98%.

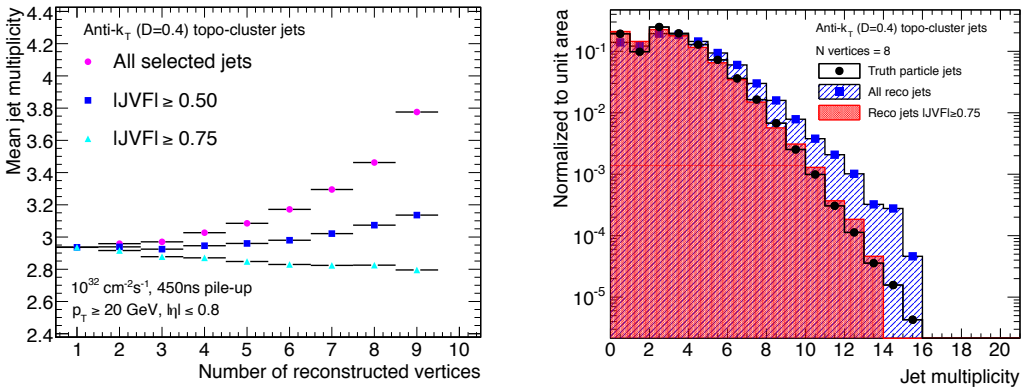

(a) Jet multiplicity vs. N_{PV}

(b) Reco and MC jet multiplicity

Figure 6.16: (a) The reconstructed jet multiplicity as a function of the reconstructed primary vertex multiplicity (N_{PV}) for various JVF selection requirements in the barrel region ($|\eta^{\text{jet}}| < 2.0$). As jets are required to have higher and higher JVF, the overall multiplicity measured decreases due to a loss in efficiency. (b) Reconstructed and MC truth jet multiplicity for events with $N_{PV} = 8$. The agreement between $N_{\text{jet}}^{\text{reco}}(JVF \geq 0.75)$ (solid circles) and $N_{\text{jet}}^{\text{truth}}$ (solid squares) indicates that JVF selection is accurately selecting the hard-scatter jets from the overall distribution $N_{\text{jet}}^{\text{reco}}(JVF \geq 0.0)$ (solid triangles).

physical quantities. The minimum bias interactions which contribute soft but non-negligible jets to the event must be identified and removed in order to maintain the high precision goal of measurements in ATLAS.

We have shown that even at the relatively low luminosity of 10^{32}cm^{-2} sec^{-1} ($\langle N_{\text{pile-up}} \rangle$=4.1) there is a non-negligible contribution to the jet multiplicity from pile-up interactions. Although JVF provides for discrimination against these jets, we expect that at higher luminosity this method will result in a significant loss of efficiency as more jets receive large contributions from pile-up and therefore fail such a simple threshold selection.

In order to achieve the goal of retaining jets that are only partially impacted by pile-up, a method for identifying and subtracting the contribution to jet energy from pile-up on a jet-by-jet basis is explored. These contributions are accounted for by parameterizing the jet response as a function of both reconstructed jet transverse

momentum, p_T^{reco}, and JVF. In this way, we provide the ability to choose between vetoing a jet due to pile-up contamination or attempting to correct for it, or both.

Note that the use of object-based corrections, such as the corrections proposed here based on tracks and vertices, is expected to perform much better in terms of computing performance during reconstruction than those based on simulating additional soft particles as suggested in [197]. This technique preserves the particle-level jet energy scale, which is an important difference compared to [197] which couples pile-up and underlying event contributions. Our approach accounts for these effects separately and allows for a factorized correction, which can be critical to understanding the different contributions of each process in the first LHC data.

Using JVF as a measure of the pile-up contribution to a jet, we define 4 regions which represent 4 distinct regimes of pile-up contamination: $[0.50, 0.75)$, $[0.75, 0.85)$, $[0.85, 0.95)$, $[0.95, 1.00]$. In each region, we first measure the jet response as function of p_T^{true} using angular matching between reconstructed and truth jets, built from all stable interacting particles from the hard-scattering vertex in the event. We then invert the parameterization as a function of p_T^{reco} using the measured jet response, defined as the ratio $R = p_T^{\text{reco}}/p_T^{\text{true}}$. This *numerical inversion* technique is needed because the reconstructed jet response is notably non-Gaussian as a function of p_T^{reco} due to the detector response and the falling p_T spectrum of jets in QCD multijet events. The matching between reconstructed and truth jets uses a $\Delta R < 0.3$ matching radius criterion. This selection is likely to be too restrictive for the most pile-up contaminated jets, and its variation can help to set one of the systematic uncertainties of the method.

The jet response in each JVF region receive its own response parameterization as a function of p_T^{reco}, described by $\alpha(p_T^{\text{reco}}, JVF)$ as

$$\alpha(p_T^{\text{reco}}, JVF) = \sum_{i=0}^{3} \frac{a_i}{[ln(p_T)]^i}. \tag{6.9}$$

The four parameters, a_i, describing the response function in each JVF region are

then smoothly connected by a second fit as a function of JVF, formally written

$$a_i = \sum_{i=0}^{2} b_i (JVF)^i. \tag{6.10}$$

The corrections are applied after the overall jet energy scale corrections in the range $25 \leq p_T^{\text{true}} \leq 500$ GeV due to threshold effects at low p_T^{reco}, and to statistical limitations and the diminishing fractional effect of pile-up at high p_T^{reco}. No η dependence is accounted for in this correction and is effectively integrated up to $|\eta| \leq 2.0$.

We evaluate the performance of the JVF selection and jet energy scale corrections in a variety of contexts. Establishing a uniform jet energy scale with $R = p_T^{\text{reco}}/p_T^{\text{true}} = 1$ in events with pile-up demonstrates the impact of the algorithm in the context of jet calibration. Using JVF to isolate and identify jets with large contributions from pile-up and thus potentially large angular biases further exemplifies the information yielded by this simple technique. Lastly, by identifying jets originating from interactions unrelated to the hard-scattering physics process, such as in $t\bar{t}$ events at moderate luminosity, the impact of JVF on crucial measurements of physical parameters is made clear. In this section we discuss each of these performance measures.

A closure test of the JVF jet energy scale correction is performed by applying the parameterized response corrections to the same sample of QCD di-jet events used to derive them. The resulting jet energy response as a function of truth jet p_T is shown in Fig. 6.18 and falls within $\pm 2\%$ for the entire range of jet p_T. We also compare the JVF jet energy scale correction to a simple p_{T} and η dependent response correction (*numerical inversion*) derived in events with pile-up. As shown in Fig. 6.17(b), such a correction does indeed restore the jet energy scale to unity even in the presence of pile-up, but that the fraction of jets with $0.6 < JVF < 0.9$ are still significantly affected by pile-up. By applying the jet-by-jet JVF correction, the jet energy scale of all jets is near unity. In addition, a consistent response near $p_T^{corr}/p_T^{truth} = 1$ is achieved as a function of η for the four JVF ranges despite not being explicitly applied as a function of η (not shown).

Additional studies using hadronic W decays ($W \to q\bar{q}$) indicate that important

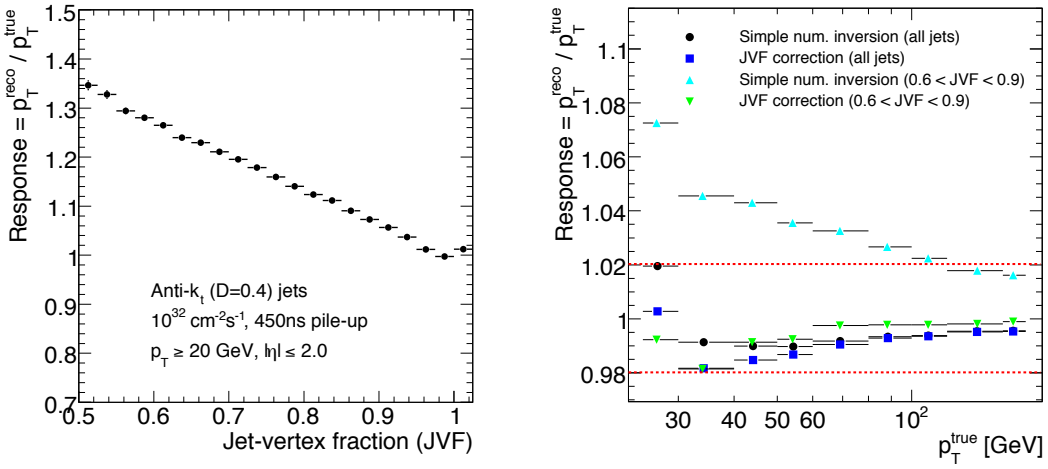

(a) Jet response vs. JVF

(b) Jet response vs. $p_{\mathrm{T}}^{\mathrm{true}}$

Figure 6.17: (a) Inclusive jet response as a function of JVF showing clearly the effect of pile-up at low JVF. (b) Comparison of a simple numerical inversion response correction (solid circles) and the JVF correction (solid squares) for all jets. The overall jet energy scale is restored on average, but jets with low JVF are only fully corrected when using the dedicated pile-up response corrections (solid triangles).

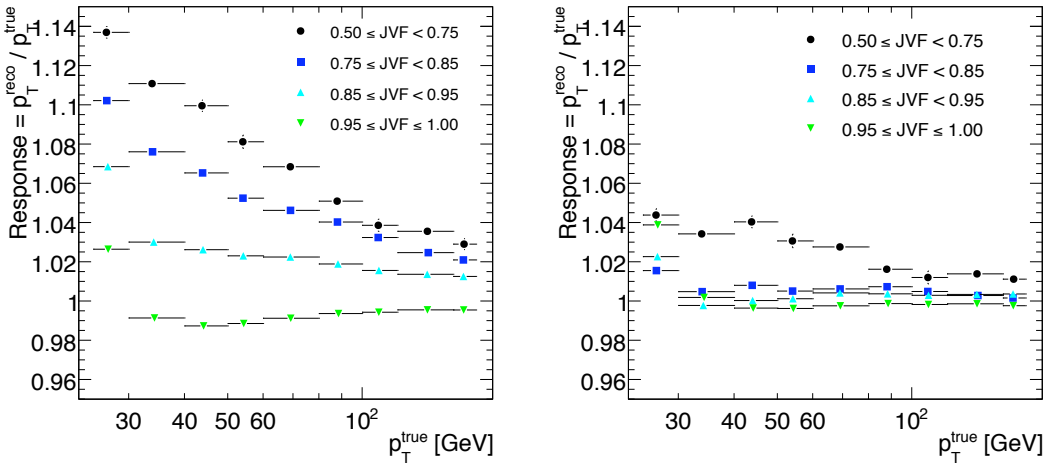

(a) Jet response before correction

(b) Jet after before correction

Figure 6.18: The response measured for jets in four ranges of JVF, corresponding to increasing impact from pile-up. (a) Jet response before pile-up and (b) after pile-up show the ability to achieve closure in each range of JVF, thereby accounting for pile-up.

mass resolutions gains of a few percent are obtainable when applying the JVF jet energy scale corrections the light quark jets used to reconstruct the W mass. By using pruning techniques [202] in conjunction with JVF to determine the pruning parameters a much improved mass resolution is expected and would be yet another application of this technique.

Pile-up also distorts the jet angular resolution, an effect termed "back-reaction" in [203]. By using JVF as a measure of the pile-up contribution to the reconstruction of a particular jet we can quantify the amount to which this results in a broader angular resolution spectrum. In Table 6.3 we summarize the measurements by evaluating the radius with respect to a truth jet axis to which one must integrate to encompass 90% of the reconstructed jets ($\Delta R^{90\%}$). This procedure is repeated for four JVF regions, demonstrating that jets with higher pile-up contamination (*lower* JVF) have worse angular resolution (larger $\Delta R^{90\%}$).

In addition, the angular distortion induced by pile-up also changes the jet energy

JVF region	$\Delta R^{90\%}$	Ratio with respect to $0.95 < JVF \leq 1.00$
$0.50 < JVF \leq 0.80$	0.22	1.83
$0.80 < JVF \leq 0.90$	0.20	1.67
$0.90 < JVF \leq 0.95$	0.16	1.33
$0.95 < JVF \leq 1.00$	0.12	1.00

Table 6.3: Change in angular resolution for each JVF region, measured by evaluating the ΔR needed to include 90% of the reconstructed jets.

response distribution as a function of the radial distance to the truth particle jet axis. In jets without large contributions from pile-up ($0.95 < JVF \leq 1.00$), the response distribution falls as a function of the radial distance between the reconstructed jet and the truth-level particle jet axis. This effect changes with the introduction of pile-up due to both the angular smearing effect and the additional energy depositions which can increase the measured jet p_T. The lowest JVF region still shows increased response at intermediate radii which might be improved with more a accurate parameterization of the fitting function derived with higher statistics. By forming jets from tracks independently ("track-jets") the calorimeter jet angular resolution can be further improved by applying a correction to the jet axis using the combination of the track-based and calorimeter-based measurements and the high angular resolution of track-jets.

An important application of the JVF jet selection criteria is the measurement of jet multiplicity in $t\bar{t}$ events at moderate luminosity. The presence of additional jets from multiple interactions in these already high jet-multiplicity events will distort the N_{jet} spectrum and lead to hard-to-isolate systematic errors for cross-section measurements and searches for new physics. By applying the JVF selection, we can mitigate these effects and improve physics measurements dependent on jet multiplicity at moderate and high-luminosities.

In Fig. 6.19 we show the results of applying the JVF selection to $t\bar{t}$ events with pile-up at 10^{32} cm^{-2} s^{-1} ($\langle N_{\text{pile-up}} \rangle$=4.1). By comparing the jet multiplicity spectrum for selected jets to both the default kinematic (no JVF) selections and to the truth jet multiplicity spectrum, the degree to which the JVF selection improves the overall

measurement is apparent. In the range $3 \leq N_{\text{jet}} \leq 6$, most relevant for many top quark measurements, deviations from the truth jet multiplicity of more than 16% ($N_{\text{jet}} = 3$) are present for the default jet selections, while a maximum difference of 4% is observed for jets required to have $JVF \geq 0.50$, a factor of 4 improvement over current techniques.

It will be necessary to measure the performance of the JVF algorithm from data in order to account for differences between the Monte Carlo simulations and the actual detector and data-taking conditions. A "tag-and-probe"-like analysis is planned in which events with only multiple interactions are selected with two back-to-back, well-isolated jets. The "tag" jet is required to have a good momentum measurement, be relatively central, and have all of its matched tracks originating in the identified hard-scattering interaction ($JVF_{\text{tag}} = 1.0$). The response of the "probe" jet is then measured as a function of JVF_{probe}.

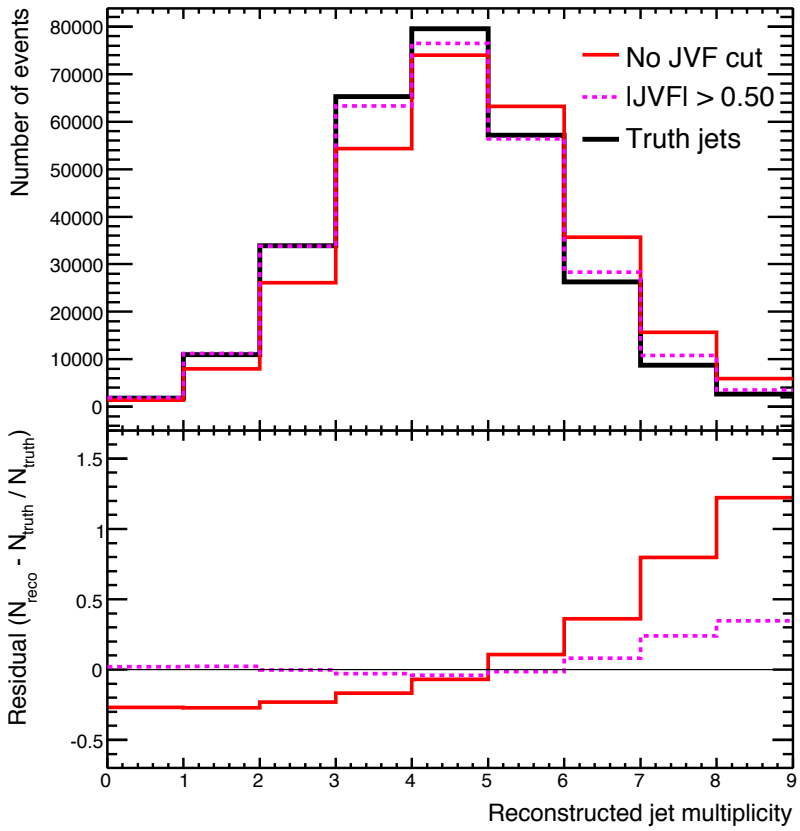

Figure 6.19: Jet multiplicity in $t\bar{t}$ events with pile-up at 10^{32} cm^{-2} s^{-1} ($\langle N_{\text{pile-up}} \rangle$=4.1). Default jet selections are compared to using the JVF selection and to the truth jet multiplicity. In the range $3 \leq N_{\text{jet}} \leq 6$, 16% deviations from the truth jet multiplicity ($N_{\text{jet}} = 3$) exist for default jet requirements, while a maximum difference of 4% is observed for jets required to have $JVF \geq 0.50$, a factor of 4 improvement over current techniques.

Chapter 7

Measurement of hadronic event shapes

This chapter presents results for the measurement of hadronic event shapes in pp collisions at $\sqrt{s} = 7$ TeV with the ATLAS detector. Six event shapes are studied, each being sensitive to different aspects of the hadronic final state: the three-jet resolution parameter, y_{23}, sphericity, S^{spheri}, and the transverse sphericity, $S_{\perp}^{spheri}$, the event thrust, $\tau_{\perp}$, along with its minor component, $T_{m,\perp}$, and the aplanarity A. These observables and their mathematical definitions are described in detail in Section 2.3. Both detector-level studies and hadron level results are presented, thereby allowing for a direct comparison of data to both exact matrix element MC generators like ALPGEN as well as more ubiquitous parton shower MC such as PYTHIA (Perugia 2010). The individual components of the generic transverse momentum tensor, $M_{\alpha\beta}$, are also provided in Appendix D.

These measurements constitute the first dedicated study of hadronic event shapes at high Q^2 in ATLAS and demonstrate not only our excellent understanding of QCD in a new energy regime but open the path to using complex event-level observables in the search for new physics. This path is a less frequently traveled one in ATLAS due to the inherently complex dependence on systematic effects and our understanding of the hadronic final state at high luminosity. Using the tools and understanding developed in the previous chapters we demonstrate that these effects are understood

well-enough to allow them to be used for even quite subtle applications and will eventually allow for a detailed comparison of the measurements to perturbative QCD calculations.

7.1 Analysis

The data used for the analysis of event shapes represent the entire 2010 dataset and corresponds to an integrated luminosity of $\int \mathcal{L}dt = (37.4 \pm 1.27)$ pb^{-1}. The uncertainty on the luminosity is obtained from the latest luminosity calibration using the full set of van der Meer (vdM) scans performed in 2010 [162]. For a full discussion of the systematic errors evaluated in determining this uncertainty see Appendix A for a description and measurement of the first vdm scan and Ref. [162] for a complete description of the methods used to determine the luminosity calibration. For a detailed description of the data used for this measurement see Appendix D.

The Monte Carlo event generators discussed in Section 2.2.1 are used here. ALPGEN 2.13 with exact matrix element calculations up to $n \leq 6$ partons is interfaced to HERWIG 6.510 [72] to provide the parton shower and hadronization model and with JIMMY 4.31 [73] for the underlying event model. The "ATLAS Underlying Event Tune 1" (AUET1) is used for ALPGEN +HERWIG/JIMMY. Comparisons are made to the predictions from the MC programs PYTHIA 6.423 [74] with the Perugia 2010 tune [75] and HERWIG++ 2.4 [76], where these are used both for the simulation of the hard $2 \to 2$ process as well as for the parton shower, underlying event, and hadronization models.

As the goal of this measurement is to test perturbative QCD in a new high-energy regime, we select a sample of high-p_{T} jets with which to measure the energy flow throughout the event. The event selection is as follows:

- **Trigger:** single jet trigger with a nominal transverse energy threshold of 95 GeV at level one (`L1_J95`). This trigger item remained in pass-through after the activation of rejection within the high-level trigger. This trigger item is 100% efficient for the offline event selection ($\frac{1}{2}H_{T,2} > 250$ GeV) described below as demonstrated in Figure 7.1 below.

- **Vertex:** at least one vertex with at least 5 tracks with $p_{\mathrm{T}}^{\mathrm{track}} > 150$ MeV used in the vertex fit must be present in the event. No requirements are placed on the longitudinal position (along the beam line) of the vertex as the beam spot is already used as a constraint when fitting the vertex. Since the primary vertex multiplicity, N_{PV}, is different in data and MC, a re-weighting factor is applied to the MC as shown in Figure 7.2.

- **Primary jet algorithm:** Jets reconstructed by the anti-k_t, $R = 0.6$ algorithm are used for all event shape measurements. This algorithm yields regular jets that are less susceptible to systematic effects, as described in Chapter 5.

- **Leading jets:** The quantity $\frac{1}{2}H_{T,2} = \frac{1}{2}(p_{T,1} + p_{T,2}) > 250$ GeV is used to select events at high Q^2 so as to be able to perform a reliable NLO calculation, as discussed in Section 2.3.

- **Jet quality:** Events with any "bad" jet (as defined by the MEDIUM criteria listed in Table 7.1) are rejected completely whereas so-called "ugly" jets for which the energy measurement might be less accurate because of problematic calorimeter regions are included in the analysis as their fraction is $\ll 1\%$.

Jet cleaning A number of jet cleaning cuts are applied to the data in order to remove jets that are likely to be originating in beam-related backgrounds or detector defects. The purpose of these cuts is largely to remove events that are classified as having activity associated with one of three phenomena:

1. Spikes in the hadronic end-cap calorimeter (HEC).

2. Coherent noise in the electro-magnetic calorimeter (EM).

3. Cosmic rays and other non-collision backgrounds.

Several variables are currently used to implement the cleaning of events. These are listed in Table 7.1. These variables are accessed on a jet-by-jet basis, and if an event contains any jet which fails the cleaning cuts, then the whole event is rejected. This selection rejects 37 events, representing an efficiency of 99.98%. The selections

Identifier (Goal)	**Criteria for bad jet**
Loose (HEC energy spikes)	$f_{\text{HEC}} > 0.5$ **AND** $\lvert Q_{\text{HEC}}\rvert > 0.5$
Loose (HEC energy spikes)	$\lvert E < 0\rvert > 60$ GeV
Loose (Noise)	$f_{\text{EM}} > 0.95$ **AND** $\lvert Q_{\text{LAr}}\rvert > 0.8$ **AND** $\lvert\eta_{\text{EM}}\rvert < 2.8$
Loose (Cosmic muons)	$\lvert t\rvert > 10$ ns
Loose (Cosmic muons)	$f_{\text{EM}} < 0.05$ **AND** $f_{\text{charged}} < 0.05$ **AND** $\lvert\eta_{EM}\rvert < 2$
Loose (Cosmic muons)	$f_{\text{EM}} < 0.05$ **AND** $\lvert\eta_{EM}\rvert \geq 2.$
Loose (Cosmic muons)	$f_{\text{Max}} > 0.99$ **AND** $\lvert\eta_{EM}\rvert < 2$
Medium (HEC energy spikes)	$f_{\text{HEC}} > (1 - \lvert f_{\text{HEC}}\rvert)$
Medium (Noise)	$f_{\text{EM}} > 0.9$ **AND** $\lvert Q_{\text{LAr}}\rvert > 0.8$ **AND** $\lvert\eta_{EM}\rvert < 2$
Medium (Cosmic muons)	$f_{\text{EM}} < 0.05$ **AND** $f_{\text{charged}} < 0.1$ **AND** $\lvert\eta_{EM}\rvert < 2$
Medium (Cosmic muons)	$f_{\text{EM}} > 0.95$ **AND** $f_{\text{charged}} < 0.05$ **AND** $\lvert\eta_{EM}\rvert < 2$

Table 7.1: Cleaning cuts optimised for anti-k_t, $R = 0.6$ jets. If any jet fails any one of the eleven cuts, then the event is discarded.

in Table 7.1 are applied only to anti-k_t, $R = 0.6$ jets with a minimum $p_{\text{T}} > 30$ GeV. The variables are defined as follows:

- f_{HEC}: energy fraction of the jet in the HEC
- Q_{LAr}: fraction of LAr cells with a cell Q-factor greater than 4000[1]
- Q_{HEC}: the same as Q_{LAr} but computed using only cells in the HEC
- f_{EM}: fraction of the jet energy in the EM calorimeters
- t: jet time computed as the energy squared cells mean time
- f_{charged}: the ratio of the total $p_{\text{T}}^{\text{track}}$ associated to the jets divided by the calibrated jet p_{T}.
- f_{Max}: maximum energy fraction in any one calorimeter layer

[1]The cell Q-factor quantifies the difference between the measured pulse shape (a_i^{meas}) and the predicted pulse shape (a_i^{pred}) that is used to reconstruct the cell energy. It is computed as $\sum_{\text{samples}} (a_i^{\text{meas}} - a_i^{\text{pred}})^2$ and it is stored as 16-bit integer.

Trigger selection and efficiency The trigger used to select events for this analysis relies primarily on the L1 calorimeter triggers. The so-called `L1_J95` nominally accepts events with energy deposits with electromagnetic-scale energies of 95 GeV or greater. This trigger was active and unprescaled during the entire data taking period so no High Level Trigger selection is applied.

Figure 7.1 shows the trigger efficiency for the jets and trigger selection used in this analysis. The efficiency is measured by bootstrapping from triggers with lower thresholds. Triggers with nominal thresholds at the L1 trigger EM scale of 5 GeVare used first and compared to those with a nominal threshold also at this approximate EM scale of 30 GeV. Subsequently, the 30 GeVtrigger threshold selectiones . With this strategy, the measured efficiency is compared to the efficiency derived from Monte Carlo (MC) samples with and without in-time pile-up overlaid with the signal interaction. The agreement between the three curves shows that the trigger efficiency is well modeled by the MC and that the effect of multiple *pp* interactions on the trigger efficiency is minor. Further details may be found in Appendix D.

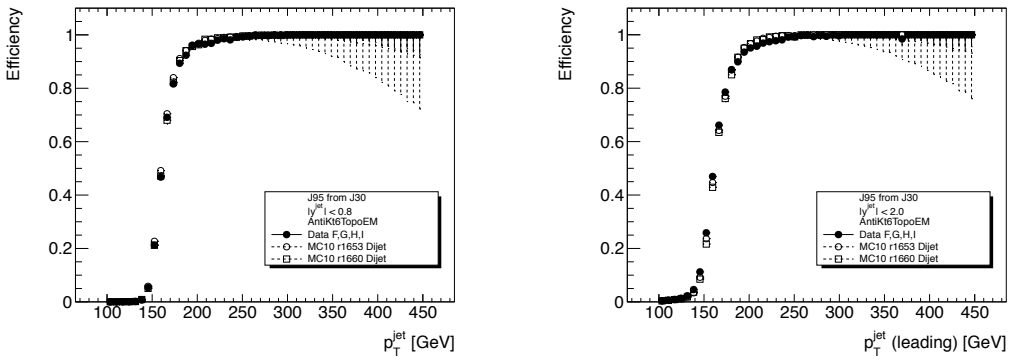

Figure 7.1: `L1_J95` trigger efficiency (per event) for each of the four jet algorithms considered in this note using the bootstrap method with respect to the `L1_J30` trigger. The results are compared to PYTHIA QCD dijet Monte Carlo samples without pile-up and with in-time pile-up overlaid with the signal interaction.

Primary vertex re-weighting In order to compensate the MC simulation for the different level of pile-up compared to the data, a re-weighting factor is applied

to each event. These factors are derived by measuring the reconstructed primary vertex multiplicity in both data and in MC simulation with pile-up added. The MC simulation uses a large 900 ns bunch spacing configuration with a Poisson mean of 3 interactions simulated per bunch crossing. This results in a slightly higher number of reconstructed primary vertices per event in the MC compared to the data. Vertices are selected with the same quality criteria as defined in the analysis selection, and must contain at least $N_{trk}^{PV} \geq 4$. Figure 7.2 shows both the re-weighting factors obtained for ALPGEN as well as the comparison of each fully re-weighted MC sample to the data. The excellent agreement indicates that the re-weighting is being applied consistently and the resulting distributions agree with the data to a very high degree.

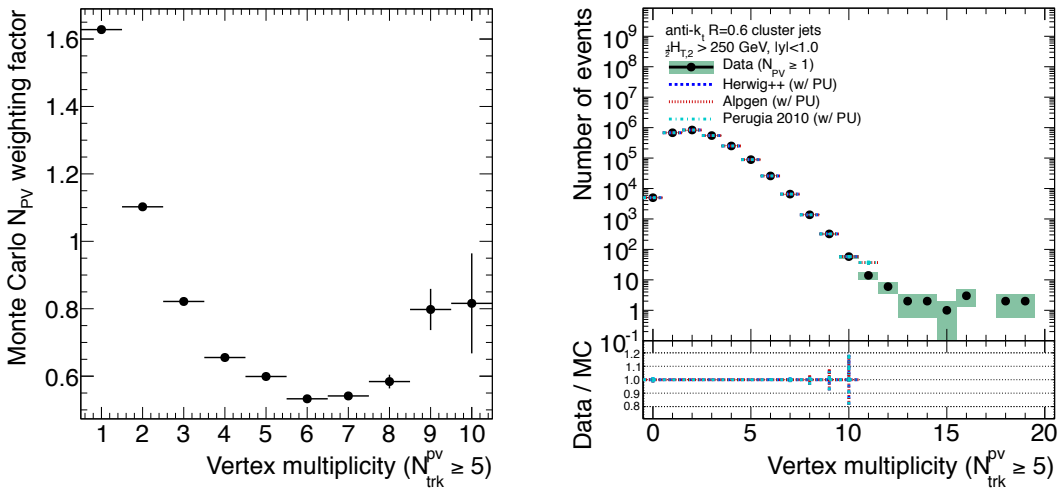

(a) (b)

Figure 7.2: (left) Re-weighting factors used to compensate the ALPGEN MC simulation for the different level of pile-up compared to the data. Vertices are selected to have at least $N_{trk}^{PV} \geq 4$ and are computed for each MC simulation independently. (right) Primary vertex multiplicity distribution after the re-weighting has been applied, demonstrating that each MC simulation agrees with the data distribution to a very high precision.

Event topology and kinematics The jet p_{T} spectra for both the inclusive jet selection used in this analysis and the leading jet separately are shown in Figures 7.3 and 7.4.

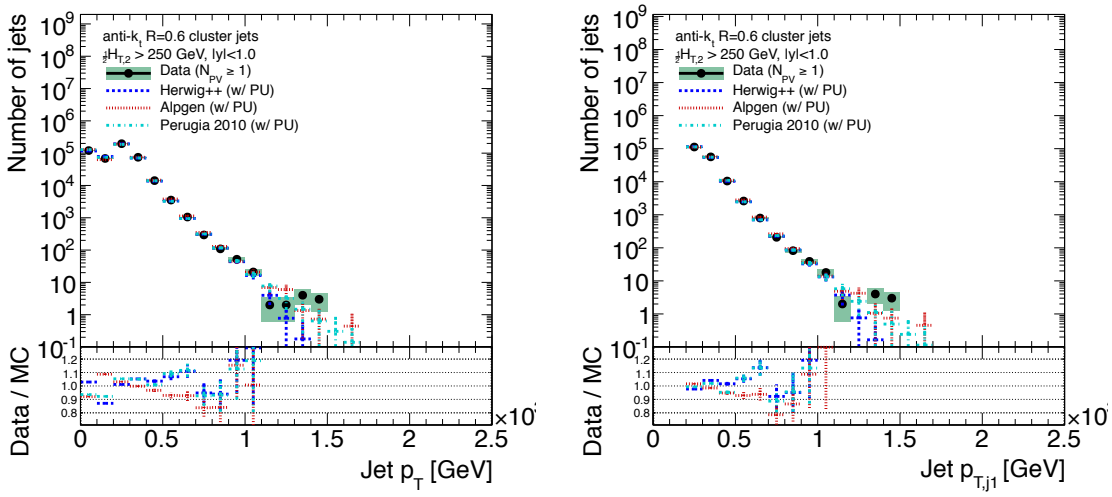

(a) Inclusive (b) Leading jet

Figure 7.3: (a) Inclusive jet p_{T} spectrum. (b) Leading jet p_{T} spectrum. These distributions are shown at the detector level prior to any particle level corrections.

7.2 Systematics and corrections

Multiple effects plague the precise measurement of event shapes due to the inclusive nature of these observables and their reliance on an accurate reconstruction of the hadronic final state, which itself is a central goal of this thesis. The jet energy scale must account for non-compensation of the calorimeter over a wide range of jet transverse momentum; the presence of multiple pp interactions and their tendency to not only contaminate jets from the hard-scatter but also to produce extraneous jets themselves; the finite resolution and fiducial range of the detector.

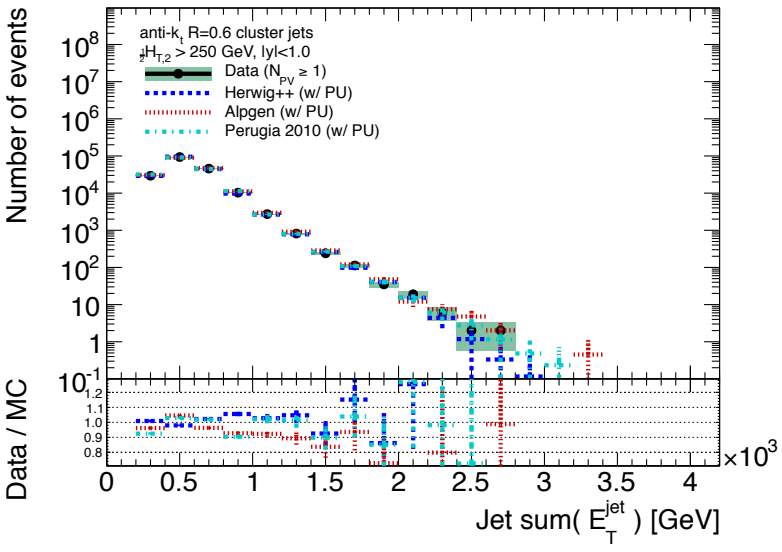

Figure 7.4: Jet $\sum E_T^{\text{jet}}$ at the detector level.

7.2.1 Jet energy scale uncertainty

The uncertainty on the jet energy scale (JES) established by the jet calibration procedure was introduced and described in detail in Section 5.3. This uncertainty can influence the final event shape measurement via multiple systematic effects. The thresholds used to select events based on the leading jet momenta and to select individual jets for use in the final measurement can both be affected. Although the significance of a JES variation on these measurements is reduced by the explicit use of ratios of jet momenta, the jet yield can still vary for a given event due to these selections.

Figures 7.5- 7.7 demonstrate the impact on event shape variables of varying the JES uncertainty within the 1 σ band determined from both the in-situ methods and simulation studies described in Section 5.3. The reference sample used to evaluate the results shown here is produced with the ALPGEN MC generator interfaced to Jimmy for the underlying event and hadronization models. The final results use the differences with respect to other MC models in order to evaluate the dependence on the underlying physics simulation, but ALPGEN exhibits the widest range of agreement

with the data and is thus deemed more appropriate for discussion of the individual systematic uncertainties. A full set of studies using each of the three primary MC generators and tunes is provided in Appendix D.4.

Since the three-jet resolution, y_{23}, is constructed as a direct ratio of jet momenta, it is not surprising that the JES uncertainty has only a very limited influence. The primary effect is that of producing a larger shift on the event Q^2 than on the momentum of the third jet. At very low $\ln y_{23}$, where the event shape configuration approaches that of a pure di-jet event with only $2 \to 2$ hard-scattering processes and very little additional radiation, a fractional increase in the leading jets' momenta of a few % has a much larger impact than that from the third leading jet. The result is an overall decrease in the value of $\ln y_{23}$ and a fractionally higher population of the lowest bins and a fractionally lower population of the highest bins. These variations per bin result in shifts of up to 10%. Evaluating this shift in MC simulated with the presence of additional interactions, also shown in Figures 7.5- 7.7, suggests that the small relative uncertainty on the JES due to pile-up has a very small effect.

Three event shapes are the product of combinations of eigenvectors computed from the transverse momentum tensor, $M_{\alpha\beta}$, in each event. The aplanarity, A, is a very steeply falling distribution computed from the third eigenvector, λ_3 of $M_{\alpha\beta}$ and thus the impact due to shifts in the JES are dominated by both generator differences and the presence of pile-up, as demonstrated in Section 7.2.2. Both the sphericity, S^{pheri}, and the transverse sphericity, $S_{\perp}^{pheri}$, are computed from ratios of eigenvalues of $M_{\alpha\beta}$ and subsequently manifest almost no discernable impact from the JES uncertainty alone.

Most affected by the JES uncertainty is the transverse thrust, $\tau_{\perp}$, and its minor component, $T_{m,\perp}$. In addition to utilizing a relative normalization to compute the thrust, a maximization of the event thrust axis, $\hat{n}_{\perp}$, is computed. In this case, the introduction of additional jets into the maximization problem can shift the measured thrust axis. Thus, the primary effect of the JES uncertainty on the transverse thrust is due shifting events into or out of the corners of the multi-jet phase space that this quantity probes. Statistically significant variations of 5% are observed and subsequently included in the error associated with this measurement.

The dominant effect observed is the impact on the jet energy scale due to pile-up. This will be discussed more explicitly in the following section by using the tools developed in Chapter 6, namely JVF. We see that the $\tau_{\perp}$, $T_{m,\perp}$, and $\ln y_{23}$ are most affected by the JES shifts induced.

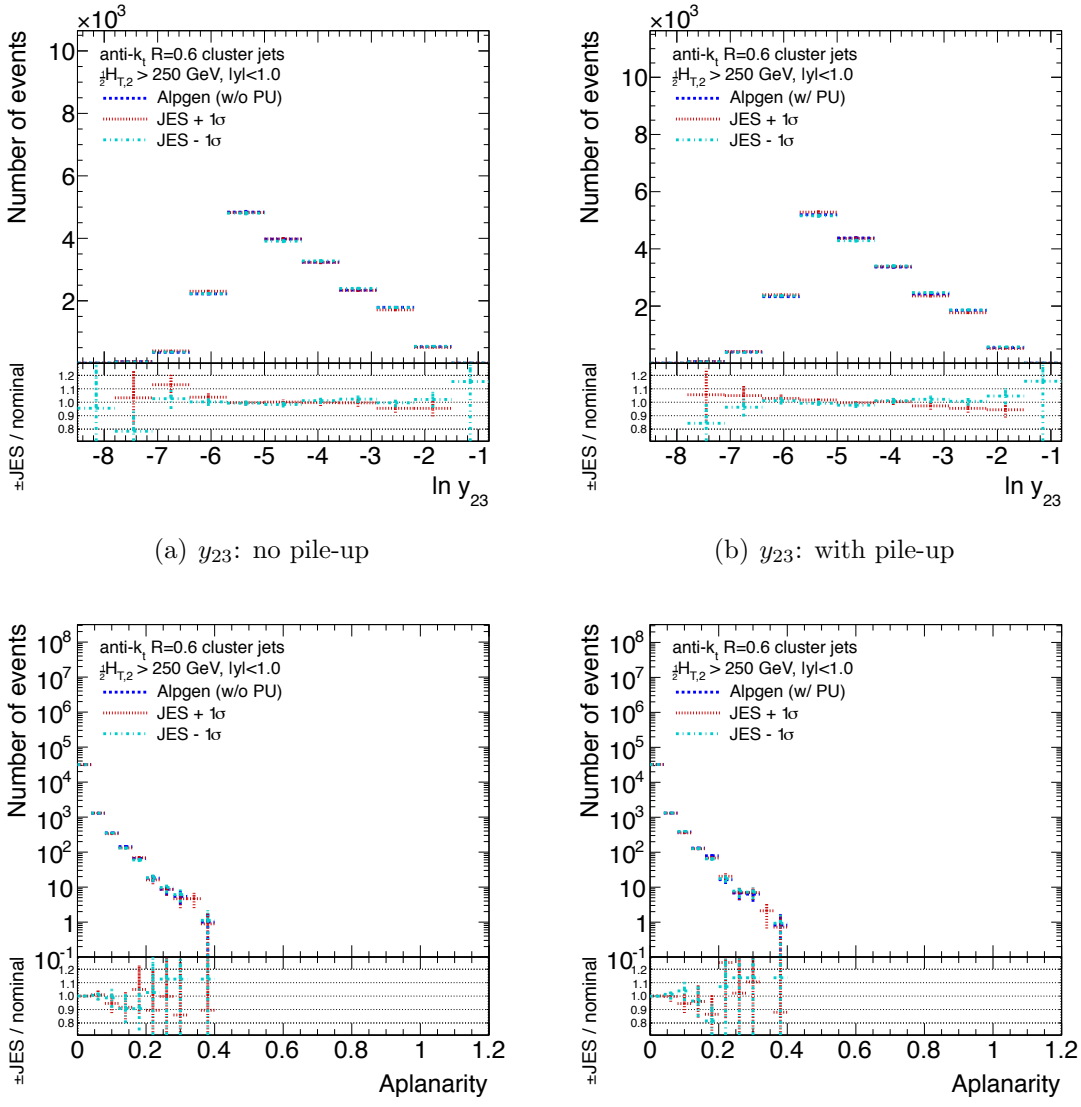

(a) y_{23}: no pile-up

(b) y_{23}: with pile-up

(c) A: no pile-up

(d) A: with pile-up

Figure 7.5: ALPGEN: Impact of the JES variation on the detector-level event shapes y_{23} (top) and A (bottom) both without (left) and with (right) pile-up.

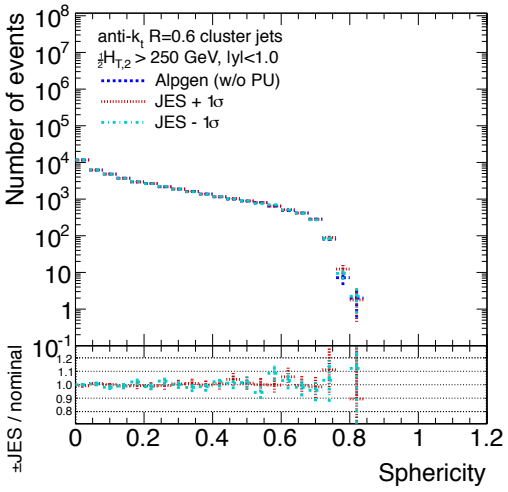

(a) S^{pheri}: no pile-up

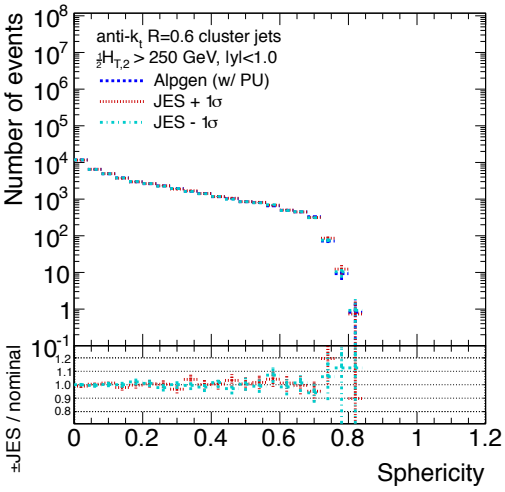

(b) S^{pheri}: with pile-up

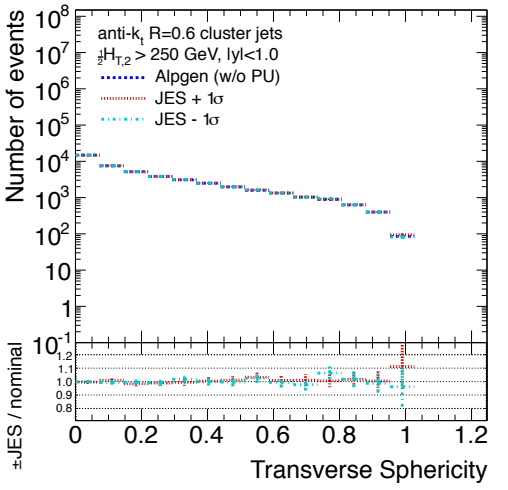

(c) $S_{\perp}^{pheri}$: no pile-up

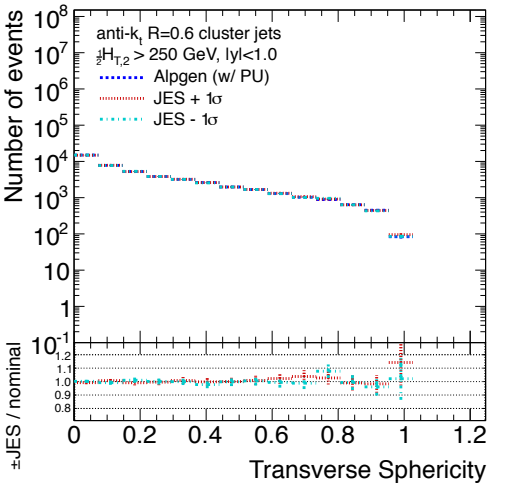

(d) $S_{\perp}^{pheri}$: with pile-up

Figure 7.6: ALPGEN: Impact of the JES variation on the detector-level event shapes S^{pheri} (top) and $S_{\perp}^{pheri}$ (bottom) both without (left) and with (right) pile-up.

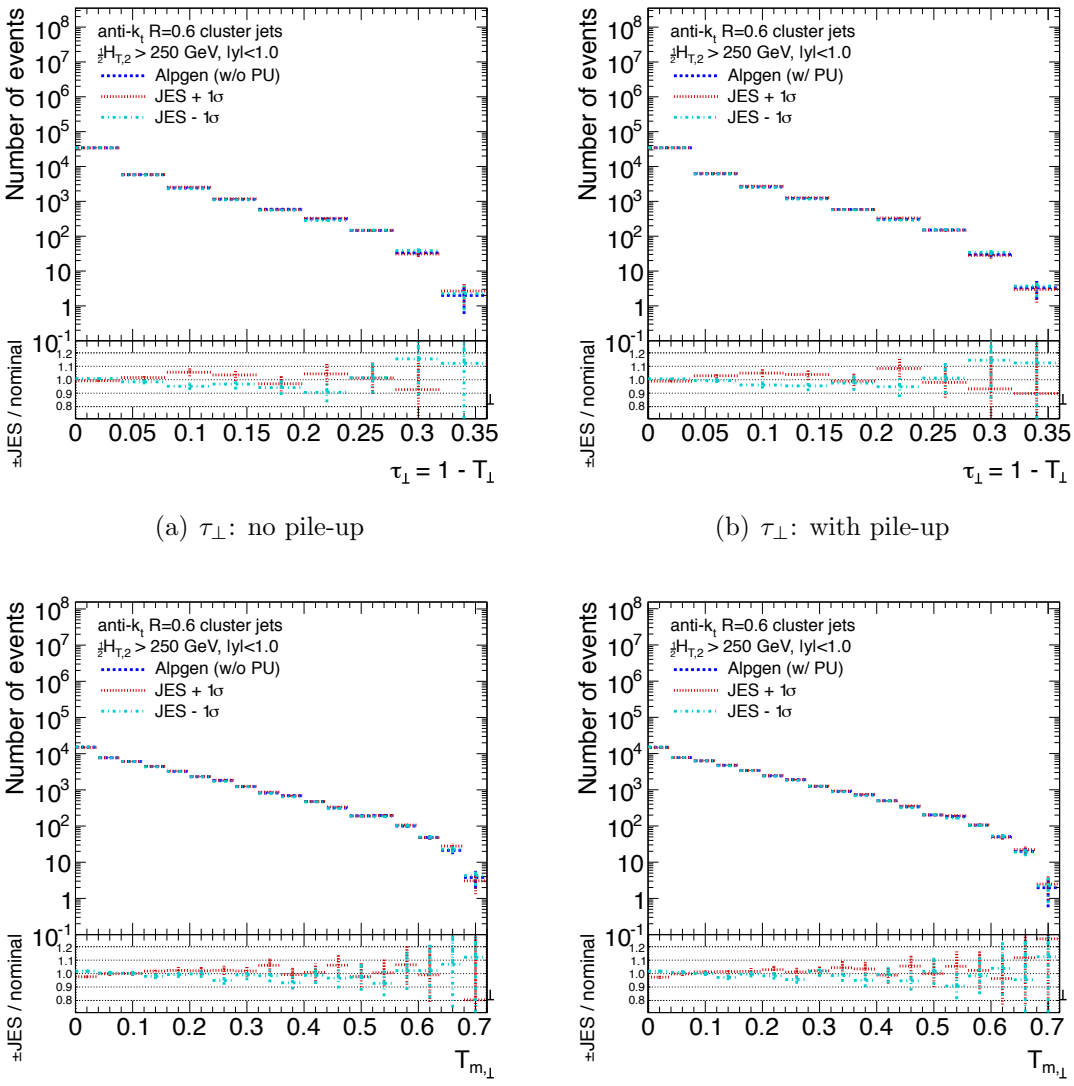

(a) $\tau_\perp$: no pile-up

(b) $\tau_\perp$: with pile-up

(c) $T_{m,\perp}$: no pile-up

(d) $T_{m,\perp}$: with pile-up

Figure 7.7: ALPGEN: Impact of the JES variation on the detector-level event shapes $\tau_\perp$ (top) and $T_{m,\perp}$ (bottom) both without (left) and with (right) pile-up.

7.2.2 Impact of pile-up

As noted above, the presence of additional jets in the event may alter the observed event shape, in particular for those measurements that are explicitly dependent upon

the jet multiplicity, such as those computed from the event transverse momentum tensor. In addition to extra jets introduced through variations in the transverse momentum threshold, additional pile-up interactions can produce jets not associated with the hard-scattering interaction responsible for the finally being considered in a given event. This topic was discussed at length in Chapter 6 and its effect on the observables considered in the event shapes analysis is described here.

Two primary effects are expected from pile-up: augmentation of the energy scale and their properties for jets actually produced in the hard-scattering and jets produced in additional pp collisions within the same bunch crossing. The consequence of the former is typically an offset energy scale, as discussed in Section 6.1. Since the offset itself is corrected by the calibration procedure and the impact remaining uncertainty is evaluated using the studies in Section 7.2.1, the effect due to additional jets is considered in more detail.

A crucial tool in the identification of jets from pile-up is the jet-vertex fraction (see Section 6.5). Figure 7.8 shows the JVF distribution in data for jets entering the event shape calculation. The rate of jets from pile-up ($JVF = 0$) increases by a factor of two from events with two primary vertices to between five and eight primary vertices. The overall fraction of events with greater than five reconstructed primary vertices is still low enough in the data sample used for this analysis that the impact is small. The most important effect is on the JES of jets with $0.75 < |JVF| < 1.0$, which the studies in Section 6.5 showed can be significant. Up to 5-10% JES shifts may be induced for a jet with significant pile-up contamination. Since all event shapes are designed as normalized ratios, however, the final impact of this uncertainty on the measurement is vastly reduced.

By comparing the observed detector-level distributions in events with and without additional reconstructed vertices the systematic effects of pile-up are assessed directly. Some slight variation at low $\ln y_{23}$ is observed as well as a relative increase in the fraction of events at higher $\tau_{\perp}$, both of which are similar conclusions reached by evaluating the impact of the JES uncertainty. This indicates that the primary effect of pile-up on the event shapes is the augmentation of the jet energy scale due to additional charged particles in the event. Furthermore, a test of the variation in $\ln y_{23}$

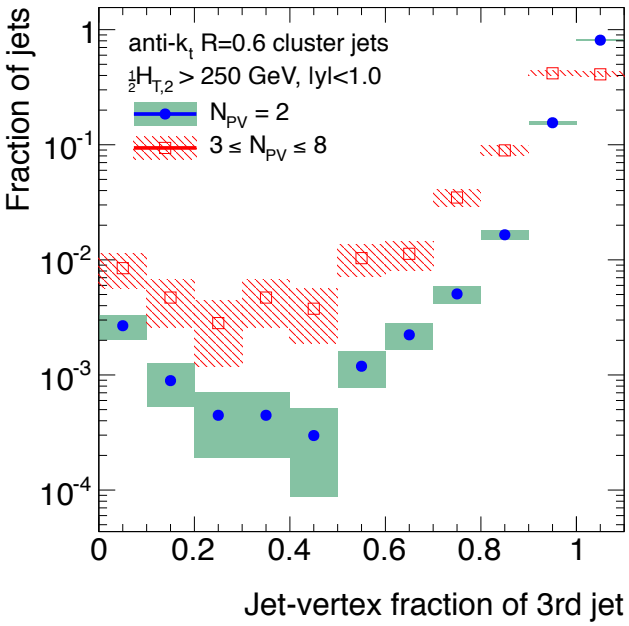

Figure 7.8: Distribution of the jet-vertex fraction, JVF, for the third leading jet in events used in the measurement of event shapes. Events are separated by primary vertex multipilicity into $N_{\mathrm{PV}} = 2$ and $5 \leq N_{\mathrm{PV}} \leq 8$ demonstrating that jets from the hard-scatter have an larger contribution from pile-up and that the rate of jets from pile-up interactions increases.

as a function of the third jet in the event is carried out to establish *in-situ* verification that the modeling of the effects on the final state observables is being done adequately. These studies are presented in Appendix D.4.

The conclusion of this systematic evaluation is that the dominant effect of pile-up is in the augmentation of the measured jet energy due to pile-up.

7.2.3 Unfolding for detector effects

In order to compare the results measured with the ATLAS detector to those predicted from MC simulations with the various generators the measurements must be fully corrected for several effects. Efficiency loss in specific regions of phase space of the final state, such as leakage beyond the fiducial range of the measurement, small detector

biases[2], and more will give rise to a measured value of event shapes that may differ from predictions made without such effects. In addition, the selections applied to the final state are all subject to systematic variation and must be corrected for in order to provide a common ground for comparison of data to the theoretical predictions. Four primary corrections are assessed for their impact on the final measurements and for the systematic uncertainty associated with each.

- Simulation of pile-up
- Jet-energy scale variations
- Pile-up filtering using N_{PV} and JVF
- Generator differences

Figure 7.9 provides an overview of these effects and their uncertainties for a single observable, y_{23}, binned in $\ln y_{23}$. In this case, the sample of jets generated with ALPGEN and with additional pp interactions included in the detector simulation is used as the reference sample. A prediction for $\ln y_{23}$ is computed using a sample of jets constructed from stable truth particles (with lifetimes longer than 10 ps). The same observable is constructed after a full detector simulation and the bin-by-bin correction factors are computed.

A migration matrix is evaluated for each of the observables both with and without pile-up added. Figures 7.13 and 7.14 show the high purity and efficiency for y_{23} which is needed in order to justify the use of bin-by-bin unfolding.

7.3 Results

The results of the event shape measurements are presented both at hadron level, after incorporating the unfolding factors and systematic effects explored in Section 7.2.3. In addition, the dependence of these observables at the detector-level are evaluated with respect to the kinematic and topological phase space available in the hadronic final

[2]Here, small takes on a very particular meaning in terms of the efficiency and purity of a given measurement and will be discussed in more detail

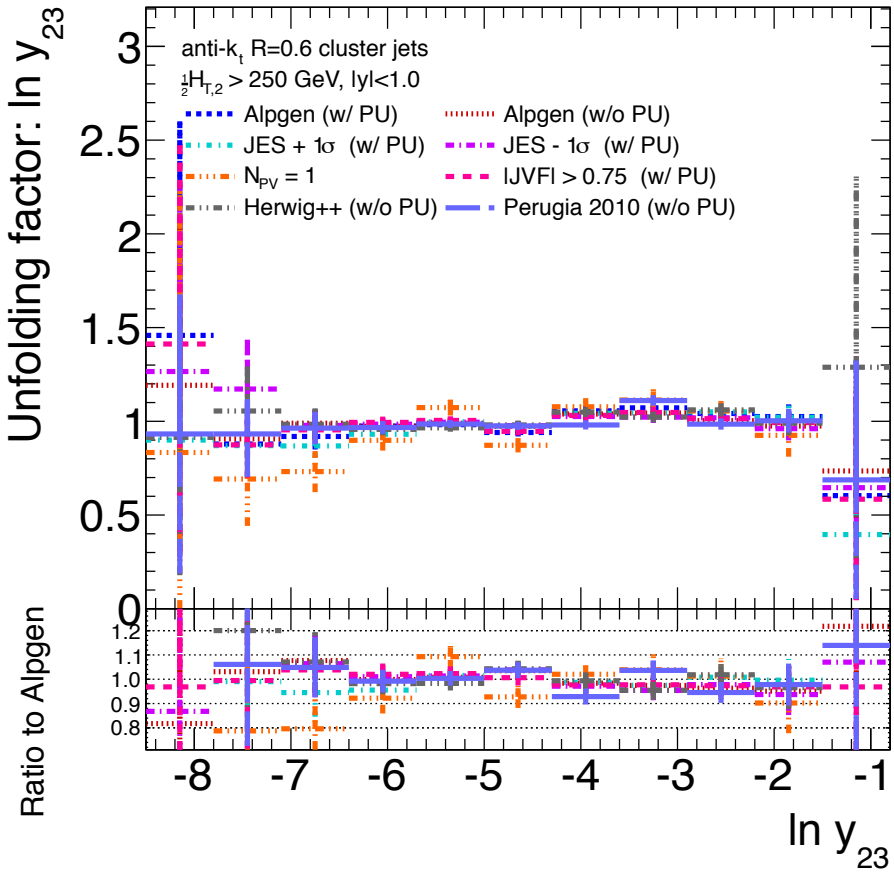

Figure 7.9: Unfolding factors for $\ln y_{23}$ computed using events simulated with ALPGEN including multiple pp interactions as the reference. Comparisons are made to ALPGEN simulated without pile-up, JES energy scale uncertainties, pile-up filtering techniques and the MC generators HERWIG++, PYTHIA (Perugia 2010) (both simulated without pile-up).

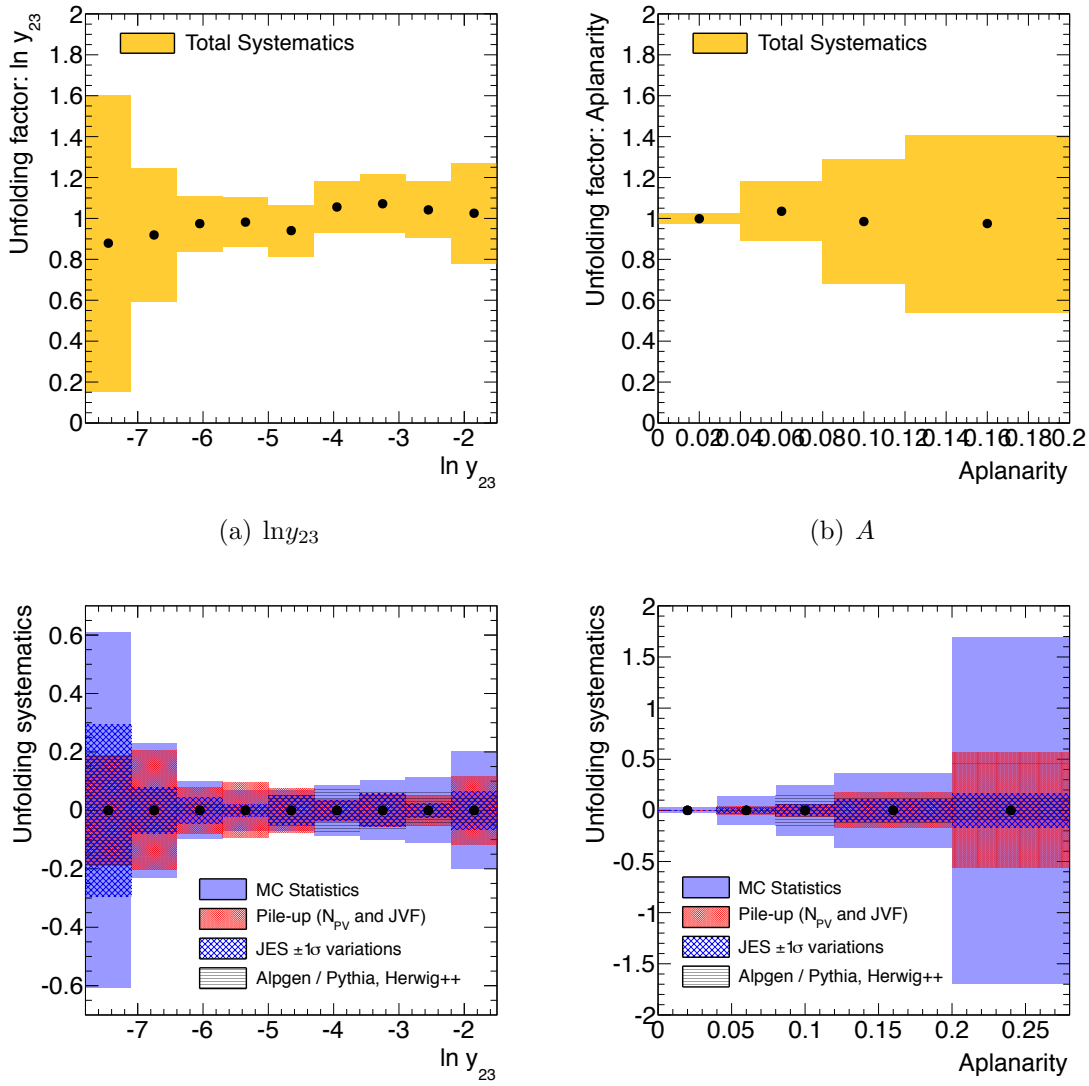

(a) $\ln y_{23}$ (b) A

(c) $\ln y_{23}$ (d) A

Figure 7.10: Unfolding factors for the (a) three-jet resolution, $\ln y_{23}$, and (b) aplanarity, A. Systematic uncertainties obtained by evaluating differences with respect to ALPGEN with pile-up are also shown for each in (c) and (d), respectively.

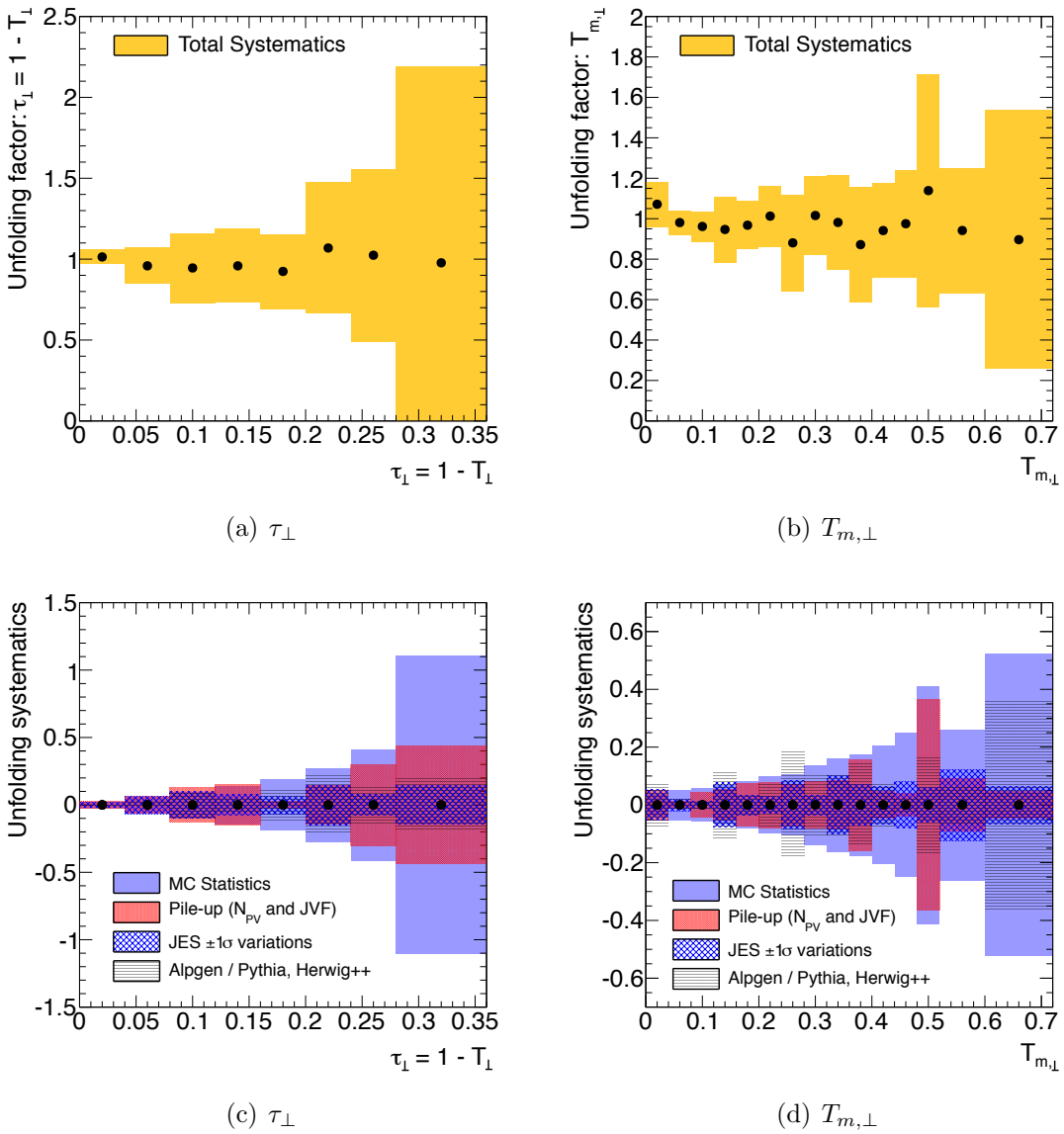

(a) $\tau_\perp$ (b) $T_{m,\perp}$

(c) $\tau_\perp$ (d) $T_{m,\perp}$

Figure 7.11: Unfolding factors for the (a) tranverse thrust, $\tau_\perp$, and (b) minor component of the transverse thrust, $T_{m,\perp}$. Systematic uncertainties obtained by evaluating differences with respect to ALPGEN with pile-up are also shown for each in (a) and (b), respectively.

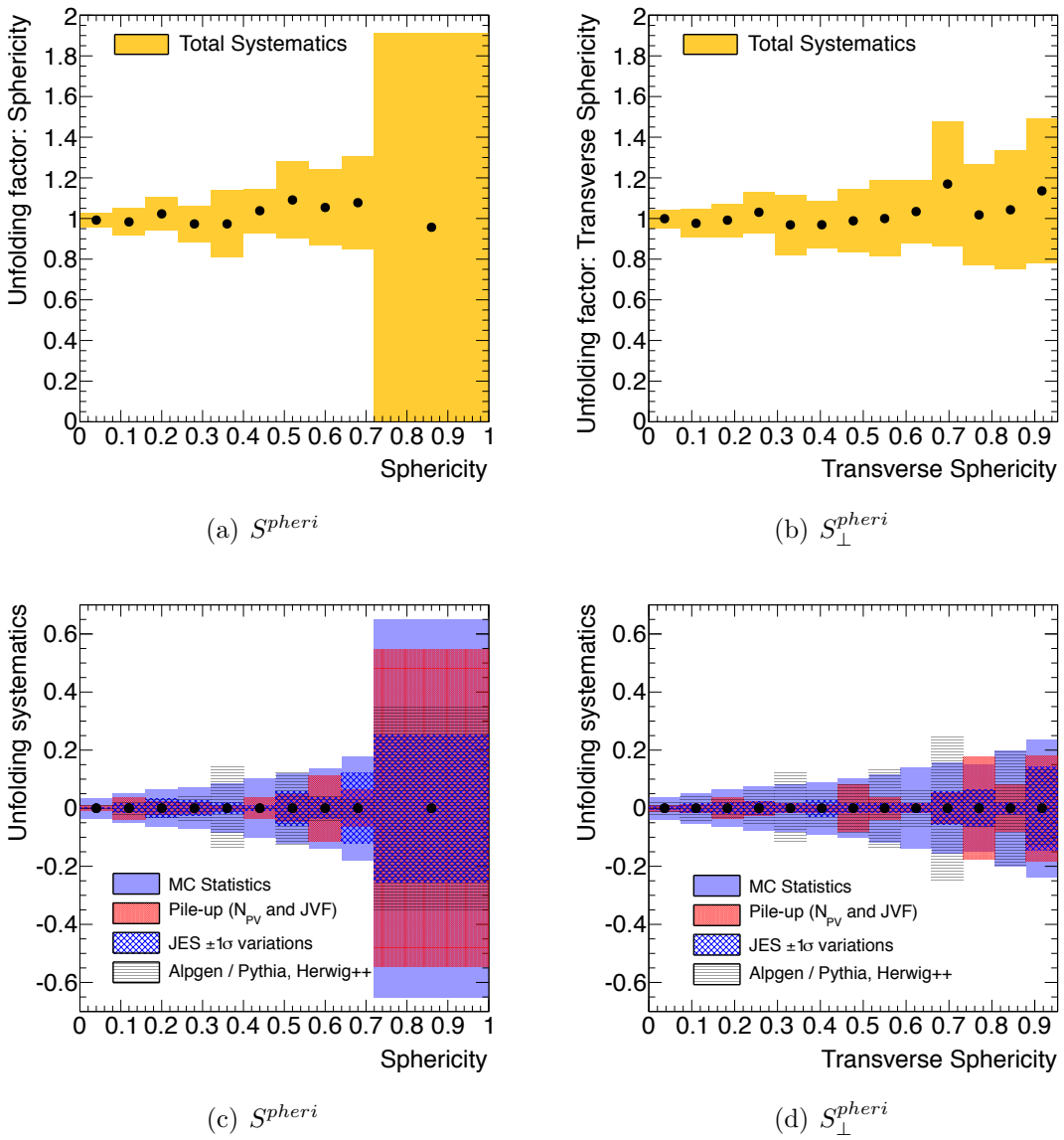

(a) S^{pheri} (b) $S_{\perp}^{pheri}$

(c) S^{pheri} (d) $S_{\perp}^{pheri}$

Figure 7.12: Unfolding factors for the (a) sphericity, S^{pheri}, and (b) transverse sphericity, $S_{\perp}^{pheri}$. Systematic uncertainties obtained by evaluating differences with respect to ALPGEN with pile-up are also shown for each in (c) and (d), respectively

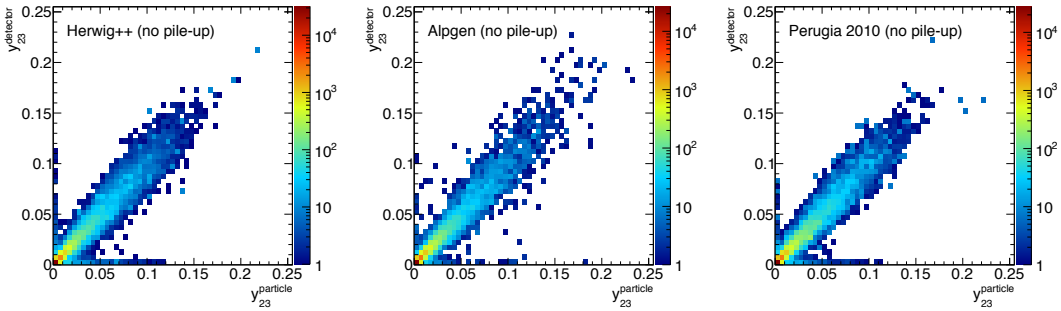

(a) Herwig++ (b) Alpgen (c) Pythia (Perugia 2010)

Figure 7.13: Migration matrices for y_{23} without pile-up.

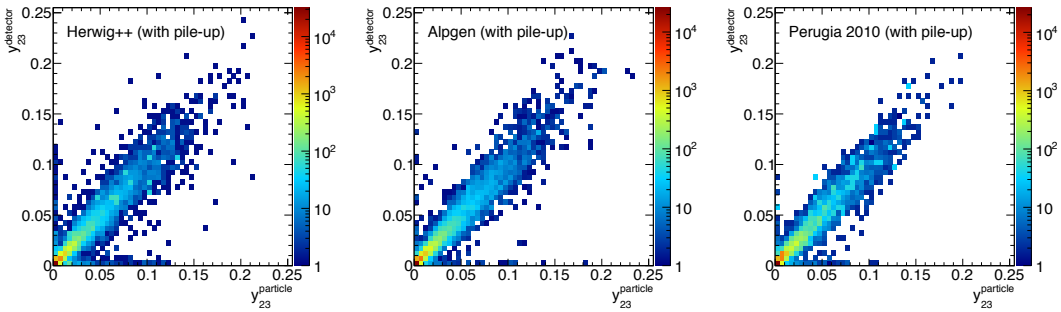

(a) Herwig++ (b) Alpgen (c) Pythia (Perugia 2010)

Figure 7.14: Migration matrices for y_{23} with pile-up.

state to both investigate the final result and to highlight regions of the measurement that might be improved up in the future.

7.3.1 Hadron level event shapes

Event shapes unfolded to the hadron level using the ALPGEN generator as the reference are shown in Figures 7.15- 7.17. ALPGEN, HERWIG++, and PYTHIA (Perugia 2010) all describe the measured event shapes well and are not dependent on the reference generator (see Appendix D.4). Some small discrepancies are observed particularly in the tails of fastly falling distributions, such as the aplanarity, or in the transverse thrust.

The three-jet resolution and aplanarity are both shown in Figure 7.15. In the case of y_{23}, where the primary sensitivity is to the parton shower or matrix element description of the momentum of the third jet, HERWIG++ is seen to be slightly better agreement with the data. Although ALPGEN provides exact matrix element calculations for up to 6 jets, a slight overestimation of events with low $\ln y_{23}$– or equivalently a small low $p_{T,3}$ to $\frac{1}{2}H_{T,2}$ ratio – is observed. This indicates that despite the more precise calculation of the high jet multiplicity states, the impact of tuning the parton shower simulation plays a significant role. The aplanarity on the other hand measures the sum of the transverse momenta out of the event plane defined primarily by the two hardest jets, as introduced in Section 2.3. Although a steeply falling distribution, the deviation of the MC prediction from the data is statistically significant for both PYTHIA (Perugia 2010) and HERWIG++. The measurements consistently support more highly "aplanar" events than predicted by HERWIG++ and fewer than PYTHIA (Perugia 2010) indicates, although the statistical significance of the latter discrepancy is not high. The agreement with ALPGEN is good throughout the range of phase space probed in a statistically significant way. These results suggest that the topological distribution of the event shape is more accurately described by the exact multi-jet prediction provided by the matrix element MC even though HERWIG++ is seen to match the three-jet resolution more accurately.

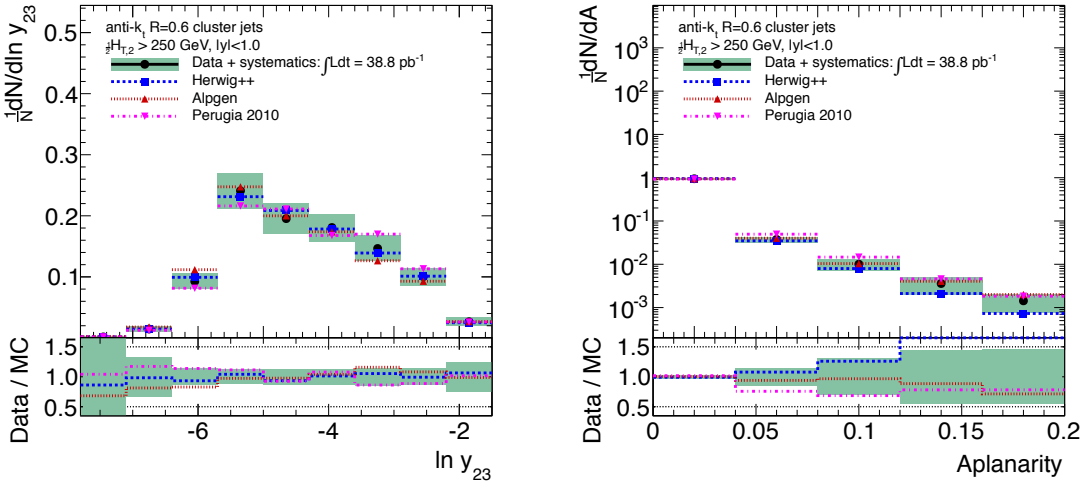

(a) $\ln y_{23}$ (b) A

Figure 7.15: Unfolded hadron level measurements of the (a) three-jet resolution, $\ln y_{23}$, and (b) aplanarity, A. The unfolding is performed using the ALPGEN generator with pile-up added.

The hypothesis that the topological distribution is more well described by ALPGEN is supported by the measurement of the transverse thrust, $\tau_\perp$. Figure 7.16(a) exhibits the same qualitative discrepancy as observed in the aplanarity: HERWIG++ predicts fewer highly isotropic events than observed. However, it should be noted that at small but significantly non-zero thrust, HERWIG++ fares much better than ALPGEN and PYTHIA where significant ($\mathcal{O}(20\%)$) differences can be seen. In this intermediate thrust range, ALPGEN and PYTHIA both predict a thrust distribution shifted towards slightly higher values. Due to this improved agreement at low but non-zero thrust, the average agreement between data and the various MC generators is closest for HERWIG++. This observation will be made again when assessing the kinematic dependence of these shapes at the detector-level in Section 7.3.2. The minor component of the thrust, $T_{m,\perp}$, or the out-of-plane thrust magnitude does not readily suggest as large of a discrepancy as observed in the aplanarity despite a nominal sensitivity to the same qualitative physics.

Lastly, the sphericity and transverse sphericity shown in Figure 7.17 exhibit very

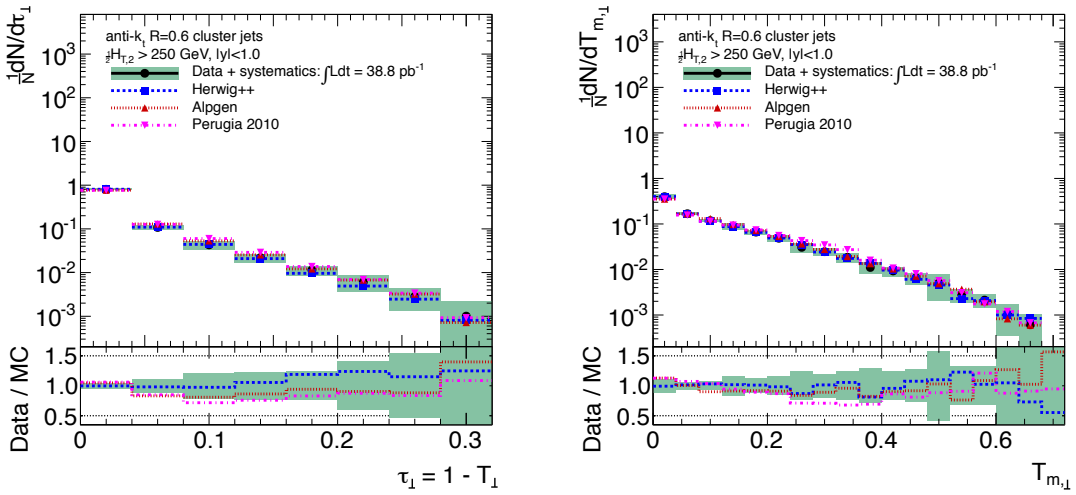

(a) $\tau_\perp$ (b) $T_{m,\perp}$

Figure 7.16: Unfolded hadron level measurements of the (a) tranverse thrust, $\tau_\perp$, and (b) minor component of the transverse thrust, $T_{m,\perp}$. The unfolding is performed using the ALPGEN generator with pile-up added.

little, if any, discernible discrepancy between the MC predictions and the data.

7.3.2 Dependence on kinematic and topological phase space

The measurement of the distribution of event shapes allows for a detailed comparison of a large phase space of kinematics and topology in multi-jet events. It is also informative to evaluate the explicit dependence of these shapes on the kinematic properties of each event in order to isolate particular corners of phase space as opposed simply to tails of the spectrum. This section seeks to highlight these correlations at the detector-level in order to assess the extent to which such trends are reproduced by the combination of MC generator and detector simulation. Furthermore, because the unfolding factors are generally very close to unity (see Section 7.2.3) the detector-level measurement is likely to represent the physics being probed quite accurately.

The first set of correlations performed is using the three-jet resolution, y_{23}. The variation of $\ln y_{23}$ as a function of the event sphericity is shown in Figure 7.18. The dependence on S^{pheri} demonstrates that very non-spherical events indeed exhibit a

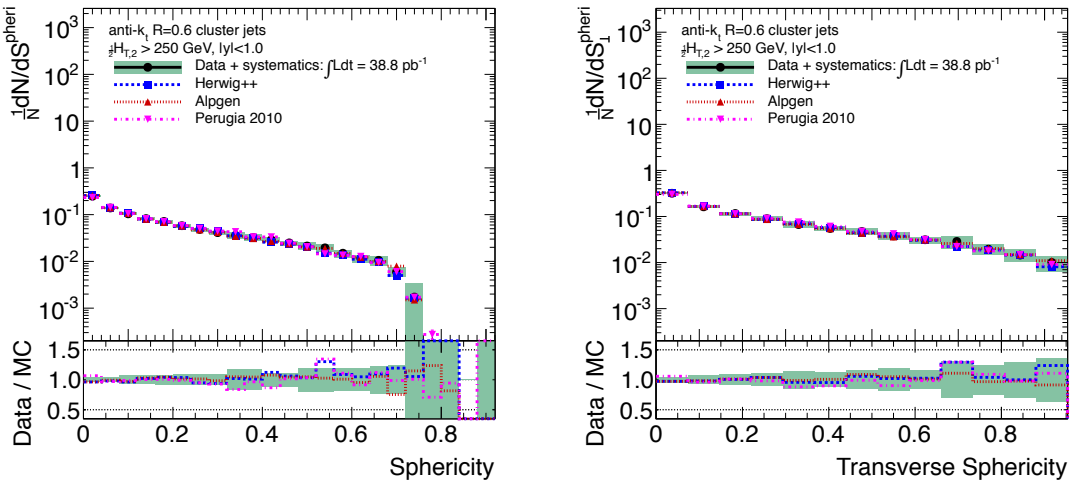

(a) S^{pheri} (b) $S_{\perp}^{pheri}$

Figure 7.17: Unfolded hadron level measurements of the (a) sphericity, S^{pheri}, and (b) transverse sphericity, $S_{\perp}^{pheri}$. The unfolding is performed using the ALPGEN generator with pile-up added.

strongly suppressed third jet momentum, or small $\ln y_{23}$. Interestingly, as S^{pheri} is increased a plateau in $\ln y_{23}$ is reached over a large range of S^{pheri}. This observation indicates that the increase of the sphericity of the event is, on average, maintaining a relatively constant fraction of the event momentum in the third jet and primarily introducing additional jets into the event. In order for the sphericity to reach large values, the transverse momentum of the third jet must be a large fraction of the two leading jets.

Another method of characterizing the kinematic dependence of event shapes is through the leading jet transverse momentum, $p_{T,1}$. Figure 7.19 uses this correlation to map the dependence of the thrust and the three-jet resolution as the kinematic reach of the event approaches 1 TeV. In all three event shapes, a general trend is observed in which the maximum is achieved around $p_{T,1} \approx 300 - 400$ GeV. That is to say, the multi-jet limit is most well reflected in this range of leading jet p_{T}, whereas the higher energy regime is dominated by more pure $2 \to 2$ processes for which NLO corrections leading to the multi-jet final state play a smaller role. The

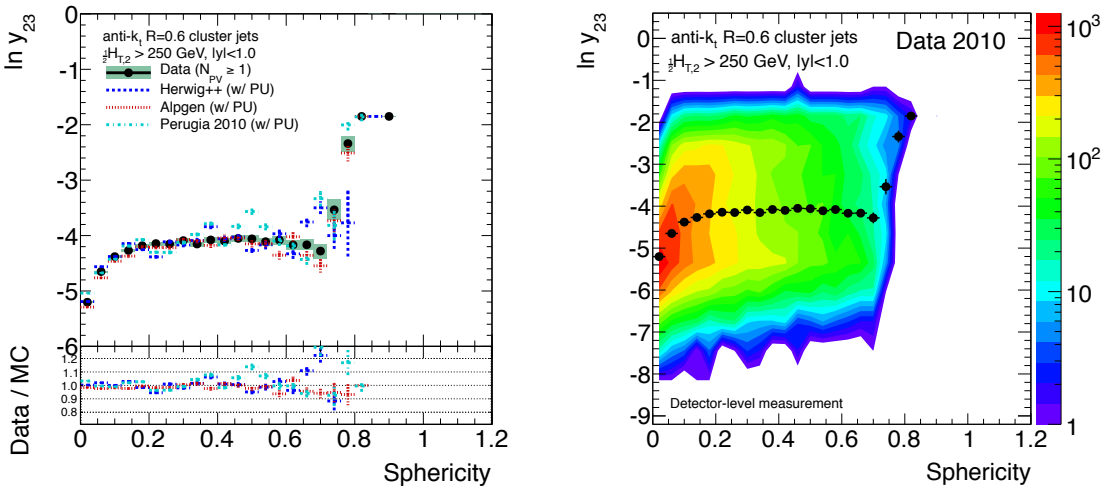

(a) $\ln y_{23}$ vs. S^{pheri}

(b) $\ln y_{23}$ vs. S^{pheri} (data only)

Figure 7.18: Detector-level measurement of the correlation of the $\ln y_{23}$ with sphericity. (a) Comparisons are made between the mean $\ln y_{23}$ ($\langle \ln y_{23} \rangle$) measured in data and the three MC generators Herwig++, Alpgen, and Pythia (Perugia 2010) simulated with pile-up. (b) The full 2D correlation shows that in order for the sphericity to reach large values, the transverse momentum of the third jet must be a large fraction of the two leading jets. Here, the z-axis colors represent the number of jets in that region.

variation as a function of $p_{T,1}$ is the largest for $\ln y_{23}$, which exhibits nearly an order of magnitude change between $p_{T,1} = 300$ GeVand $p_{T,1} = 800$ GeV. Nonetheless, the agreement between the MC prediction at the detector-level and the observed event shape dependence on $p_{T,1}$ is best for $\ln y_{23}$ for all generators. In contrast, both $\tau_\perp$ and $T_{m,\perp}$ show significant differences. ALPGEN and PYTHIA consistently predict higher mean transverse thrust than HERWIG++ predicts and higher than is supported by the measurements. The agreement among all three MC generators and the data improves beyond $p_{T,1} > 500$ GeV, but the statistical significance is not as great.

In order to verify that these measurements and the small discrepancies observed are not the result of a mismeasurement of the thrust axis, Figure 7.20 displays the Angular correlation between the thrust vector $\hat{n}_\perp$ and the leading jet ϕ_{j1} and sub-leading jet ϕ_{j2}. In both cases, $\hat{n}_\perp$ is overwhelmingly peaked in the direction of the leading jet or the sub-leading jet and is well reproduced by the MC and detector simulation.

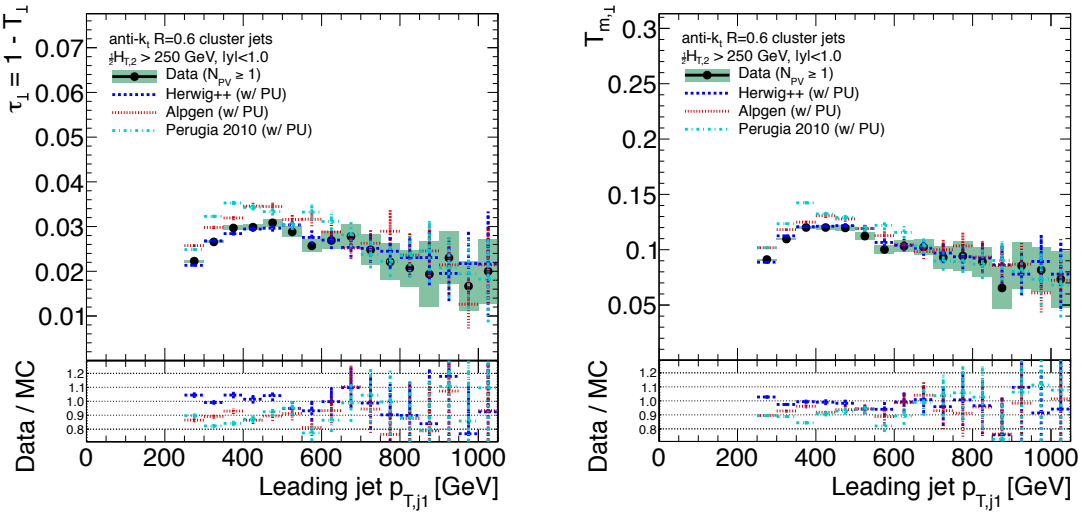

(a) $\tau_\perp$ vs. $p_{T,1}$

(b) $T_{m,\perp}$ vs. $p_{T,1}$

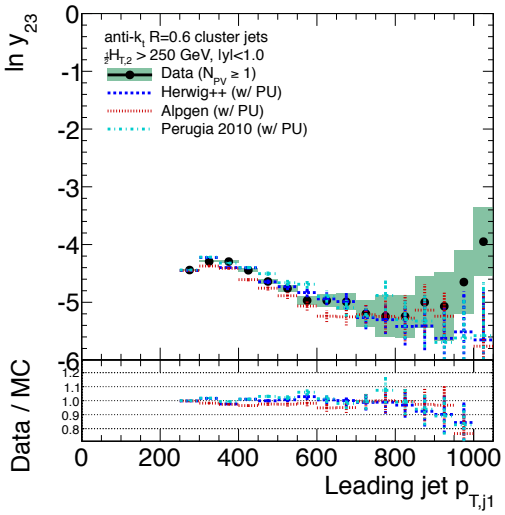

(c) lny_{23} vs. $p_{T,1}$

Figure 7.19: Correlation of (a) $\tau_\perp$ and (b) $T_{m,\perp}$ and (c) y_{23} with $p_{T,1}$. Comparisons are made between the MC generators HERWIG++, ALPGEN and PYTHIA (Perugia 2010) simulated with pile-up.

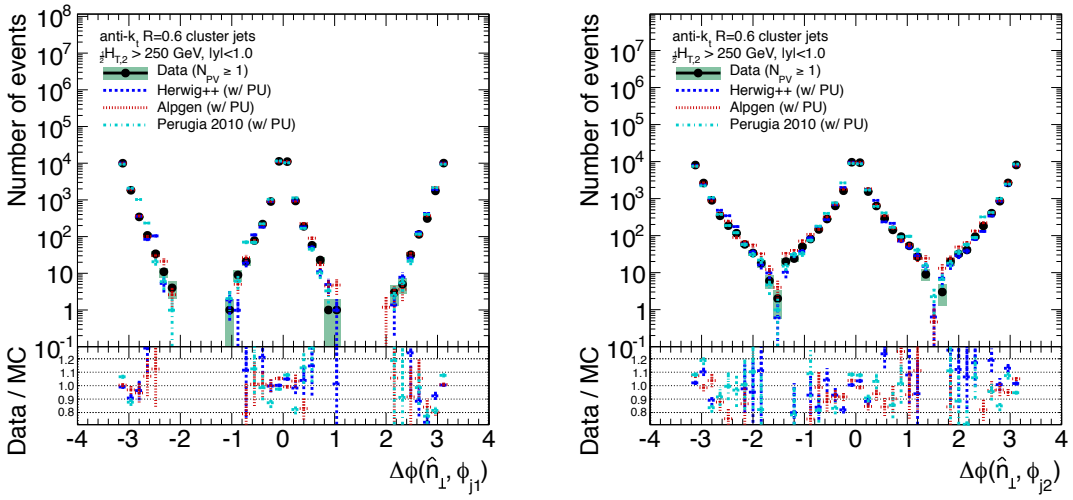

(a) (b)

Figure 7.20: Angular correlation between (a) the leading jet and (b) sub-leading jet and the thrust vector. Comparisons are made between the MC generators Herwig++, Alpgen and Pythia (Perugia 2010) simulated with pile-up.

Chapter 8

Jet substructure

The studies of event shapes presented in Chapter 7 illustrate a degree of understanding of the hadronic final state that allows for detailed measurements in regions of phase space not previously accessible to either hadron or e^+e^- colliders. We now focus on understanding the internal structure of jets using the tools developed in the last few years for both mapping the process of parton showering in a jet and for distinguishing the signatures of new boosted massive particles in the hadronic final state. Many of the issues related to pile-up and jet energy scale will reappear here, and again the tools developed for understanding, assessing, and mitigating the most pernicious of those effects will be employed.

Two "fat" jet algorithms are used, along with the filtering jet grooming technique that was developed in part in ATLAS and introduced in Section 2.3. Jet mass, subjet definitions, and measures of the color flow within a jet are all compared between detector-level simulations and measurements in the data. Procedures are established for assessing systematic effects due to detector effects and the busy hadronic final state within ATLAS. A first measurement of the jet mass scale uncertainty is made, and consequences for searches based on jet mass are discussed. New jet substructure observables are compared for the first time to data at the LHC. Finally, a sample of candidate boosted top quark events collected in the 2010 data is analyzed in detail for the jet substructure properties of hadronic "top-jets" in the final state.

The Monte Carlo (MC) samples used to compare to the data are the same those

described in Chapter 2 and used for the event shapes analysis in Chapter 7. ALPGEN 2.13 with exact matrix element calculations up to $n \leq 6$ partons is interfaced to HERWIG 6.510 to provide the parton shower and hadronization model and with JIMMY 4.31 for the underlying event model. PYTHIA 6.423 with the Perugia 2010 tune and HERWIG++ 2.4 are also used as standalone event generators with their own underlying event and hadronization models.

8.1 "Fat jet" reconstruction and calibration

Jet substructure techniques are studied primarily using two jet algorithms, the standard anti-k_t algorithm and the angular ordered Cambridge-Aachen algorithm, or C/A, both introduced in Chapter 2. However, instead of the more traditional distance parameters of $R \sim 0.4 - 0.7$, characteristic "fat" jet radii of $R \sim 1.0 - 1.2$ are used. Wide jet radii are favored within boosted object searches in order to enhance the efficiency to capture the decay products of a single boosted object that subsequently decays to hadrons. Even for highly boosted – and thus highly collimated – objects, it is preferable to use a slightly larger value of R and to therefore improve the overall efficiency while using the substructure tools to maintain purity. In addition to these "un-groomed" jets, the filtering procedure described in detail in Section 2.3 is investigated. The procedure is applied to reconstructed C/A, $R = 1.2$ jets yielding a sample of *filtered* C/A jets whose properties have never been studied in experimental data prior to this analysis.

Several technical hurdles must be overcome in order to utilize these jets for physics analysis. First, because it is a non-standard jet algorithm, the procedures to establish a precise jet energy scale described in Section 5.3 were not carried out prior to this analysis. Second, due to the large jet radii considered and the susceptibility of the jet mass to even soft wide angle energy depositions (see Eq. 2.17), care must be taken to assess the impact of multiple pp interactions in the data and MC simulations. Jet cleaning criteria defined in Table 7.1 are applied to anti-k_t $R = 0.6$ jets for this analysis as well, and events containing any such "bad" jets are rejected altogether. The reason for this is that the jet quality selections contain fractional quantities and

are defined and optimized for the smaller radius jets, and even a single bad jet has the potential to skew measurements of the substructure of other nearby jets.

8.1.1 Reconstruction

Inputs to the jet finding and reconstruction are the topological clusters that are described in Section 5.1 in detail. These objects provide a three-dimensional, dynamic representation of energy depositions in the calorimeter with a nearest neighbor noise suppression algorithm [189]. Topoclusters are thus conceptually better suited to the identification of both hard and soft substructure within a jet since they are designed to reflect the hadronic shower as it develops both laterally and longitudinally. However, as the techniques being studied here present a new approach to the hadronic final state in ATLAS, we also consider the canonical geometrical picture using the $\Delta\eta \times \Delta\phi$ tower grid for comparison.

One of the primary considerations for fat jets is the impact of pile-up. The wide area subtended by these jets make them more susceptible to the impacts of the diffuse soft radiation created by additional pp collisions. Figure 8.1 compares the mean number of constituents inside of jets in the data for three different selections in the data: (a) events with only a single reconstructed primary vertex, $N_{\mathrm{PV}} = 1$, (b) jets selected to have $|JVF| > 0.99$ and thus little to no impact from pile-up, and (c) all events, including those with significant pile-up. In all cases, the leading jet is required to have $p_{\mathrm{T}} > 300$ GeV. Jets reconstructed with both topoclusters and towers for each of the three jet algorithms considered for their substructure properties are shown. All jet types exhibit an excess in their mean constituent multiplicity compared to events without pile-up, in particular at low-p_{T} where the fractional impact of pile-up is greatest. By using the JVF discriminant the majority of this discrepancy is removed, thereby reducing a 10% effect due to pile-up to a 1-5% effect. Interestingly, filtered C/A jets are very minimally impacted above $p_{\mathrm{T}} > 100$ GeV, a feature of the filtering procedure which will be demonstrated in a variety of ways. Finally, a plateau in the constituent multiplicity is reached for all jet algorithms and constituent types at approximately $p_{\mathrm{T}} > 300$ GeV, above which the discrepancy between the jet

composition with and without pile-up effects very slightly increases.

The filtering prescription implemented here states that for a filtering radius $R_{b\bar{b}} < 0.3$ (where $R_{b\bar{b}} = \Delta R_{j1,j2}$ when the de-clustering step has completed), the jet is not a suitable candidate for final reconstruction. The resolution of this angular scale for de-clustering can be studied and then compared to the data by using tracking information. To the extent to which the two hardest tracks in a jet represent the two hardest partons, it is possible to use this opening angle, $\Delta R(\mathrm{trk}_1, \mathrm{trk}_2)$, to measure the scale at which the declustering becomes resolution limited. Figure 8.2 shows the difference between $R_{b\bar{b}}$ calculated at particle level using events generated with PYTHIA with that measured at the detector level following the full detector simulation. These studies suggest that as $\Delta R(\mathrm{trk}_1, \mathrm{trk}_2)$ approaches $\Delta R(\mathrm{trk}_1, \mathrm{trk}_2) \approx 0.3$, the ability to resolve the splitting scale observed in the particle-level picture is degraded when using clusters to reconstruct the calorimeter energy. However, towers, whose rigid granularity is already approximately 0.1×0.1 in $\Delta\eta \times \Delta\phi$, exhibit a slightly better performance, with a degradation in $R_{b\bar{b}}$ resolution occurring at approximately the scale of their granularity. To quantify this observation, the fraction of jets with $|\Delta R_{b\bar{b}}(\mathrm{reco}, \mathrm{true})| < 0.175$ is 87% for topocluster jets and 92% for tower jets, an absolute difference of 5%. For the results presented below, all jets are thus required to exhibit a filtering radius $R_{b\bar{b}} > 0.3$.

8.1.2 Calibration

Due to the complex and delicate procedure needed to provide a full calibration for jets that accounts for the myriad effects discussed in Section 5.3, no calibration was available for the fat jets used in substructure analysis here prior to these studies. Consequently, the derivation of both energy, angular and mass correction factors as well as techniques for validating these calibration factors was undertaken.

The standard ATLAS jet calibration described in Section 5.3 utilizes topoclusters at the electromagnetic energy scale with calibration factors applied at the jet level. Such corrections are base on an average response functions derived from Monte Carlo generators passed through the full detector simulation. The resulting jet energy scale

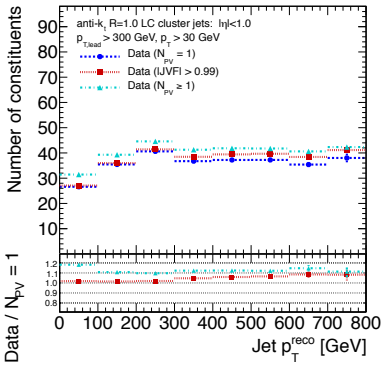

(a) anti-k_t, $R = 1.0$ (clusters)

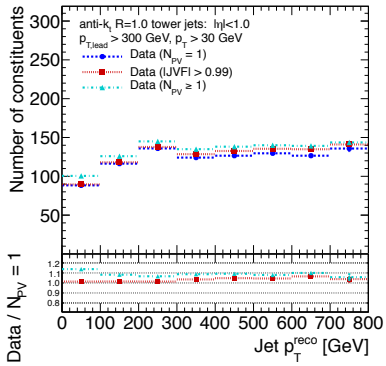

(b) anti-k_t, $R = 1.0$ (towers)

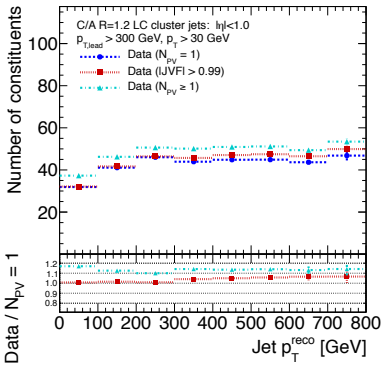

(c) C/A, $R = 1.2$ (clusters)

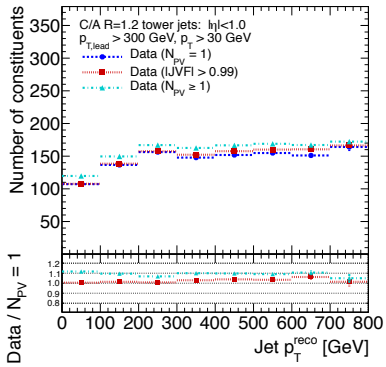

(d) C/A, $R = 1.2$ (towers)

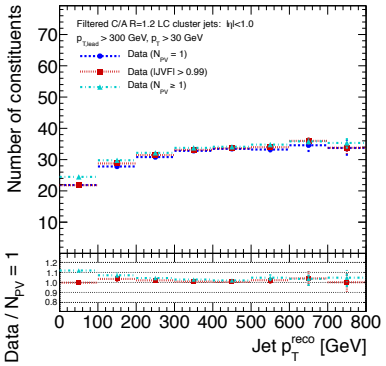

(e) C/A, $R = 1.2$ (filtered) (clusters)

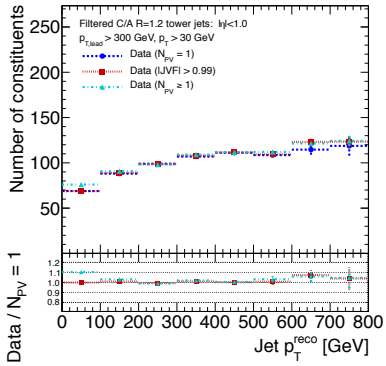

(f) C/A, $R = 1.2$ (filtered) (towers)

Figure 8.1: Mean number of constituents as a function of the jet p_{T} for each jet algorithm and input constituent type compared between events with only a single reconstructed primary vertex, $N_{\mathrm{PV}} = 1$ (dashed blue with circles), jets selected to have $|JVF| > 0.99$ and thus little to no impact from pile-up (dotted red with squares) and all events, including significant pile-up (dot-dashed cyan with triangles).

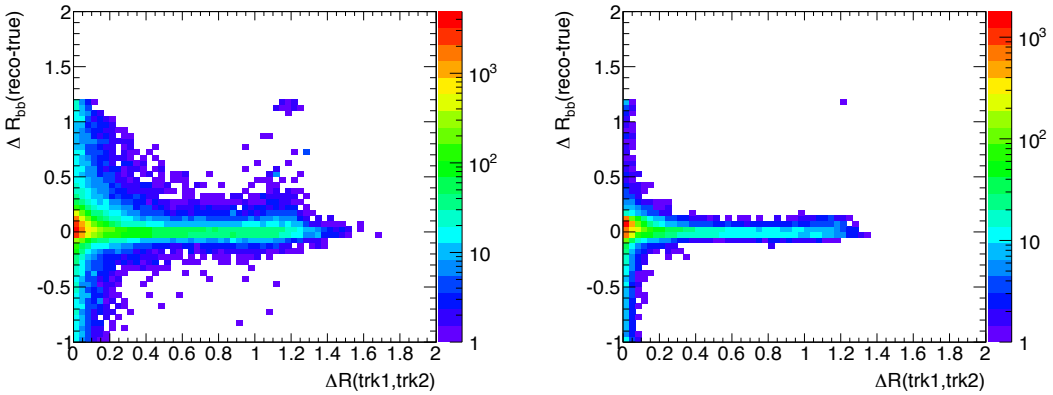

(a) C/A, $R = 1.2$ (clusters) (b) C/A, $R = 1.2$ (towers)

Figure 8.2: $R_{b\bar{b}}$ resolution measured between jets at the particle level ("true") and (a) cluster jets or (b) tower jets a function of the opening angle of the two highest transverse momentum tracks in the jet, $\Delta R(\mathrm{trk}_1, \mathrm{trk}_2)$. The fraction of jets contained within $|\Delta R_{b\bar{b}}(\mathrm{reco}, \mathrm{true})| < 0.175$ is 87% for topocluster jets and 92% for tower jets, an absolute difference of 5%.

(JES) correction [194, 198] is applied directly to the electromagnetic energy scale (EM scale) and is referred to as the "EM+JES" calibration scheme. This scheme accounts for energy loss in dead material, calorimeter non-compensation, out-of-cone energy loss, and detector inter-calibration on average. Extensive *in-situ* tests of this procedure verify that it is both working as expected and that the resulting uncertainty on the energy scale for standard jet algorithms (anti-k_t $R = 0.4, 0.6$) is at the level of 3-4%.

Precise reconstruction of the internal structure of jets benefits from using topoclusters that are first classified as either electromagnetic or hadronic energy depositions, in contrast to the established procedure. This classification is based on their energy, depth within the calorimeter, and shape properties. A Monte Carlo based calibration dependent only on cluster pseudo-rapidity, energy, and hadronic classification is applied to each cluster prior to jet finding in a procedure known as "local cluster weighting" (LCW). This so-called local calibration (LC) represents the best available approximation of individual particle reconstruction in the calorimeter and has been shown to improve the energy resolution of jets [186].

A dedicated jet-level calibration is derived for each jet type and tested with both in-situ techniques and direct Monte Carlo comparisons among generators, detector geometries, hadronic shower models and material descriptions in the detector simulation. Jet-level corrections that are applied in addition to the LCW calibration of the constituents are determined using a similar procedure to the default ATLAS calibration described above. In this case, the initial scale at which the jet-level calibration is applied is the locally calibrated topocluster scale instead of the EM scale. Since the dominant sources of mis-calibration (dead material and calorimeter non-compensation) are primarily accounted for by the LCW approach, the jet-level energy correction is typically $< 15\%$ in the energy range of interest, compared to 20-30% for EM+JES (see Figures 5.4 and 5.5). This is clear in Figure 8.3 which shows the response both before and after energy calibration for jets with a minimum $p_{\mathrm{T}} > 15$ GeV. For the jet energy range of interest for boosted objects – approximately $p_{\mathrm{T}} > 300$ GeV – the response prior to the final jet-level corrections is already $< 5\%$.

In order to study the jet mass precisely this procedure is extended with a determination of the response for the individual jet invariant mass. A jet-level mass correction is derived, again as a function of jet energy and pseudo-rapidity. The mass correction is slightly larger than the energy scale correction and is typically of order 15-20% for jets above 300 GeV. For all results involving these fat jets presented here, the jet mass scale correction is applied along with the corrections to jet energy and pseudo-rapidity. The correction factors as a function of η_{det} and jet energy can be seen in Figure 8.4.

In addition to these MC-derived jet-level calibration factors, the systematic uncertainty in the calibration itself can be tested by varying several parameters of the MC generators and detector simulation. As mentioned above, the largest contributors to the overall jet energy scale uncertainty are the dead material description and the hadronic shower modeling used in the full detector simulation. The former has a 2-3% uncertainty at the 300 GeV lead jet threshold used in the analysis, which steadily shrinks to less than 1% above 1 TeV. The hadronic shower model can be varied between two extremes given by the QGSP and FTFP_BERT models (see Appendix E.2 for descriptions of these models).

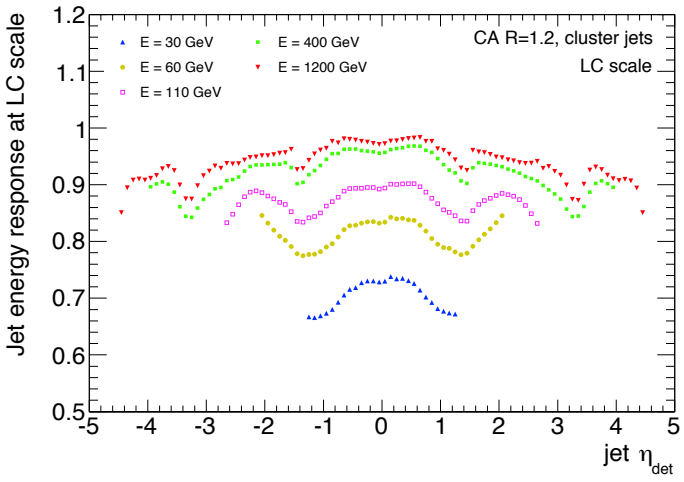

(a) C/A, $R = 1.2$ energy response before calibration

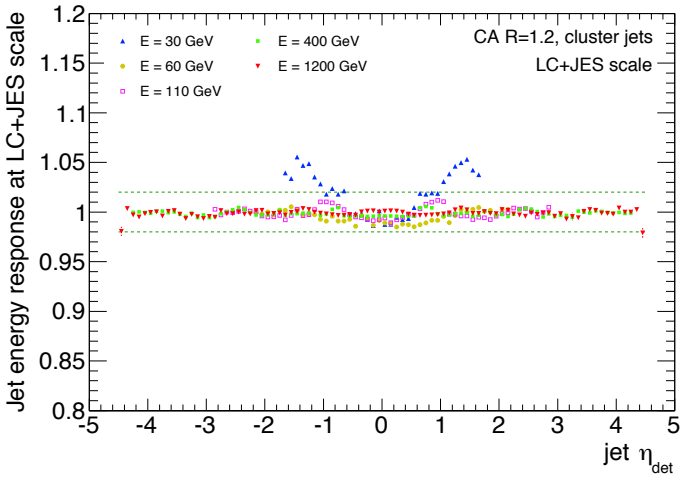

(b) C/A, $R = 1.2$ energy response after calibration

Figure 8.3: The MC based jet energy calibration procedure for C/A, $R = 1.2$ jets to the LC+JES scale, showing the jet response before and after calibration as a function of η_{det} for jets with a minimum $p_{\text{T}} > 15$ GeV. (a) The uncorrected jet energy response showing the effect of the local cluster (LC) weighting factors. (b) The closure after the correction factors are applied as a function of E and η_{det}. The closure uncertainty is approximately 1.5% above 60 GeV.

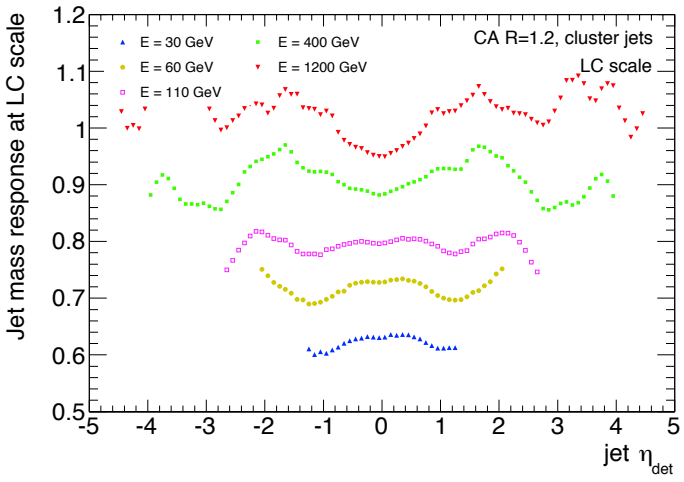

(a) C/A, $R = 1.2$ mass response before calibration

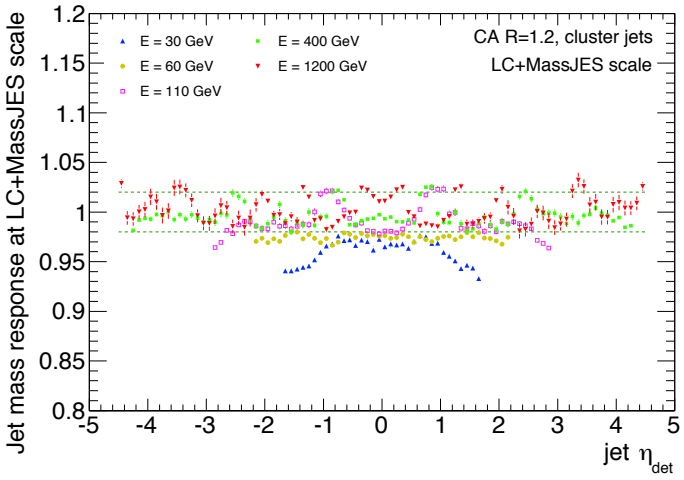

(b) C/A, $R = 1.2$ mass response before calibration

Figure 8.4: The MC based jet mass calibration procedure for C/A, $R = 1.2$ jets to the LC+JES scale, showing the jet response before and after calibration as a function of η_{det}. (a) The uncorrected jet mass response showing wide variation prior to calibration. (b) The closure after the correction factors are applied as a function of E and η_{det}. The closure uncertainty is approximately 3% above 60 GeV.

8.1.3 Trigger

Events used in this analysis undergo a very similar trigger selection as that described in Chapter 7. Because the focus here is on jets that are reconstructed with a large radius parameter compared to $R = 0.6$ it is important to reassess the trigger efficiency. The lowest unprescaled L1 jet trigger, `L1_J95`, is again used and a bootstrapping technique is applied with respect to the lower threshold trigger, `L1_J30`. Figure 8.5 demonstrates the turn-on curve for each of the dat jet algorithms used, as well as the C/A, $R = 1.2$ (filtered) algorithm, in addition to the standard anti-k_t, $R = 0.6$ jet algorithm for comparison. For each curve, the impact of using MC simulated with pile-up added at the level of an additional $\langle N_{pp} \rangle = 3.2$ added per event is also evaluated and has a very small impact. In each case, the 99.5% efficiency is reached at or below the leading jet selection of $p_{\mathrm{T}} > 300$ GeV used for the substructure analysis. It is interesting to note that the C/A, $R = 1.2$ (filtered) algorithm exhibits a slightly degraded turn-on compared to the unfiltered fat jets.

8.1.4 Jet energy scale and mass scale uncertainty

The largest uncertainty for nearly all physics analyses conducted in 2010 that involve any aspect of the hadronic final state is the jet energy scale uncertainty. In order to provide a complete set of tools and understanding within the contexts of boosted object analyses and jet substructure, systematic uncertainty association with the calibrations derived above must be provided.

The four categories of systematic uncertainty considered in this study are the uncertainties on the jet energy scale (JES), jet mass scale (JMS), jet energy resolution (JER) and jet mass resolution (JMR). The JES and JMS uncertainties are determined from in-situ comparisons using track-jets. A track-jet is constructed from charged particles that originate only from the selected pp collision of interest. This not only reduces or eliminates the impact of additional pp collisions, but also provides a reference with which to compare the calorimeter jet measurement in both the data and the MC. The JER and JMR are primarily assessed via the MC simulation, with a discussion of the extrapolation of the JER derived *in-situ* for standard jets to fat jets.

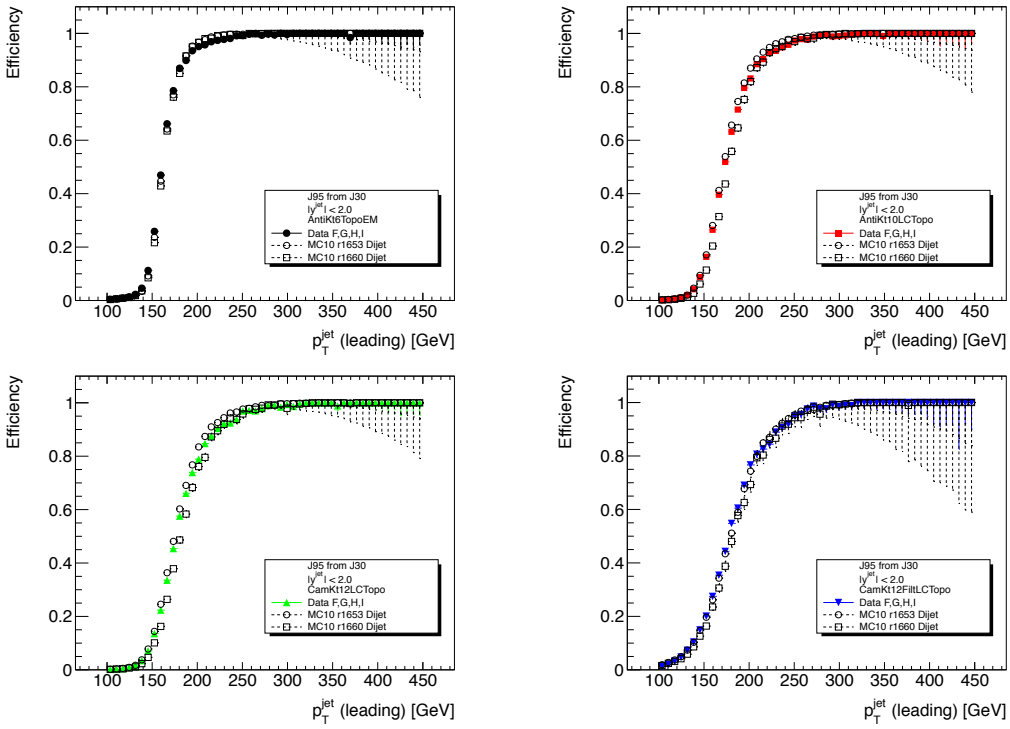

Figure 8.5: L1_J95 trigger efficiency (per event) for each of the four jet algorithms considered in this note using the bootstrap method with respect to the L1_J30 trigger. The results are compared to PYTHIA QCD dijet Monte Carlo samples without pile-up and with in-time pile-up overlaid with the signal interaction.

One important aspect of these assessments is the ability to both validate the JES and JMS established by the Monte Carlo tests and also to directly estimate the pile-up energy contribution to jets. The latter will be discussed in detail in the following section, whereas the strategy to utilize the tracking system to asses the overall scale are discussed here.

The inner detector and calorimeter have largely uncorrelated systematic effects. Therefore, comparison of variables such as jet mass and energy between the two sub-detectors allows for separation of physics and detector effects. The goal of these studies is to establish that the modeling of detector and experimental effects is well under control so that one may distinguish them from physics effects and thus account for detector uncertainties via unfolding techniques with confidence. A similar

approach is used to establish the extent to which the calibration of standard jets ($R = 0.4, 0.6$) agrees between the data and the MC simulation and in the derivation of *in-situ* jet energy scale corrections. Detailed discussions may be found in Ref. [204]. The approach followed here is in addition to the standard ATLAS jet energy scale uncertainty [194] which combines information from test-beam data, LHC collision data and MC simulations to obtain the uncertainty while using track-jets as a cross-check. Heavy use is made of the track-jet comparisons and correlations as a primary mode of determining consistency and uncertainty in the calibration. A similar approach [205] has been applied to the standard ATLAS jet collections and been found to agree with the standard jet energy scale uncertainty determination. The main advantages of the track-based approach for this study are simplicity and easy extensibility to jet mass scale uncertainty.

The standard procedure jet energy scale uncertainty approach is effectively used as an additional cross-check. Monte Carlo-based tests are used to determine the dependence of the detector response on a number of different variables. These include samples with modified detector geometry, different low-energy physics models and different high-energy physics models. These tests provide an independent validation of the results from the track-jet comparison. A more complete description of the samples and systematic effects evaluated using MC only can be found in Appendix E.

In-situ tests of the JER [206] indicate that the jet resolution predicted by the Monte Carlo for standard jet algorithms is in good agreement with that observed in the data. The JER uncertainty and the JMR uncertainty for fat jets are taken from the Monte Carlo tests only, primarily because the JMR is difficult to measure *in-situ* with the current dataset. It is also worth noting that the resolution is a comparatively small uncertainty in the final results. When more data are collected, it will be necessary to perform in-situ tests of the mass resolution by using heavy objects. For example, hadronic W decays in a very clean top quark sample would likely provide enough statistics to measure the width of the hadronic W peak and therefore directly test the calibration and resolution uncertainties.

The method used to determine the uncertainty from *in-situ* tests utilizes the ratio of the calorimeter $p_{\mathrm{T}}^{\mathrm{jet}}$ (m^{jet}) to the track-jet transverse momentum, $p_T^{\mathrm{track-jet}}$

($m^{\text{track-jet}}$). The ratios may be defined explicitly as

$$r^{p_T}_{\text{track-jet}} = \frac{p_{\text{T}}^{\text{jet}}}{p_T^{\text{track-jet}}}, \qquad r^{m}_{\text{track-jet}} = \frac{m^{\text{jet}}}{m^{\text{track-jet}}}, \tag{8.1}$$

where the matching between calorimeter and track-jets is performed using a matching radius of $\Delta R < 0.3$. These ratios are expected to be well described by Monte Carlo and detector simulation in the case that physics effects are well modeled. That is to say, even if a discrepancy were to exist in the distribution of any one of these quantities, by comparing the ratios in both data and MC this discrepancy can be determined to be either a detector related discrepancy or a difference in the physics present in the simulation. The *double ratios* constructed in order to evaluate this agreement, $R^{p_T}_{r\text{track-jet}}$ and $R^{m}_{r\text{track-jet}}$, are defined as

$$R^{p_T}_{r\text{track-jet}} = \frac{r^{p_T,\text{data}}_{\text{track-jet}}}{r^{p_T,\text{MC}}_{\text{track-jet}}}, \qquad R^{m}_{r\text{track-jet}} = \frac{r^{m,\text{data}}_{\text{track-jet}}}{r^{m,\text{MC}}_{\text{track-jet}}}. \tag{8.2}$$

The dependence of $R^{p_T}_{r\text{track-jet}}$ and $R^{m}_{r\text{track-jet}}$ on $p_{\text{T}}^{\text{jet}}$ and m^{jet} provides a handle on the deviation between data and Monte Carlo, and thus allows for an estimation on the calibration uncertainty which can then be combined with the physics uncertainties from the MC tests.

The distribution of $r^{p_T,\text{data}}_{\text{track-jet}}$ and $r^{p_T,\text{MC}}_{\text{track-jet}}$, as well as the double ratio, $R^{p_T}_{r\text{track-jet}}$, are shown for the three jet algorithms used for substructure measurements as well as the standard anti-k_t, $R = 0.6$ jets in Figure 8.6. The slight up-turn in the ratio at high p_{T} in the data are due to statistical fluctuations that result from the very strict $N_{\text{PV}} = 1$ selection applied, as can be seen by comparing to the same results without this requirement in Appendix E, Figure E.6. The cusp observed near $p_{\text{T}} = 300$ GeV is due to the leading jet requirement. The Alpgen +Herwig/Jimmy sample exhibits a systematically higher $r^{p_T,\text{MC}}_{\text{track-jet}}$ than the data suggests – and thus lower $R^{p_T}_{r\text{track-jet}}$– by between 2-4%. The Pythia (Perugia 2010) and Herwig++ samples show $R^{p_T}_{r\text{track-jet}}$ consistently closer unity. These observations are fully consistent with the inclusive jet shapes measurements presented in Ref. [200] in which Alpgen +Herwig/Jimmy

Jet Algorithm	JES	JMS	JER	JMR
anti-k_t $R = 1.0$	5%	7%	20%	20%
C/A $R = 1.2$	5%	6%	20%	20%
C/A filtered $R = 1.2$	6%	7%	20%	20%

Table 8.1: Uncertainty on the p_T and mass scale of the three jet algorithms used in this study for events with only a single primary vertex.

exhibited significantly narrower jets than seen in the data. Narrow jets, with a large concentration of their energy near the core of the jet, have a higher jet energy scale response than more diffuse jets, which is the observation made in Figure 8.6.

The observed jet mass double ratio, $R^m_{r\text{track}-\text{jet}}$, is also shown as a function of $p_{\text{T}}^{\text{jet}}$ in Figure 8.7. The same four jet algorithms and distance parameters are presented and again ALPGEN +HERWIG/JIMMY is observed to have a slightly higher mean response than that of the PYTHIA (Perugia 2010) or HERWIG++ samples.

Finally, the same measured distributions and double ratios binned in terms of mass instead of p_{T} can be found in Appendix E, Figures E.7 and E.8. Similar qualitative features are observed, such as the higher response in the ALPGEN sample. The shape of the $r^m_{\text{track}-\text{jet}}$ distribution is slightly different for the C/A jets compared to the anti-k_t jets for both filtered and unfiltered C/A, but the MC and the data very closely track each other.

In Table 8.1 the p_T and jet mass scale uncertainties for jets with $p_{\text{T}} > 300$ GeV are given with a requirement of only one primary vertex per event. These uncertainties are determined directly from the variation in the double-ratios $R^m_{r\text{track}-\text{jet}}$ and $R^{p_T}_{r\text{track}-\text{jet}}$, from the different Monte Carlo generators. In the case of $R^m_{r\text{track}-\text{jet}}$, the variation is measured with respect to both m^{jet} and $p_{\text{T}}^{\text{jet}}$ and so the uncertainty listed in Table 8.1 represents the maximum deviation from unity in the two cases. Note that statistical uncertainties tend to dominate the precision.

8.1.5 The effect of pile-up

Substructure observables are expected to be especially sensitive to pile-up [143, 144]. Furthermore, pile-up is relevant even at the relatively low levels observed in the 2010

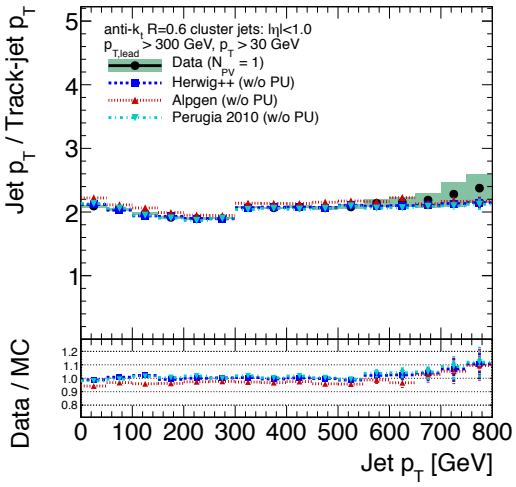

(a) anti-k_t, $R = 0.6$

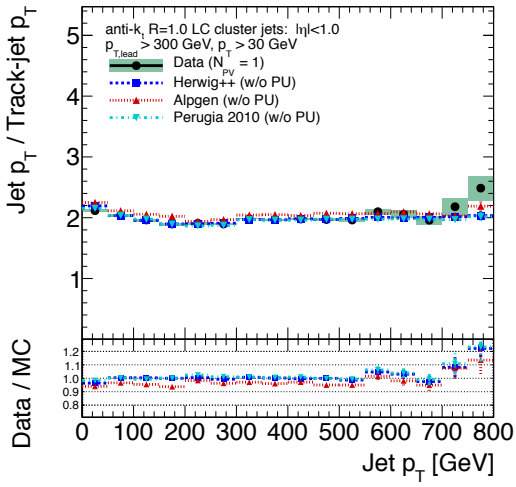

(b) anti-k_t, $R = 1.0$

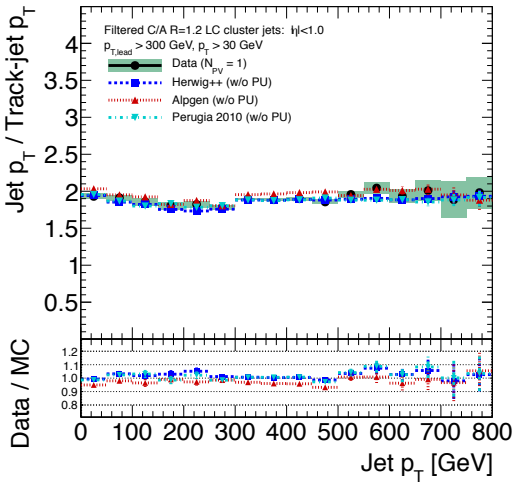

(c) C/A, $R = 1.2$

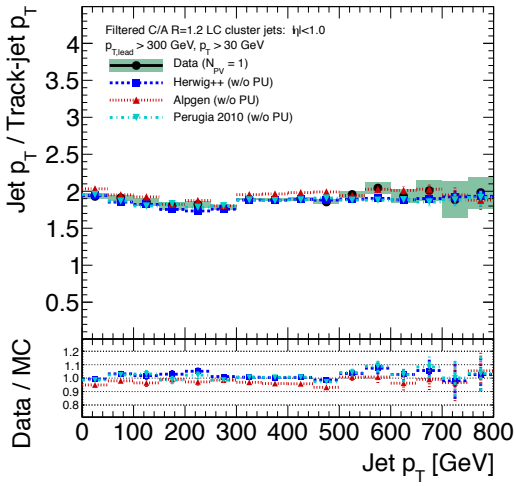

(d) C/A, $R = 1.2$ (filtered)

Figure 8.6: Distributions of $r^{p_T,\mathrm{data}}_{\mathrm{track-jet}}$ and $r^{p_T,\mathrm{MC}}_{\mathrm{track-jet}}$, as well as the double ratio, $R^{p_T}_{r\mathrm{track-jet}}$, versus $p_{\mathrm{T}}^{\mathrm{jet}}$ for jets reconstructed with the three algorithms considered as well as the standard anti-k_t, $R = 0.6$ jet algorithm. Events in the data are required to have $N_{\mathrm{PV}} = 1$ and the MC samples are simulated without pile-up overlaid.

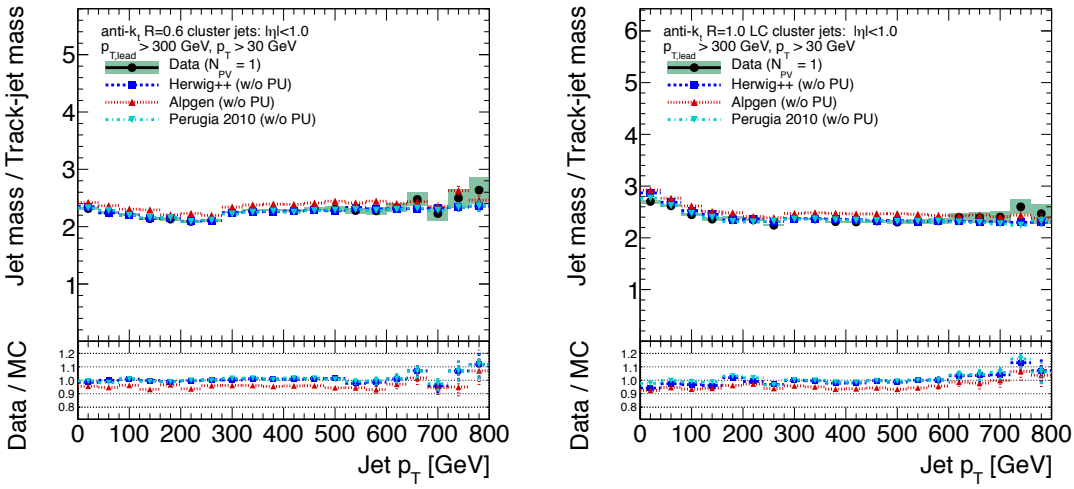

(a) anti-k_t, $R = 0.6$

(b) anti-k_t, $R = 1.0$

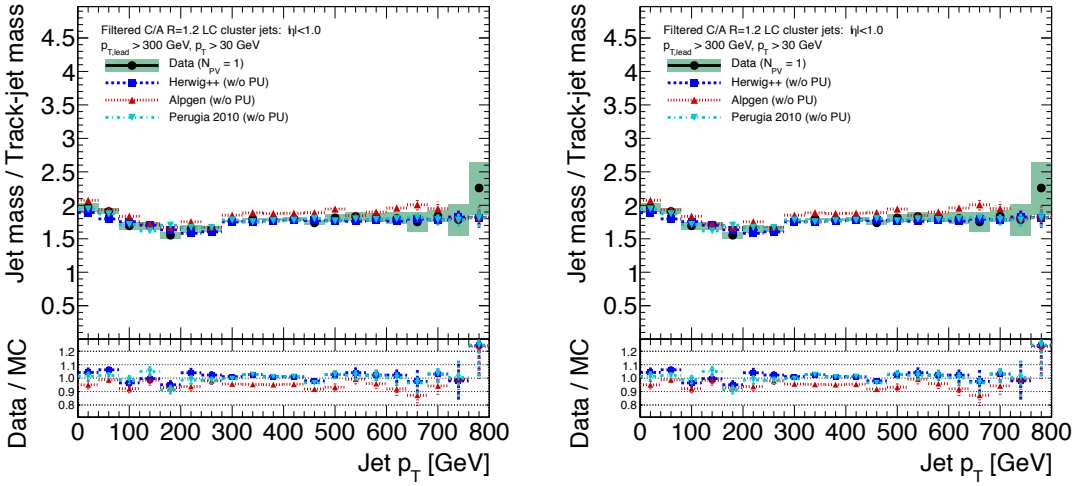

(c) C/A, $R = 1.2$

(d) C/A, $R = 1.2$ (filtered)

Figure 8.7: Distributions of $r^{m,\mathrm{data}}_{\mathrm{track-jet}}$ and $r^{m,\mathrm{MC}}_{\mathrm{track-jet}}$, as well as the double ratio, $R^{m}_{r\mathrm{track-jet}}$, versus $p^{\mathrm{jet}}_{\mathrm{T}}$ for jets reconstructed with the three algorithms considered as well as the standard anti-k_t, $R = 0.6$ jet algorithm. Events in the data are required to have $N_{\mathrm{PV}} = 1$ and the MC samples are simulated without pile-up overlaid.

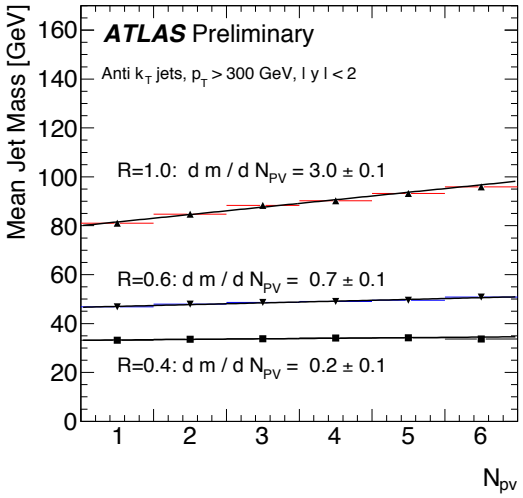

Figure 8.8: The mean mass for jets with $p_{\mathrm{T}} > 300$ GeV as a function of the number of primary vertices identified in the event. Comparisons show the effect for anti-k_t jets with different resolution parameters

data for jets with a large area such as those used here. For example, Ref. [207] predicts that the contribution from pile-up and underlying event to the invariant mass Δm_{jet} scales as R^4, and the results presented in Figure 8.8 suggest that for light quark jets the scaling is approximately R^3.

Methods to reduce the scale uncertainty due to multiple proton-proton interactions are, however, found to be quite effective. We compare the impact of both a strict $N_{\mathrm{PV}} = 1$ selection as done in the previous section with a JVF selection designed to be more efficient than a blind cut while obtaining similar performance. In almost all cases, the JVF selection is just as effective at mitigating the effects due to pile-up as a strict selection on N_{PV}, while it has the added benefit of being significantly more efficient: the $JVF > 0.99$ selection is 58% efficient for anti-k_t, $R = 1.0$ and 49% efficient for C/A, $R = 1.2$ jets with $p_{\mathrm{T}}^{\mathrm{jet}} > 300$ GeV, nearly a factor of 3.5 higher efficiency than the strict N_{PV} selection for a similar resulting purity. Grooming techniques [143, 144] also reduce the effective area of large jets, thus indirectly reducing the impact of pile-up and underlying event.

Figure 8.9 exemplifies the potential for adverse pile-up effects as well as the power

of grooming techniques such as jet filtering. The mass increase of calorimeter jets is measured as a function of the number of additional interactions in the event. The slope is approximately $\Delta m^{\text{jet}} = (5.3 \pm 0.2)$ GeV per vertex for C/A, $R = 1.2$ jet with $300 < p_{\text{T}} < 325$ GeV prior to the filtering procedure. Similar results are obtained for anti-k_t, $R = 1.0$, although the mass increase is measured to be $\Delta m^{\text{jet}} = (3.2 \pm 0.2)$ GeV per vertex due to the smaller radius and the anti-k_t algorithm. After applying the filtering procedure to C/A, $R = 1.2$ jets, the mass increase per additional pp interaction is consistent with zero to within 400 MeV per reconstructed vertex, which is a significant improvement. These features of the filtering procedure are also well-described by the MC and detector simulation. The full set of results and fits for all jet algorithms, input constituent types and 6 $p_{\text{T}}^{\text{jet}}$ ranges are shown in Appendix E, Figure E.10. Jets constructed from towers are also observed to be slightly less impacted than those constructed from topoclusters.

For jets that do not utilize filtering, other tools are necessary to reduce the impact of pile-up on both the jet energy and mass scales. While the average jet energy scale corrections discussed in Chapter 6 were used heavily in the event shapes analysis presented in Chapter 7, the use of locally calibrated topoclusters for the substructure analysis does not permit the use of the offset pile-up correction. Instead, JVF is heavily relied upon to indicate and discriminate between jets that have large (small JVF) and small (large JVF) contributions from additional pp interactions. While the full distributions of JVF for each jet type are given in Appendix E, Figure 8.10 demonstrates the impact that using this discriminant can have in events with pile-up by reducing the systematic shift incurred on the mass distribution as the level of in-time pile-up increases. By using the measured increase in the calorimeter jet mass to track-jet mass ratio, $r^{m}_{\text{track-jet}}$, we specifically isolate the fractional increase in the uncertainty determined in Section 8.1.4. This allows analyses that do not use the JVF discriminant to extrapolate the JMS uncertainties estimated using track-jets to higher pile-up scenarios. More importantly, though, the use of the JVF selection significantly reduces the overall uncertainty in the jet energy and mass scales. This reduction can be seen by comparing the results in Table 8.2.

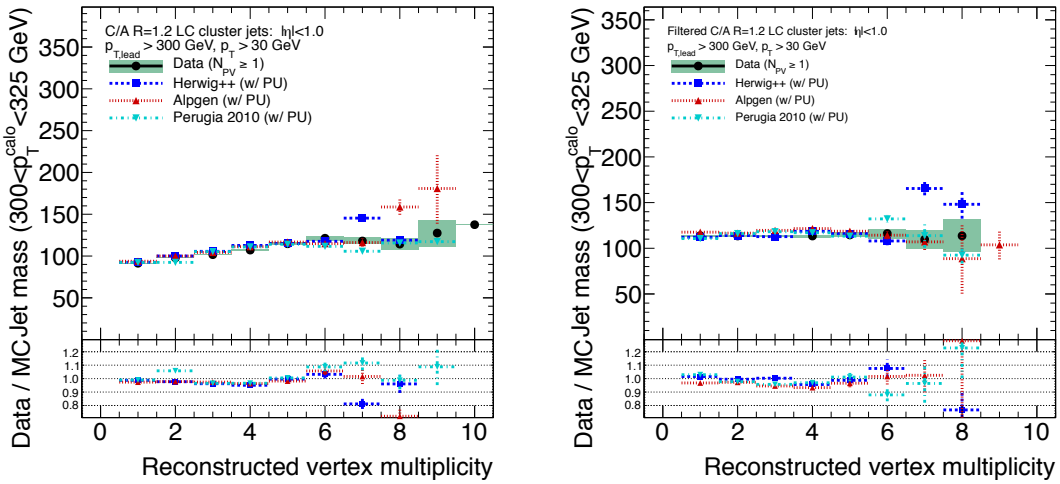

(a) C/A, $R = 1.2$ (b) C/A, $R = 1.2$ (filtered)

Figure 8.9: Measured increase in the jet mass for calorimeter jets as a function of the number of additional interactions in the event. The difference between (left) C/A, $R = 1.2$ jets and (right) C/A, $R = 1.2$ (filtered) jets demonstrates the positive impact that filtering has on the sensitivity to pile-up. The slope is approximately $\Delta m^{\text{jet}} = (5.3 \pm 0.25)$ GeV per vertex for C/A, $R = 1.2$ jet with $300 < p_{\text{T}} < 325$ GeV prior to the filtering procedure and $\Delta m^{\text{jet}} = (-0.04 \pm 0.41)$ GeV per vertex after filtering.

	Inclusive sample		JVF selection	
Jet Algorithm	JES	JMS	JES	JMS
anti-k_t, $R = 1.0$	6%	9%	3%	4%
C/A, $R = 1.2$	8%	10%	3%	4%
C/A, $R = 1.2$ (filtered)	6%	8%	4%	4%

Table 8.2: Uncertainty on the p_T and mass scale of the three jet algorithms used in this study. Numbers are given for the case where no attempt is made to reject pile-up and where a JVF selection is used. This is in contrast to Table 8.1 where only events with a single primary vertex are considered.

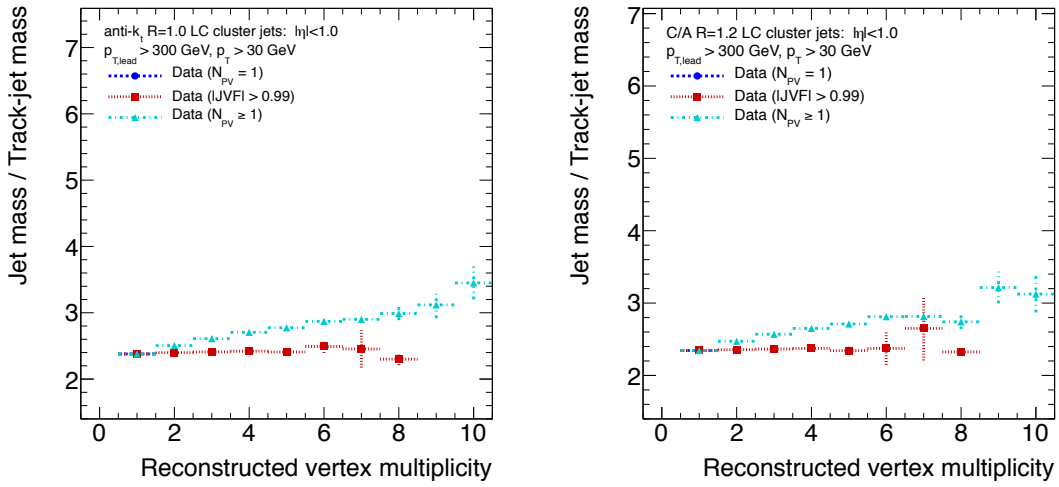

(a) anti-k_t, $R = 1.0$ (b) C/A, $R = 1.2$

Figure 8.10: Comparison of the measured increase in the calorimeter jet mass to track-jet mass ratio, $r^m_{\text{track-jet}}$, as a function of the number of additional interactions in the event with and without a $|JVF| > 0.99$ selection applied. Events required to have only a single reconstructed vertex for comparison.

8.2 Commissioning jet substructure tools in data

Of the many approaches to examining the internal structure of highly boosted jets – some of which are described in detail in Chapter 2 – very few, if any, of the tools developed in recent years have been tested in *pp* collision data at the LHC. Jet mass and subjet multiplicity are perhaps the most studied observables overall [141, 208, 209, 210, 211, 212, 213, 214], yet the filtering procedure, color flow, and the use of boosted top quarks as a testing ground are all relatively new [215] and thus require experimental validation of their efficacy and ease of use in real data.

Each of these subjects will be presented at the detector level and compared across several MC generators, kinematic regimes, and event selections. We first discuss the subjet multiplicity within QCD jets. The presence, number, and topological structure of subjets is a natural lead-in to jet substructure in general and will allow for comparisons of jet mass and color flow observables to be discussed in the context of and compared against subjet structure. Several observables, such as dipolarity and N-subjettiness, are directly related to the subjet topology of fat jets. The jet mass is then presented and the various experimental issues surrounding the measurement of jet mass are discussed in detail, along with comparisons to the subjet structure of massive jets. The performance of the filtering algorithm itself is then presented in more detail than discussed in previous sections, with a focus on the experimental modeling of the algorithm in the detector simulation. New color flow and jet substructure observables dipolarity and N-subjettiness are then shown for the first time in the ATLAS data. These quantities were specifically designed for their use in discriminating signal from background, and so the final discussion presents an analysis of the first boosted top quark candidates observed in the data and how these new variables perform *in-situ*.

8.2.1 Subjet multiplicity and scales

As a step towards the use of subjets in more complex observables, the subjet multiplicity and energy scales are shown in Figure 8.11 and 8.12. Subjets are defined using the $k_\perp$algorithm with a distance parameter of $R = 0.3$ applied to the constituents of the parent jet, regardless of the jet algorithm used to find the parent jet. Subjets

are then required to have at least 5% of the parent jet p_{T} which for the leading jet implies $p_{T,\mathrm{sj}} > 15$ GeV. The general approach used here is to make maximal use of the tracking system to isolate effects which are inherent to the substructure of the jet and not only manifestations of the calorimeter granularity or noise.

Figure 8.11 focuses on the subjet multiplicity in C/A, $R = 1.2$ jets with comparisons to MC simulated with additional pile-up interactions, but re-weighted to agree with the distribution observed in the data, as described in Section 7.1. Figure 8.11(a) shows the full distribution of the subjet multiplicity in both data and the multiple MC samples considered. Although the core of the distribution agrees well, an increase in the data at high multiplicities over what is expected from simulations is observed at the detector level. This is particularly true for events generated with Alpgen +Herwig/Jimmy. The agreement is slightly better for Herwig++ and Pythia (Perugia 2010), which will be a common theme in these results. Figure 8.11(b) shows how the mean subjet multiplicity varies as a function of the parent jet p_{T}, wherein a plateau similar to that demonstrated in the constituent multiplicity in Figure 8.1 is observed. A very good agreement is observed between the data and the MC for the average multiplicity, with deviations beyond 3% primarily occurring for the subleading jets ($p_{\mathrm{T}} < 300$ GeV) and at very high p_{T} where the statistical power of the comparison is degraded. Finally, Figure 8.11(c) demonstrates the power of the strategy to combine information from the tracker and calorimeter by comparing the subjet multiplicity in both the calorimeter and in jets formed from charged particle tracks only. As in previous comparisons of this sort, since the physics of the events in question is captured by both the tracking and calorimeter systems, differences in the subjet multiplicities measured by each are due to either inherent differences in the use of charged particles versus calorimeter clusters (which include neutral particles) or in the modeling of detector effects. A similar deviation in the calorimeter subjet multiplicity at high track-jet multiplicity is again observed for Alpgen, as indicated by Figure 8.11(a), whereas Pythia (Perugia 2010) shows an excellent agreement across the full range.

With the description of the subjet multiplicity in hand, Figure 8.12 turns to the energy scale of these objects. Because techniques for probing the internal structure

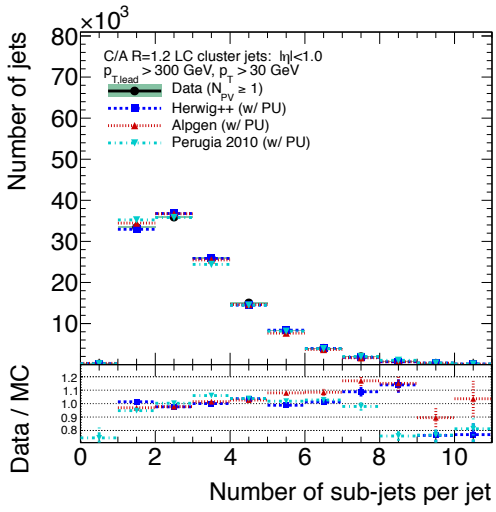

(a) Subjet multiplicity

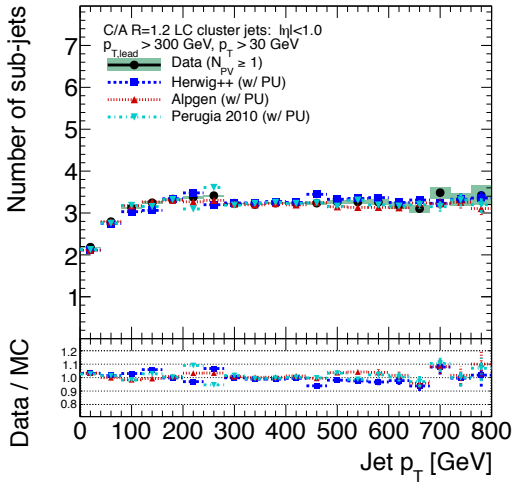

(b) Subjet multiplicity vs. p_{T}

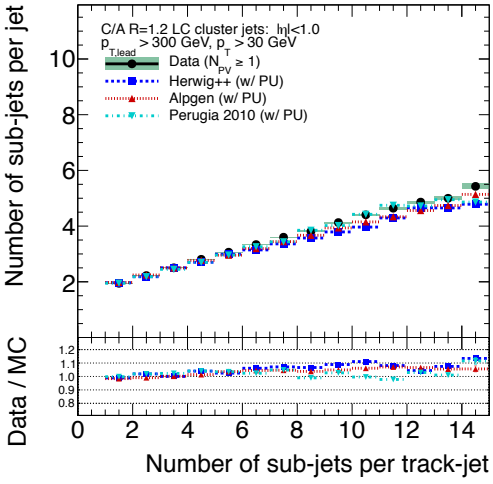

(c) Correlation to track-jets

Figure 8.11: Subjet observables at the detector-level for the C/A, $R = 1.2$ algorithm. Subjets are defined using the $k_{\perp}$algorithm with $R = 0.3$ and are required to have at least 5% of the parent jet p_{T}.

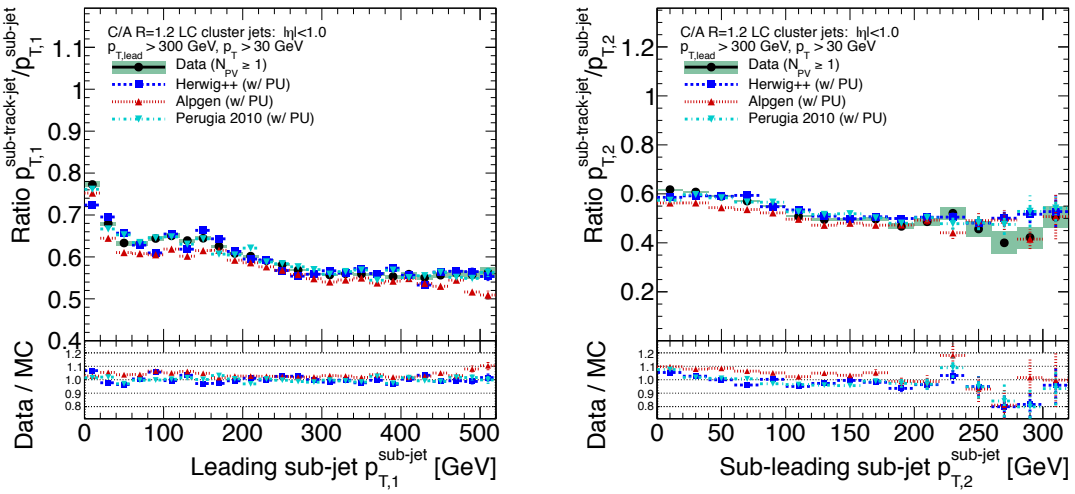

(a) Leading subjet, $j1$ (b) Sub-leading subjet, $j2$

Figure 8.12: Ratio of sub-track-jet p_{T} to calorimeter subjet p_{T} using C/A, $R = 1.2$ parent jets in order to assess the JES systematics associoated with subjets. Both (a) leading, $j1$, and (b) sub-leading, $j2$, subjets exhibit very similar energy response in the data and the MC as compared to subjets within track-jets.

of the jet necessitate a dense environment, it is by no means certain that the energy scale of objects defined *within* this environment will be well described. In general, the hardest objects found within a jet will be the subject of further analysis in the context of heavy particle searches as these are most likely to represent the decay products of the parent particles. Figures 8.12(a) and Figures 8.12(b) separate the ratio of calorimeter subjet momentum to track-jet subjet momentum into the leading, $j1$, and sub-leading, $j2$, subjets within the parent calorimeter jet and track-jet. This ratio is very well predicted among all MC generator samples for $j1$, whereas for $j2$ ALPGEN again overestimates the calorimeter response similarly to the observation made in the parent jet performance in Figure 8.6.

The final aspect of the subjet kinematics and topology to assess prior to analyzing the observables directly related to the grooming techniques such as pruning [121] and filtering is the angular distribution of subjets within fat jets. Both the jet mass and the topology of the parton shower are quite sensitive to this description. Figure 8.13 shows the angular separation between the leading, $j1$, and sub-leading, $j2$, subjets

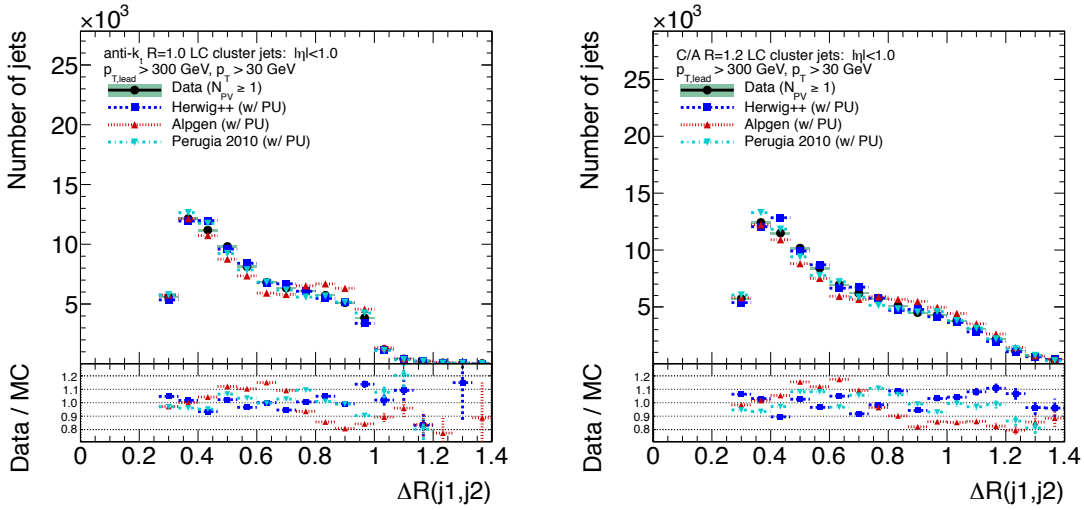

(a) anti-k_t, $R = 1.0$ (b) C/A, $R = 1.2$

Figure 8.13: Angular separation, ΔR, between the leading, $j1$, and sub-leading, $j2$, subjets within both (a) anti-k_t, $R = 1.0$ and (b) C/A, $R = 1.2$ parent jets. The MC samples include pile-up overlaid to match the data.

within both anti-k_t and C/A parent jets. While HERWIG++ and PYTHIA (Perugia 2010) both show relatively good agreement across a large angular range – within 5% for the majority of that range – ALPGEN shows large discrepancies, rising to nearly 20% for large separations. The MC samples used for these measurements, as before, include pile-up overlaid to match the data. However, as demonstrated in Appendix E in Figure E.16, this result seems to actually be exacerbated when removing the slight smearing affect of pile-up, indicating that it is indeed a mis-modeling within the ALPGEN +HERWIG/JIMMY MC. It should be noted, though, that this suggests that the smearing due to pile-up is being modeled well by the MC and detector simulation which includes pile-up. It would be interesting to select a subsample of jets

Two quantities that depend crucially on the subjet energy scales and topologies are z and the related quantity x_J. The quantity z measures a relative energy sharing of subjets within a jet whereas x_J expands on z by using angular information of the

subjets with respect to the parent jet axis. These observables are defined as

$$z = \frac{\min(p_{T,j1}, p_{T,j2})}{p_{T,J}}, \tag{8.3}$$

$$x_J = z(1-z)\Delta R^2_{j1,j2}, \tag{8.4}$$

where $\Delta R_{j1,j2}$ represents the angle between the two leading subjets within the parent jet. Figure 8.14 demonstrates a reasonably good agreement between the data and the parton shower MC programs for z (Herwig++ and Pythia), while again Alpgen +Herwig/Pythia exhibits large deviations. The extent to which x_J approximates the phase space for the parton shower is also evaluated since this is expected to describe the mass of QCD jets, as discussed at length in Ref. [121]. Herwig++ and Pythia (Perugia 2010) consistently describe the distribution of each of these quantities more accurately than Alpgen, although this observation is more clear in the case of z. This fact is directly related again to the overall response of jets in the Alpgen sample, such that the ratio of track-jet momentum to calorimeter jet momentum is lower than in the data. Interestingly, when binning in terms of m^2/p_T^2 of the parent jet, the discrepancy is largely removed since this captures the energy scale differences.

The discussion of the correlation with x_J naturally leads to the discussion of the individual invariant jet mass itself.

8.2.2 Jet mass

The jet mass is a ubiquitous jet shape observable for discriminating new heavy objects decaying into a single jet from the QCD background. However, large fluctuations in that background as well as the enormous cross-section to produce high p_{T} – and thus high mass – jets in dijet and multijet QCD final states make use of this single observable quite difficult. Pile-up and noise present a pernicious but manageable problem for the measurements of the jet transverse momentum, as discussed at length in Chapter 6. The jet mass, though, can be significantly more affected as a single low-energy deposition at a wide angle from the jet can contribute to the mass much

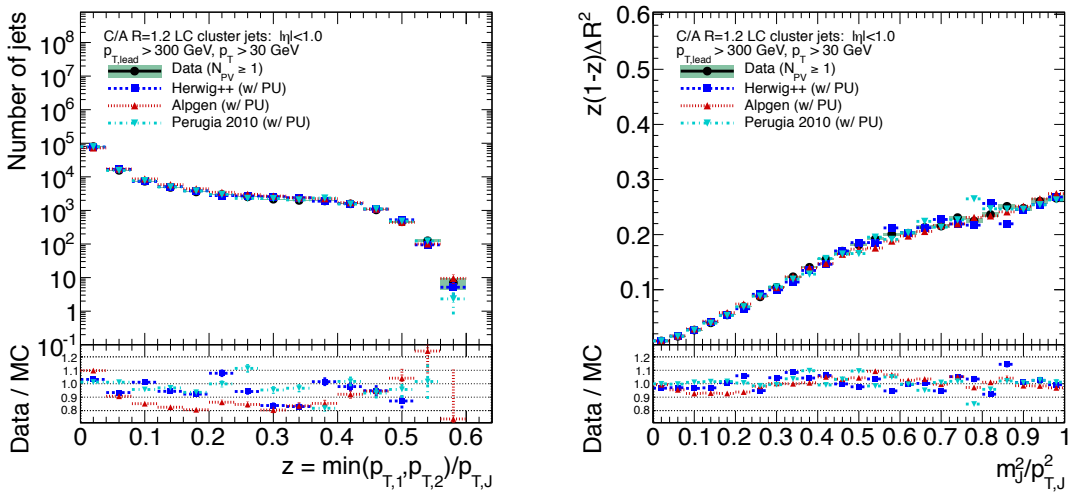

(a) C/A, $R = 1.2$, z (b) C/A, $R = 1.2$, x_J correlation

Figure 8.14: (a) Subjet relative transverse momentum sharing characterized by $z = \min(p_{T,j1}, p_{T,j2})/p_{T,J}$ and (b) the correlation of $x_J = z(1-z)\Delta R^2_{j1,j2}$ with the relative mass, m^2/p_T^2 of the parent jet.

more so than to the total momentum.

Detector level jet mass distributions for jets selected to have 300 GeV $< p_{\mathrm{T}} <$ 500 GeV are shown in Figure 8.15 for anti-k_t, $R = 0.6$, anti-k_t, $R = 1.0$, C/A, $R = 1.2$, and C/A, $R = 1.2$ (filtered) . Events in the data are selected to have only a single primary vertex in order to isolate the modeling of the mass itself. These jets are compared to the three MC generators for events simulated without the addition of pile-up interactions. In each case, the MC distributions are independently normalized to the data in order to compare the shape of the distribution itself. Some general features among these distributions are worth noting:

- Jets constructed from the angular ordered C/A algorithm show somewhat better agreement with the data compared to the anti-k_t, $R = 1.0$ jets for each of the MC samples. This is particularly true for the high mass range near the top quark mass (140 GeV $< m^{\mathrm{jet}} <$ 200 GeV).

- Herwig++ predicts a harder jet mass spectrum than Alpgen and Pythia (Perugia 2010), which improves agreement with the data for anti-k_t, $R = 1.0$,

but slightly overshoots the data for C/A, $R = 1.2$.

- After filtering the C/A, $R = 1.2$ jets, the Sudakov peak near $m^{\text{jet}} = 75$ GeV is not as well described by ALPGEN.

Within the context of a search for a new heavy particle that is expected to decay into a single hadronic jet, the sort of systematic shift or jet mass broadening induced by pile-up must be minimized. The two methods at our disposal in the present study are the rejection of events with multiple interactions and JVF. As pointed out in Section 8.1.5, the former has such a low efficiency as to render it relatively useless at high luminosity. JVF on the other hand allows one to tune the selection based on the tolerance of the analysis to cope with detector level corrections (for example, in an unfolding process).

To assess the impact of pile-up on the jet mass and on the use of the JVF discriminant to reduce its effect, Figure 8.16 compares the C/A, $R = 1.2$ jet mass distribution and the evolution of the jet mass with $p_{\text{T}}^{\text{jet}}$ with and without pile-up rejection. Figures for all jet algorithms and input constituent types can be found in Appendix E, Figures E.19-E.21. Pile-up has a larger impact (15-20%) at very low jet momentum, but still a measurable effect at several hundred GeV due to the potential for even relatively soft wide angle contributions to affect a change in the jet mass. This tends to shift the jet mass to higher values, as well as to slightly broaden the width of the distribution, both of which are reduced by the use of JVF to effectively filter-out jets that are contaminated.

With the above considerations in mind, the leading and sub-leading jet masses can be evaluated at the detector level with the majority of the effect of pile-up removed. Figures 8.17-8.19 show the jet mass distribution compared to MC simulated with only hard-scattering events (i.e. no additional pile-up interactions are overlaid onto the di-jet MC). Jets in the data are selected to have $|JVF| > 0.99$ in order to more precisely compare the detector level descriptions, while maintaining a higher efficiency than is possible with a simple N_{PV} selection criterion. Clearly the description is quite good, although far from perfect. By using the JVF selection, the distributions match very closely the result with no additional pile-up.

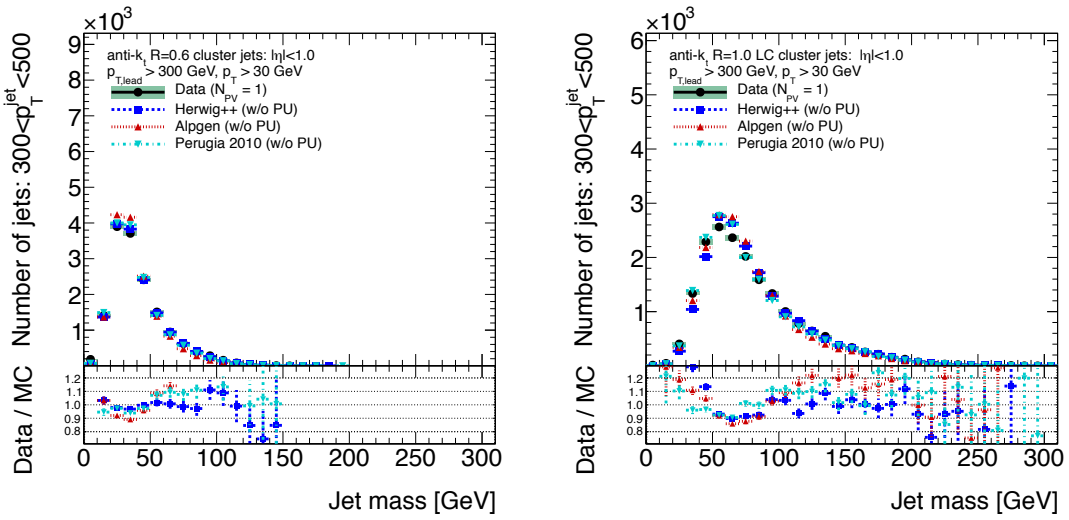

(a) anti-k_t, $R = 0.6$

(b) anti-k_t, $R = 1.0$

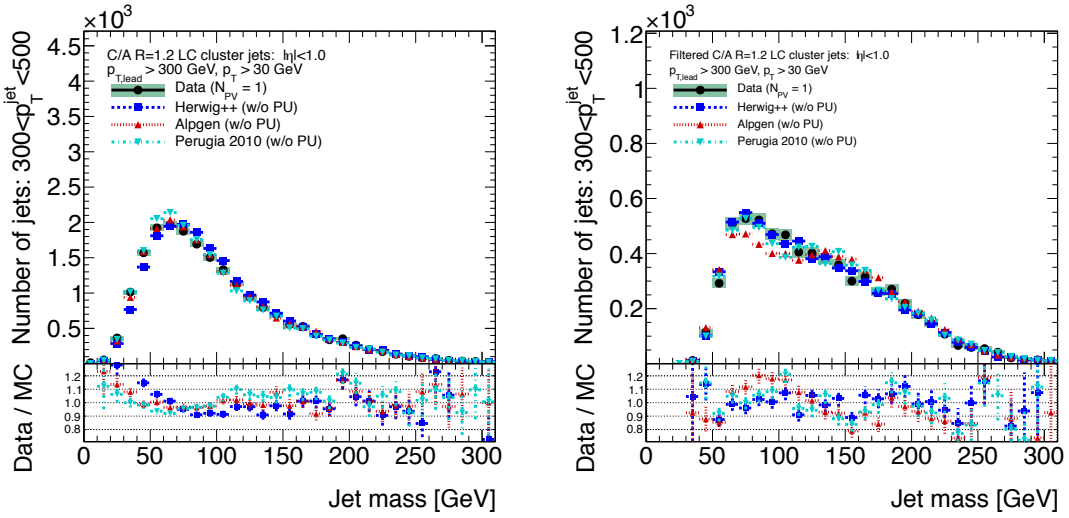

(c) C/A, $R = 1.2$

(d) C/A, $R = 1.2$ (filtered)

Figure 8.15: Jet mass at the detector level for each jet algorithm and MC generator considered in the substructure analysis, as well as the anti-k_t, $R = 0.6$ algorithm for reference. Jets are selected to have 300 GeV $< p_{\mathrm{T}} <$ 500 GeV. The MC is simulated without additional pile-up interactions and the data are selected to only have a single reconstructed primary vertex ($N_{\mathrm{PV}} = 1$).

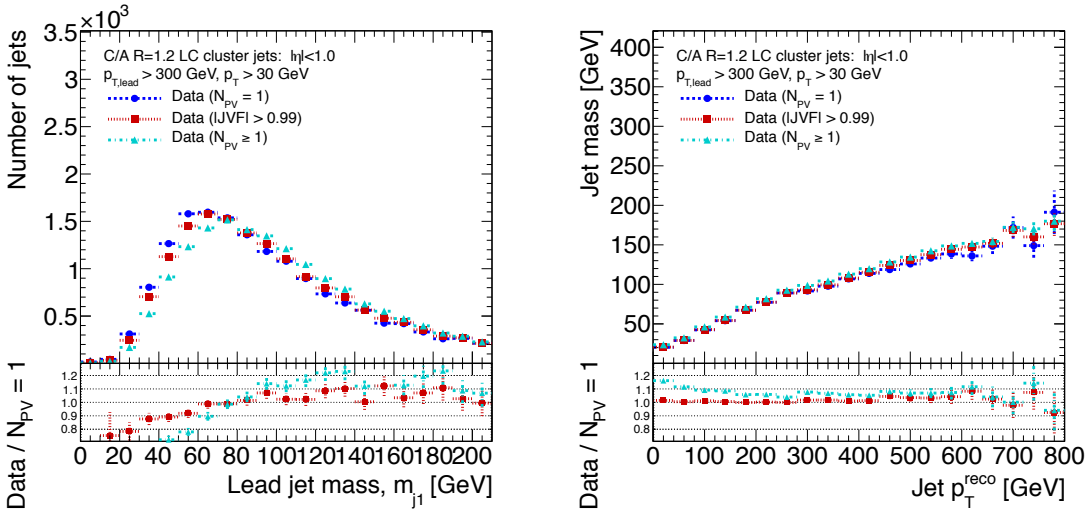

(a) C/A, $R = 1.2$ leading jet mass

(b) Mean C/A, $R = 1.2$ mass vs $p_{\mathrm{T}}^{\mathrm{jet}}$

Figure 8.16: (a) Leading jet mass distribution in data for events with a single reconstructed primary vertex, $N_{\mathrm{PV}} = 1$ (dashed blue with circles), jets selected to have $|JVF| > 0.99$ and thus little to no impact from pile-up (dotted red with squares) and all events, including significant pile-up (dot-dashed cyan with triangles). (b) Inclusive average jet mass as a function of the jet $p_{\mathrm{T}}^{\mathrm{jet}}$ for the same jet selections.

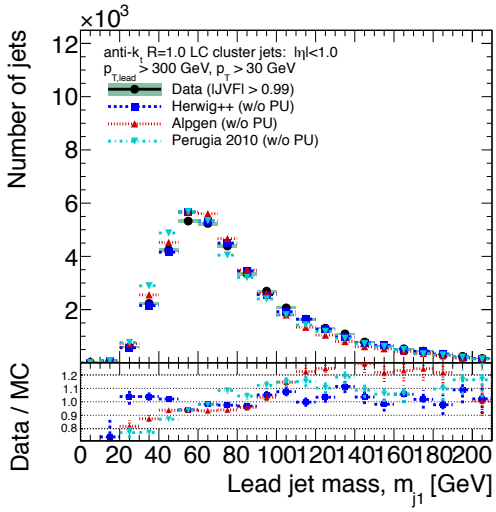

(a) anti-k_t, $R = 1.0$ leading jet mass

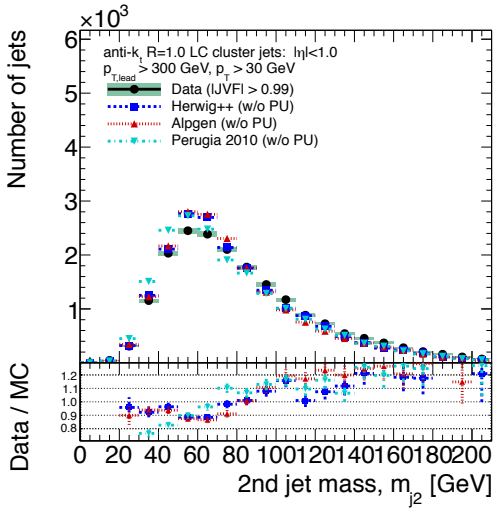

(b) anti-k_t, $R = 1.0$ sub-leading jet mass

Figure 8.17: (a) Leading jet mass distribution. (b) Sub-leading jet mass distribution. Jets in data are selected to have $|JVF| > 0.99$ and thus little to no impact from pile-up, whereas the MC contains only hard-scattering events.

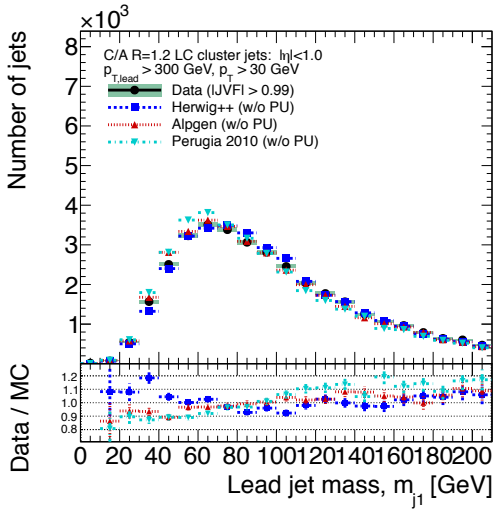

(a) C/A, $R = 1.2$ leading jet mass

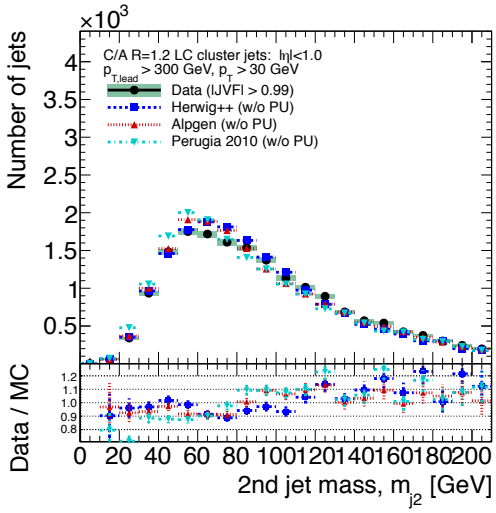

(b) C/A, $R = 1.2$ sub-leading jet mass

Figure 8.18: (a) Leading jet mass distribution. (b) Sub-leading jet mass distribution. Jets in data are selected to have $|JVF| > 0.99$ and thus little to no impact from pile-up, whereas the MC contains only hard-scattering events.

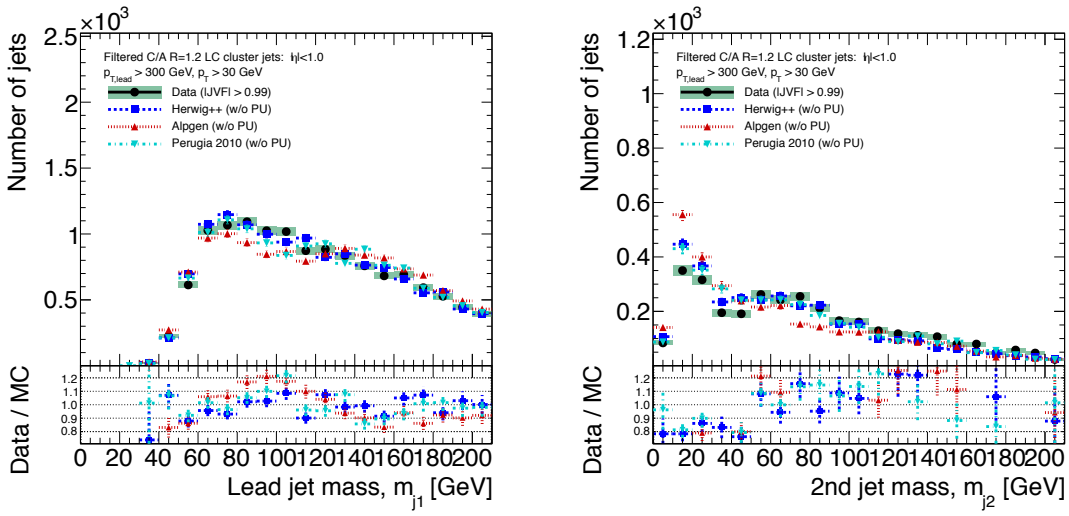

(a) C/A, $R = 1.2$ (filtered) leading jet mass (b) C/A, $R = 1.2$ (filtered) sub-leading jet mass

Figure 8.19: (a) Leading jet mass distribution. (b) Sub-leading jet mass distribution. Jets in data are selected to have $|JVF| > 0.99$ and thus little to no impact from pile-up, whereas the MC contains only hard-scattering events.

Of particular interest, though, is the sub-leading filtered jet mass distribution. Figure 8.19(b) clearly shows that the filtering procedure sculpts the sub-leading jet mass in a way that is quite different from the leading jet, although the description in the MC is also clearly worse in this case. The reason for this is primarily the low p_{T} end of the spectrum for the sub-leading jet.

The excellent convergence of the filtered jet masses begs the question of the actual performance of the filtering procedure, a topic to which we turn now.

8.2.3 Jet filtering

The BDRS filtering procedure has several benefits. The algorithm is specifically designed to isolate the hardest definable components within a jet and to remove soft, wide angle emissions that are not likely to be part of the hard part of the parton shower or of the decay of a heavy particle within the jet. Originally developed within the revived $H \to b\bar{b}$ search [216], the so-called BDRS algorithm (after the authors of

Ref. [216]) has come to be one of the primary methods of jet grooming, along with pruning and trimming [143, 144]. Among the benefits of filtering is the resilience of the resulting jet mass to diffuse radiation contributions from pile-up, demonstrated quite clearly by Figure 8.9. Filtering is also known to improve the mass resolution of boosted objects quite significantly (see Figure 2.11 and Ref. [134]). In this section, we focus on the experimental determination of the algorithm's performance and its stability under LHC conditions in 2010.

Since the primary aim of filtering is to remove soft components of the jet in order to enhance those properties which more accurately define the substructure it is natural to assess the fraction of the jet that is removed. The ratio of jet kinematics for C/A, $R = 1.2$ jets before and after the filtering procedure provides both a snapshot of how the jet filtering procedure affects jets and a means to compare data to MC and detector simulation. Figure 8.20 shows both the jet p_{T} and mass ratios, where the ratios are computed as the kinematic quantity measured after filtering to that of the unfiltered jet for jets within the $300 < p_{\mathrm{T}} < 500$ GeV range. A lower ratio implies a larger impact of the filtering procedure on the kinematic properties of the jet. In both cases, Herwig++ seems to predict a slightly more aggressive filtering with a higher fraction of jets with low ratio values. Alpgen exhibits the opposite behavior, while Pythia (Perugia 2010) resides approximately in the middle. These discrepancies originate primarily in the sub-leading jets. In all cases, the agreement is at the level of 10-20% across the full spectrum.

In order to map the evolution of the effect of filtering as a function of the energy and mass regime of the jet, Figure 8.21 presents the *mean* of the above measured filtering ratios as a function of the jet p_{T}. The mean value of these ratios are very well described by the MC simulation, with deviations of no more than 5% observed with respect to the data. An additional comparison of these ratios as the jet mass increases, provided in Appendix E, shows a similar dependence and agreement between data and MC.

Figure 8.22 repeats the studies shown in Section 8.2.1 on the subjet multiplicity in C/A, $R = 1.2$, but now for filtered C/A, $R = 1.2$ jets. Two important differences are observed with respect to the unfiltered results:

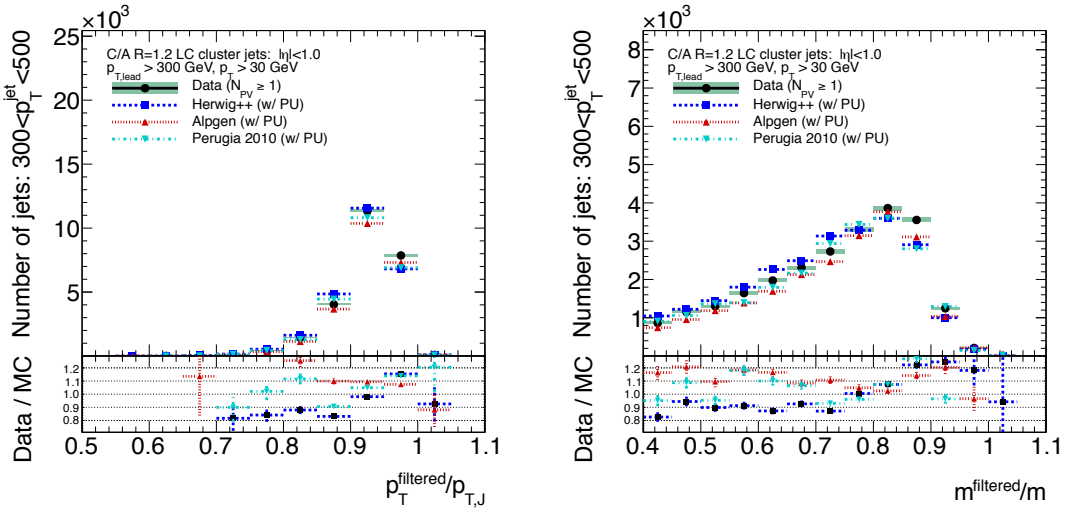

(a) p_{T} filtering ratio

(b) Mass filtering ratio

Figure 8.20: Ratios of jet kinematics after the filtering procedure compared to the unfiltered jet kinematics for jets within the $300 < p_{\mathrm{T}} < 500$ GeV range. (a) Ratio of the filtered jet p_{T} to the unfiltered p_{T}. (b) Ratio of the filtered jet mass to the unfiltered mass.

- The slightly different behavior of the filtering on the three MC generators for the full subjet multiplicity distribution is observed here. In the core of the distribution ($2 \leq N_{\mathrm{subjet}} \leq 5$) ALPGEN +HERWIG/JIMMY is observed to deviate by as much as 10%.

- Despite the slightly worse shape agreement, the mean subjet multiplicity in bins of track-jet multiplicity is shown to be in considerably *better* agreement after filtering.

These results suggest that the differences in the shape distribution are likely due to differences in the actual particle spectrum contained in the simulated events since the agreement is significantly restored when binning in the track-jet subjet multiplicity.

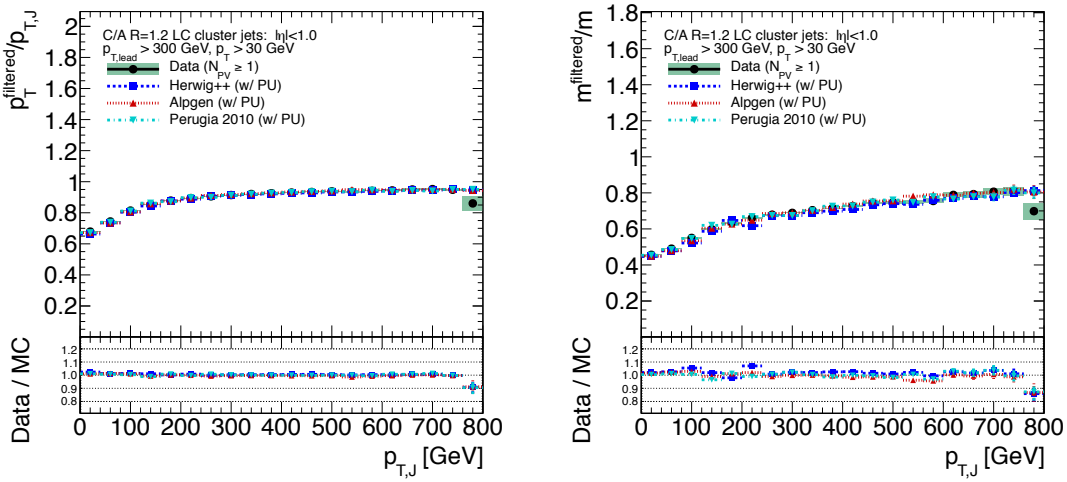

(a) p_{T} filtering ratio

(b) Mass filtering ratio

Figure 8.21: Ratios of jet kinematics after the filtering procedure compared to the unfiltered jet kinematics for jets within the $300 < p_{\mathrm{T}} < 500$ GeV range. (a) Ratio of the filtered jet p_{T} to the unfiltered p_{T}. (b) Ratio of the filtered jet mass to the unfiltered mass.

8.2.4 Color flow and heavy object discriminants

One of the most promising new avenues of study to arise in the last few years is the measurement of color flow within jets and the advent of jet discriminants designed specifically to quantify the liklihood that a given jet derives from a multi-body decay. These two goals are intimately related, since the radiation pattern between the decay products of a heavy object are theoretically distinct from those expected within the parton shower of a single hard quark or gluon. Such measurements are possible in part because of the advent of advanced techniques like those discussed above; theoretically well-defined jet algorithms, well-motivated subjet definitions, and other tools devoted to measuring heavy boosted objects. In addition, the ATLAS detector provides a superb *experimental* tool: a highly granular calorimeter with both longitudinal and lateral segmentation combined with a high resolution silicon tracker offers the precision necessary to measure complex structure within jets.

As described in Section 2.3, jets produced by the decay of a color singlet into

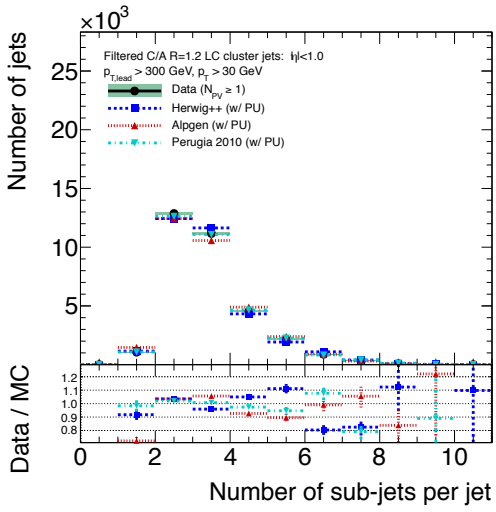

(a) Subjet multiplicity

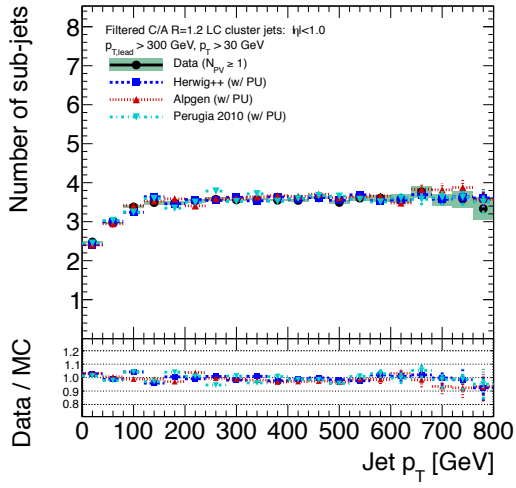

(b) Subjet multiplicity vs. p_{T}

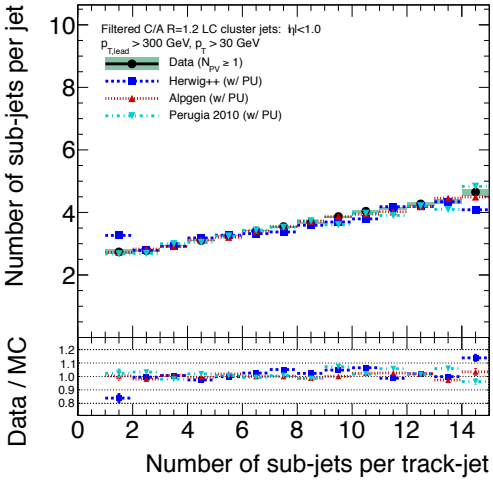

(c) Correlation to track-jets

Figure 8.22: Subjet observables at the detector-level for the *filtered* C/A, $R = 1.2$ algorithm. Subjets are again defined using the $k_{\perp}$algorithm with $R = 0.3$ and are required to have at least 5% of the parent jet p_{T}.

two nearby quarks are expected to exhibit a different intra-jet pattern of radiation than the QCD background. For exaple, a W boson that decays hadronically should contain a significant amount of radiation between the two quarks as compared to a QCD jet with a mass near M_W. Two observables related to color flow and multi-body decays within jets are N-subjettiness, τ_N, and dipolarity, $\mathcal{D}$, with the latter designed expressly to quantify the amount of dipole-like radiation within a jet. Each of these quantities are defined and discussed in Section 2.3 in terms of their theoretical features and underpinnings. In this Section, the first experimental measurement of these quantities is presented for a sample of QCD jets that constitute a background to searches for heavy objects with masses up to a few hundred GeV.

Figure 8.23 shows the distributions of $\frac{\tau_2}{\tau_1}$, $\frac{\tau_3}{\tau_2}$ with $\beta = 2$ as well as $\mathcal{D}_{12}$, and $\mathcal{D}_{23}$ for jets with $300 < p_{\mathrm{T}} < 500$ GeV for both data and MC. In both cases the MC simulation models the distribution observed in the data, with no generator exhibiting a larger than 20% discrepancy with respect to the data. All generators show an approximately 10% difference near the peak at $\frac{\tau_2}{\tau_1}$ compared to the data, yet ALPGEN seems to deviate much more than HERWIG++ and PYTHIA in the lower end of the spectrum. For $\frac{\tau_3}{\tau_2}$, the MC distributions are underestimating the fraction of jets with $0.3 < \frac{\tau_3}{\tau_2} < 0.7$, which as we will see is the primary range for the boosted top quark candidates. Since these observables are intended to be used as discriminants for signal and background, such differences are important for the resulting estimation of signal efficiency compared to background rejection. However, the differences observed in the distribution of each observable translate into much smaller differences in efficiency and rejection. A more clear picture of the modeling of the signal efficiency and background rejection is obtained by evaluating the means of these quantities as a function of jet mass and subjet topology.

Dipolarity is primarily sensitive to the topology of the subjet distribution within a jet, and of course to the soft radiation between those subjets. Two tests sensitive to the MC simulation's description of the data are the dependence of $\mathcal{D}$ on the anglular distribution of subjets and on z, defined by Eq. 8.3, where the subjets used in the calculation are constructed using the inclusive $k_\perp$ algorithm with $R = 0.3$. Figure 8.24 presents these dependencies for the C/A, $R = 1.2$ jet algorithm. This is a natural

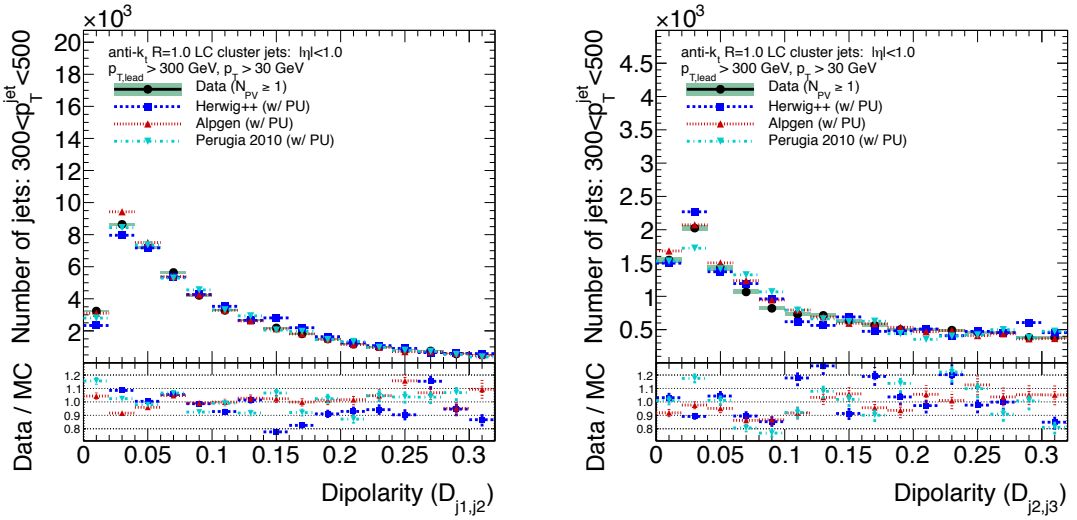

(a) $\mathcal{D}_{12}$ (b) $\mathcal{D}_{23}$

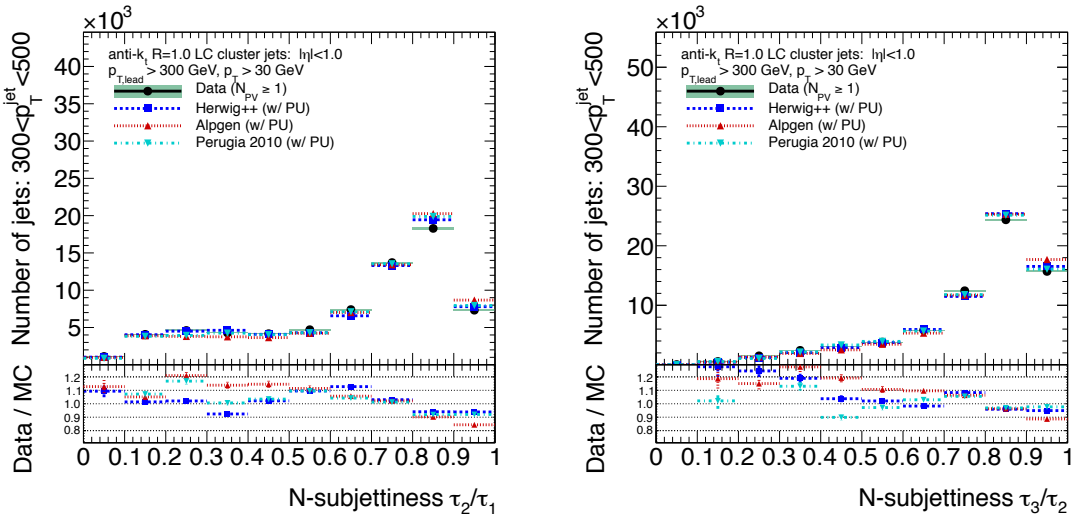

(c) $\frac{\tau_2}{\tau_1}$ (d) $\frac{\tau_3}{\tau_2}$

Figure 8.23: Dipolarity, $\mathcal{D}_{12}$ and $\mathcal{D}_{23}$, and the N-subjettiness ratios, $\frac{\tau_2}{\tau_1}$ and $\frac{\tau_3}{\tau_2}$, for jets with $300 < p_{\mathrm{T}} < 500$ GeV.

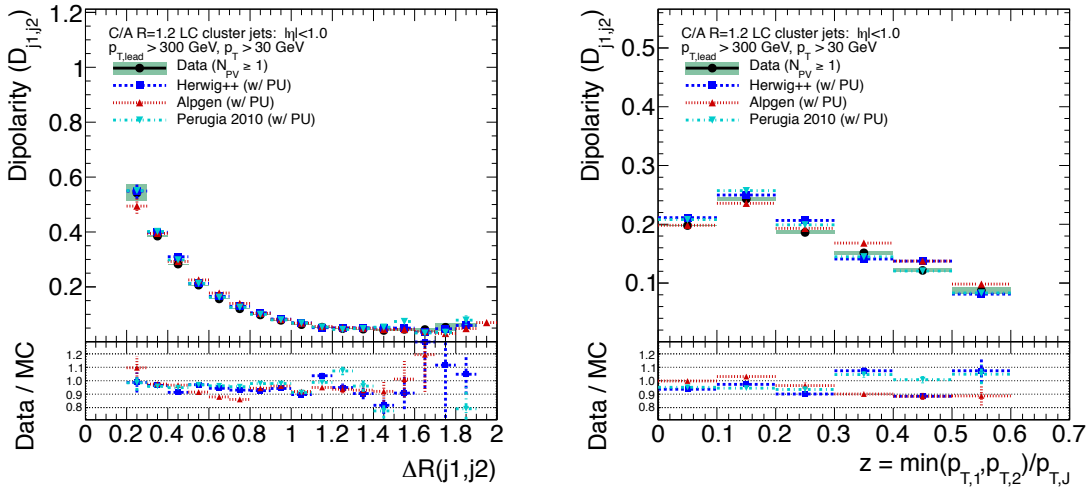

(a) $\mathcal{D}_{12}$ vs. $\Delta R_{j1,j2}$ (b) $\mathcal{D}_{12}$ vs. z

Figure 8.24: Dipolarity, $\mathcal{D}_{12}$, for C/A, $R = 1.2$ jets as a function of (a) $\Delta R_{j1,j2}$, where the subjets are defined using the inclusive $k_\perp$algorithm with $R = 0.3$ and (b) z, defined by Eq. 8.3 using the same inclusive subjet definition.

algorithm to use for the evaluation of the topological dependence of the dipolarity since it is a strictly angular ordered recombination algorithm. Similar distributions may be found in Appendix E for anti-k_t, $R = 1.0$ jets.

8.2.5 Boosted top quarks

A handful of candidate boosted top quark events have been observed in the 2010 data and provide a unique first opportunity to test the techniques described in above *in-situ*. This sample has been collected using the relatively lepton+jets channel, which has a signal-to-background (S/B) ratio on the order 2 to 3 [217]. This selection has since been applied to the entire 2010 data set [218] and used to search for high invariant mass top-quark pairs that would be an indication of a new massive particle coupled to the third generation. The four events discussed in detail below were selected to have $m_{t\bar{t}} > 700$ GeV. The candidate pair with highest invariant mass is observed to have $m_{t\bar{t}} > 1.5$ TeV.

For this subsample of candidate boosted top-quark events, the invariant mass and splitting scales are discussed in detail in Ref. [219]. These events offer a much more fertile testing ground for the substructure techniques discussed so far in this thesis. Figure 8.25 shows a single ATLAS event display for one of the selected candidate boosted top quark events. In this display, anti-k_t jets with $R = 0.4$ are indicated in red whereas large radius anti-k_t jets with $R = 1.0$ are shown in green in the same figure. The leading $R = 0.4$ jet in the event corresponds to the leptonic leg of the top event and has $p_{\mathrm{T}} = 199$ GeV. It is also tagged as a b-jet with high probability via both a track impact parameter-based tagger and via a secondary-vertex + impact parameter tagger. The leading $R = 0.4$ jet in the opposite hemisphere, corresponding to the hadronic leg of the event has $p_{\mathrm{T}} = 157$ GeV and no b-tag, whereas the second leading jet in the hemisphere of the hadronic candidate has a strong tag. When re-clustering the event with $R = 1.0$ jet corresponding to the hadronic leg has $p_{\mathrm{T}} = 327$ GeV and $m^{\mathrm{jet}} = 206$ GeV. With all of these observations, this event is considered to be a strong candidate for a boosted top quark event.

To study this particular event even further, the event display presented in Figure 8.26 shows more clearly the substructure features discussed in the previous sections. The large radius anti-k_t jets are shown as a colored circles, whereas the subjets defined by the $k_\perp$algorithm with $R = 0.3$ as well as the tracks found by the fat track-jet and sub-track-jet algorithms are shown as crosses and small dots, respectively. This highlights the usefulness of tracking information for its angular resolution. The b-tagged $R = 0.4$ anti-k_t jets are shown a magenta colored dots in this figure. It is very clear that each of the detailed substructure observables – subjets, tracks in sub-track jets and the overall fat jet reconstruction – are working extremely well in this case.

Since the filtering procedure discussed above played such a prominent role in reducing the systematic effects due to pile-up, we analyze this event for each of the jet types and grooming techniques presented. Figure 8.27 shows the same jet – the hadronic leg of the candidate boosted top quark events – re-clustered using each of the algorithms considered. The effect of the filtering in removing extraneous wide angle emissions is clearly shown. Furthermore, the subjets remaining in the filtered

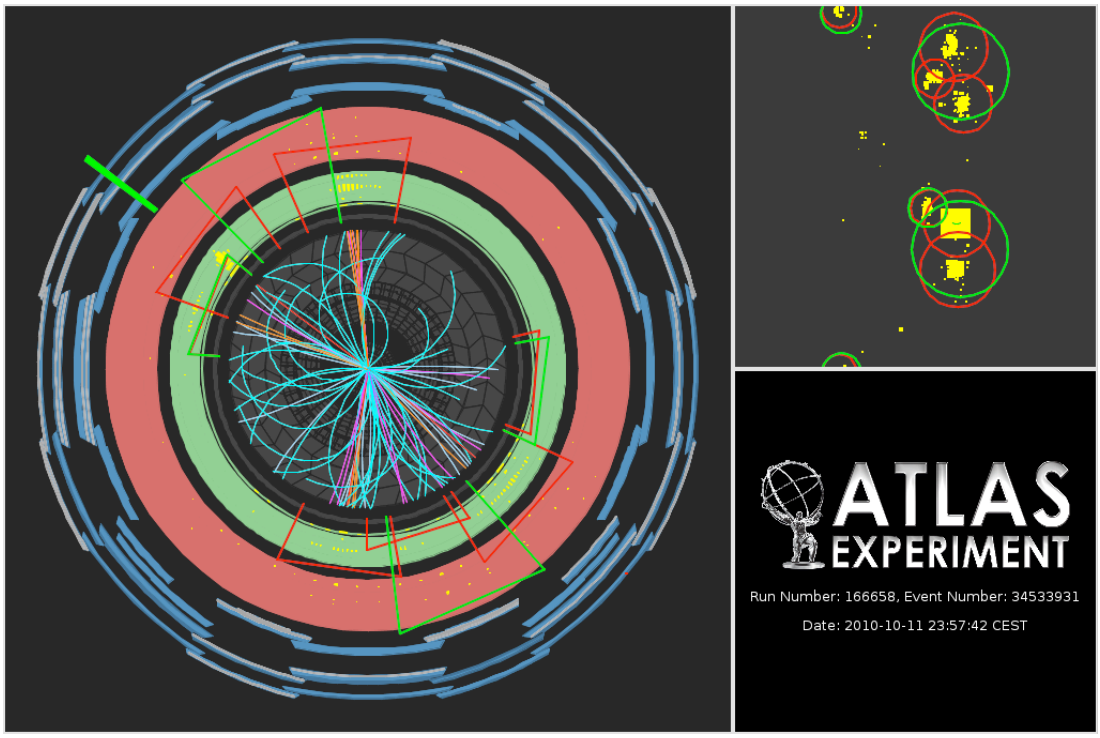

Figure 8.25: Run 166658, event 34533931 (Oct. 11, 2010): ATLAS event display of a single boosted top quark candidate. The leading $R = 0.4$ jet in the event corresponds to the leptonic leg of the top event and has $p_{\mathrm{T}} = 199$ GeV. It is also tagged as a b-jet with a b-tagging weight for the likelihood of being produced by a light-quark of $w_{\mathrm{JetProb}} = 2.8 \times 10^{-5}$ (via the "JetProb" tagger) and a vertex b-tag weight of $w_{\mathrm{SV1IP3D}} = 15.9$ (via the secondary-vertex + impact parameter SV1IP3D tagger). The leading $R = 0.4$ jet in the opposite hemisphere, corresponding to the hadronic leg of the event has $p_{\mathrm{T}} = 157$ GeV and no b-tag, whereas the second leading jet in the hemisphere of the hadronic candidate has a strong tag $w_{\mathrm{SV1IP3D}} = 5.4$ with $w_{\mathrm{JetProb}} = 3.1 \times 10^{-3}$. When re-clustering the event with $R = 1.0$ jet corresponding to the hadronic leg has $p_{\mathrm{T}} = 327$ GeV and $m^{\mathrm{jet}} = 206$ GeV.

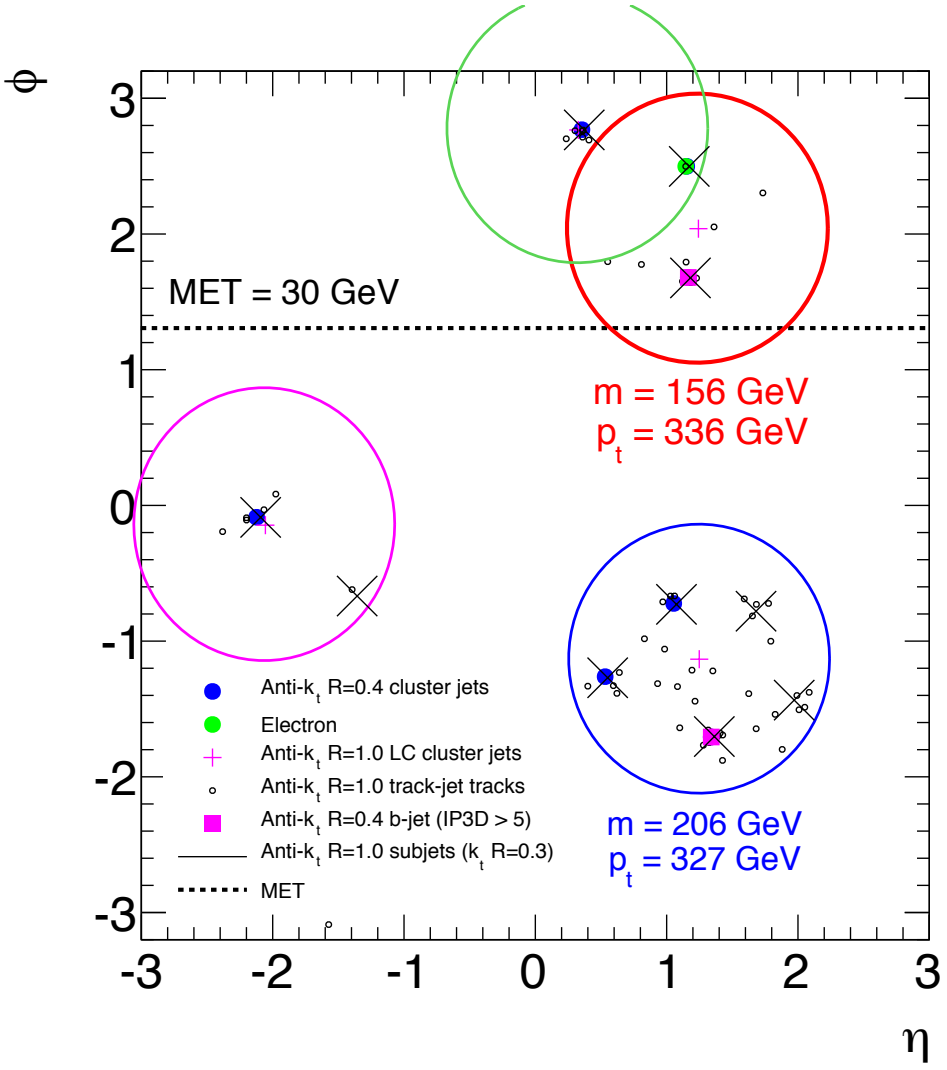

Figure 8.26: Run 166658, event 34533931 (Oct. 11, 2010): the same event shown in Figure 8.25 (rotated by π in ϕ) but now displaying the substructure components discussed in the text, including the subjets defined by the $k_\perp$algorithm as well as the tracks found by the fat track-jet and sub-track-jet algorithms.

jet exactly correspond to the two candidate light quark jets from the W and the b-tagged jet which presumably represents the b-quark from the top quark decay. Note also that the values of $\frac{\tau_2}{\tau_1}$ and $\frac{\tau_3}{\tau_2}$ fall significantly below the peaks of the distribution for QCD jets shown in Figure 8.23. The dipolarity, $\mathcal{D}$, on the other hand seems to be rather high for these jets compared to where the background peaks in Figure 8.23. It is also interesting to note that the values of these observables depend very little on the parent jet algorithm used to find and reconstruct the original jet. Filtering also shifts the measured value of $\frac{\tau_3}{\tau_2}$ to lower values.

Finally, in order to study the difference between high mass top quark jets and high mass QCD jets, a single event from each process has been selected and analyzed in same way as the boosted top quark candidate event taken from the data and shown above. Figure 8.28 shows a single boosted hadronic top quark decaying into a fully reconstructed jet with a mass between $170 < m^{\text{jet}} < 190$ GeV depending on the algorithm used for jet finding. Figure 8.29 shows a high mass ($m^{\text{jet}} \sim 120-220$ GeV), high transverse momentum ($p_{\text{T}}^{\text{jet}} \sim 340\ GeV$) jet from $g \to q\bar{q}$. Although the masses of these jets are similar, their substructure properties are significantly distinct. The sample top jets consistently exhibit $\frac{\tau_2}{\tau_1}$ and $\frac{\tau_3}{\tau_2}$ values significantly below the peak observed in data dominated by QCD jets, which the sample QCD jets consistently fall within it. Moreover, the mass of the filtered top jet remains very close to the mass measured prior to filtering while the filtered QCD jets show a strong mass difference; a change of nearly 50% is seen in the case of the LC cluster C/A, $R = 1.2$ jets.

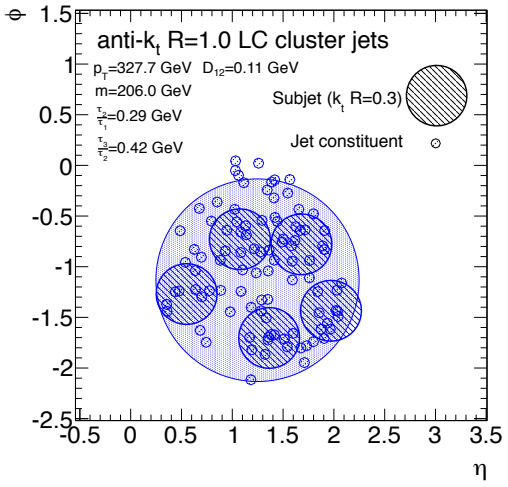

(a) anti-k_t, $R = 1.0$

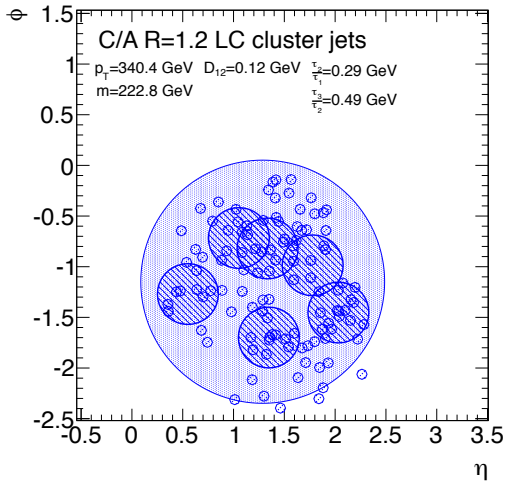

(b) C/A, $R = 1.2$

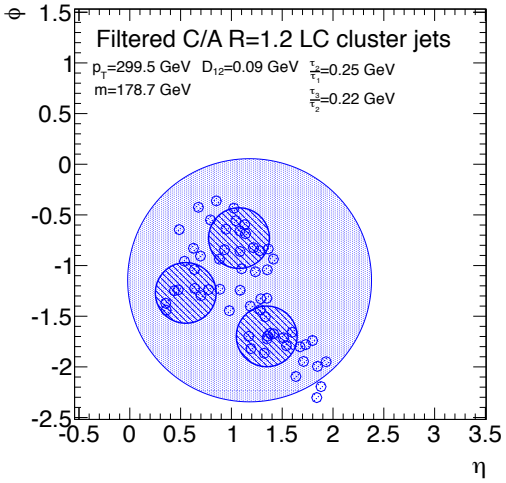

(c) C/A, $R = 1.2$ (filtered)

Figure 8.27: Run 166658, event 34533931 (Oct. 11, 2010): the same event shown in Figure 8.25 but now displaying only the hadronic leg of the $t\bar{t}$ event along with the constituents of the jet. In this case, the smaller circles represent the subjets defined by the $k_\perp$algorithm. The same event is re-clustered using each of the jet algorithms and grooming techniques described in the text: (a) anti-k_t, $R = 1.0$, (b) C/A, $R = 1.2$, (c) and C/A, $R = 1.2$ (filtered) . The effect of the filtering in removing extraneous wide angle emissions is clearly shown.

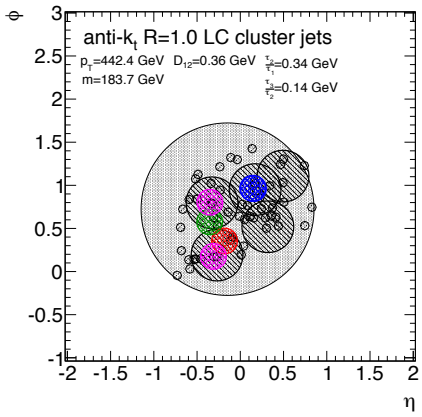

(a) anti-k_t, $R = 1.0$ (clusters)

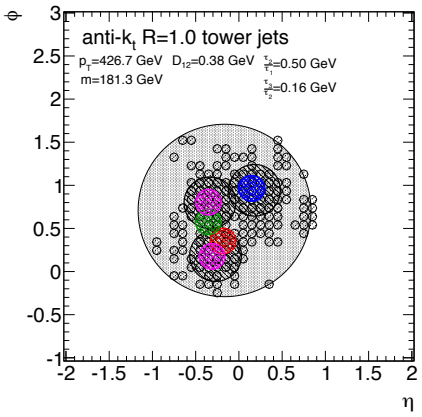

(b) anti-k_t, $R = 1.0$ (towers)

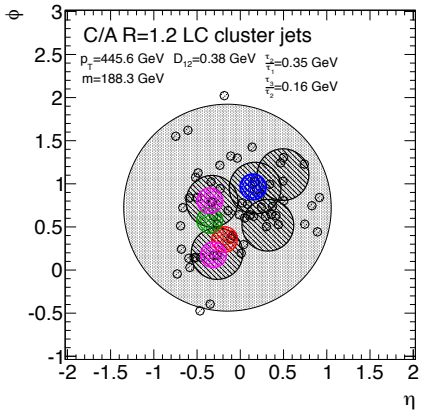

(c) C/A, $R = 1.2$ (clusters)

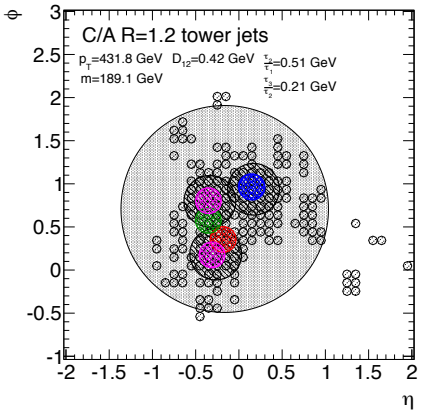

(d) C/A, $R = 1.2$ (towers)

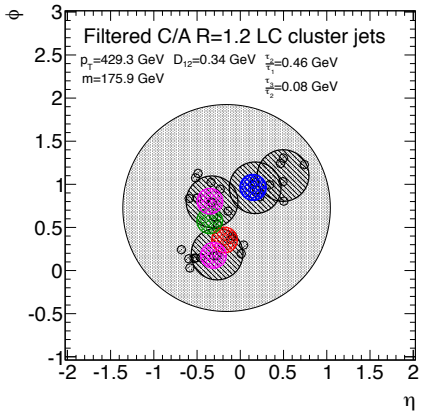

(e) Filtered C/A, $R = 1.2$ (clusters)

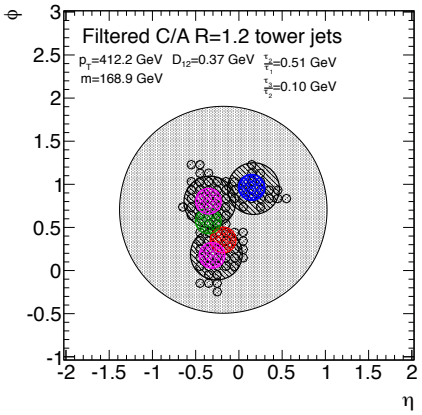

(f) Filtered C/A, $R = 1.2$ (towers)

Figure 8.28: Simulated event of a boosted top quark decay ($p_T^{\bar{t}} = 337$ GeV). In this event, $\bar{t} \to W^- \bar{b} \to q\bar{q}\bar{b}$, where a single high mass ($m^{\text{jet}} \sim 160 - 190$ GeV), high transverse momentum ($p_{\text{T}}^{\text{jet}} \sim 450\ GeV$) jet is produced.

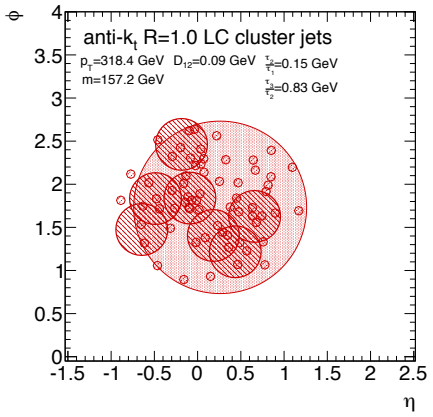

(a) anti-k_t, $R = 1.0$ (clusters)

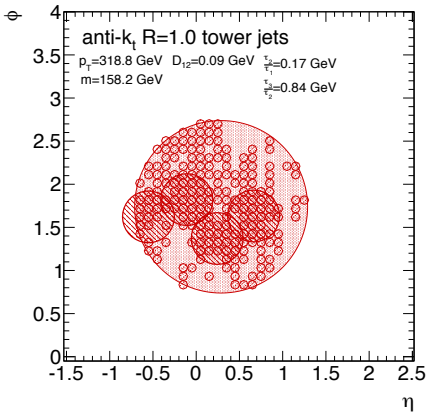

(b) anti-k_t, $R = 1.0$ (towers)

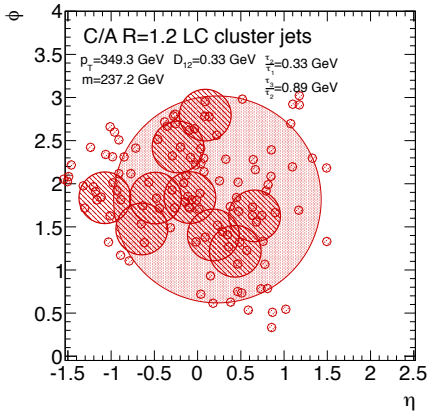

(c) C/A, $R = 1.2$ (clusters)

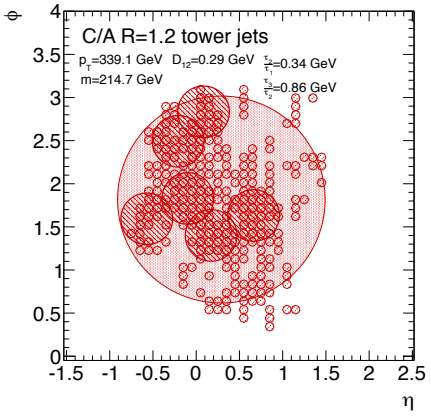

(d) C/A, $R = 1.2$ (towers)

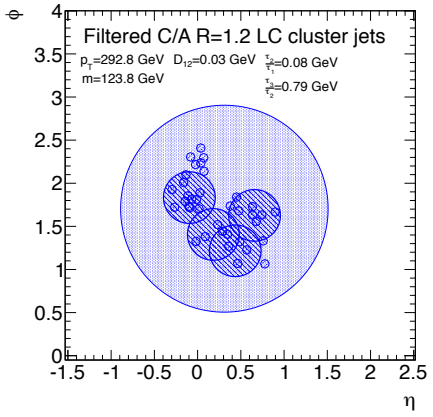

(e) Filtered C/A, $R = 1.2$ (clusters)

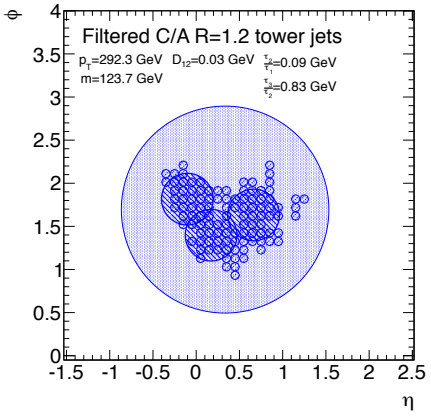

(f) Filtered C/A, $R = 1.2$ (towers)

Figure 8.29: Simulated event of a single high mass ($m^{\text{jet}} \sim 120 - 220$ GeV), high transverse momentum ($p_{\text{T}}^{\text{jet}} \sim 340\ GeV$) jet from $g \to q\bar{q}$. Filtering reduces the mass of this jet significantly.

Chapter 9

Conclusions

This thesis represents a comprehensive study of the hadronic final state in ATLAS, carried out in a new energy regime, with a new detector, at the energy frontier. An analysis of six hadronic event shapes – A, S^{pheri}, $S_{\perp}^{pheri}$, $\ln y_{23}$, $\tau_{\perp}$, and $T_{m,\perp}-$ was conducted at high Q^2 and compared among multiple Monte Carlo event generators and with a variety of detector environments applied to the simulation. A good agreement with a data sample of 38 pb^{-1} is observed in most kinematic and topological regions. Indications suggest that the modeling of the data by Pythia (Perugia 2010) can be improved with further tuning and that the relatively new incarnation of the Herwig++ Monte Carlo and parton shower model provides a very good description of most of the data, except for highly aplanar events where the multi-jet description of Alpgen +Herwig/Jimmy still performs extremely well. The systematic uncertainties within the measurement of S^{pheri} and $S_{\perp}^{pheri}$ are very small, which suggests that discriminating variables based on these event-level observables – such as those proposed for black hole searches – can be well established in the search for new physics.

The study of the full event shape is then extended in its philosophy into the realm of jet substructure and a series of detailed detector level measurements is presented. These measurements include the jet mass, subjet structure and topology, and color flow where new techniques and jet algorithms are used. An intensive study of detector effects such as the energy calibration and multiple proton-proton interactions is

carried out in order to validate the measurements performed. The well-tuned shower model of HERWIG++ exhibits excellent agreement with the data at both high and low subjet multiplicity and in the topological distribution of subjets within a jet. ALPGEN with the HERWIG/JIMMY hadronization and underlying event models shows departures from the data that suggest – in conjunction with the above measurements of the multi-jet topology in event shapes – that improvements in these models may be needed for more precise agreement. The multi-parton simulation present in ALPGEN appears to predict the widely separated realm of multi-jet topologies very well but deficiencies in the underlying event and hadronization models prevent it from describing the jet internal structure well. New techniques for mitigating the experimental effects of multiple pp interactions on the jet mass are also presented and are demonstrated to reduce the experimental uncertainty on the jet mass scale more than a factor of two in some cases. HERWIG++ again demonstrates a very good agreement with the data, to within experimental uncertainties in the jet mass distributions for several jet types. The modeling of the jet mass by PYTHIA and ALPGEN can be improved, likely with underlying event model developments. The technique of jet filtering is established for the first time in data at the LHC and is shown to not only be well described by the MC in terms of its performance but also to ameliorate the effects of pile-up. Finally, two recently proposed jet substructure observables are measured in a sample of QCD di-jet events and used to compare to a handful of boosted top quark events in the data. A significant discrimination between the background and the signal is observed for N-subjettiness, supporting the phenomenological studies presented in Ref. [130] with both full detector simulation and candidate boosted top quarks in the data. This represents a significant advance in the attempt to tag boosted top quarks with substructure techniques.

Of crucial importance for the full advancement and leverage of these techniques are pile-up corrections that can be applied dynamically and event-by-event. The jet area-based approach represents the most promising way forward in terms of allowing for individual jet corrections regardless of the input signal type or jet algorithm. In addition, the combination of dynamic yet precise correction with grooming tools such as jet filtering offer the toolbox necessary to conduct precision substructure

measurements in 2011. This thesis demonstrates those facilities for the first time at the Large Hadron Collider.

Within these results lie the inherent need to understand the jet composition and the experimental hurdles present in measurements of the hadronic final state at a very deep level. Chapter 6 presented a variety of techniques and tools – some of which are completely new to hadron-hadron colliders – for achieving such an understanding. These tools play a role in the analyses presented in this thesis as well as in almost all analyses taking place within ATLAS throughout 2011.

In order to expand up the results presented here, and to make further quantitative advancements in the predictive ability of the theoretical tools, at least two improvements must be made. The dominant limiting factor in the precision of the event shapes analysis is the statistical power of the Monte Carlo samples used to compare to the data. A dedicated sample of fully simulated high Q^2 events, or a more thoroughly validated fast simulation sample, would alleviate this issue and allow for a statistical precision capable of providing comparisons that might improve the Monte Carlo tuning. Secondly, a sample of hadronic decays of heavy particles, W bosons or top quarks, is needed to fully establish the scale uncertainties and modeling of the substructure tools presented in Chapter 8. Nonetheless, the analyses presented here demonstrate that both event shapes and jet substructure measurements may already begin to be used in the search for heavy particles and physics beyond the Standard Model within ATLAS.

Appendix A

Characterization of the interaction region

A.1 Reconstruction of Primary-Vertex Distributions and Luminous-Region Parameters

The basic approach used here to measure luminous-region parameters is to reconstruct the pp interaction point from tracks observed in the ATLAS detector. Thus, all positions and angles are measured with respect to the ATLAS coordinate system, which has its origin in the center of the detector, with the positive x-axis, $+x$, pointing to the center of the ring, $+y$ pointing upwards, and $+z$ pointing along the outgoing beam 2 (which runs counter-clockwise around the ring). The precise position of the origin as well as the orientation of the coordinate axes are defined as the result of a multi-level alignment procedure performed on the ATLAS Inner Detector.

A.1.1 Online Luminous-Region Measurement in the Level 2 Trigger

Online Event Selection

We use a dedicated algorithm in L2 (the so-called "online beam spot algorithm") that reconstructs and monitors primary-vertex distributions, aggregated across the processor farm in real time, from which we extract the position, size and tilt angles of the luminous region. Simultaneously, we count these reconstructed vertices as a measure of the delivered luminosity.

The L2 luminous-region measurements are initiated by a minimum-bias trigger at L1. This trigger is based on signals from the minimum-bias trigger scintillators (MBTS), which are scintillating plastic counters located inside the inner cavity in front of the end-cap cryostats on both sides of the interaction region. Two different trigger conditions are used in which at least one, or at least two, signals above threshold are required on either side of the MBTS, referred to as "MBTS_1" and "MBTS_2", respectively. For the $\sqrt{s} = 900$ GeV commissioning data, the higher rate MBTS_1 trigger is used and no coincidence requirement is applied. At $\sqrt{s} = 7$ TeV, the L1 seed is tightened to MBTS_2 and required to be in coincidence with a colliding proton bunch pair from the LHC. For each trigger, data from the entire Inner Detector are collected by the L2 tracking algorithms for pattern recognition and track fitting. This mode is referred to as a "full-scan."

Online Tracking and Vertex Fitting at Level 2

The L2 track reconstruction is performed using specialized, fast algorithms, optimized for the average processing-time constraint at L2 of only a few tens of milliseconds. The pattern recognition is based on the silicon detectors, and tracks found there are subsequently extended to the TRT in order to improve the momentum measurement ("inside-out" strategy). Details of the L2 tracking algorithms and their performance in the first $\sqrt{s} = 900$ GeV data are described in [220].

The online beam spot algorithm employs a fast vertex fitter [221, 222] in order to reconstruct primary vertices on an event-by-event basis. Tracks reconstructed at L2

in the full-scan mode are first grouped into clusters with similar impact parameter (z_0) along the nominal beam-line at the center of ATLAS. A track-p_{T} ordered list is formed and a cluster of tracks is initiated with the highest-p_{T} track above 0.7 GeV in the event. The input to the vertex fitter is assembled from this "seed" track and the neighboring tracks with $p_{\mathrm{T}} > 0.5$ GeV and within $\Delta z_0 < 1$ cm of the seed track. The average z-centroid of the track cluster is then used as a starting point for the vertex fitter in the longitudinal direction. All tracks are required to have at least four silicon space points, with at least one in the Pixel detector and three in the SCT. A very loose selection on the transverse impact parameter with respect to the nominal beam-line of $|d_0| < 1$ cm is applied. To maximize the available statistics in the early, low-intensity running, we reconstruct vertices with two or more tracks of $p_{\mathrm{T}} > 1$ GeV covering a rapidity range of $|\eta| < 2.5$.

Online Primary-Vertex Distributions

Using the vertices reconstructed at L2, we obtain three-dimensional distributions whose projections carry information about the luminous centroid position, sizes and tilts. In Sec. A.2 we present these primary-vertex distributions for both the $\sqrt{s} =$ 900 GeV and 7 TeV data. The impact of the intrinsic resolution of the vertexing algorithm on the longitudinal distribution is negligible, while that on the transverse distributions is not. The distributions are not corrected for resolution, but the observed beam spot widths as a function of the estimated per-event vertex error show consistent variation as expected from simulation, which confirms the transverse vertex resolution of 200 μm for the worst case of low-p_{T} two-track vertices, down to 70 μm for the highest-multiplicity vertices.

A.2 Experimental Characterization of the Luminous Region

The spatial distribution of the pp interactions can be quantitatively described in terms of the parameters of the luminous ellipsoid. These luminous-region parameters

depend on the emittances, the β-functions at the IP, and the relative position and orientation of the two beams at the IP (Sec. A.2). The distribution of event vertices, which mirrors that of the luminosity, lends itself to a detailed experimental characterization of the beam orbits close to the IP (Sec. A.2) and of the longitudinal and transverse luminous sizes (Sec. A.2).

A.2.1 Experimental Observables and IP Beam Parameters

Assuming dispersion and transverse coupling remain negligible, the parameters determining the transverse distributions close to the IP are, for each beam, the x and y emittances ϵ and β-functions. The transverse beam sizes σ_{ib} ($i = x, y$ and $b = 1, 2$) are given by

$$\sigma_{ib} = \sqrt{\epsilon_{ib}\beta_{ib}} \, . \tag{A.1}$$

These are not directly measurable at the IP, but can be inferred from synchrotron-light or wire-scanner beam-profile measurements elsewhere in the rings, provided the lattice functions are known with sufficient accuracy.

Under the additional assumption of Gaussian beams, the particle distribution in a bunch can be written as

$$\rho_b(x, y, z, t) = \frac{N_b}{\sqrt{(2\pi)^3}\sigma_{xb}\sigma_{yb}\sigma_{zb}} \times e^{-\frac{(x-\overline{x}_b)^2}{2\sigma_{xb}^2} - \frac{(y-\overline{y}_b)^2}{2\sigma_{yb}^2} - \frac{(z \pm ct)^2}{2\sigma_{zb}^2}} \, , \tag{A.2}$$

where $b = 1$ and $b = 2$ are associated with LHC rings 1 and 2, respectively. N_b is the number of protons in the bunch, the σ_{jb} ($j = x, y, z$) are the transverse and longitudinal single-beam sizes, and $\overline{x}_b$ and $\overline{y}_b$ are the transverse bunch centroids. The three-dimensional spatial luminosity distribution $\mathcal{L}(x, y, z)$, parameterized by the *luminous ellipsoid*, is determined by the time-integrated product of the overlapping particle densities of the two colliding beams.

In general, luminosity-weighted observables can be calculated by taking the appropriate moment of the product of beam particle densities. For example, the vertical

luminous centroid is given by

$$\overline{y}_{\mathcal{L}}(z) \;=\; \frac{\int y\,\rho_1\rho_2\;dt\,dx\,dy}{\int \rho_1\rho_2\;dt\,dx\,dy}\;. \tag{A.3}$$

Similarly, the vertical (or y-z) *luminous tilt* is defined as $\overline{y}'_{\mathcal{L}} = \frac{\partial \overline{y}_{\mathcal{L}}}{\partial z}$. Equivalent expressions hold for the horizontal centroid and luminous tilt, and for the longitudinal centroid. These parameters define the position and orientation of the luminous ellipsoid. They are continuously monitored online, independently reconstructed offline for further validation, and archived for analyzing long-term trends.

For head-on collisions (no relative transverse offsets, negligible crossing angles), the longitudinal luminosity distribution is given by

$$\frac{d\mathcal{L}}{dz} = 2c\int \rho_1\rho_2\;dt\,dx\,dy = \frac{2N_1N_2}{\sqrt{(2\pi)^3}\Sigma_z\Sigma_x\Sigma_y}\times e^{-\frac{(z-z_c)^2}{2(\Sigma_z/2)^2}}\;, \tag{A.4}$$

where z_c is the longitudinal location where the bunches collide and

$$\Sigma_j = \sqrt{{\sigma_{j1}}^2 + {\sigma_{j2}}^2} \tag{A.5}$$

are the *convolved beam sizes*. In the absence of any significant hourglass effect ($\beta^*/\sigma_z \gg 1$), the longitudinal convolved beam size Σ_z is equal to twice the *luminous length* $\sigma_{z\mathcal{L}}$; it can be extracted directly from the longitudinal luminosity distribution. The transverse convolved beam sizes Σ_x, Σ_y can be measured by transverse luminosity scans, as described in Sec. A.3.

The *specific luminosity* $\mathcal{L}_{sp}$ is defined as the luminosity per bunch and per unit bunch charges. Integrating Eq. A.4 yields $\mathcal{L}_{sp} \sim 1/\left(\Sigma_x\,\Sigma_y\right)$. This observable, which is also continuously monitored online, can therefore be used to constrain measurements of the convolved or individual beam sizes.

A related – albeit distinct – measure of transverse phase space is supplied by the vertical *luminous size* $\sigma_{y\mathcal{L}}$, also referred to as *vertical beam spot width* and defined by

$$\sigma^2_{y\mathcal{L}} = \overline{y^2}_{\mathcal{L}}(z) - \overline{y}^2_{\mathcal{L}}(z)\;, \tag{A.6}$$

which is related to the stored-beam sizes by

$$\sigma_{y\mathcal{L}} = \left(\frac{1}{{\sigma_{y1}}^2} + \frac{1}{{\sigma_{y2}}^2} \right)^{-1/2} , \tag{A.7}$$

with equivalent expressions for the horizontal luminous size $\sigma_{x\mathcal{L}}$. These two parameters describe the transverse shape of the luminous ellipsoid. They are directly measurable (provided the ATLAS vertexing resolution is properly taken into account) as the Gaussian widths of the event-vertex distribution projected onto the x-y plane, and carry information about β-functions and emittances. In the limiting case where the transverse sizes of beams 1 and 2 are equal pair-wise, one recovers the familiar expressions valid in single-ring colliders:

$$\sigma_{i\mathcal{L}} = \frac{\sigma_{ib}}{\sqrt{2}} = \frac{\Sigma_i}{2} . \tag{A.8}$$

A.2.2 Position and Orientation of the Luminous Region

In this and the following section, we describe characteristic features of the luminous region and their time evolution. These time histories, binned in short intervals called "luminosity blocks" and typically two minutes long, exhibit structures that can be linked to tuning and dynamical effects in the accelerator.

Luminous Centroids

The three-dimensional distribution of event vertices can be characterized very precisely due to the high rate of usable events. The average position of the collision point, or luminous centroid, is directly extracted online as the mean of this distribution projected onto the transverse plane (Fig. A.1) or the beam axis (Fig. A.2). Offline, the luminous centroid position is obtained from the maximum-likelihood fit. The online centroids presented in these two figures agree with the offline measurement to within a few μm (tens of μm) in the transverse (longitudinal) plane. Even before the vertexing resolution is corrected for, the reduction in transverse luminous width associated with the energy increase is striking; it is dominated by the change in geometrical emittance, which scales like the inverse of the beam energy.

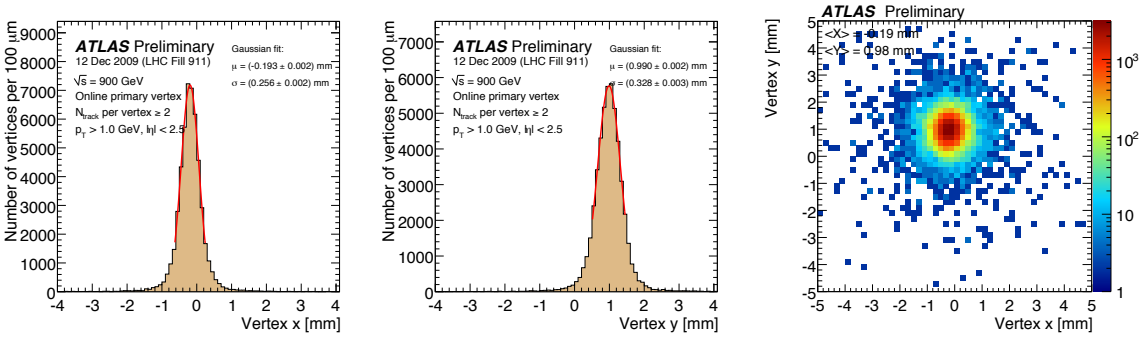

(a) Primary vertex x (900 GeV). (b) Primary vertex y (900 GeV). (c) Primary vertex x vs. y (900 GeV).

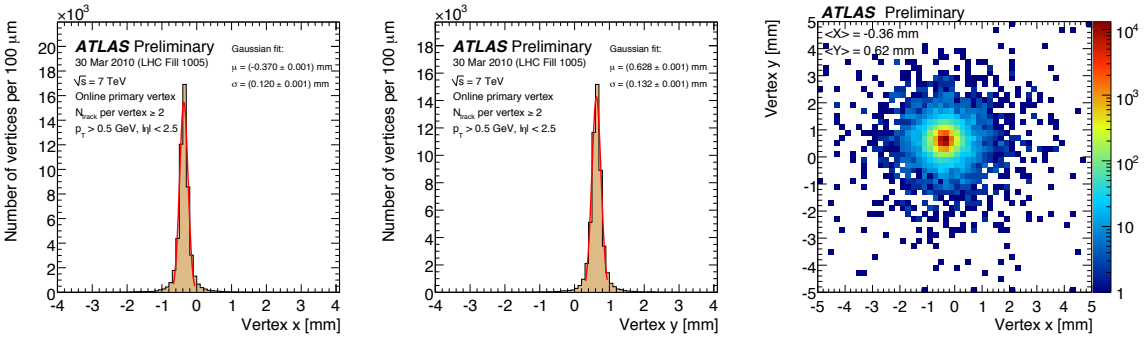

(d) Primary vertex x (7 TeV). (e) Primary vertex y (7 TeV). (f) Primary vertex x vs. y (7 TeV).

Figure A.1: Primary-vertex distributions in the transverse plane as produced by the ATLAS HLT, before correcting for vertexing resolution. The data were recorded with unsqueezed optics ($\beta^* = 11$ m). Gaussian fits are used to extract the mean position and observed width; the fitting range is limited to ± 1 RMS to reduce the sensitivity to resolution tails.

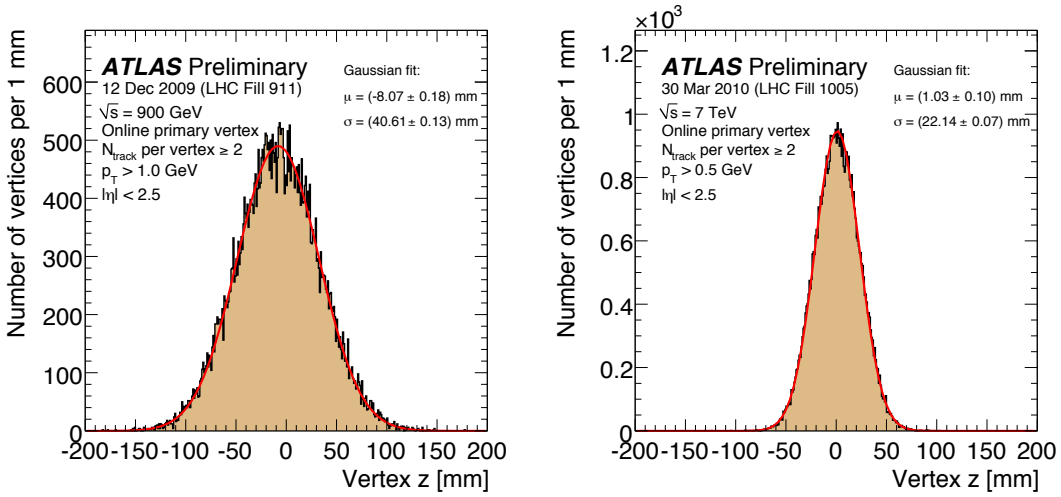

(a) Primary vertex z (900 GeV). (b) Primary vertex z (7 TeV).

Figure A.2: Longitudinal primary-vertex distributions as produced by the ATLAS HLT. The impact of the vertexing resolution is negligible. A Gaussian fit is used to extract the luminous length and the position of the longitudinal luminous centroid.

The time evolution of the luminous-centroid position is recorded online in approximately two-minute intervals, as illustrated in Figs. A.3 and A.4 for part of the 900 GeV running period. It is independently reconstructed offline with updated detector-calibration and alignment constants and using more efficient (but more CPU-intensive) tracking and vertexing algorithms. The transverse-position histories are consistent, in most luminosity blocks, to 20 μm or better. With the exception of a couple of step changes that can be associated with beam-orbit readjustments, the transverse luminous centroid remained within at most a ± 25 μm envelope over a two-week period, implying a stability of the orbit at the level of a few percent of the IP beam size at 450 GeV.

The vertex-based determinations of the luminous centroid can be compared (Fig. A.4) to the longitudinal position of the collision point extracted from the arrival times of the colliding bunches, that are measured by electrostatic beam-pickup detectors (BPTX) [154]. These pick-ups are installed as part of the LHC beam instrumentation, and are used by ATLAS for timing and beam-monitoring purposes. After accounting for cable-length delays in the signal propagation, the measured longitudinal collision

point is found to be in good agreement with that expected from the BPTX.

In very early running (not shown), the longitudinal crossing point was observed several centimeters off the nominal IP-position; it was promptly moved within a few mm of its nominal position by adjusting the relative RF phase between the two LHC rings, and thereafter remained stable within a few mm (Fig. A.4). The longitudinal position of the collision point was further adjusted in 7 TeV running to be nearly perfectly centered, as shown in the longitudinal vertex distribution of Fig. A.2(b), which was used online to verify the RF adjustments.

Luminous Tilts

The orientation of the luminous ellipsoid in the horizontal and vertical planes can be measured in the ATLAS coordinate system by slicing the transverse vertex distribution in bins along the z axis, and performing Gaussian fits to the horizontal and vertical projections in each slice; the slope of the resulting correlation (Fig. A.5) equals the luminous tilt in the two respective planes. The offline maximum-likelihood fit extracts the luminous tilt directly as a fit parameter. Its time history at 900 GeV, as reconstructed offline, is presented in Fig. A.6. The non-zero horizontal luminous tilt is consistent between 2009 and 2010 data and is attributed to a small residual relative misalignment of the ATLAS Inner Detector with respect to the LHC beam axis: the ATLAS detector z-axis is collinear with the beam line to well within 1 mrad.

A.2.3 Size of the Luminous Region

Luminous Length

The extent of the luminous region along the beam axis is extracted online from a Gaussian fit to the longitudinal distribution of primary vertices (Fig. A.2), or equivalently from the offline maximum-likelihood fit to the full vertex distribution. (The impact of the vertexing resolution is negligible here.)

The value of $\sigma_{z\mathcal{L}} = 40$-$45$ mm typically observed in 900 GeV running is noticeably smaller than that expected from the nominal bunch length of 110 mm at that energy

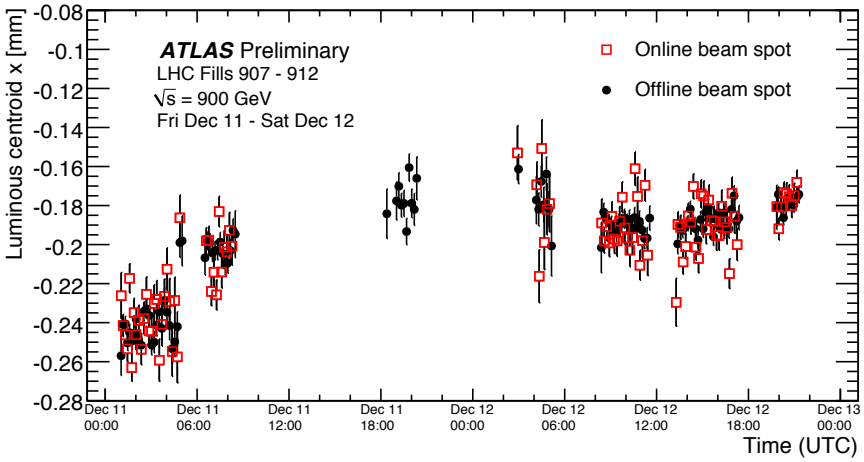

(a) Evolution of the horizontal IP position $\overline{x}_{\mathcal{L}}$ over several fills.

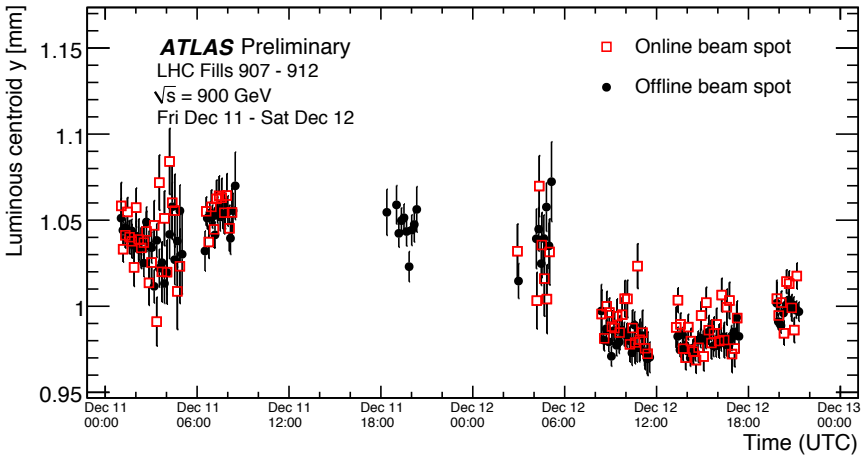

(b) Evolution of the vertical IP position $\overline{y}_{\mathcal{L}}$ over several fills.

Figure A.3: Evolution of the transverse centroid positions over several fills at $\sqrt{s} =$ 900 GeV as measured online (red squares) and as extracted from the offline beam spot maximum-likelihood fit (black circles). Errors are statistical only. No online data are available on Dec 11 because the corresponding HLT algorithm was left unactivated for this particular run.

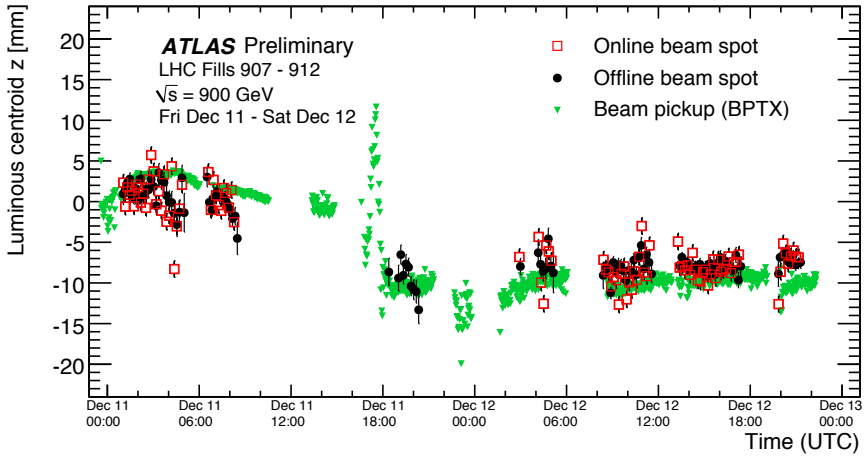

Figure A.4: Evolution of the longitudinal centroid position over several fills at $\sqrt{s} = 900$ GeV as measured online via vertex fitting (red squares) or using the electrostatic beam pickups (BPTX, green triangles), and as extracted from the offline beam spot maximum-likelihood fit (black circles). No online data are available on Dec 11 because the corresponding HLT algorithm was left unactivated for this particular run. Errors are statistical only.

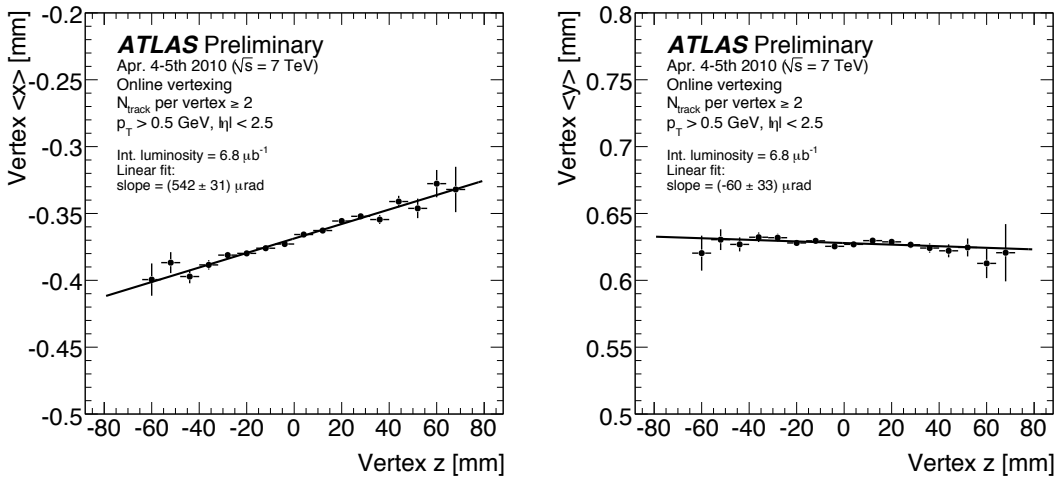

(a) x-z luminous tilt.

(b) y-z luminous tilt.

Figure A.5: Longitudinal dependence of the horizontal (left) and vertical (right) position of the luminous centroid, measured online at $\sqrt{s} = 7$ TeV. The slope of the fitted line measures the luminous tilt in each plane. The errors are statistical only.

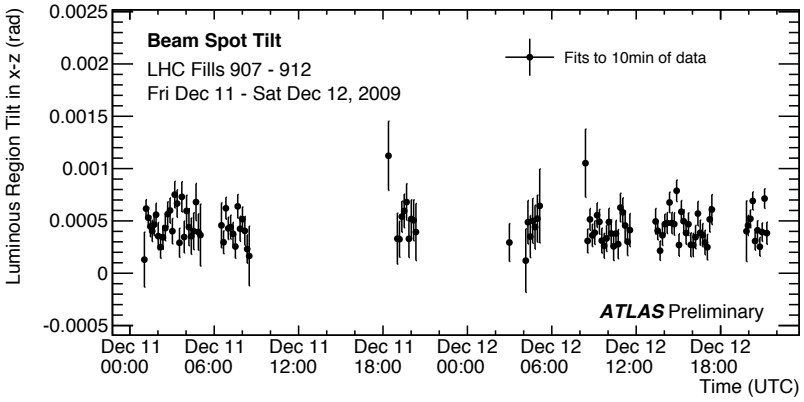

(a) Evolution of horizontal luminous tilt over several fills.

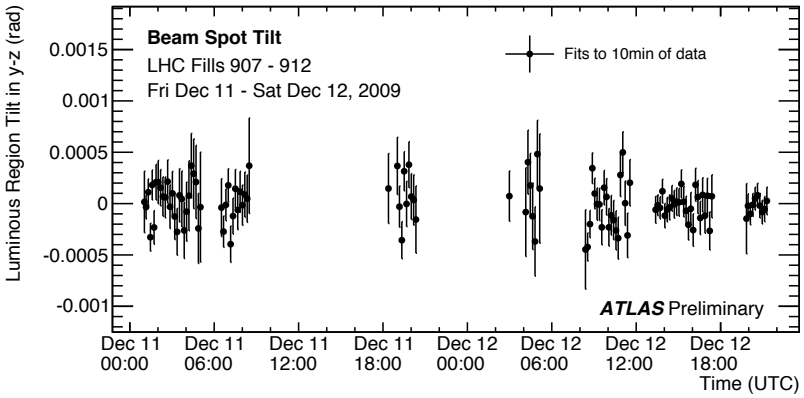

(b) Evolution of vertical luminous tilt over several fills.

Figure A.6: Evolution of the transverse luminous tilt over several fills at $\sqrt{s} = 900$ GeV, as determined by the offline beam spot maximum-likelihood fit. Errors are statistical only.

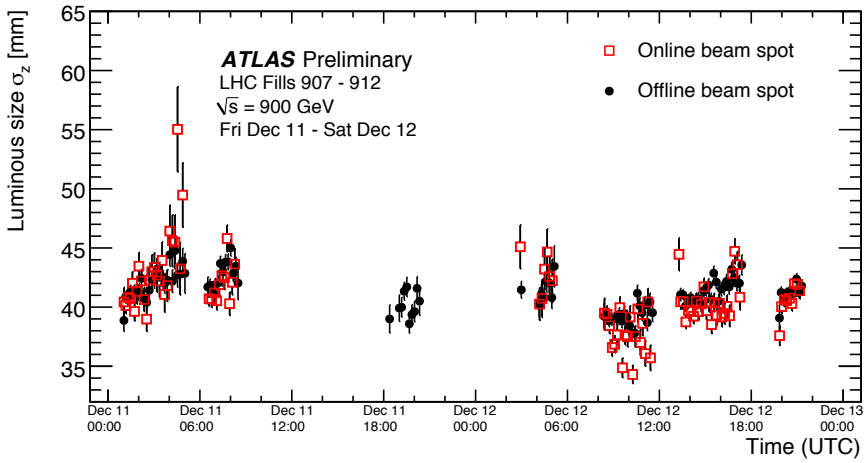

Figure A.7: Evolution of the luminous length over several fills at $\sqrt{s} = 900$ GeV, as measured online from the primary vertex distribution (red squares) and as extracted from the offline beam spot maximum-likelihood fit (black circles). Errors are statistical only. No online data are available on Dec 11 because the corresponding HLT algorithm was left unactivated for this particular run.

($\sigma_{z\mathcal{L}} \approx \sigma_z/\sqrt{2}$). This is primarily due to the fact that the longitudinal emittance injected into the LHC was significantly lower than nominal. Fig. A.7 illustrates the evolution of the luminous length during the 2009 run. The rate of increase is about 2.5 % over 3.5 hours, indicating a longitudinal-emittance growth in the LHC, which is fairly reproducible from fill to fill.

The luminous length decreases significantly in the 7 TeV data (Fig. A.2(b)). This is caused not only by the larger beam energy, but also by markedly different injection conditions during the two running periods, specifically the smaller injected longitudinal emittance and different RF voltages in 2010.

Transverse Luminous Size

The transverse luminous sizes $\sigma_{x\mathcal{L}}$ and $\sigma_{y\mathcal{L}}$ are extracted from the maximum-likelihood fit described in Sec. A.1. Here the vertexing resolution contributes significantly (and, at high energy, dominates) the observed width of the transverse vertex distributions. The transverse luminous size scales as $\sigma_{\mathcal{L}} \sim 1/\sqrt{E_{\text{beam}}}$ (E_{beam} being the beam energy), assuming ϵ_N and β^* remain unchanged. This kinematic shrinking, already

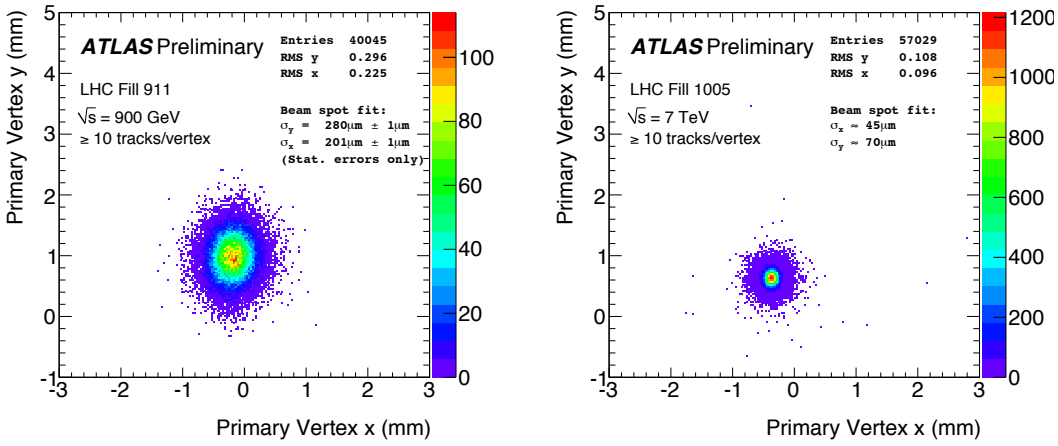

(a) Primary vertices in the x-y plane at $\sqrt{s} = 900$ GeV.

(b) Primary vertices in the x-y plane at $\sqrt{s} = 7$ TeV.

Figure A.8: Offline primary-vertex distributions in the transverse plane, uncorrected for resolution, at $\sqrt{s} = 900$ GeV (left) and $\sqrt{s} = 7$ TeV (right), requiring at least 10 tracks per vertex. With the selection used for this figure, vertexing resolutions of about 100 μm (75 μm) are achieved at $\sqrt{s} = 900$ GeV (7 TeV). The fact that the luminous size is larger in the vertical than in the horizontal is apparent in the $\sqrt{s} = 900$ GeV plot and quantified by the resolution-corrected fit results displayed in the two figures. The data were recorded with unsqueezed optics ($\beta^* = 11$ m).

apparent before any resolution correction (Fig. A.1), can be illustrated more accurately (Figs. A.8 and A.9) by requiring at least 10 tracks per vertex in order to improve the resolution. The fit results reported in these figures are corrected for resolution effects; they are reasonably consistent with the luminous sizes of 200 μm (74 μm) predicted at $\sqrt{s} = 900$ GeV (7 TeV) for unsqueezed optics using the nominal value of ϵ_N.

The history of the transverse luminous size, over part of the 2009 run and corrected for resolution, is presented in Fig. A.10. The vertical size $\sigma_{y\mathcal{L}}$ is systematically 20 % to 50 % larger than that in the horizontal plane ($\sigma_{x\mathcal{L}}$). Its systematic increase during most fills, illustrated in more detail in Fig. A.11, was found to be correlated with a concomitant vertical-emittance growth of beam 2 observed on the synchrotron-light monitor (Fig. A.12). While transverse-emittance growth over the course of a fill is fully expected, the observed vertical growth rate appears larger than anticipated.

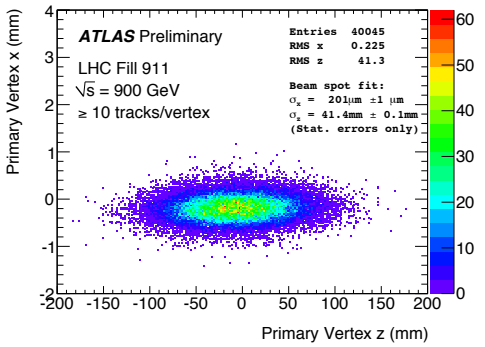

(a) Primary vertices in the x-z plane at $\sqrt{s} = 900$ GeV.

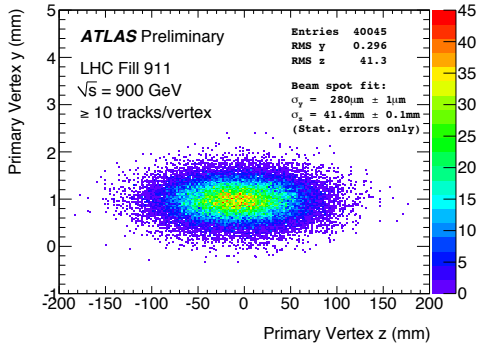

(b) Primary vertices in the y-z plane at $\sqrt{s} = 900$ GeV.

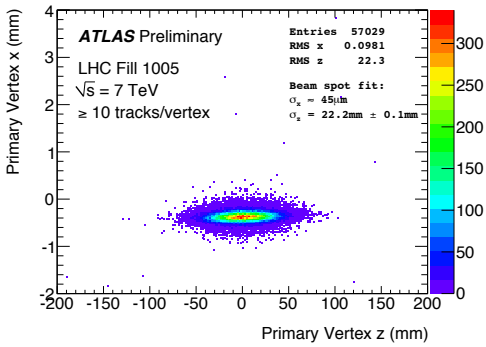

(c) Primary vertices in the x-z plane at $\sqrt{s} = 7$ TeV.

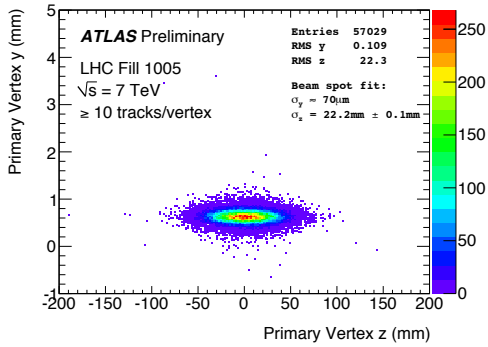

(d) Primary vertices in the y-z plane at $\sqrt{s} = 7$ TeV.

Figure A.9: Two-dimensional distributions of offline primary vertices, uncorrected for resolution, in the horizontal (left) and vertical (right) planes, at $\sqrt{s} = 900$ GeV (top) and $\sqrt{s} = 7$ TeV (bottom), requiring at least 10 tracks per vertex. The data were recorded with unsqueezed optics ($\beta^* = 11$ m).

The fact that the beam-2 profile monitor was not calibrated at the time, and that the beam-1 monitor had not been commissioned yet, make a more quantitative consistency assessment difficult. The mechanism for the simultaneous decrease in horizontal luminous size, also apparent in these two figures, remains to be understood. We note, however, that a decrease in horizontal emittance during fills has been observed on the synchrotron-light monitor during early $\sqrt{s} = 900$ GeV running.

A more systematic comparison between measured and expected luminous sizes at $\sqrt{s} = 7$ TeV is illustrated in Fig. A.13 and confirms the above-mentioned vertical-emittance growth observed at injection energy in 2009. Here ATLAS measurements are compared with the luminous sizes predicted using frequent wire-scanner measurements of the horizontal and vertical emittances in both rings, together with the corresponding β^* values measured by the phase-advance method during a separate, dedicated machine-development session. The single-beam sizes can then be computed using Eq. A.1, and can be combined to predict the luminous size as in Eq. A.7. The errors affecting the luminous-size measurements are statistical only; the corresponding systematic uncertainty on $\sigma_{x\mathcal{L}}$, $\sigma_{y\mathcal{L}}$ is 5 to 10 μm, dominated by the correction for the vertexing resolution. No error bar is shown on the luminous sizes inferred from accelerator parameters. As of this writing, the corresponding systematics have not been fully analyzed yet; they are roughly estimated to be about 10 % on each of ϵ_N and β^*. The agreement between these two very different methods is excellent.

A.3 Luminosity Monitoring and Calibration

Besides monitoring the IP orbits and luminous sizes during routine physics running, the reconstructed vertices are used online as an additional relative-luminosity monitor (Sec. A.3), which can be absolutely calibrated, together with the other ATLAS luminosity monitors, using beam-separation scans (Sec. A.3). One of the dominant systematic uncertainties affecting this calibration procedure, and that impacts all currently available ATLAS luminosity measurements, has been significantly reduced by comparing the beam-separation settings in the LHC control system with the measured displacements of the luminous centroid (Sec. A.3). Finally, the simultaneous

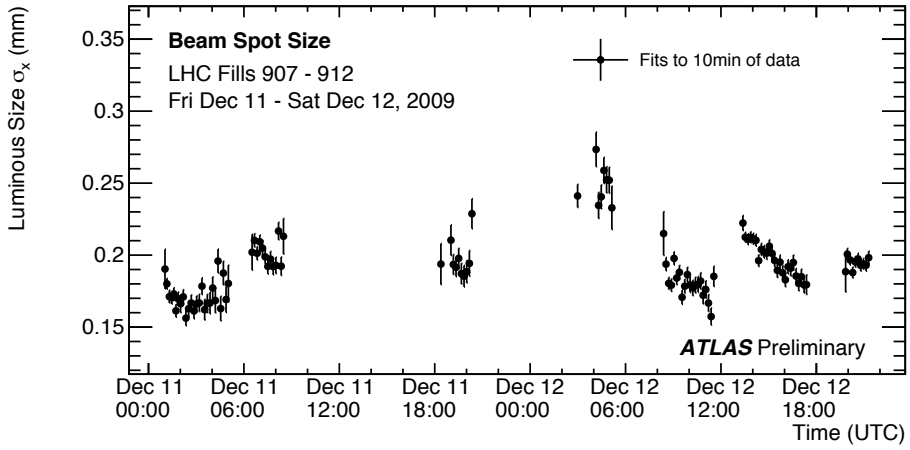

(a) Evolution of $\sigma_{x\mathcal{L}}$.

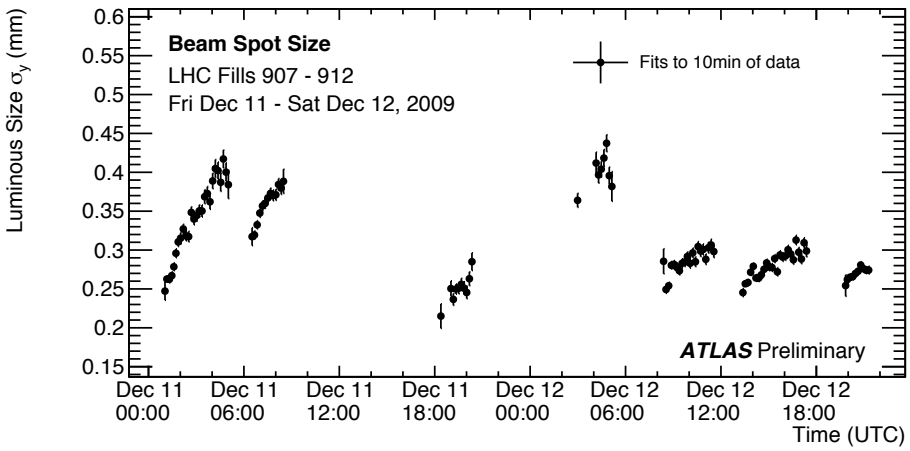

(b) Evolution of $\sigma_{y\mathcal{L}}$.

Figure A.10: Evolution of the transverse luminous size over several fills at $\sqrt{s} = 900$ GeV, after correcting for the instrumental resolution using the offline beam spot maximum-likelihood fit. Errors are statistical only.

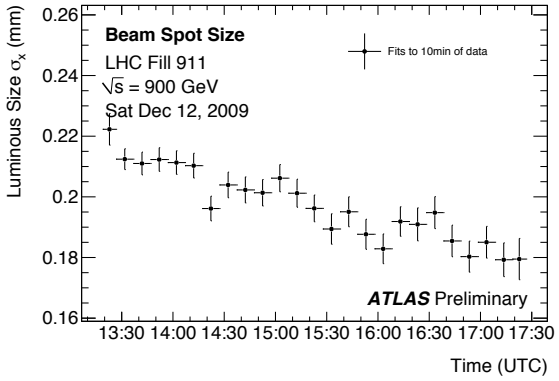

(a) Horizontal luminous size.

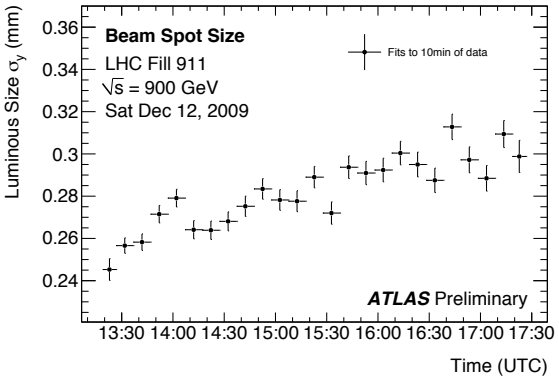

(b) Vertical luminous size.

Figure A.11: Evolution of the transverse luminous sizes $\sigma_{x\mathcal{L}}$ and $\sigma_{y\mathcal{L}}$, corrected for instrumental resolution using the offline fit, over the course of ATLAS run 142193 (LHC fill 911). The points show the results of fits to samples of 10 minutes of data. During the period considered here, $\sigma_{x\mathcal{L}}$ decreased by about 20 %, while $\sigma_{y\mathcal{L}}$ increased by approximately 25 %. Errors are statistical only.

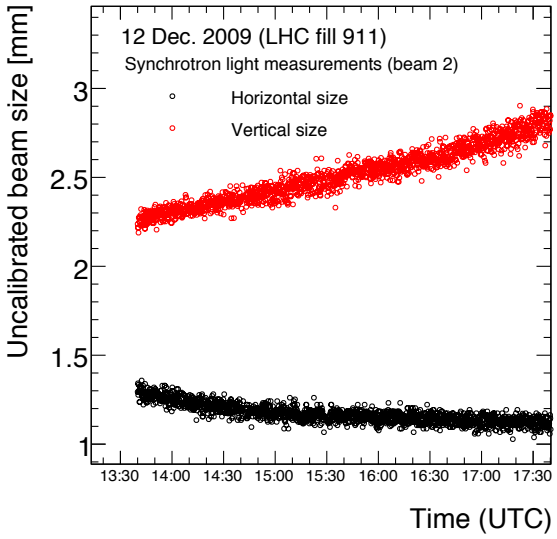

Figure A.12: Evolution of the transverse sizes of beam 2 at the synchrotron-light profile monitor over the course of ATLAS run 142193 (LHC fill 911).

determination of the transverse convolved beam sizes (from the separation scans), and of the corresponding luminous sizes under the same beam conditions, can yield a direct measurement of the transverse IP sizes of the two beams that cannot be obtained by conventional accelerator techniques (Sec. A.3).

A.3.1 Primary Vertex Count as a Measure of Luminosity

The time history of the online vertex-counting rate, over several fills at $\sqrt{s} = 900$ GeV, is presented in Fig. A.14 and clearly exhibits the typical luminosity decay within a given fill. The vertex counting rate is compared to the luminosity measured using the ATLAS Liquid Argon calorimeter (LAr) for a single fill in Fig. A.15. The LAr measurement is based on events satisfying the MBTS_1 trigger requirement (see Sec. A.1) and on minimum energy depositions in electromagnetic-calorimeter cells covering the pseudo-rapidity range $2.5 < |\eta| < 4.9$. LAr calorimeter cells are required to have an energy $5\,\sigma$ above the noise and exceeding 250 MeV (resp. 1200 MeV) in the inner wheel of the electromagnetic endcap calorimeter (resp. in the forward calorimeter). There must be at least two cells passing these requirements on both the forward ("A")

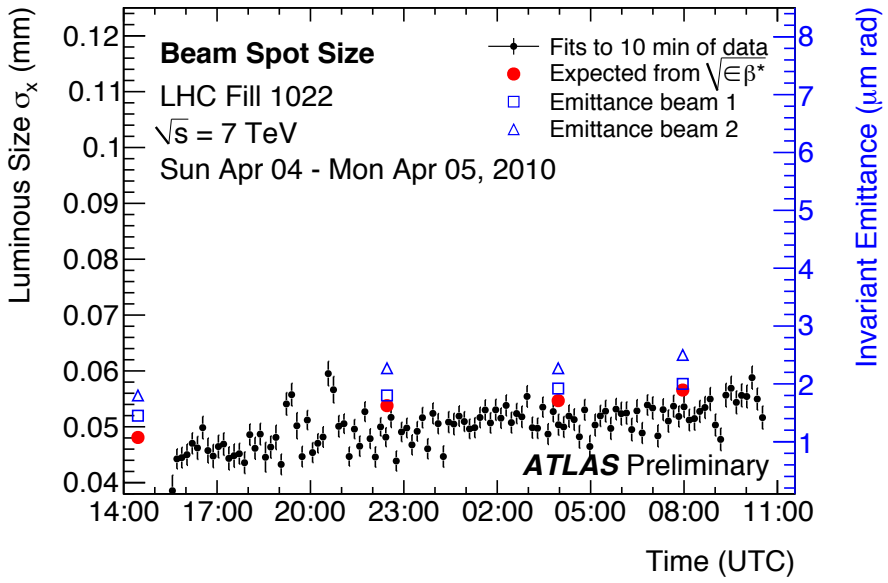

(a) Evolution of $\sigma_{x\mathcal{L}}$ and horizontal emittances during the fill.

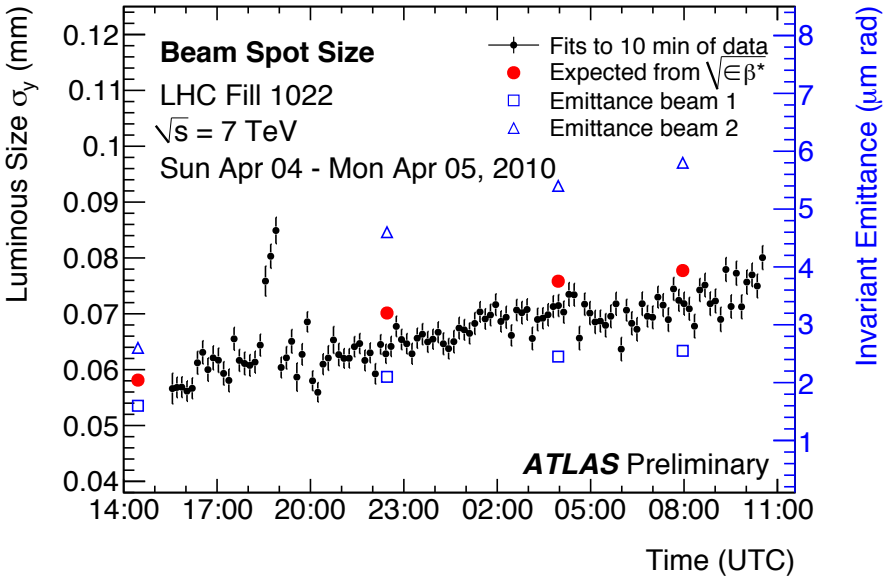

(b) Evolution of $\sigma_{y\mathcal{L}}$ and vertical emittances during the fill.

Figure A.13: Comparison of the luminous sizes $\sigma_{x\mathcal{L}}$ and $\sigma_{y\mathcal{L}}$ measured offline by ATLAS and corrected for instrumental resolution (points with error bars), with the values (red circles) predicted using emittances (blue squares and triangles) and IP β-functions measured by conventional accelerator techniques. The data were recorded with unsqueezed optics. The outliers visible in the luminous size measurements between 18:00 and 21:00 UTC are an artifact of luminosity-optimization scans carried out at that time; such scans bring the beams partially out of collision, thereby invalidating any straightforward interpretation of these particular data points. The errors are statistical only; the systematic uncertainties are discussed in the text.

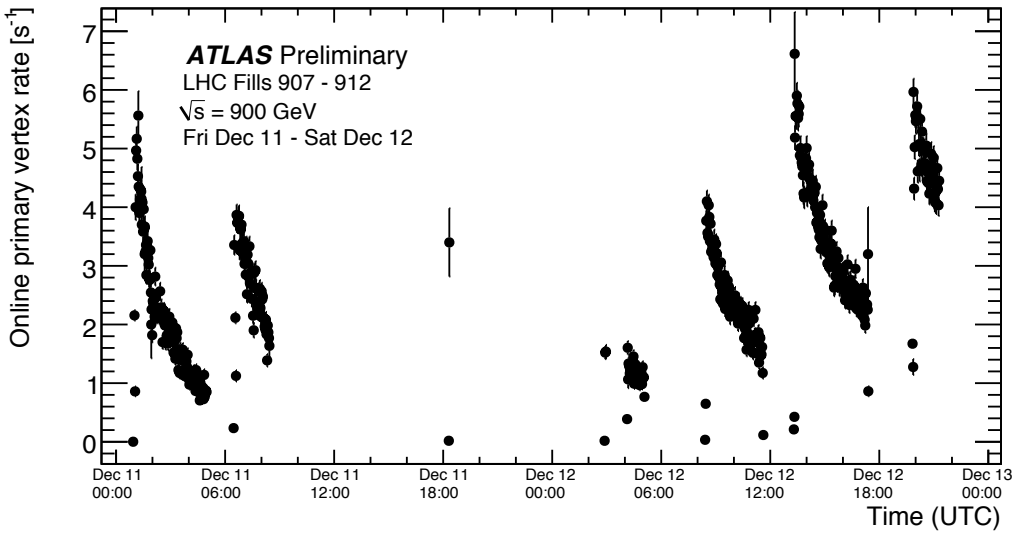

Figure A.14: Time history of the primary-vertex rate recorded by the ATLAS High-Level Trigger.

and backward ("C") sides of ATLAS. Requiring a time difference of $|\Delta t| < 5$ ns between cells on the two sides eliminates beam-halo triggers and provides a very-high purity sample of collision events. The systematic uncertainty on the absolute luminosity from this method is estimated at about 21 %, dominated by the difference in physics modeling by various event generators.

The events used for online vertex-reconstruction and -counting were selected as described in Sec. A.1, independently from the LAr-based event selection. The reconstruction of event vertices is effectively restricted by the Inner Detector acceptance to the range of $|\eta| < 2.5$, which is complementary to the acceptance of the LAr selection detailed above; the two samples are therefore built from a rather different mix of non-diffractive, single-diffractive and double-diffractive events. The time evolutions of the two luminosity measurements follow each other to very high precision, suggesting that the background is very low in both samples (or that in both cases it represents a constant fraction of the collision rate).

Fig. A.16 shows the average position of the luminous centroid, as well as the average number of reconstructed vertices per event and per colliding bunch pair as a function of the bunch-crossing identifiers (BCID) of the associated events. This

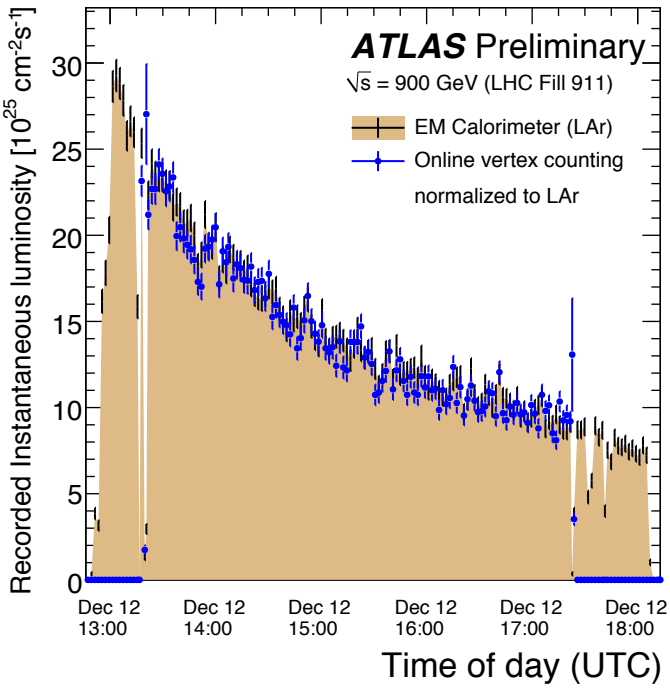

Figure A.15: Relative-luminosity measurement by online vertex counting, compared to the Liquid-Argon (LAr) calorimeter measurement for LHC fill number 911 (Dec 12, 2009). The vertex-counting rate is normalized to the LAr luminosity using only the time bin with the largest number of reconstructed vertices, i.e. with the highest luminosity. The online beam spot algorithm in the HLT is only active in the period of stable beams when the Pixel and SCT detectors are both ramped up.

fill contained 8 non-colliding bunches in each ring, 8 pairs of medium-intensity bunch pairs colliding in ATLAS, as well as one low-intensity (pilot) colliding-bunch pair. The fact that only the 9 colliding bunch pairs result in reconstructed vertices confirms that the contribution of single-beam backgrounds to vertex counting is negligible.

A.3.2 Luminosity-Calibration Scans

Beam-separation scans, originally proposed by S. van der Meer [161] and since routinely used at most high-energy particle colliders, provide a simple method for calibrating the absolute luminosity by measuring simultaneously the collision rate and the fundamental accelerator parameters (Sec. A.2) that determine the luminosity. The bunch charges N_1, N_2 are measured by beam-current transformers; the transverse convolved beam sizes Σ_x, Σ_y are determined by scanning one beam across the other, first horizontally and then vertically, and recording the relative collision rate as a function of the two-beam separation. If the individual beams are Gaussian, the instantaneous luminosity is itself a Gaussian function of the horizontal (vertical) separation, with a standard deviation equal to Σ_x (Σ_y). The absolute luminosity at zero beam-separation can then be computed from the measured bunch charges and convolved beam sizes. An extensive discussion of the systematic uncertainties affecting the absolute luminosity calibration by this method is available in [223]. This approach will be used to calibrate the LHC luminosity at all four experimental IPs, using the procedure detailed in [224].

A preliminary luminosity scan was performed at the ATLAS IP using the 3.5 TeV beams in April 2010. Using both online and offline reconstruction, we monitored the centroid positions and the interaction rate via vertex counting as a function of the nominal horizontal and vertical beam separations programmed into the accelerator control system. The IP positions of each beam and their separation (up to an arbitrary relative offset) were also recorded using the beam-position monitors (BPMs) located ± 21.5 m from the ATLAS IP, on the IP-side of the final-triplet quadrupoles. A total of 9 separation steps were performed in each of the horizontal and vertical planes, of which 7 or 8 points were used for the luminosity calibrations.

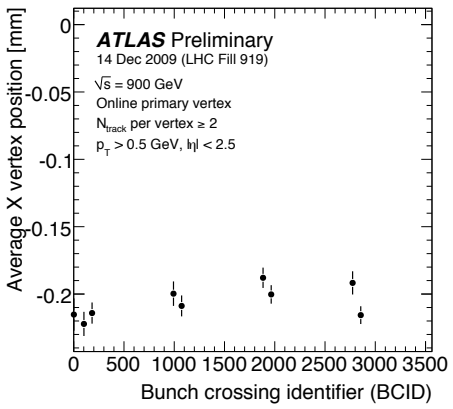

(a) Horizontal luminous centroid vs. BCID.

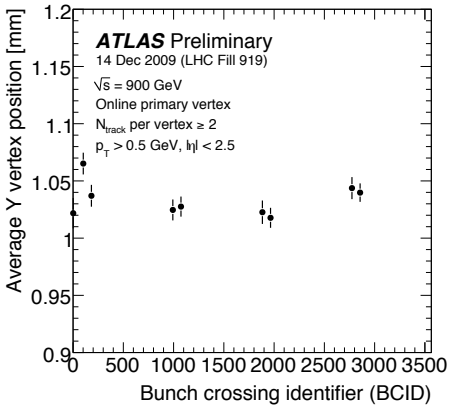

(b) Vertical luminous centroid vs. BCID.

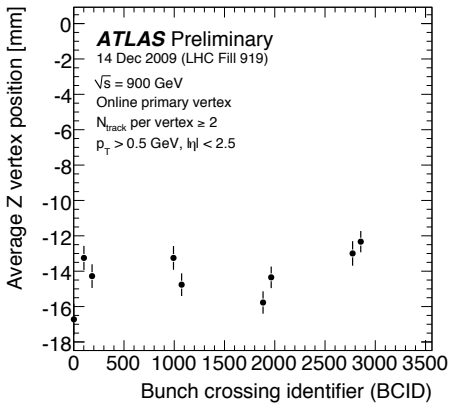

(c) Longitudinal luminous centroid vs. BCID.

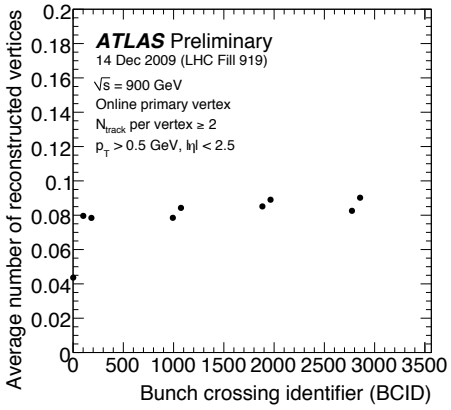

(d) N_{vertex} vs. BCID.

Figure A.16: (x, y, z) position of the luminous centroid and relative luminosity per bunch (N_{vertex}), averaged over an ATLAS run and displayed as a function of the bunch-crossing identifier along the bunch pattern stored in the LHC rings. These quantities are available online for every luminosity block and provide information relevant to ATLAS trigger performance and data quality, as well as to machine conditions.

The online measurements performed during this scan, which provided fast feedback on both luminous-centroid positions and vertex rates in two-minute intervals, are in excellent agreement with the corresponding precision-measurements performed offline (Fig. A.17). Fig. A.18 shows the result of the luminosity scan in each plane as a function of the nominal beam separation. A Gaussian fit to the counting rate yields $\Sigma_x = (94 \pm 1)$ μm and $\Sigma_y = (123 \pm 1)$ μm, where the errors are statistical only. The results constitute a demonstration of the feasibility of the method at the LHC; but they should be interpreted with caution. These scans were performed only for luminosity-optimisation purposes, and were in no way tailored to careful Σ measurements:

- because they were performed during physics running, these particular scans were restricted by machine- and detector-protection considerations to the very narrow range of $\pm 2\,\sigma_{ib}$, thereby limiting the lever arm of the beam-size fit;

- no attempt was made to re-measure the convolved width after ensuring that the beams were properly centered on each other in both x and y, potentially biasing both the width determination and that of the peak event rate;

- the two-minute luminosity blocks were not strictly synchronized with the scan steps. (However, comparisons of the BPM and reconstructed-vertex data indicate that the two were in phase with each other, and aligned to within the measurement uncertainties obtained.)

Full-fledged luminosity-calibration scans that correct these early operational shortcomings will shortly become available. Potential systematic uncertainties on the convolved beam sizes measured by vertex counting may include effects associated with the tracking and vertexing performance or the internal alignment of the ATLAS Inner Detector. One of the dominant instrumental uncertainties is likely to be that associated with the calibration of the length scale attached to the beam separation, which is the topic of the next section.

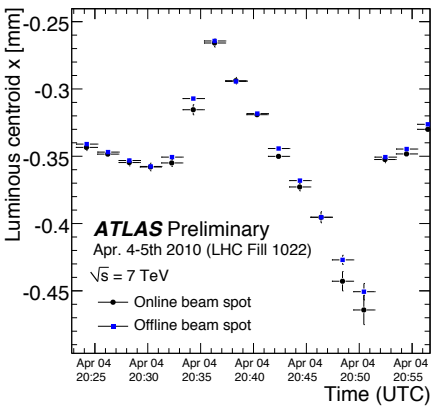

(a) Horizontal luminous centroid.

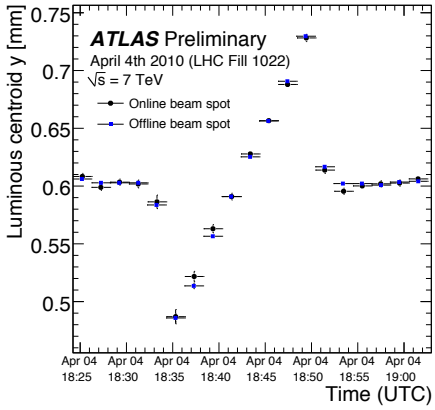

(b) Vertical luminous centroid.

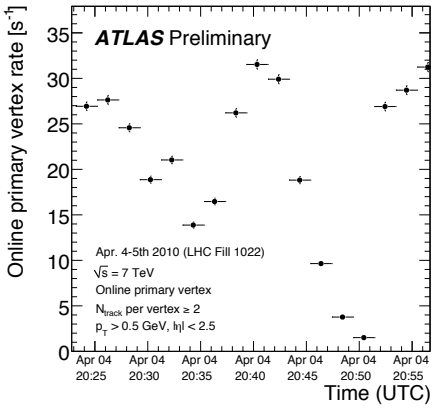

(c) Vertex rate during horizontal scan.

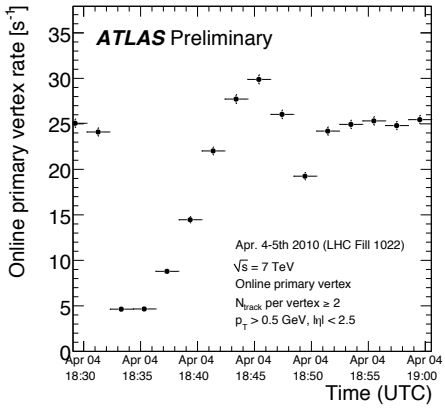

(d) Vertex rate during vertical scan.

Figure A.17: Top: position of the transverse luminous centroids during the luminosity-optimization scans, as monitored online (black circles) and later reconstructed offline (blue squares). Bottom: primary-vertex rates measured online during the luminosity-optimization scans.

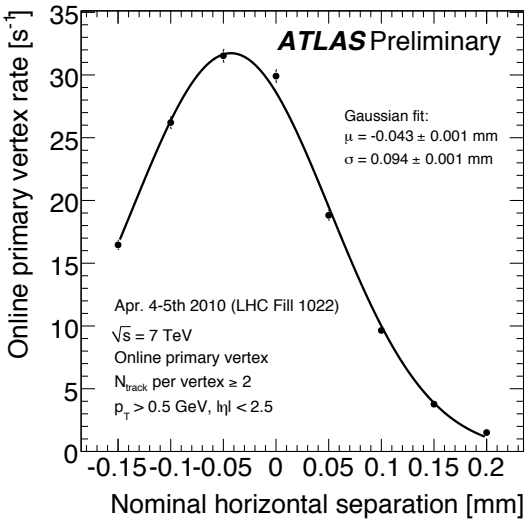

(a) Horizontal luminosity scan.

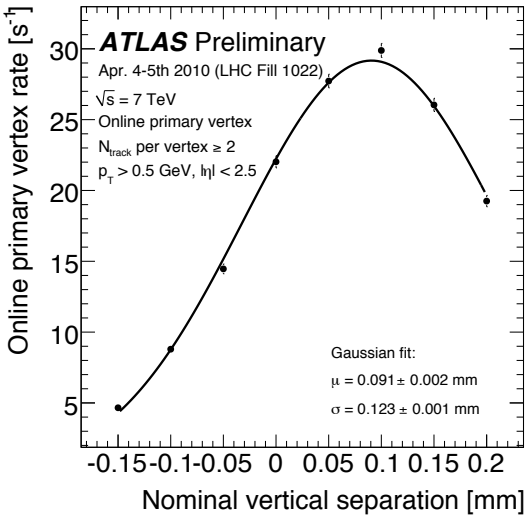

(b) Vertical luminosity scan.

Figure A.18: Luminosity scan data for the (a) horizontal and (b) vertical planes using online primary-vertex counting.

A.3.3 Length-Scale Calibration

In order to extract the luminosity from the scan data, it is critical to know with great precision the absolute length scale that corresponds to the magnet settings on the closed orbit bumps that generate the beam separation. A relative scale uncertainty at the few percent level would directly translate into the same systematic uncertainty on Σ_x and/or Σ_y.

The only accelerator instrumentation against which to calibrate this length scale would be beam-position monitors, the short-term stability and reliability of which have so far proven insufficient in view of the accuracy required. In contrast, the vertexing ability of the ATLAS Inner Detector, together with its precisely-known geometry, provide a viable alternative.

The calibration of the beam-separation scale is performed by displacing both beams from the nominal collision point while maintaining the optimal luminosity (i.e. by ensuring that the two beams remain well centered on each other). Specifically, a "mini" luminosity scan is first performed at the nominal collision point in both the horizontal and vertical planes in order to determine the optimal relative beam positions, after which enough events are recorded for a precision measurement of the transverse IP position. Both beams are then displaced in the horizontal direction by as large an offset as possible (typically +1.5-2.0 σ_{ib}) while remaining safely within the available aperture at the nearby collimators. A second optimization is then performed in both dimensions, and the displacement of the horizontal luminous centroid is measured via event vertices. Next, the two beams are both moved horizontally, by the same offset on the other side of the original collision point, and a third optimization is performed, followed again by the measurement of the luminous-centroid position. A constrained linear fit of the horizontal-centroid position vs. the nominal horizontal separation provides the distance scale, together with goodness-of-fit and error estimates. The entire procedure is then repeated for the vertical length-scale calibration.

Such a length-scale calibration was performed at IP1 in late April 2010, following the procedure described above. Three collision points were measured in both the horizontal and vertical planes with luminous centroid offsets of ± 100 μm in each case

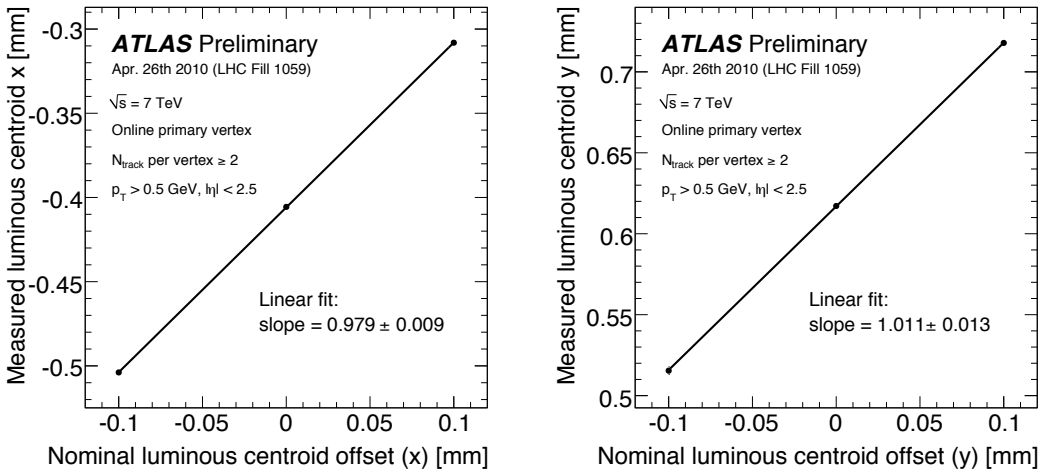

(a) Horizontal length scale.

(b) Vertical length scale.

Figure A.19: Length scale calibration of the nominal luminous centroid offset programmed into the LHC control system in (a) the horizontal and (b) the vertical direction. The measured luminous centroid offset in the ATLAS coordinate system is observed to follow the nominal offset with a calibration factor of 0.979 ± 0.009 and 1.011 ± 0.013 in the horizontal and vertical directions.

as compared to the nominal collision point. At each point, the luminous centroid is determined online using event vertices, yielding a precision of approximately 2 μm or better. Comparing these measurements to the relative positions expected from the magnet settings (Fig. A.19), we find the absolute length-scale calibration needed for a full determination of Σ_x and Σ_y to be 0.979 ± 0.009 and 1.011 ± 0.013 in the horizontal and vertical directions, respectively. In each case, the χ^2 probability (or "p-value") is greater than 79 %, indicating a very high goodness-of-fit. The associated systematic uncertainty is roughly estimated to be ± 2 %, dominated by the precision to which the two beams could be kept transversely aligned.

A.3.4 Disentangling of Individual Transverse Beam Sizes

Because the transverse convolved beam sizes (Eq. A.5) and the luminous widths (Eq. A.7) depend differently on the single-beam sizes σ_{ib} ($i = x, y$; $b = 1, 2$), a simultaneous measurement of Σ_x, Σ_y and of $\sigma_{x\mathcal{L}}$, $\sigma_{y\mathcal{L}}$ at zero beam separation yields

Beam i b	$\bar{\epsilon}_{ib}$ (μm rad)	β^* (m)	$\sigma_{i\mathcal{L}}$ (μm) (expected)	$\sigma_{i\mathcal{L}}$ (μm) (measured)	Σ_i (μm) (measured)	σ_{ib} (μm) (expected)	σ_{ib} (μm) (measured)
1 x	1.71	11	53.0	46 ± 2	94 ± 1	71.0	59^{+7}_{-6}
2 x	2.15					79.6	73^{+4}_{-7}
1 y	1.85		60.0	60 ± 2	123 ± 1	73.9	77^{+10}_{-6}
2 y	3.60					103.0	96^{+4}_{-9}

Table A.1: Measurement of the individual beam sizes using Eq. A.9 and comparisons to wire-scanner based emittances. $\sigma_{i\mathcal{L}}$ is measured using the offline beam spot determination while Σ_i is measured using online vertex counting. The errors are statistical only. The time evolution of the normalized emittances ($\bar{\epsilon}_{ib}$) is displayed in Fig. A.13, where the corresponding luminous-size predictions are compared with the offline result for $\sigma_{i\mathcal{L}}$. The emittances listed in this table were linearly interpolated from the measurements immediately before and after the scan period.

a direct determination (up to a two-fold ambiguity) of the individual transverse sizes of beams 1 and 2,

$$\sigma_{1,2}{}^2 = \Sigma^2/2 \pm \sqrt{\Sigma^4/4 - \Sigma^2\ \sigma_{\mathcal{L}}{}^2}\ . \tag{A.9}$$

The method was successfully applied at the PEP-II B-factory [160]. The results can be validated (and the ambiguity sometimes lifted) by comparing them to single-beam IP sizes determined from emittances measured at wire scanners or synchrotron-light monitors combined with lattice functions extracted from β-beat measurements.

The online Σ measurements shown in Fig. A.18 and the offline measurements of $\sigma_{\mathcal{L}}$, input to Eq. A.9, yield a measurement of the individual beam sizes. Using the values $\Sigma_x = (94 \pm 1)\ \mu$m, $\Sigma_y = (123 \pm 1)\ \mu$m, $\sigma_{x\mathcal{L}} = (46 \pm 2)\ \mu$m and $\sigma_{y\mathcal{L}} = (60 \pm 2)\ \mu$m, we obtain

$$\begin{aligned} \sigma_{x1,2} &= 59^{+7}_{-6}\ \mu\text{m},\ 73^{+4}_{-7}\ \mu\text{m}\ , \\ \sigma_{y1,2} &= 77^{+10}_{-6}\ \mu\text{m},\ 96^{+4}_{-9}\ \mu\text{m}\ . \end{aligned}$$

The extraction of single-beam sizes using Eq. A.9 and their comparison with wire-scanner-based emittances and measured lattice functions are summarized in Tab. A.1.

Only the statistical errors associated with the convolved- and luminous-size measurements are considered here; the systematic uncertainties affecting the emittances and β-functions, as well as those associated with the vertexing resolution, are neglected at this time. Consequently, the comparison between measured and expected beam sizes, meant only, at this stage, as a test of the validity of the method, is more demanding than if those uncertainties had been taken into account.

While the horizontal luminous size predicted using the emittance measurements is somewhat larger than the observed value, the expected vertical luminous size is in fact very close to the one measured directly. Therefore, the individual beam sizes computed from the combined measurement of the convolved and luminous sizes agree rather well with the expectations from the emittance measurements in the vertical plane, while the agreement of the horizontal sizes with the expectation is at least fair. In spite of the operational limitations outlined in Sec. A.3 and of the $\sim 10\,\%$ uncertainties affecting the measured values of ϵ and β^*, the level of agreement is, at such an early stage, rather satisfactory.

Appendix B

Noise suppression for tower jets

Until this work only the 3-dimensional topological clustering method applied any noise suppression in order to select cells with significant energy content compared to the expected noise. In this approach, the so-called "4-2-0" noise suppression algorithm is used which applies an iterative selection of cells based on the signal-to-noise ratio in three steps, where the integers refer to the signal-to-noise ratio, or number of σ above the noise, required for each step [225]. We instead use the 4-2-0 algorithm as a way of selecting cells to fill the $\eta \times \phi$ tower grid and thus restore the fixed geometrical tower picture of the jet input but with topological noise suppression applied. By using all cells included in topo-clusters, noise suppressed towers remain independent of the full topo-cluster formation algorithm which must be tuned in order to optimize the size, shape and energy content of clusters, and only make use of the inherent noise-suppression. A schematic representation of each input constituent type is shown in Section 5.1 Figure 5.1[1].

The motivation for this approach is to retain the tower-based object as input to the jet reconstruction but to render it much more robust against the effects of noise and high calorimeter occupancy, such as is expected in events with many simultaneous proton-proton collisions, or "pile-up." Towers provide a clearly defined geometrical phase space in which to define the input to jet reconstruction at the expense of losing some of the high-granularity provided by the ATLAS calorimeters. Applying noise

[1]Representations of input types courtesy of K. Perez.

suppression to tower-objects before jet finding and reconstruction will be shown to greatly improve the jet-energy resolution in events at moderate LHC luminosities. In addition, certain jet energy scale corrections such as the tower-based baseline offset correction (see Section 6.1), benefit from a geometrical description of the underlying jet constituents.

B.1 Optimization

By recomputing the geometrical tower grid using only those cells selected by the topological clustering algorithm, the opportunity exists to compare the response and resolution of jets constructed from noise-suppressed towers constructed using further sub-samples of those cells.

In the following study, seven configurations are considered:

1. **"topo-towers (4-2-0)":** The standard 4-2-0 configuration in which all cells selected by the clustering are included in the noise-suppressed tower definition.

2. **"4-2-0 ($E_{\text{cell}} > 0$)":** The same as above, but where the cells are further required to have $E_{\text{cell}} > 0$ in order to be included into the tower grid.

3. **"4-2-1":** The final step in the topological clustering algorithm is restricted to adding a last layer of cells for only those cells which have an energy that is at least $E_{\text{cell}}/\sigma > 1$ above the expected noise RMS.

4. **"4-2":** The final step in the clustering algorithm is omitted altogether (and only those cells with $E_{\text{cell}}/\sigma > 2$ are included)

5. **"4-2-1 ($E_{\text{cell}} > 0$)":** The same approach as in (3), but only cells with positive energy are included.

6. **"4-2 ($E_{\text{cell}} > 0$)":** The same approach as in (4), but only cells with positive energy are included.

7. **"4-2-0 (seeded)":** The original 4-2-0 approach defined in (1) is used, but resulting noise-suppressed towers are required to contain at least one cell with

$E_{\text{cell}}/\sigma > 4$ (i.e. a "seed" cell).

B.2 Performance

The performance of each jet input definition is assessed by evaluating the fractional jet transverse momentum resolution for jets built from towers, topological clusters, and topo-towers at three representative luminosities. The three equivalent luminositites considered are: (1) no pile-up, (2) $10^{32}\text{cm}^{-2}\text{s}^{-1}$ with 450ns bunch spacing, and (3) $2\times10^{33}\text{cm}^{-2}\text{s}^{-1}$ with 25ns bunch spacing. As shown in Figure B.2, tower-jets show the greatest sensitivity to pile-up while jets built from both clusters and topo-towers show very little change as the luminosity increases and are consistent with each other. The degradation only appears significantly for the higher luminosity sample, which is one reason why the performance of standard towers persisted as the default geometric configuration for jet inputs [183].

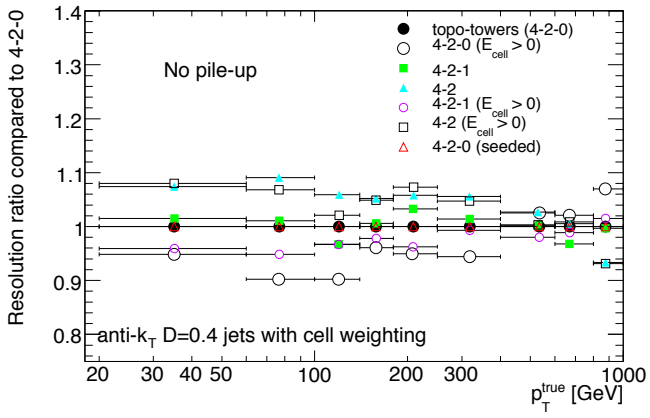

(a) No pile-up

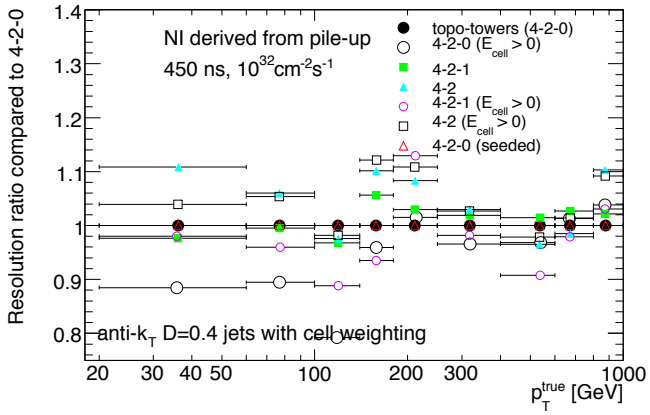

(b) $\mathcal{L} = 10^{32}$ cm^{-2}s^{-1}, 450ns)

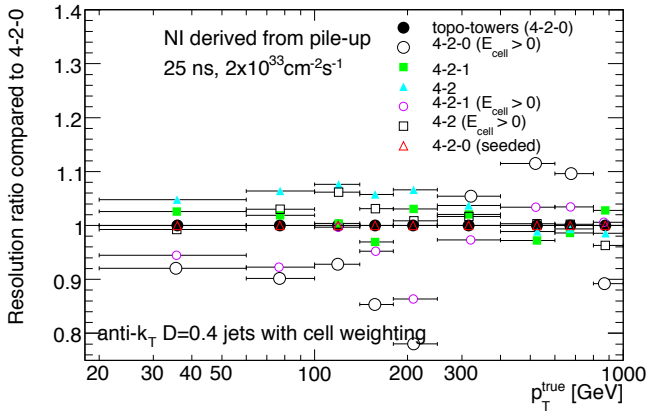

(c) $\mathcal{L} = 2 \times 10^{33}$ cm^{-2}s^{-1}, 25ns

Figure B.1: Ratio of the jet energy resolution for anti-k_t topo-tower jets compared to the default 4-2-0 setting.

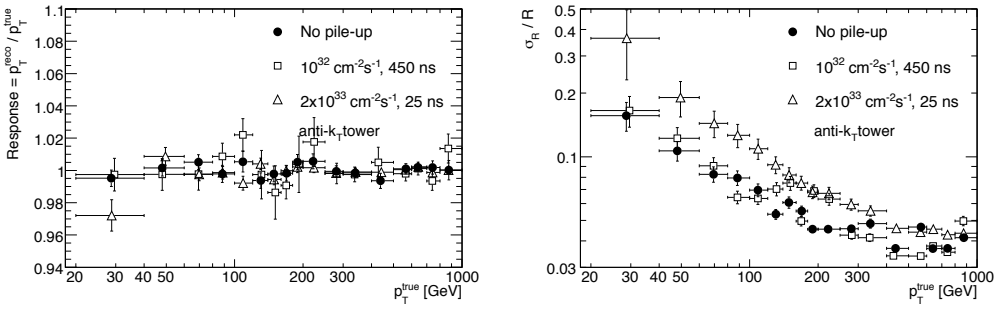

(a) Towers: response (b) Towers: resolution

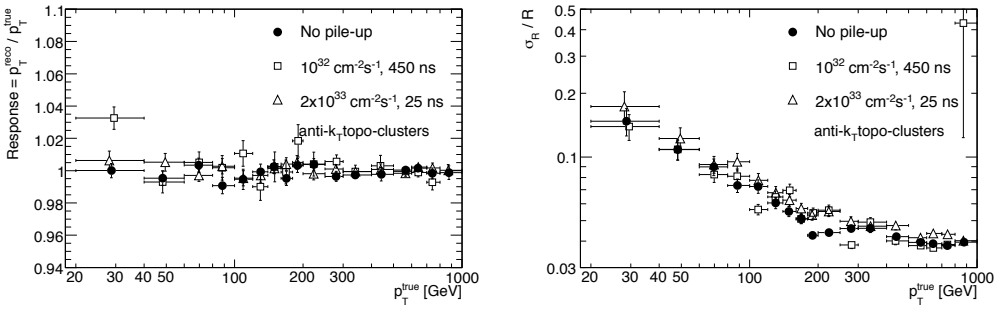

(c) Topo-clusters: response (d) Topo-clusters: resolution

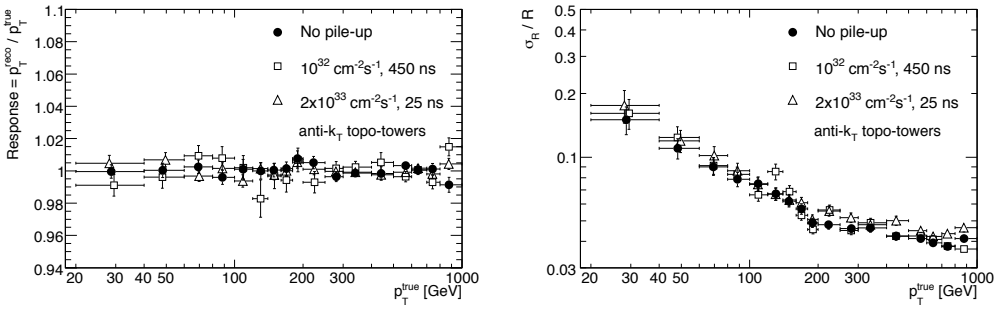

(e) Topo-towers: response (f) Topo-towers: resolution

Figure B.2: Fractional jet transverse momentum resolution for jets built from towers (left) topological clusters (center) and topo-towers (right) and at three representative luminosities, no pile-up (solid circles), $10^{32}\text{cm}^{-2}\text{s}^{-1}$, 450ns bunch spacing (open squares) and $2 \times 10^{33}\text{cm}^{-2}\text{s}^{-1}$, 25ns bunch spacing (open triangles). Tower-jets show the greatest sensitivity to pile-up while jets built from both clusters and topo-towers show very little change as the luminosity increases and are consistent with each other.

Appendix C

Pile-up offset correction derived from Monte Carlo

C.1 Monte Carlo samples

In order to simulate the effect of pile-up, additional interactions are overlaid onto a given signal event during the simulation of the digital electronics or "digitization" [226]. Events of each type to be included are generated independently, but then passed through the digitization and detector reconstruction chain together. The electronics simulation for each sub-detector uses a time-window determined by that sub-detector's integration time (which can be several bunch crossings). For example, the ATLAS Monitored Drift Tube (MDT) muon drift chambers require an overall integration time window from -36 to +32 bunch-crossings due to the ∼400-1200 ns drift time [227], where the reference bunch-crossing is the simulated signal event. Thus, "pile-up" correctly refers to both the in-time MB and cavern background interactions as well out-of-time (all others), although the sensitivity to these events is not identical for all sub-detectors.

Two luminosities and bunch spacing scenarios are considered, as both aspects of the running conditions will affect the pile-up subtraction techniques used. A "low" and a "high" luminosity scenario have been generated with luminosities of

$\mathcal{L} = 10^{32}$ cm^{-2}s^{-1} and 2×10^{33} cm^{-2}s^{-1}, respectively. The low luminosity configuration corresponds roughly to the running conditions expected during 2010 and 2011 and has a per-event average vertex multiplicity of $\langle N_{\mathrm{PV}} \rangle = 4.1$ and a large 450 ns bunch spacing. The high luminosity configuration has a per-event average vertex multiplicity of $\langle N_{\mathrm{PV}} \rangle = 4.6$ and the nominal 25 ns bunch spacing.

C.1.1 Application of the tower-based offset correction

The correction is derived in minimum bias events with multiple interactions, simulated with two different luminosity and bunch spacing configurations of $\mathcal{L} = 10^{32}$ cm^{-2}s^{-1} with a 450 ns bunch spacing and $\mathcal{L} = 2 \times 10^{33}$ cm^{-2}s^{-1} with a 25 ns spacing. The average interaction rate per event for these samples is $\langle N_{\mathrm{PV}} \rangle_{\ 450\mathrm{ns}} = 4.1$ and $\langle N_{\mathrm{PV}} \rangle_{\ 25\mathrm{ns}} = 4.6$, respectively. Although similar, they represent two very different configurations in terms of the relative contribution of in-time and out-of-time pile-up effects. With bunch spacings larger than 400 ns, the response the front-end electronics in the calorimeter is essentially negligible whereas with the nominal 25 ns spacing, significant out-of-time effects will be observed. Therefore it is important to asses the performance of the offset correction in both configurations.

Using the energy density distributions we derive the offset correction with respect to events with a single interaction for the large 450 ns bunch spacing scenario and with respect to the average number of interactions for the nominal bunch spacing of 25 ns. The energy density offset as a function of η and N_{PV} for each $\Delta\eta \times \Delta\phi = 0.1 \times 0.1$ tower is shown in Figure C.1 where it is clear that the reference N_{PV} for each configuration is different. We also clearly see the increase in energy density as the number of in-time interactions increases in each case; there is nearly an order of magnitude difference between $N_{PV} = 2$ and $N_{PV} = 8$ across the entire detector.

We apply the offset correction as an overall scale difference for each luminosity scenario by using the energy density offset and the number of towers present in each jet. The jet axis is used to determine the η range of the energy density correction, which a simple approximation of which range dominates the jet energy measurement. This method provides a continuous spectrum of applied offsets which is only dependent

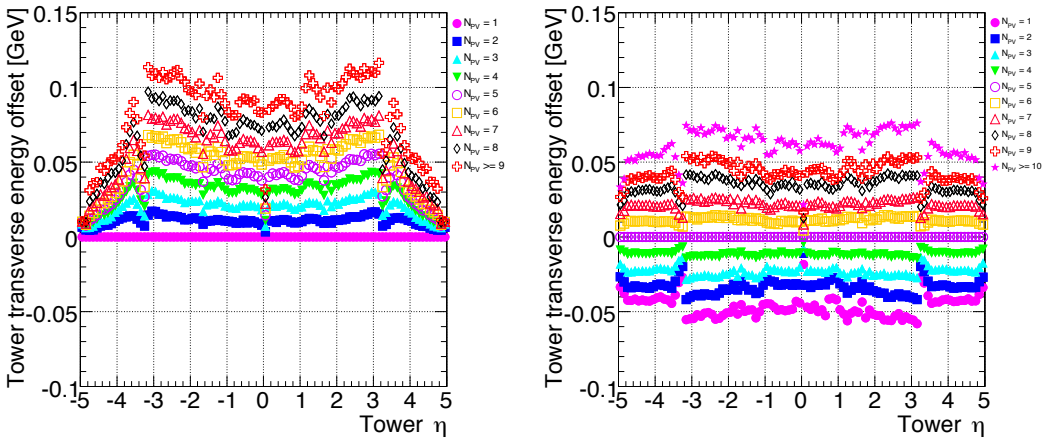

(a) (b)

Figure C.1: Derived offset correction for (a) $\mathcal{L} = 10^{32}$ cm^{-2}s^{-1}, 450 ns bunch spacing and (b) $\mathcal{L} = 2 \times 10^{33}$ cm^{-2}s^{-1}, 25 ns bunch spacing.

on the number of reconstructed vertices in the event and the size of each jet. Distributions of the applied correction factors are shown in Figure C.2. Several notable features are evident:

- Jets in events with the reference number of interactions (N_{PV} =1 or 5 for $\mathcal{L} = 10^{32}$ or 2×10^{33} cm^{-2}s^{-1}, respectively) receive no offset correction.

- For the nominal 25 ns bunch spacing, the average applied offset is approximately zero because the the reference number of interactions is explicitly defined as the mean of the Poisson distribution at that luminosity.

- Peaks in the applied offset represent jets with the average area in each class of events (N_{PV} = 2, 3, 4, etc) with a distribution representative of the spread in the number of towers clustered into each jet.

- The magnitude of the difference in applied offset between the highest and lowest jets is larger in the higher luminosity sample by nearly 20% (10 GeV compared to 8 GeV).

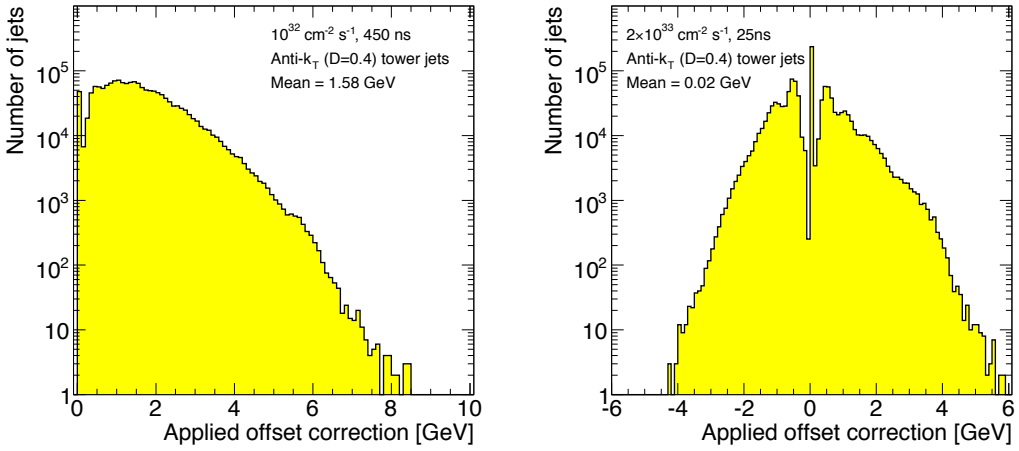

(a) (b)

Figure C.2: Applied offset correction for (a) $\mathcal{L} = 10^{32}$ cm^{-2}s^{-1}, 450 ns bunch spacing and (b) $\mathcal{L} = 2 \times 10^{33}$ cm^{-2}s^{-1}, 25 ns bunch spacing.

C.1.2 Performance of the tower-based offset correction

The primary figure of merit used for evaluating the performance of the offset correction is the linearity of the response as a function of the number of reconstructed primary vertices. A flat response establishes a baseline jet energy scale which is independent of event-by-event fluctuations in the number of interactions. Since the offset correction must establish this independence prior to the application of any of the following jet energy scale corrections (in order to avoid the need to derive subsequent corrections as a function of the number of additional interactions) we define the response as the ratio of the uncalibrated electromagnetic (EM) scale reconstructed jet transverse momentum to the matched truth particle jet transverse momentum, where a match is defined as $\Delta R = \sqrt{\Delta\eta^2 + \Delta\phi^2} < 0.3$. In addition, reconstructed jets are required to be isolated within a cone of 1.5 times the jet radius, or $\Delta R_{\text{isolation}} = 1.0$ for anti-k_t jets with $R = 0.4$.

In Figure C.3 we show the jet response across η for events with various numbers of reconstructed vertices. Structural variations are present both before and after the offset correction which are due to variations in the detector segmentation, response

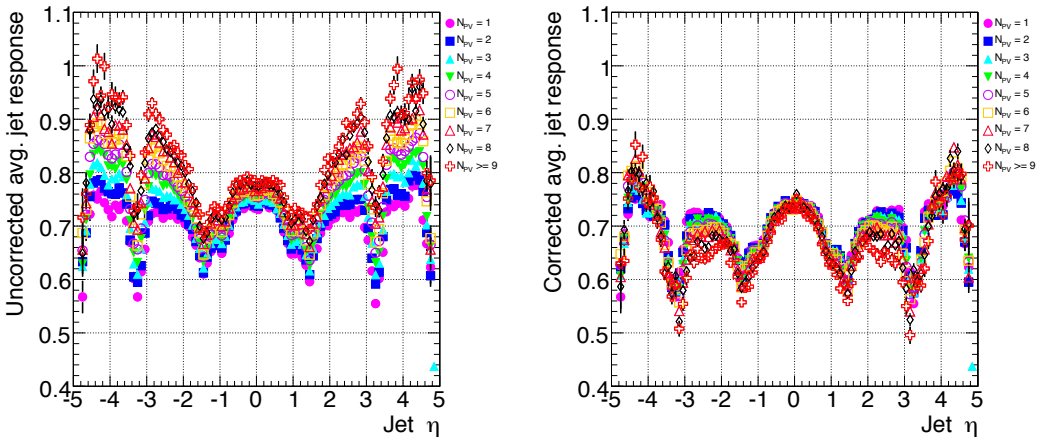

(a) Uncorrected, 10^{32} cm^{-2}s^{-1}, 450 ns

(b) Corrected, 10^{32} cm^{-2}s^{-1}, 450 ns

(c) Uncorrected, 2×10^{33} cm^{-2}s^{-1}, 25 ns

(d) Corrected, 2×10^{33} cm^{-2}s^{-1}, 25 ns

Figure C.3: Response of anti-k_t $R = 0.4$ noise-suppressed tower jets in events at low (10^{32} cm^{-2}s^{-1}) and high (2×10^{33} cm^{-2}s^{-1}) luminosity as a function of η. Pile-up subtraction demonstrates good closure across the entire η range.

and dead material distributions in different regions. Despite this large-scale structure, the increase in EM scale response as the number of interactions increases is clear both at low and high luminosities and is a direct reflection of the increase in average calorimeter response as the instantaneous luminosity rises. Both the magnitude of the response and it's shape as a function of η changes, as is most clear in the region $2.0 \leq |\eta| \leq 3.0$. By applying the offset correction derived in Figure C.1, both the scale and shape vs. η are approximately restored.

The relevant closure test of the offset correction is the linearity as a function of N_{PV}. Because of the large variation in detector response and the charged particle multiplicity spectrum across η, it is necessary to evaluate this closure test in many η ranges independently. In Figure C.4 we present the closure test in the most important barrel η ranges $0 \leq |\eta| < 0.3$ and $0.3 \leq |\eta| < 0.8$. Not only do these represent the ranges in which most measurements will focus in the first years of operation, but they also form the regions that are used as references in calibration schemes for higher η. It is therefore most crucial in the central η region that the offset correction provides a uniform response as a function of N_{PV}.

For both the low (10^{32} cm^{-2}s^{-1}) and high (2×10^{33} cm^{-2}s^{-1}) luminosity scenarios, the closure test exhibits excellent linearity as a function of N_{PV}. This is true both for all jets, as well as for jet matched to lower p_T truth particle jets which are the most sensitive to pile-up effects. Results for closure tests across the entire calorimeter can be found in Appendix C.2. In general, the tower-based offset correction demonstrates extremely good performance across a range of detector regions and luminosities. The higher luminosity sample does exhibit some slight over-corrections (i.e. a slightly negative slope after the offset correction) particularly in the high-η region. This may indicate that the propensity of a jet to cluster uncorrelated soft particles into itself is over-estimated by the tower-energy density method. One candidate for this over-estimation is in the importance of out-of-time energy depositions, which may have a large effect when summed linearly across an entire η range, yet are not as likely to be clustered into a jet from the hard-scatter interaction. A simpler possibility is that the approximation that energy density to be subtracted from the jet is found using the jet axis is too naive.

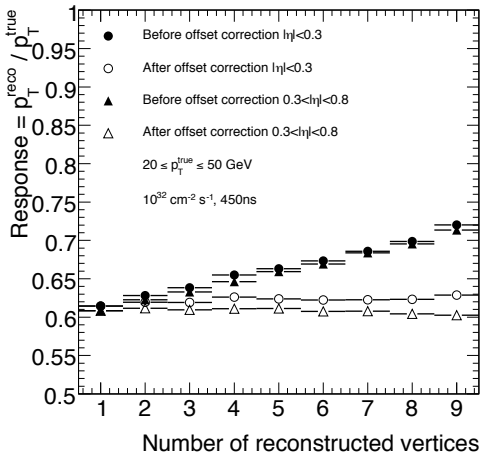

(a) $20 \leq p^{\text{true}} \leq 50$ GeV

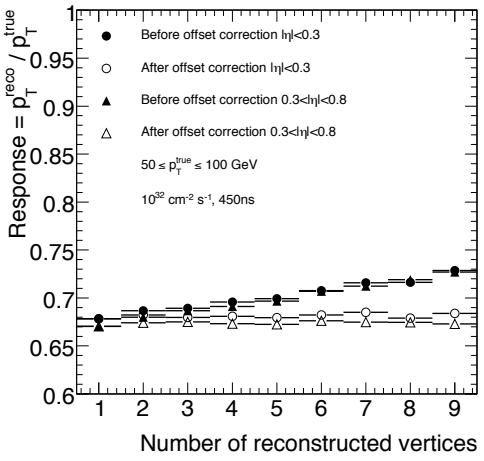

(b) $50 \leq p^{\text{true}} \leq 100$ GeV

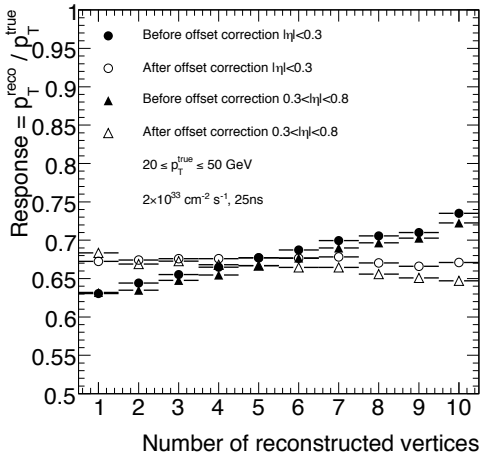

(c) $20 \leq p^{\text{true}} \leq 50$ GeV

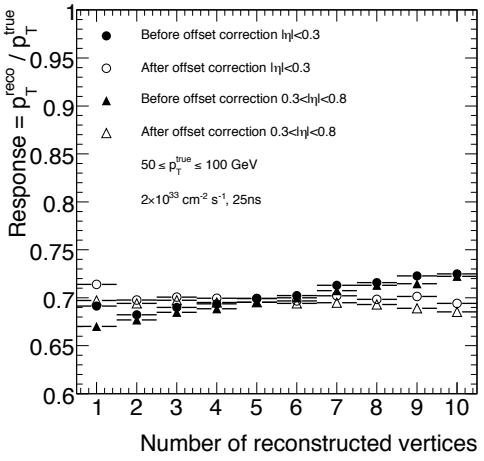

(d) $50 \leq p^{\text{true}} \leq 100$ GeV

Figure C.4: Response of anti-k_t $R = 0.4$ noise-suppressed tower jets in events at $\mathcal{L} = 10^{32}$ cm^{-2}s^{-1} (top) and $\mathcal{L} = 2 \times 10^{33}$ (bottom) as a function of the number of reconstructed vertices for two central η regions, $0 \leq |\eta| < 0.3$, (circles) and $0.3 \leq |\eta| < 0.8$ (triangles) before any offset correction is applied (solid) and after the tower-based offset (open). We also show the closure test applied to only low p_{T} (left) and only mid-range p_{T} (right) jets. All other η ranges can be found in Appendix C.2.

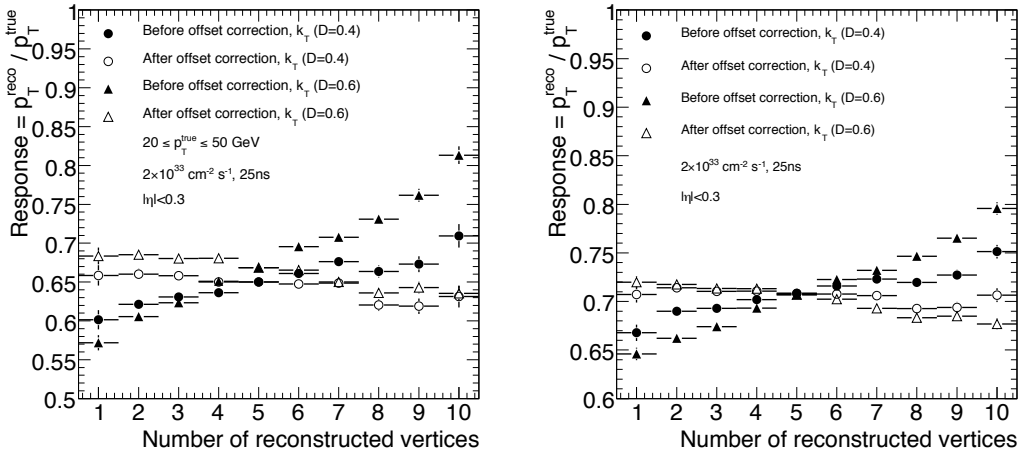

(a) $20 \le p^{\text{true}} \le 50$ GeV (b) $p^{\text{true}} \ge 20$ GeV

Figure C.5: Response of k_T $R = 0.4$ and 0.6 noise-suppressed tower jets et the EM scale as a function of truth jet p_T. All jets are restricted to the very central η range $|\eta| < 0.3$ and for the high luminosity, small bunch spacing scenario. Results are shown for (a) low $20 \le p^{\text{true}} \le 50$ GeV and (b) for $p_T^{\text{true}} \ge 20$ GeV, inclusively.

To demonstrate the wide applicability of this form of the offset correction, Figure C.5 shows the closure test for k_T jets of two different radii at high luminosity. Prior to the correction, the EM scale jet response is significantly more affected by the presence of pile-up due mostly to the design of the k_T algorithm to cluster low p_T particles into the jet. This results in a larger uncorrelated pile-up energy content of the resulting jet which must then be accounted for, and is clearly more difficult due to the non-cone-like nature of the algorithm itself. Following the offset correction, the linearity of the response is dramatically improved, particularly for jets with $20 \le p^{\text{true}} \le 50$ GeV. Although the closure is not perfect, this is expected to be due to the approximation mentioned above, namely that that energy density to be subtracted from the jet is determined using the position of the jet axis which for the k_T algorithm is not a good assumption for the η ranges contributing to the jet. Nonetheless, this is a direct demonstration of the flexibility of this approach to subtracting pile-up contributions to jets.

Figure C.6 provides a direct comparison of the EM scale jet response as a function

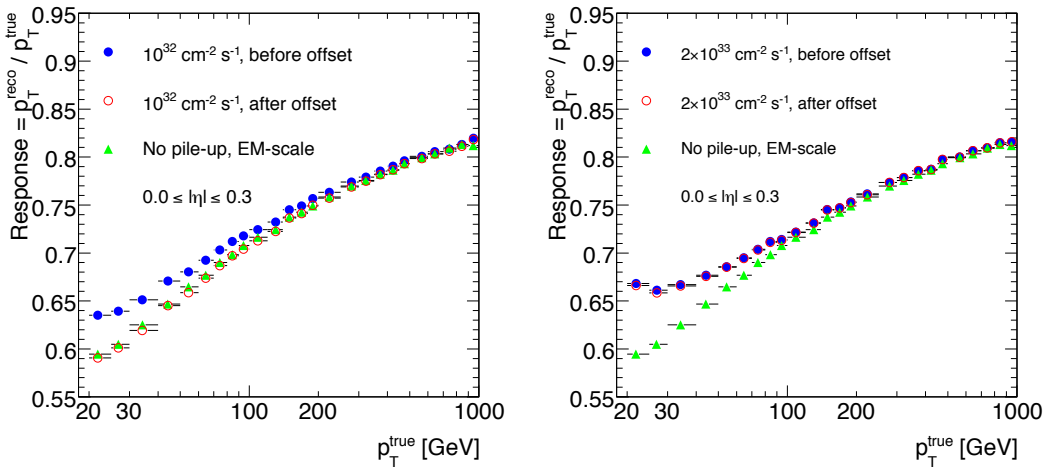

(a) $\mathcal{L} = 10^{32}$ cm^{-2}s^{-1}, 450 ns (b) $\mathcal{L} = 2 \times 10^{33}$ cm^{-2}s^{-1}, 25 ns

Figure C.6: Response of anti-k_t $R = 0.4$ noise-suppressed tower jets et the EM scale as a function of truth jet p_{T}. Results are shown for (a) $\mathcal{L} = 10^{32}$ cm^{-2}s^{-1} with a 450 ns bunch spacing and (b) for $\mathcal{L} = 2 \times 10^{33}$ cm^{-2}s^{-1} with a 25 ns bunch spacing, both for the very central η range $0 \leq |\eta| < 0.3$. All other η ranges can be found in Appendix C.3.

of truth particle jet p_T both with and without pile-up, and before and after the offset correction. Both the low and high luminosity ranges are shown and each exemplify relevant features of the offset correction in each scenario. For the low luminosity, large bunch spacing scenario, one sees that the response after the offset correction more closely resembles that without pile-up. Although the exact shape is certainly not expected to be exactly reproduced because the correction is meant to restore closure in bins of N_{PV}, not in bins of p_T^{true}, the agreement is excellent. Alternatively, for the high luminosity, short bunch spacing scenario, the response curves before and after the offset correction are identical by construction. In this case, the offset itself is zero for the *average* event (specifically, for the average N_{PV}). Again, since the correction is meant to restore closure in bins of N_{PV} and not in bins of p_T^{true}, this is the expected behavior. Similar response functions for all other η ranges can be found in Appendix C.3.

C.2 Response vs. N_{PV} for all η ranges

The full set of η regions corresponding to different detector regions are presented here, in addition to the barrel region shown in Figure C.4:

- Transition region: $0.8 \leq |\eta| < 1.7$
- Endcap region: $1.7 \leq |\eta| < 2.8$
- Endcap and forward region: $2.8 \leq |\eta| < 4.5$

C.2.1 Transition region: $0.8 \leq |\eta| < 1.7$

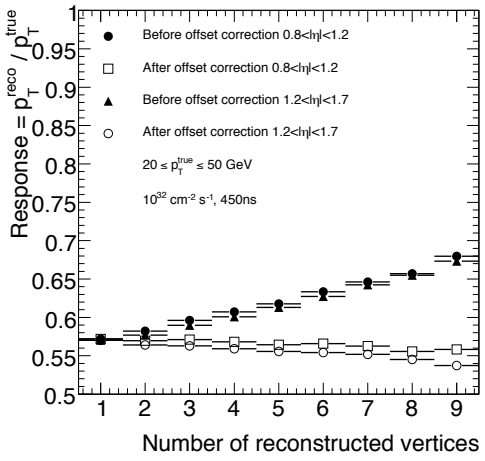

(a) $\mathcal{L} = 10^{32}$ cm^{-2}s^{-1}, 450 ns, low p_T

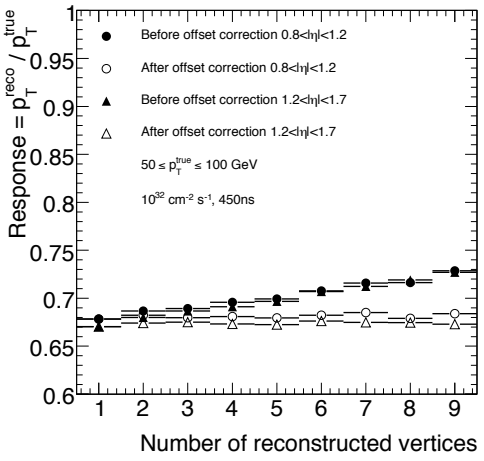

(b) $\mathcal{L} = 10^{32}$ cm^{-2}s^{-1}, 450 ns

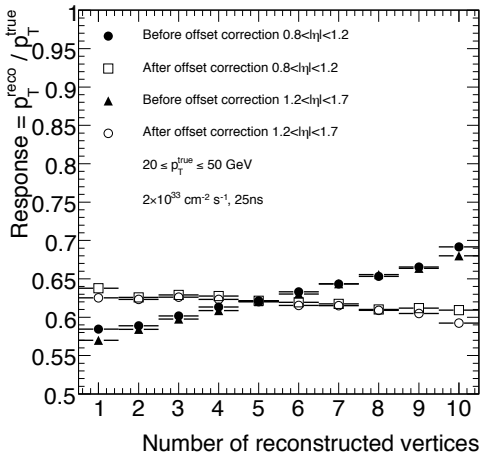

(c) $\mathcal{L} = 2 \times 10^{33}$ cm^{-2}s^{-1}, 25 ns, low p_T

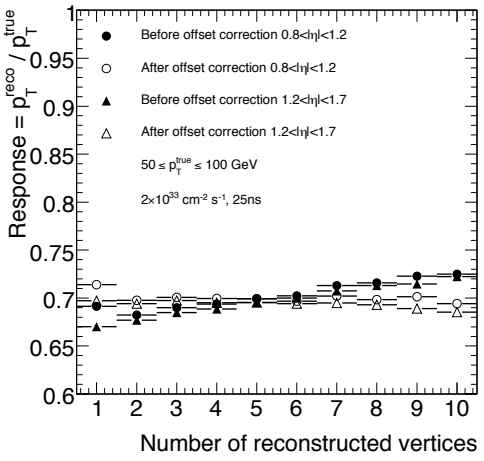

(d) $\mathcal{L} = 2 \times 10^{33}$ cm^{-2}s^{-1}, 25 ns

Figure C.7: Response of anti-k_t $R = 0.4$ noise-suppressed tower jets in events at low (10^{32} cm^{-2}s^{-1}) and high (2×10^{33} cm^{-2}s^{-1}) luminosity as a function of the number of reconstructed vertices. Pile-up subtraction demonstrates good closure for two central η regions, $0.8 \leq |\eta| < 1.2$, (circles) and $1.2 \leq |\eta| < 1.7$ (triangles) before any offset correction is applied (solid) and after the tower-based offset (open).

C.2.2 Endcap region: $1.7 \leq |\eta| < 2.8$

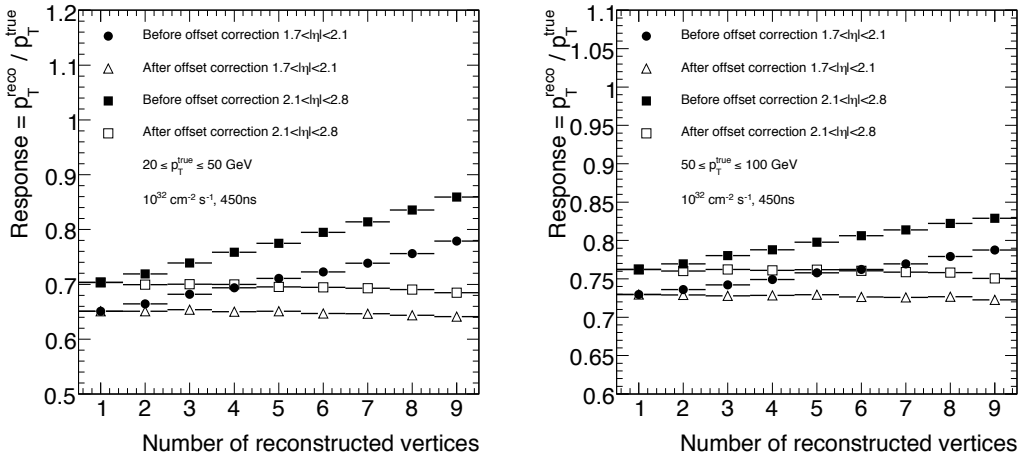

(a) $\mathcal{L} = 10^{32}$ cm^{-2}s^{-1}, 450 ns, low p_T

(b) $\mathcal{L} = 10^{32}$ cm^{-2}s^{-1}, 450 ns

(c) $\mathcal{L} = 2 \times 10^{33}$ cm^{-2}s^{-1}, 25 ns, low p_T

(d) $\mathcal{L} = 2 \times 10^{33}$ cm^{-2}s^{-1}, 25 ns

Figure C.8: Response of anti-k_t $R = 0.4$ noise-suppressed tower jets in events at low (10^{32} cm^{-2}s^{-1}) and high (2×10^{33} cm^{-2}s^{-1}) luminosity as a function of the number of reconstructed vertices. Pile-up subtraction demonstrates good closure for two central η regions, $1.2 \leq |\eta| < 1.7$, (circles) and $1.7 \leq |\eta| < 2.1$ (triangles) before any offset correction is applied (solid) and after the tower-based offset (open).

C.2.3 Endcap and forward region: $2.8 \leq |\eta| < 4.5$

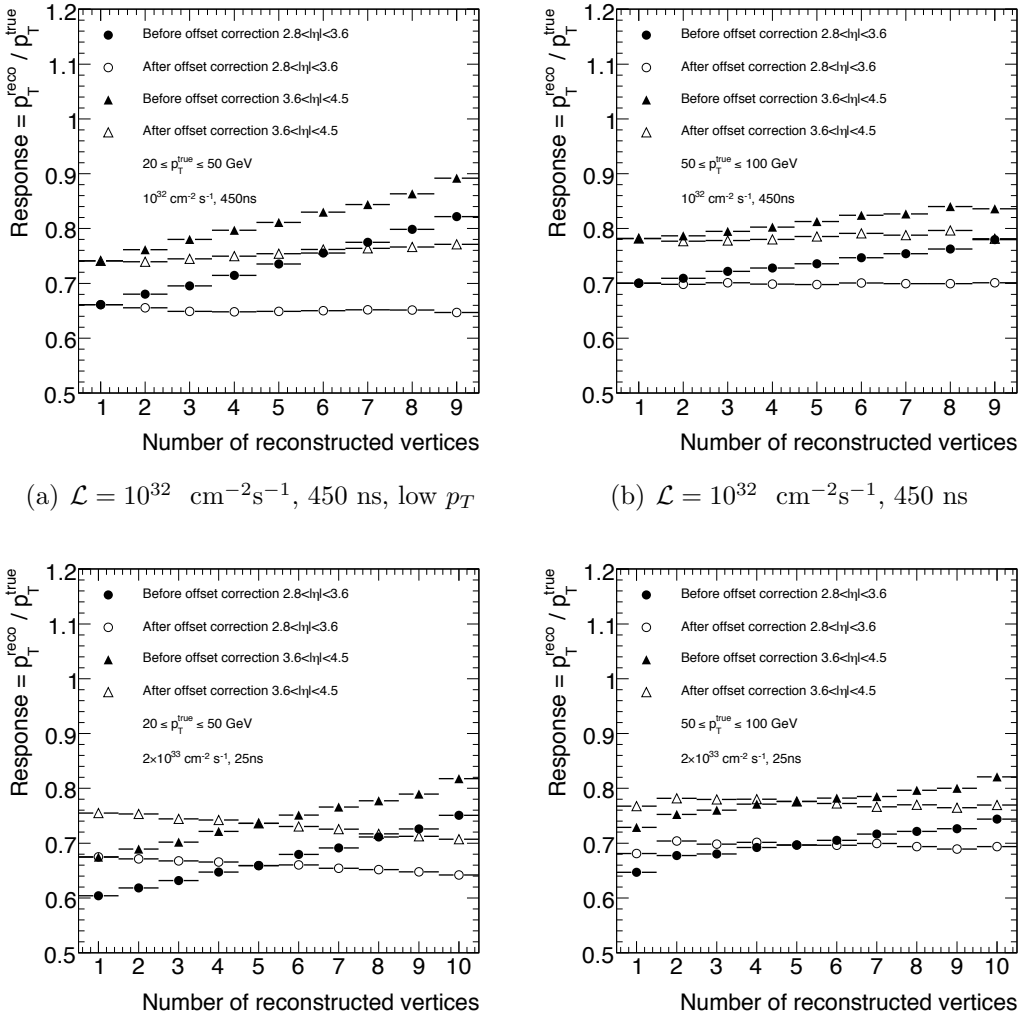

(a) $\mathcal{L} = 10^{32}$ cm^{-2}s^{-1}, 450 ns, low p_T

(b) $\mathcal{L} = 10^{32}$ cm^{-2}s^{-1}, 450 ns

(c) $\mathcal{L} = 2 \times 10^{33}$ cm^{-2}s^{-1}, 25 ns, low p_T

(d) $\mathcal{L} = 2 \times 10^{33}$ cm^{-2}s^{-1}, 25 ns

Figure C.9: Response of anti-k_t $R = 0.4$ noise-suppressed tower jets in events at low (10^{32} cm^{-2}s^{-1}) and high (2×10^{33} cm^{-2}s^{-1}) luminosity as a function of the number of reconstructed vertices. Pile-up subtraction demonstrates good closure for two central η regions, $2.8 \leq |\eta| < 3.6$, (circles) and $3.6 \leq |\eta| < 4.5$ (triangles) before any offset correction is applied (solid) and after the tower-based offset (open).

C.3 Response vs. p_T^{true} for all η ranges

The remaining η regions not presented above are shown here.

C.3.1 Barrel region: $0.3 \leq |\eta| < 1.2$

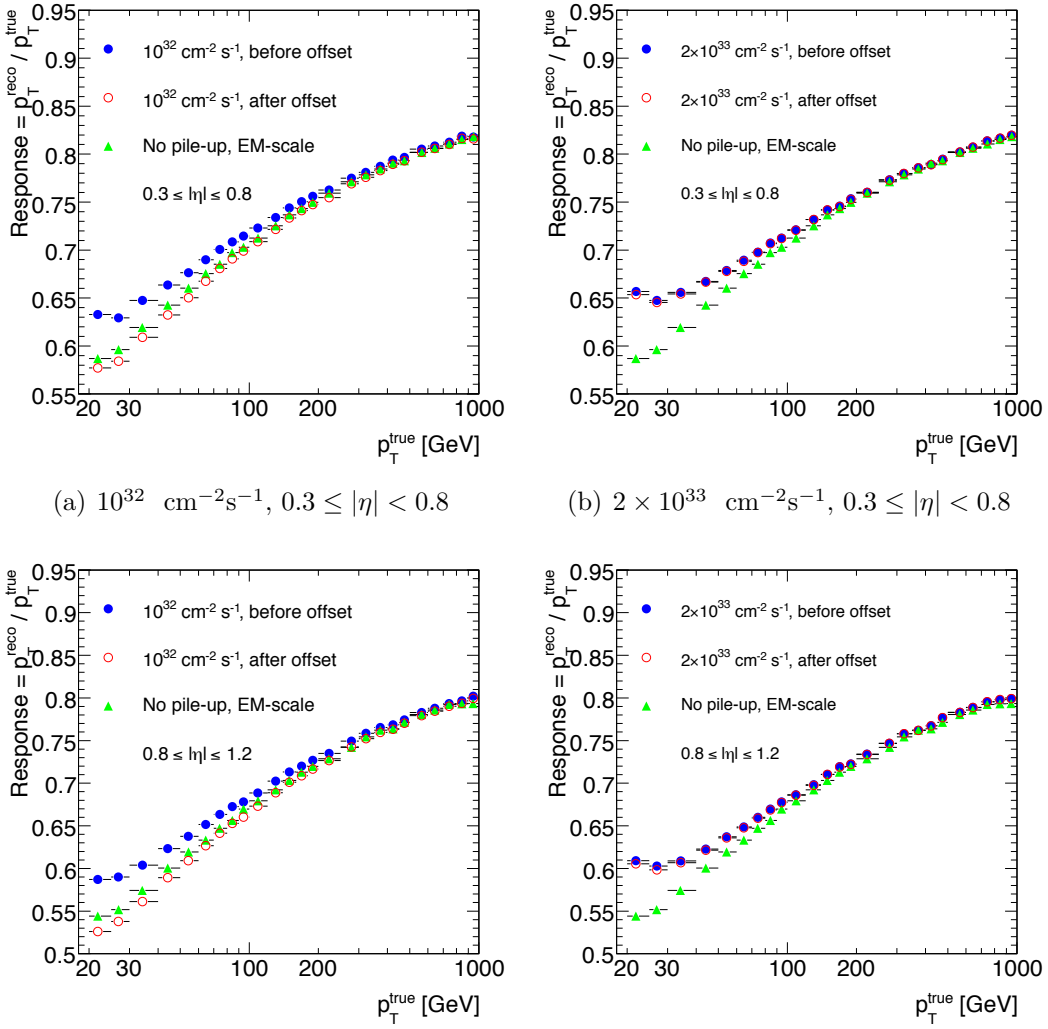

(a) 10^{32} cm^{-2}s^{-1}, $0.3 \leq |\eta| < 0.8$

(b) 2×10^{33} cm^{-2}s^{-1}, $0.3 \leq |\eta| < 0.8$

(c) 10^{32} cm^{-2}s^{-1}, $0.8 \leq |\eta| < 1.2$

(d) 2×10^{33} cm^{-2}s^{-1}, $0.8 \leq |\eta| < 1.2$

Figure C.10: Response of anti-k_t $R = 0.4$ noise-suppressed tower jets in events at low (10^{32} cm^{-2}s^{-1}) and high (2×10^{33} cm^{-2}s^{-1}) luminosity as a function of truth jet p_T.

C.3.2 Transition region: $1.2 \leq |\eta| < 2.1$

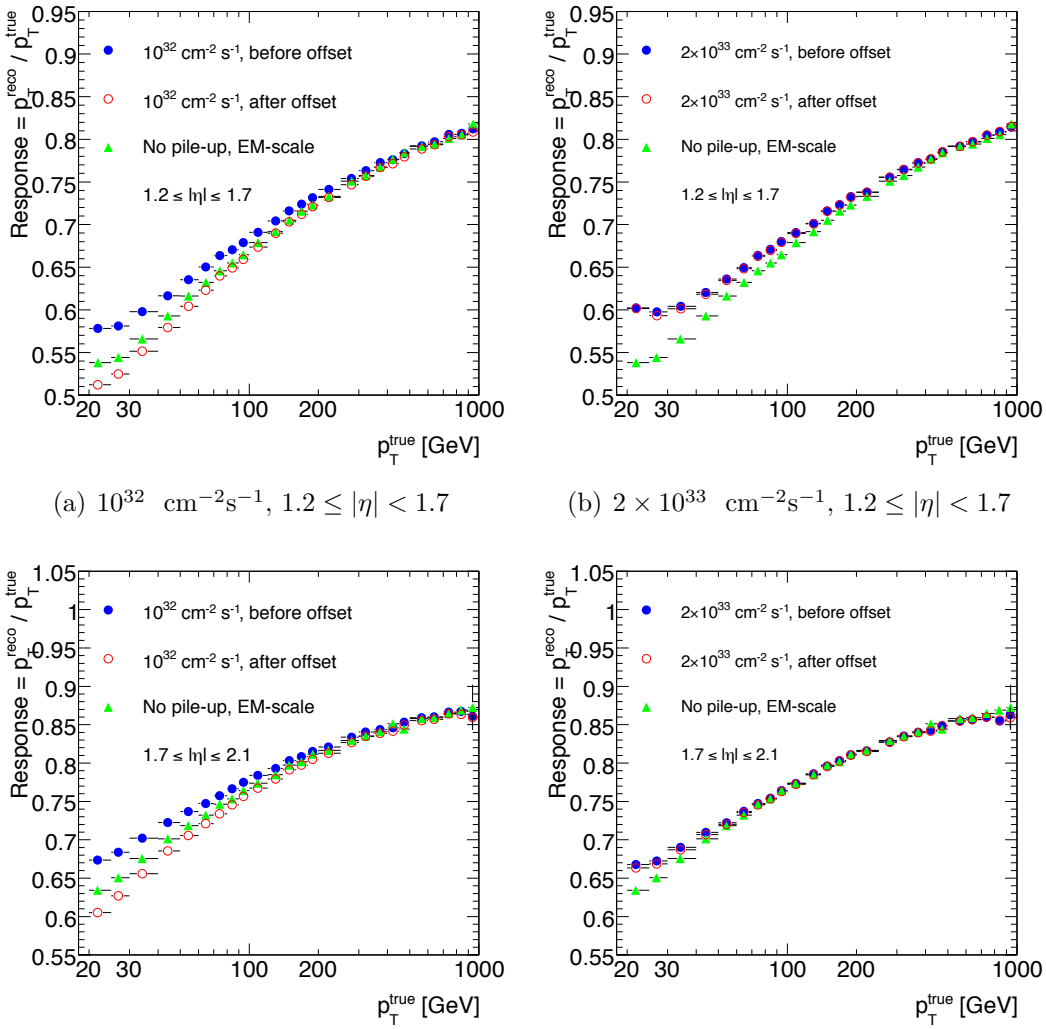

(a) 10^{32} cm^{-2}s^{-1}, $1.2 \leq |\eta| < 1.7$

(b) 2×10^{33} cm^{-2}s^{-1}, $1.2 \leq |\eta| < 1.7$

(c) 10^{32} cm^{-2}s^{-1}, $1.7 \leq |\eta| < 2.1$

(d) 2×10^{33} cm^{-2}s^{-1}, $1.7 \leq |\eta| < 2.1$

Figure C.11: Response of anti-k_t $R = 0.4$ noise-suppressed tower jets in events at low (10^{32} cm^{-2}s^{-1}) and high (2×10^{33} cm^{-2}s^{-1}) luminosity as a function of truth jet p_T.

C.3.3 Endcap region: $2.1 \leq |\eta| < 3.6$

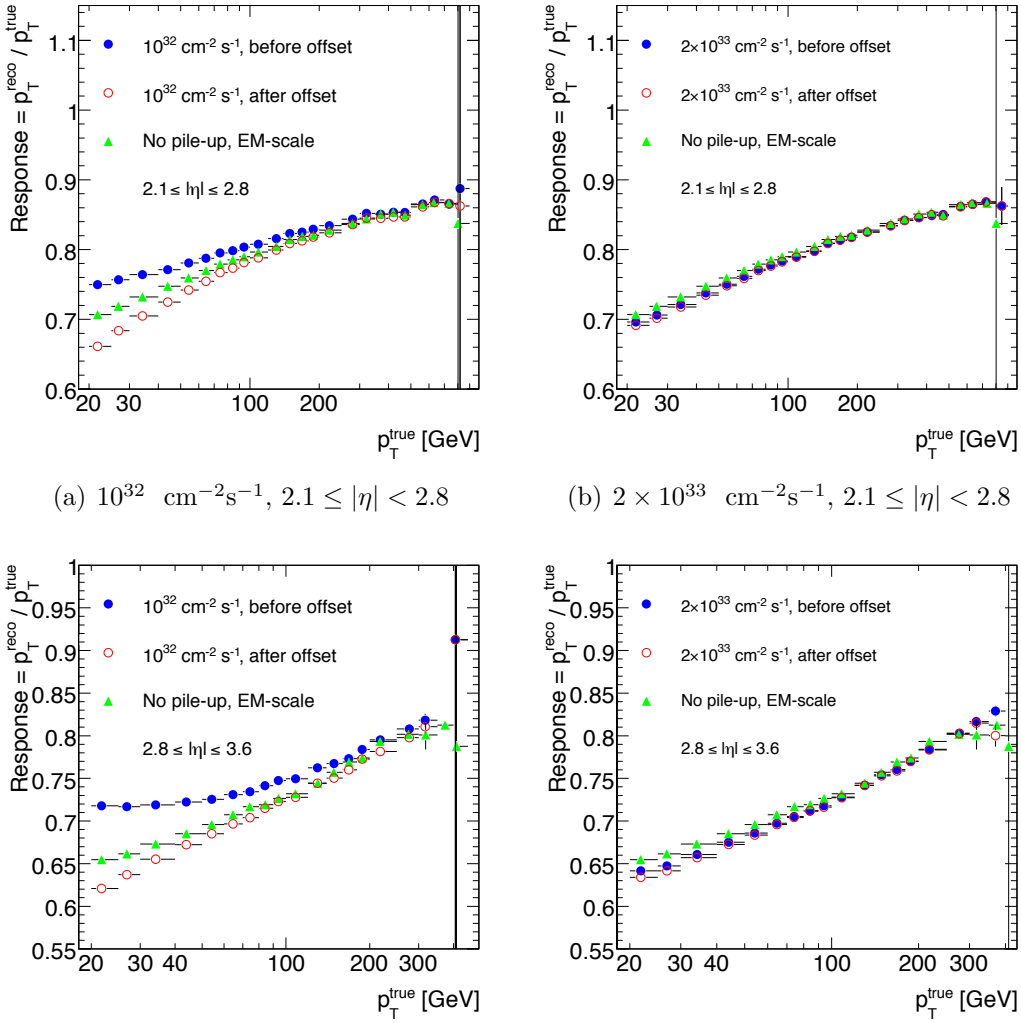

(a) 10^{32} cm^{-2}s^{-1}, $2.1 \leq |\eta| < 2.8$

(b) 2×10^{33} cm^{-2}s^{-1}, $2.1 \leq |\eta| < 2.8$

(c) 10^{32} cm^{-2}s^{-1}, $2.8 \leq |\eta| < 3.6$

(d) 2×10^{33} cm^{-2}s^{-1}, $2.8 \leq |\eta| < 3.6$

Figure C.12: Response of anti-k_t $R = 0.4$ noise-suppressed tower jets in events at low (10^{32} cm^{-2}s^{-1}) and high (2×10^{33} cm^{-2}s^{-1}) luminosity as a function of truth jet p_T.

C.3.4 Forward region: $3.6 \leq |\eta| < 4.5$

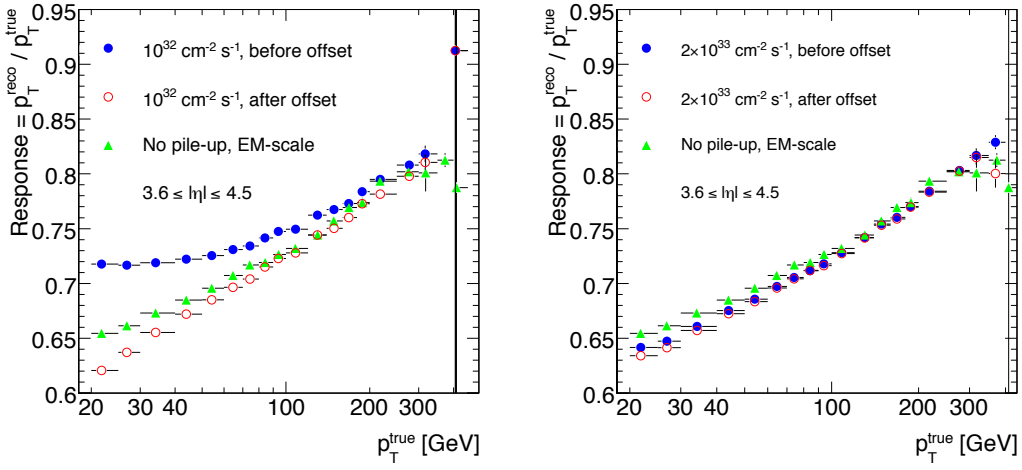

(a) 10^{32} cm^{-2}s^{-1}, $3.6 \leq |\eta| < 4.5$ (b) 2×10^{33} cm^{-2}s^{-1}, $3.6 \leq |\eta| < 4.5$

Figure C.13: Response of anti-k_t $R = 0.4$ noise-suppressed tower jets in events at low (10^{32} cm^{-2}s^{-1}) and high (2×10^{33} cm^{-2}s^{-1}) luminosity as a function of truth jet p_T.

Appendix D

Event shape analysis and luminosity estimates

The technical details related to the luminosity determination and run and event selection are described here.

D.1 Luminosity uncertainty

The systematic uncertainty on the luminosity determination is the measurement of the total number of protons in each bunch, or the total bunch charge product. The sub-dominant systematic uncertainties are the variations in the transverse size of the beam, which can affect the luminosity overlap determination (known as a transverse emittance growth) and correlations among the transverse sizes of the beam.

The systematics evaluated in Ref. [162] are listed in Table D.1. The final result is a systematic uncertainty on the luminosity measurement of $\pm 3.4\%$ for the 2010 data.

Scan Number	I	II–III	IV–V	
Fill Number	1059	1089	1386	
Bunch charge product	5.6%	4.4%	3.1%	Partially correlated
Beam centering	2%	2%	0.04%	Uncorrelated
Emittance growth and other	3%	3%	0.5%	Uncorrelated
Beam-position jitter	–	–	0.3%	Uncorrelated
Length scale calibration	2%	2%	0.3%	Partially Correlated
Absolute ID length scale	0.3%	0.3%	0.3%	Correlated
Fit model	1%	1%	0.2%	Partially Correlated
Transverse correlations	3%	2%	0.9%	Partially Correlated
μ dependence	2%	2%	0.5%	Correlated
Total	7.8%	6.8%	3.4%	

Table D.1: Relative systematic uncertainties on the determination of the visible cross section σ_{vis} [162].

D.2 Full 2010 dataset used

Summary of the full 2010 dataset used for the analysis of hadronic event shapes.

- Luminosity DB tag: `OflLumi-7TeV-002`
- Live fraction trigger: `L1_MBTS_2`
- Physics triggers:
  - `L1_J55` (Runs $\leq$ 152777)
  - `L1_J95` (152844 $\leq$ Runs $\leq$ 159224)
  - `EF_L1J95_NoAlg` (Runs $\geq$ 160387)
- Good runs list (GRL) definition from Standard Model QCD Jet Physics Group: `final_MergedAtoI_AutumnRepro_E1-E4_incl_2010.xml`

Run	$\mathbf{N}_{\mathrm{LB}}^{\mathrm{good}}$	$\mathbf{N}_{\mathrm{LB}}^{\mathrm{bad}}$	$\mathcal{L}$ **Delivered** [nb^{-1}]	$\mathcal{L}$ **Live** [nb^{-1}]	$\mathcal{L}$ **Prescale**	**Live %**	**Prescale %**
152844	57	0	0.00755473	0.00754959	0.00754959	99.93	1.0
152845	213	0	0.02272257	0.02270909	0.02270909	99.94	1.0
152878	85	0	0.01848756	0.01845311	0.01845311	99.81	1.0
152933	130	0	0.0207636	0.0207473	0.0207473	99.92	1.0
152994	61	0	0.00520205	0.00519752	0.00519752	99.91	1.0
153030	63	0	0.01710422	0.01709275	0.01709275	99.93	1.0
153134	23	0	0.00304433	0.0030145	0.0030145	99.02	1.0
153136	3	0	2.81449e-05	2.81286e-05	2.81286e-05	99.94	1.0
153159	70	0	0.00846635	0.00845318	0.00845318	99.84	1.0
153200	23	0	0.00492865	0.00492572	0.00492572	99.94	1.0
153565	883	0	0.7285474	0.72743726	0.72743726	99.85	1.0
155073	324	0	1.1416378	1.127295	1.127295	98.74	1.0
155112	474	0	3.340977	3.2883667	3.2883667	98.43	1.0
155116	79	0	0.4621205	0.4550606	0.4550606	98.47	1.0
155160	264	0	1.28692	1.28136	1.28136	99.57	1.0
155228	18	0	0.039644	0.0395446	0.0395446	99.75	1.0
155280	16	0	0.148292	0.0273932	0.0273932	18.47	1.0
155569	240	0	0.97303	0.955253	0.955253	98.17	1.0
155634	188	0	1.0307937	1.0263601	1.0263601	99.57	1.0
155669	55	0	0.453838	0.426524	0.426524	93.98	1.0
155678	68	0	1.15748	1.14952	1.14952	99.31	1.0
155697	240	0	3.3588068	3.2993924	3.2993924	98.23	1.0
156682	106	0	1.2627038	1.2606816	1.2606816	99.84	1.0

158045	61	0	0.703381	0.694569	0.694569	98.75	1.0
158116	377	0	13.05983081	13.00493837	13.00493837	99.58	1.0
158269	65	0	2.890812	2.881586	2.881586	99.68	1.0
158299	64	0	1.162449	1.159034	1.159034	99.71	1.0
158392	185	0	6.5164196	6.4074225	6.4074225	98.33	1.0
158443	17	4	1.057954	1.055701	0.811736	99.79	1.301
158466	13	1	1.283522	1.282012	1.234041	99.88	1.039
158545	23	1	1.298991	1.2931034	1.2857311	99.55	1.006
158548	192	0	10.2411806	9.519994617	9.519993617	92.96	1.0
158549	81	0	3.1383252	2.919098433	2.919098433	93.01	1.0
158582	306	0	15.494848	15.448327	15.448327	99.7	1.0
158632	107	0	5.1579726	5.1459816	5.1459816	99.77	1.0
158801	177	0	6.91819	6.90619	6.90619	99.83	1.0
158975	219	0	19.856739	19.774458	19.774458	99.59	1.0
159041	257	1	24.6399078	24.5684268	24.5376768	99.71	1.001
159086	404	1	52.309788	52.169889	52.101179	99.73	1.001
159113	256	2	27.16855	27.09942	27.0276	99.75	1.003
159179	108	0	14.556917	14.475795	14.475795	99.44	1.0
159202	81	1	9.57383	9.49222	9.44705	99.15	1.005
159203	79	0	7.99674	7.9914	7.9914	99.93	1.0
159224	163	0	24.857182	24.467044	24.467044	98.43	1.0
160387	234	0	56.30412	56.10002	56.10002	99.64	1.0
160472	365	0	73.83086	73.35318	73.35318	99.35	1.0
160479	25	0	4.53469	4.52937	4.52937	99.88	1.0
160530	421	0	92.02616	88.42454	88.42454	96.09	1.0
160613	188	0	46.58971	46.07715	46.07715	98.9	1.0
160736	59	0	16.7575	16.5416	16.5416	98.71	1.0
160800	61	3	18.298622	15.632305	15.548435	85.43	1.005
160801	400	2	82.202094	78.712619	78.644179	95.76	1.001
160879	430	0	82.5491	81.8826	81.8826	99.19	1.0
160899	15	0	4.63969	4.63339	4.63339	99.86	1.0
160953	53	0	21.08605	18.71196	18.71196	88.74	1.0
160954	24	0	7.799261	7.788756	7.788757	99.87	1.0
160958	195	2	40.17611	39.291769	39.167769	97.8	1.003
160963	13	2	2.44476	2.34214	2.24994	95.8	1.041
160975	22	0	6.63967	4.31444	4.31444	64.98	1.0
160980	30	0	8.67108	8.66271	8.66272	99.9	1.0
161118	97	0	32.8484	32.8163	32.8163	99.9	1.0
161379	356	0	92.416095	92.222822	92.222822	99.79	1.0
161407	101	0	38.62225	38.58945	38.58945	99.92	1.0
161520	351	0	109.845485	109.756496	109.756496	99.92	1.0
161562	221	0	70.1648	69.7215	69.7215	99.37	1.0
161948	352	0	87.2434	85.871	85.871	98.43	1.0
162347	408	0	211.31518	208.95093	208.95093	98.88	1.0
162526	355	0	241.139423	240.080608	240.080608	99.56	1.0
162576	47	1	37.65612	36.08927	35.8939	95.84	1.005
162577	9	2	6.50995	6.31521	6.18577	97.01	1.021

162620	66	0	67.80247	64.72136	64.72136	95.46	1.0
162623	319	2	230.15061	224.30155	224.30115	97.46	1.0
162690	349	0	311.38764	309.85754	309.85754	99.51	1.0
162764	76	0	80.06262	76.60012	76.60012	95.68	1.0
162843	378	0	295.86726	294.63864	294.63864	99.58	1.0
162882	318	0	281.15944	279.94263	279.94263	99.57	1.0
165591	366	2	143.459401	142.614023	142.229623	99.41	1.003
165632	367	0	563.40829	515.325392	515.325392	91.47	1.0
165703	42	0	84.6882	84.3652	84.3652	99.62	1.0
165732	360	0	879.12737	870.47583	870.47583	99.02	1.0
165767	329	0	903.06468	889.75006	889.75006	98.53	1.0
165815	40	0	154.05782	151.12277	151.12277	98.09	1.0
165817	2	2	9.31957	5.423135	0.2142889	58.19	25.31
165818	77	1	264.364	209.0259	206.0464	79.07	1.014
165821	72	1	219.4732	205.4188	203.5156	93.6	1.009
165954	36	0	179.3178	146.26006	146.26006	81.56	1.0
165956	18	2	91.9503	89.7685	87.3903	97.63	1.027
166097	48	0	224.96743	222.80612	222.80612	99.04	1.0
166142	136	0	642.06043	626.20284	626.20284	97.53	1.0
166143	57	0	250.165	244.9465	244.9465	97.91	1.0
166198	247	0	1238.03591	1165.90183	1165.90183	94.17	1.0
166305	23	0	173.99763	173.25888	173.25888	99.58	1.0
166383	136	0	927.72561	915.69014	915.69014	98.7	1.0
166466	155	0	1287.2223	1251.97205	1251.97205	97.26	1.0
166658	248	0	1946.33524	1867.55453	1867.55453	95.95	1.0
166786	231	0	1784.0934	1775.18782	1775.18682	99.5	1.0
166850	134	0	5.55994	5.351974	5.351974	96.26	1.0
166856	19	0	287.1841	283.2515	283.2515	98.63	1.0
166924	150	0	1179.37984	1174.64177	1174.64177	99.6	1.0
166927	89	2	537.7502	536.0291	525.3175	99.68	1.02
166964	11	0	148.4391	142.1227	142.1227	95.74	1.0
167575	8	0	70.7393	36.3606	36.3606	51.4	1.0
167576	268	0	3381.5324	3362.8191	3362.8191	99.45	1.0
167607	312	0	5020.13713	4801.81072	4801.81072	95.65	1.0
167661	65	0	1279.492	1237.749	1237.749	96.74	1.0
167680	223	0	3516.542	3391.871	3391.87	96.45	1.0
167776	407	0	5638.0898	5580.743	5580.744	98.98	1.0
167844	183	0	2341.0834	2324.0764	2324.0764	99.27	1.0
Total	**18115**	**35**	**38397.1**	**37410.5**	**37385.5**	**97.43**	**1.001**

Table D.2: default

D.3 Trigger efficiency determination

The method of determining the trigger efficiency shown in Section 7.1 relies on the bootstrapping of multiple lower threshold triggers together in order to measure the fraction of events with a higher threshold trigger that also pass.

Figure D.1 shows both the bootstrapping of the lower energy trigger `L1_J30` from `L1_J5` (a nominal 5 GeV threshold at L1) as well as a comparison with multiple data periods. Central ($|\eta| < 0.8$) and leading jet efficiencies are considered, demonstrating that there is very little, if any, bias incurred with the event selection used for the event shapes analysis

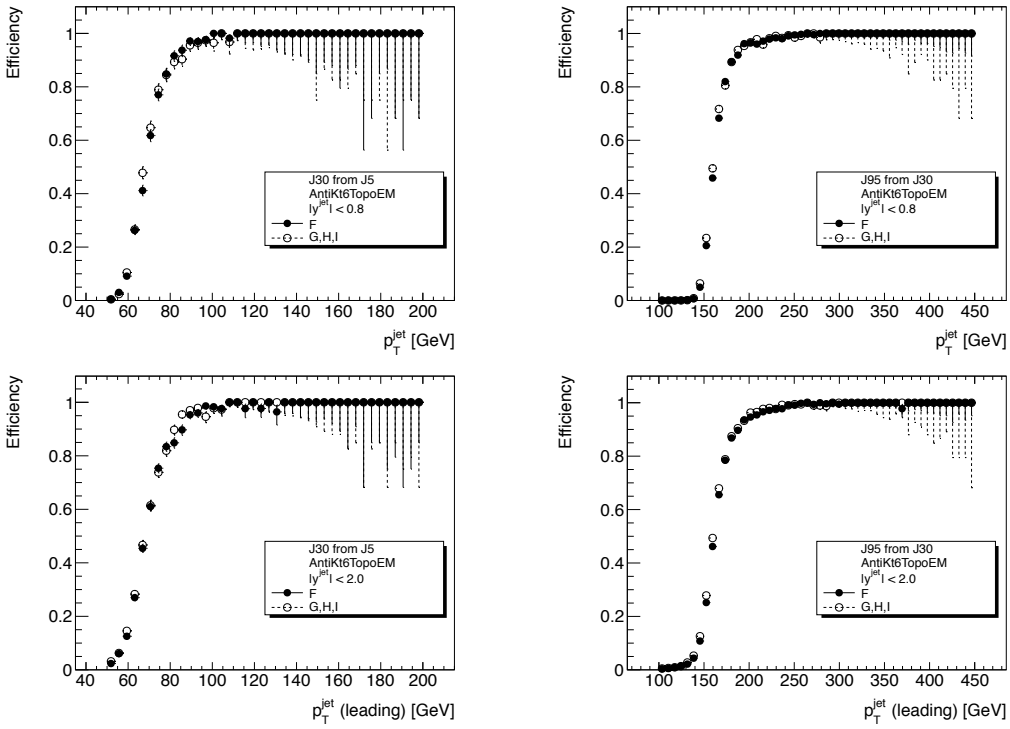

Figure D.1: L1_J95 trigger efficiency (per event) for (left) central, $|\eta| < 0.8$, jet and (right) leading jets within $|\eta| < 2.0$. The results are compared between the primary data periods during the 2010 data taking.

Figure D.2 again shows leading jets within $|\eta| < 2.0$, but here the bootstrapping efficiency is computed with respect to L1_J5 for the L1_J30 trugger. Results are evaluated in comparison to MC efficiencies computed using samples simulated both without ("r1653") and with ("r1660") pile-up.

D.4 Systematics and corrections

As described in the Section 7.1, the impact of the JES, pile-up and the resultant unfolding factors can vary slightly among the various MC predictions. For completeness, the full complement of studies is presented here for the alternative MC generators not used as the reference in Section 7.1.

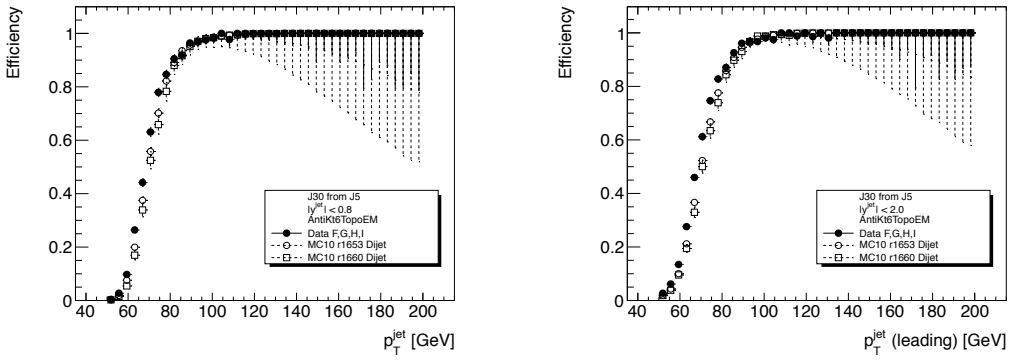

Figure D.2: L1_J30 trigger efficiency (per event) for (left) central, $|\eta| < 0.8$, jet and (right) leading jets within $|\eta| < 2.0$ using the bootstrapping with respect to L1_J5. Results are evaluated in comparison to MC efficiencies computed using samples simulated both without ("r1653") and with ("r1660") pile-up.

D.4.1 Jet energy scale uncertainty

Due to the lack of strong variation between the MC generators, the reference sample used to evaluate the JES uncertainty in Section 7.2.1 was taken to be ALPGEN as this sample best describes the widest range of event shapes throughout the analysis. For completeness, the same study conducted using PYTHIA (Perugia 2010) and HERWIG++ are presented below.

D.4.2 Systemtatics due to multiple *pp* interactions

Comparisons are made between events with only a single interaction and multiple interactions. Figure D.9 shows both y_{23} and $\tau_{\perp}$, each of which have different sensitivities to pile-up. The variation observed is similar to that seen to be due to the JES uncertainty.

The mean JVF for each of the three leading jets in the event as a function of the primary vertex multiplicity if shown in Figure D.10. The variation is largest for the third, softest jet and is not modeled well by the MC simulation, suggesting in fact that the pile-up simulation creates a slightly more "active" environment than observed in the data. However, Figure D.11 demonstrates that when the observable

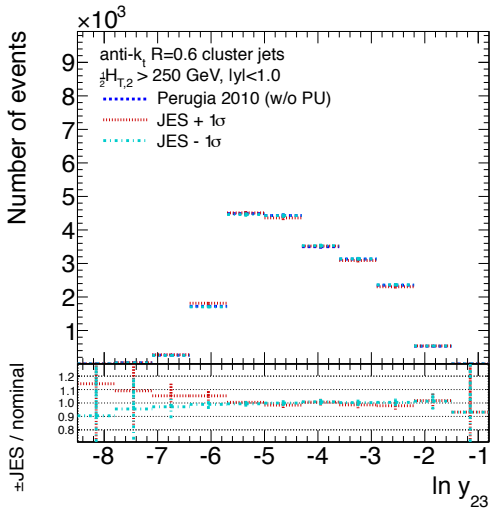

(a) y_{23}: no pile-up

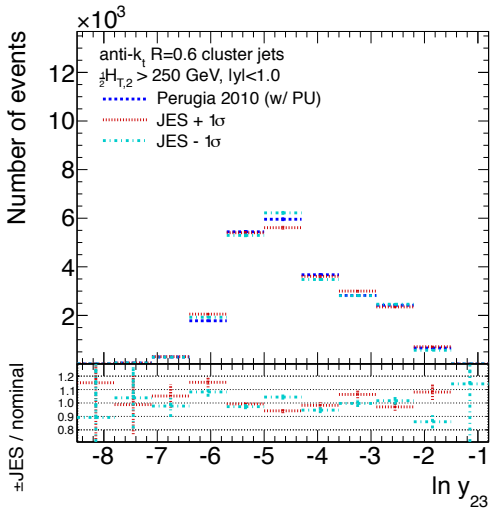

(b) y_{23}: with pile-up

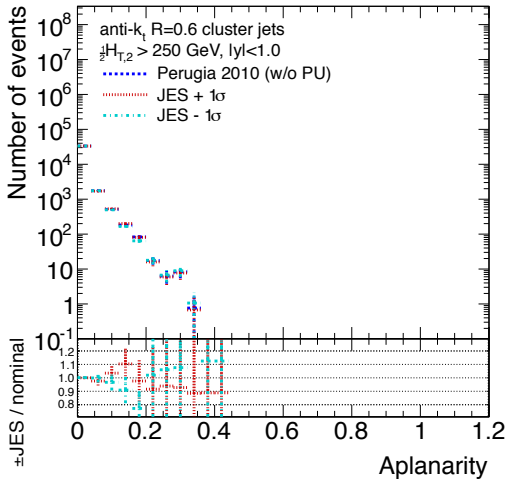

(c) A: no pile-up

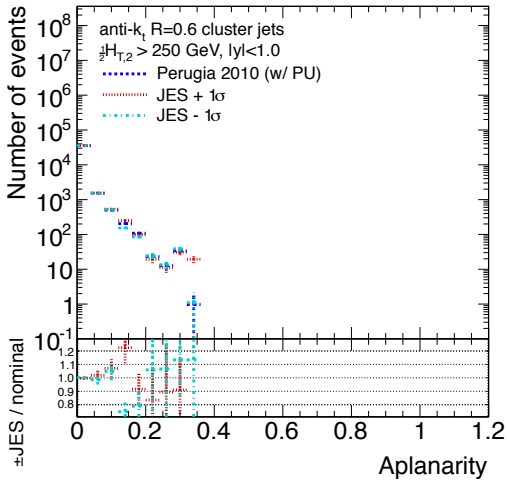

(d) A: with pile-up

Figure D.3: PYTHIA (Perugia 2010): Impact of the JES variation on the detector-level event shapes y_{23} (top) and A (bottom) both without (left) and with (right) pile-up.

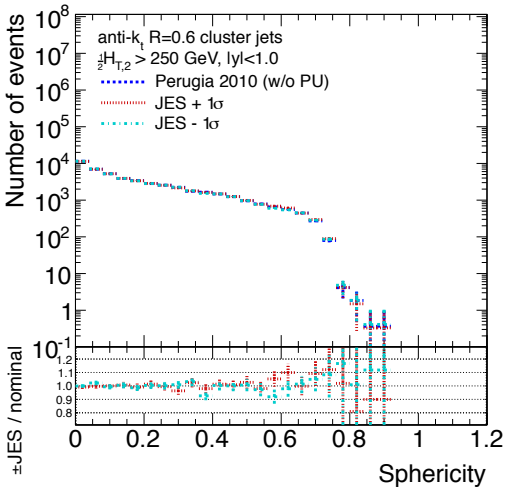

(a) S^{pheri}: no pile-up

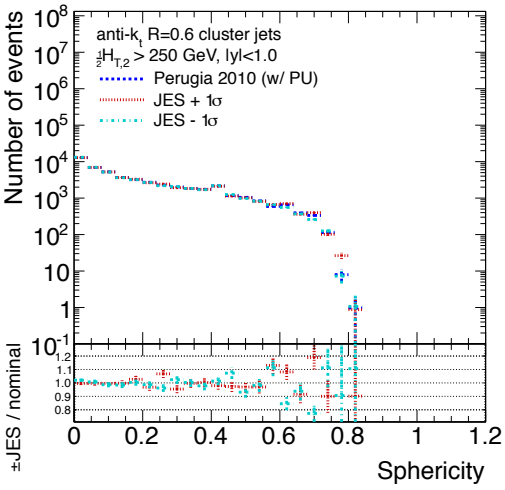

(b) S^{pheri}: with pile-up

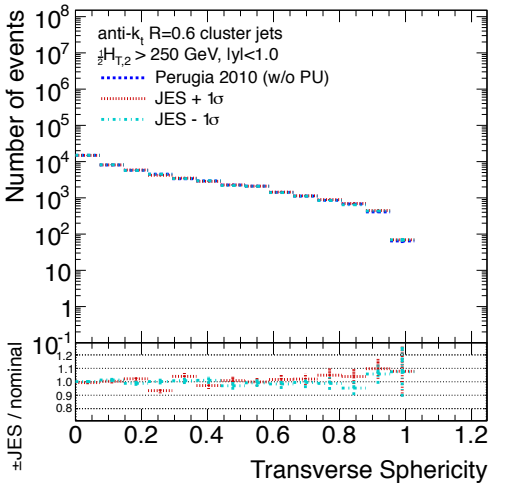

(c) $S_{\perp}^{pheri}$: no pile-up

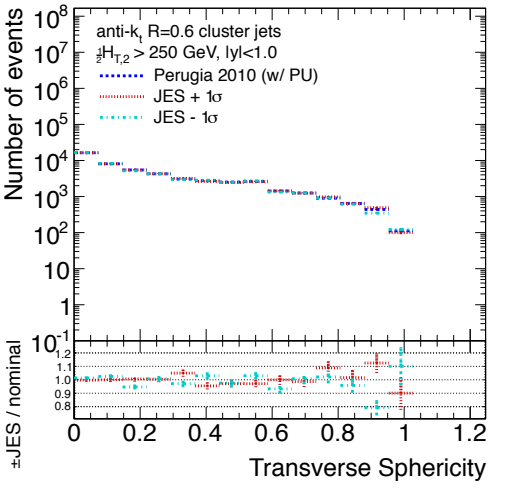

(d) $S_{\perp}^{pheri}$: with pile-up

Figure D.4: PYTHIA (Perugia 2010): Impact of the JES variation on the detector-level event shapes S^{pheri} (top) and $S_{\perp}^{pheri}$ (bottom) both without (left) and with (right) pile-up.

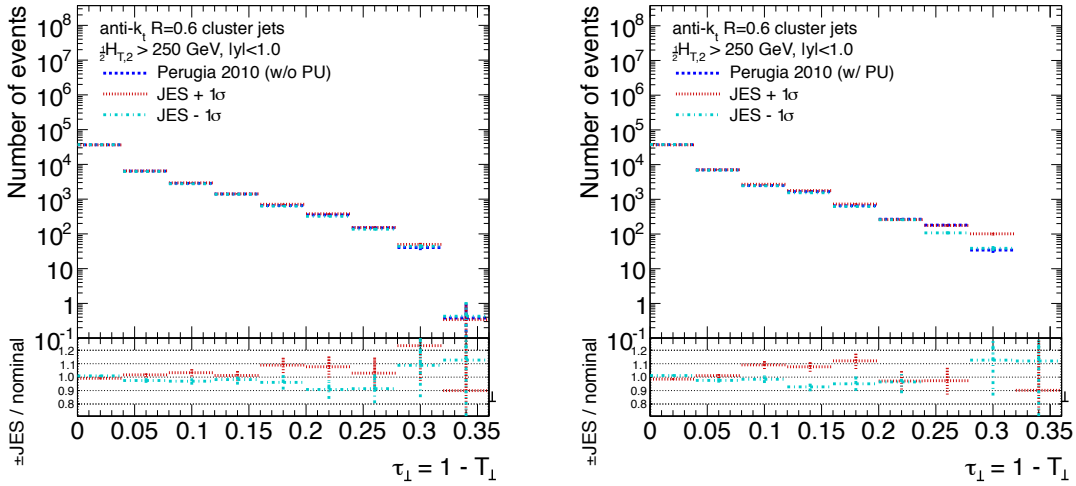

(a) $\tau_\perp$: no pile-up

(b) $\tau_\perp$: with pile-up

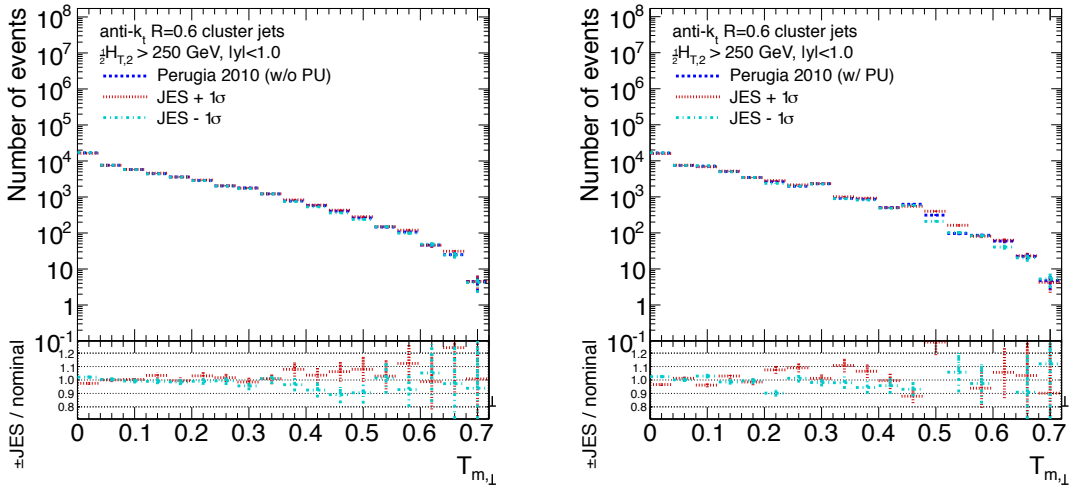

(c) $T_{m,\perp}$: no pile-up

(d) $T_{m,\perp}$: with pile-up

Figure D.5: PYTHIA (Perugia 2010): Impact of the JES variation on the detector-level event shapes $\tau_\perp$ (top) and $T_{m,\perp}$ (bottom) both without (left) and with (right) pile-up.

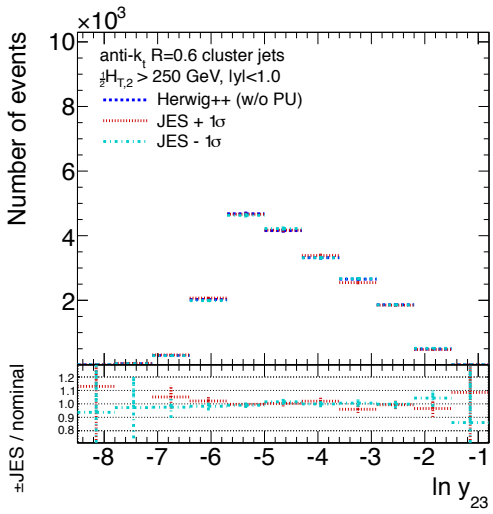

(a) y_{23}: no pile-up

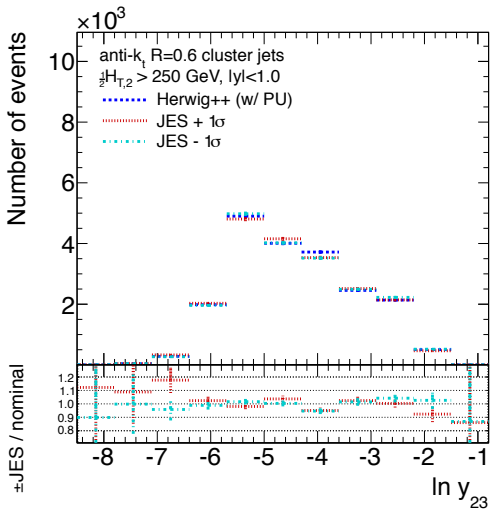

(b) y_{23}: with pile-up

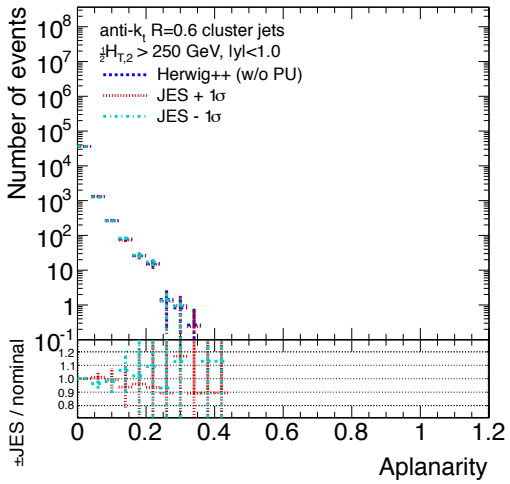

(c) A: no pile-up

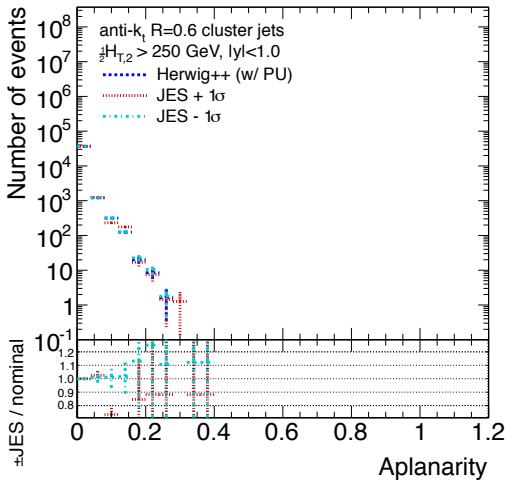

(d) A: with pile-up

Figure D.6: HERWIG++: Impact of the JES variation on the detector-level event shapes y_{23} (top) and A (bottom) both without (left) and with (right) pile-up.

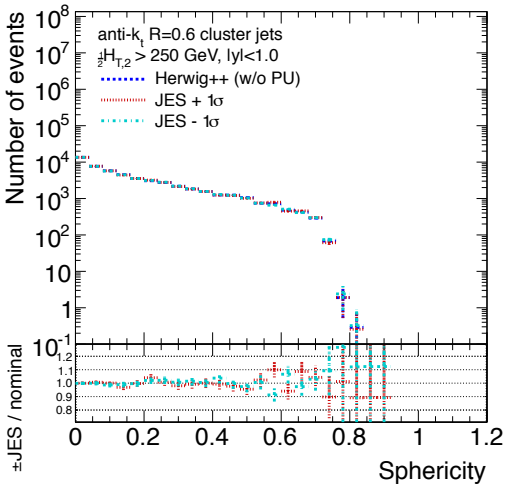

(a) S^{pheri}: no pile-up

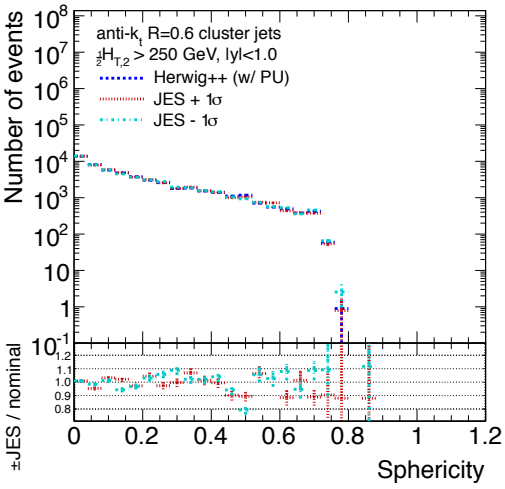

(b) S^{pheri}: with pile-up

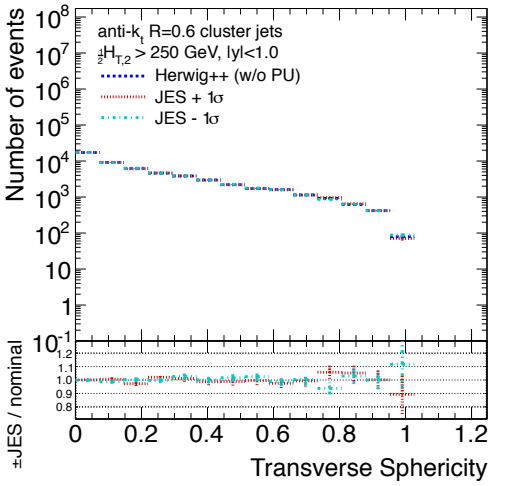

(c) $S_{\perp}^{pheri}$: no pile-up

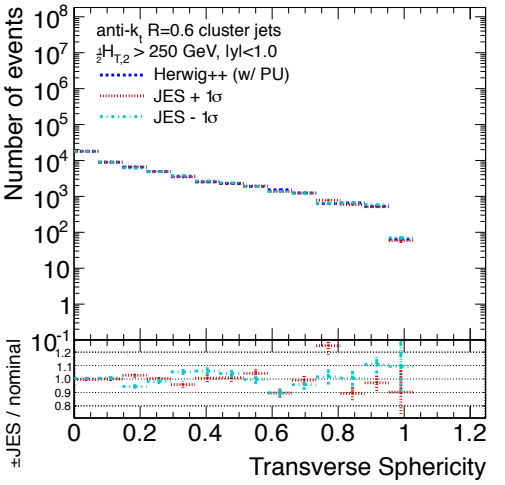

(d) $S_{\perp}^{pheri}$: with pile-up

Figure D.7: HERWIG++: Impact of the JES variation on the detector-level event shapes S^{pheri} (top) and $S_{\perp}^{pheri}$ (bottom) both without (left) and with (right) pile-up.

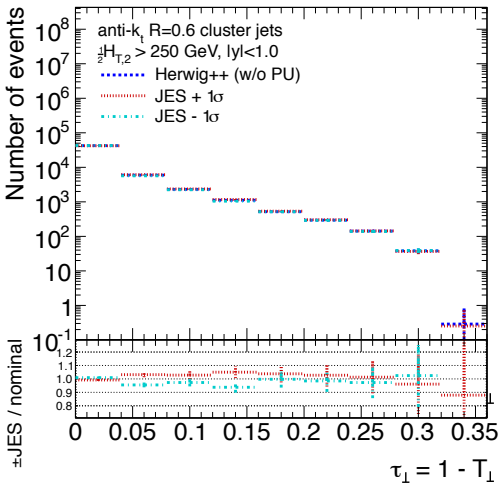

(a) $\tau_\perp$: no pile-up

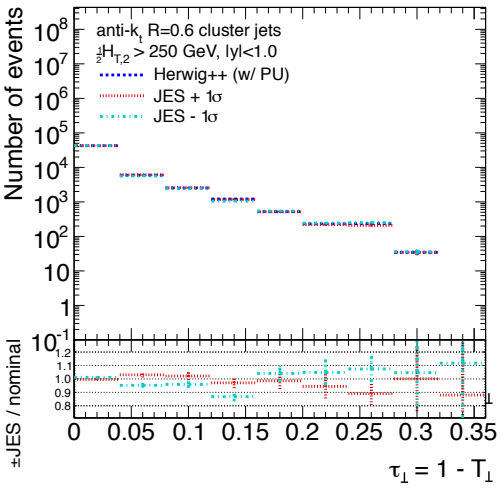

(b) $\tau_\perp$: with pile-up

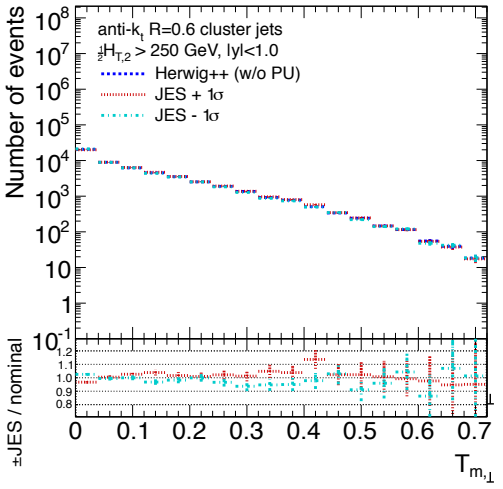

(c) $T_{m,\perp}$: no pile-up

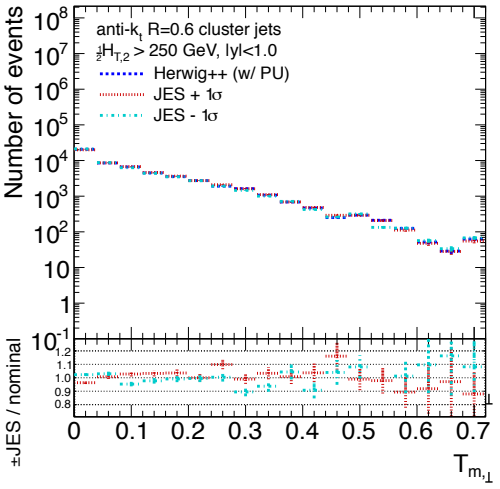

(d) $T_{m,\perp}$: with pile-up

Figure D.8: HERWIG++: Impact of the JES variation on the detector-level event shapes $\tau_\perp$ (top) and $T_{m,\perp}$ (bottom) both without (left) and with (right) pile-up.

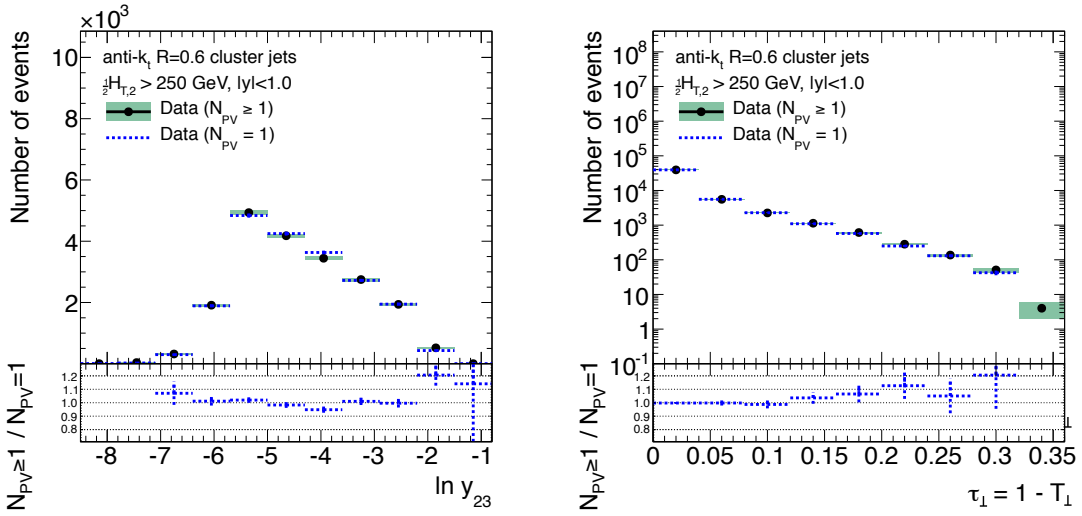

(a) y_{23} (b) $\tau_{\perp}$

Figure D.9: Variations in the measurements of y_{23} for the inclusive data sample with $N_{\mathrm{PV}} \geq 1$ (solid circles) and for an exclusive sample selected by requiring only a single reconstructed primary vertex, $N_{\mathrm{PV}} = 1$ (blue dashed lines). (a) The full distribution of $\ln y_{23}$ for the two samples and (b) the full distribution of $\tau_{\perp}$ for the two samples.

is evaluated explicitly as a function of JVF, then this discrepancy is largely removed, as the quantity that is discrepant – i.e. JVF– still accurately reflects the impact of pile-up on the measurement.

D.4.3 Unfolding factors calculated using various MC generators

D.4.4 Hadron level results for all generators

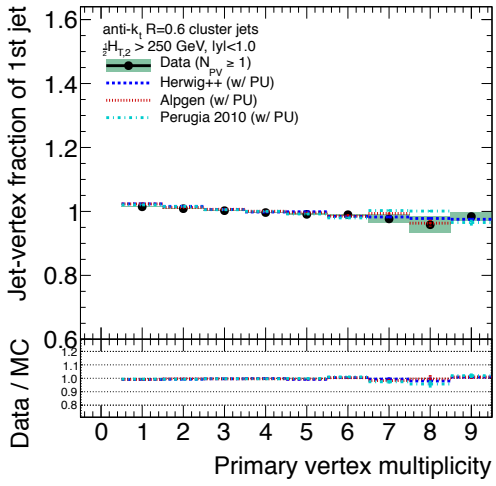

(a) JVF_{j1}

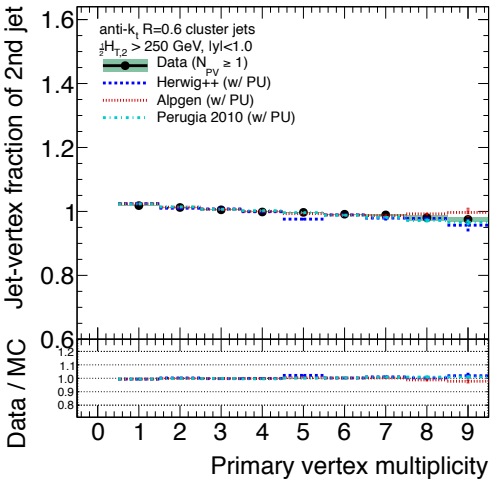

(b) JVF_{j2}

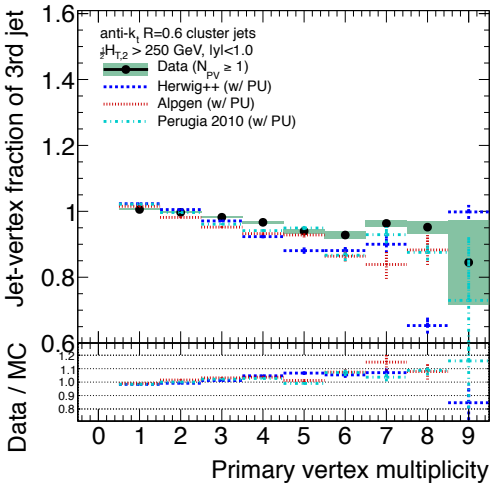

(c) JVF_{j3}

Figure D.10: Mean JVF for the (a) first, (b) second, and (c) third leading jets.

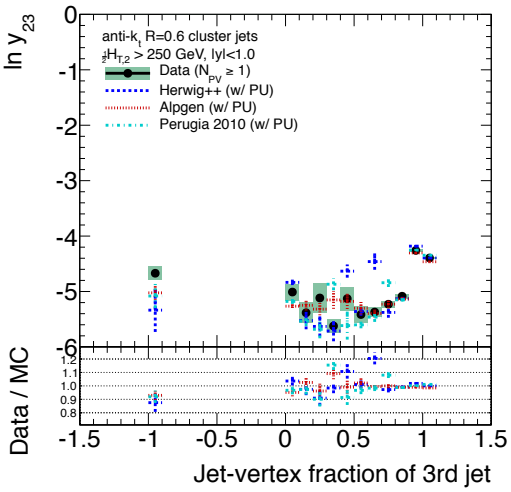

Figure D.11: Mean lny_{23} as a function of the JVF of the third jet.

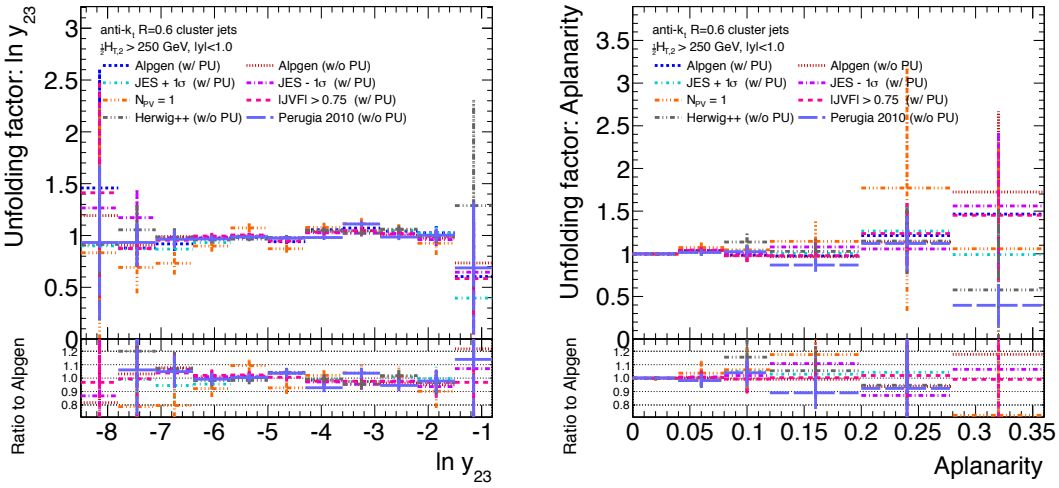

Figure D.12: Unfolding factors for lny_{23} and A using ALPGEN including multiple pp interactions as the reference. Comparisons are made to ALPGEN simulated without pile-up, JES energy scale uncertainties, pile-up filtering techniques and the MC generators HERWIG++, PYTHIA (Perugia 2010), both simulated without pile-up.

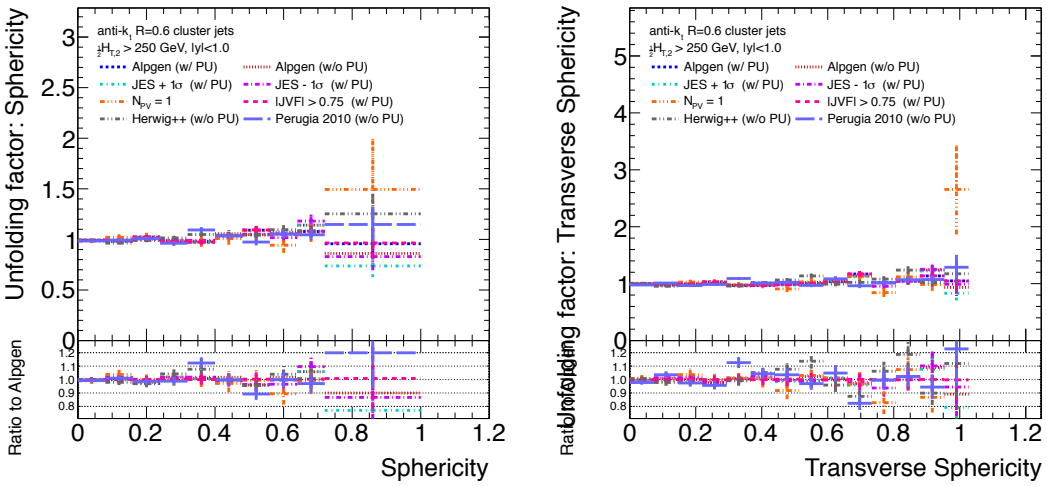

Figure D.13: Unfolding factors for S^{pheri} and $S_{\perp}^{pheri}$ using ALPGEN including multiple *pp* interactions as the reference. Comparisons are made to ALPGEN simulated without pile-up, JES energy scale uncertainties, pile-up filtering techniques and the MC generators HERWIG++, PYTHIA (Perugia 2010), both simulated without pile-up.

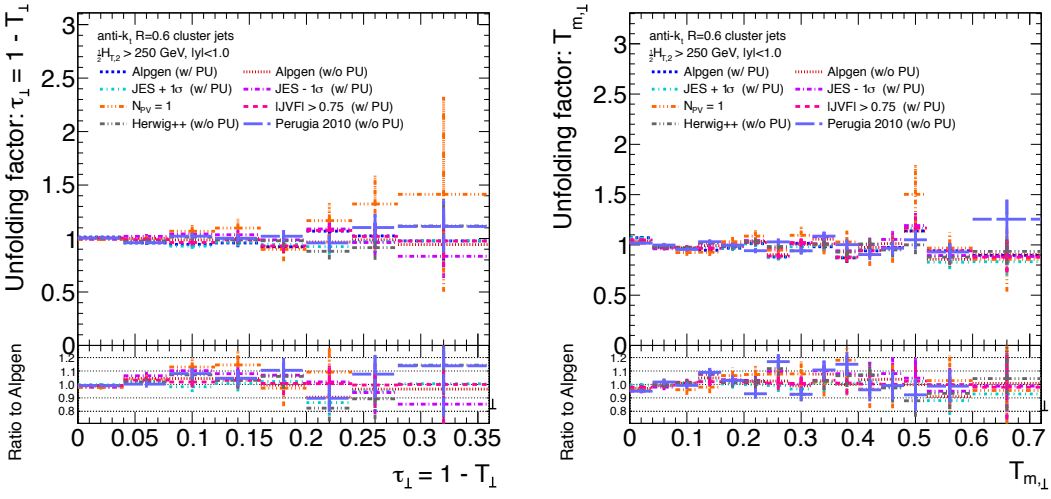

Figure D.14: Unfolding factors for $\tau_{\perp}$ and $T_{m,\perp}$ using ALPGEN including multiple *pp* interactions as the reference. Comparisons are made to ALPGEN simulated without pile-up, JES energy scale uncertainties, pile-up filtering techniques and the MC generators HERWIG++, PYTHIA (Perugia 2010), both simulated without pile-up.

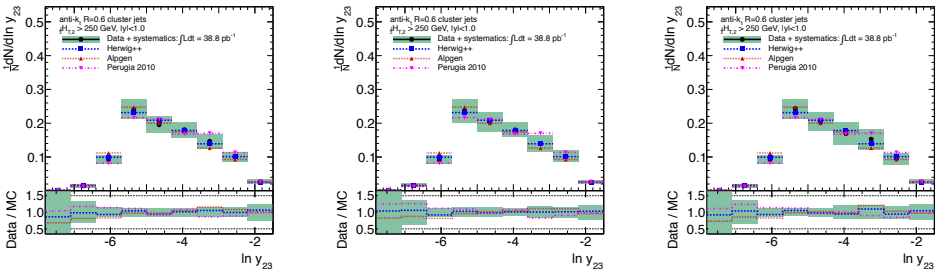

(a) $\ln y_{23}$ using ALPGEN (b) $\ln y_{23}$ using HERWIG++ (c) $\ln y_{23}$ using PYTHIA Perugia 2010

Figure D.15: Unfolded hadron level measurements of $\ln y_{23}$, where results are performed with and evaluated agains each MC generator.

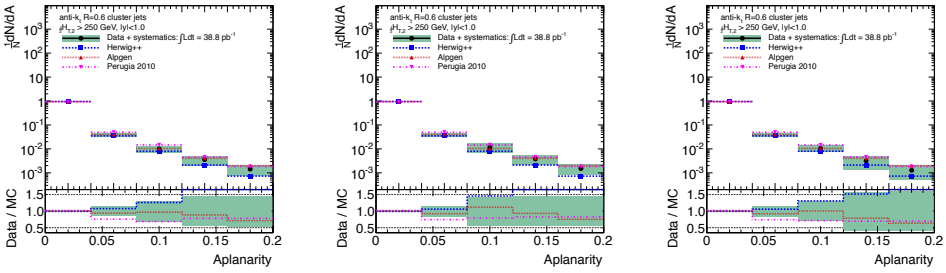

(a) A using ALPGEN (b) A using HERWIG++ (c) A using PYTHIA (Perugia 2010)

Figure D.16: Unfolded hadron level measurements of A, where results are performed with and evaluated agains each MC generator.

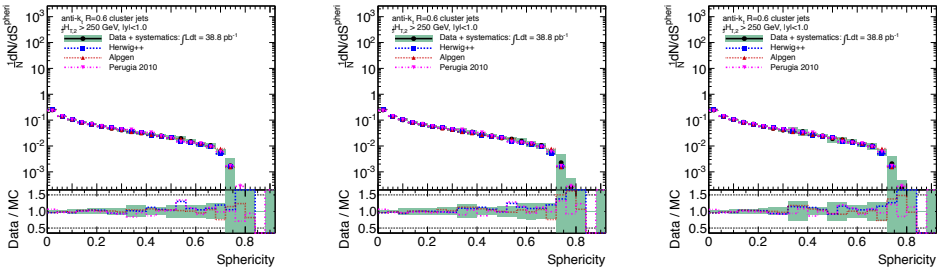

(a) S^{pheri} using ALPGEN (b) S^{pheri} using HERWIG++ (c) S^{pheri} using PYTHIA (Perugia 2010)

Figure D.17: Unfolded hadron level measurements of S^{pheri}, where results are performed with and evaluated agains each MC generator.

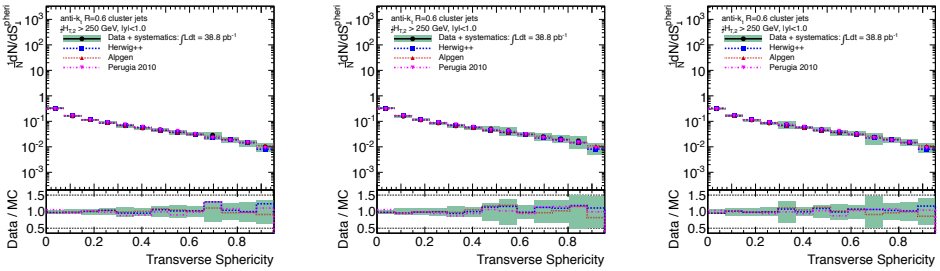

(a) $S_\perp^{pheri}$ using ALPGEN (b) $S_\perp^{pheri}$ using HERWIG++ (c) $S_\perp^{pheri}$ using PYTHIA (Perugia 2010)

Figure D.18: Unfolded hadron level measurements of $S_\perp^{pheri}$, where results are performed with and evaluated agains each MC generator.

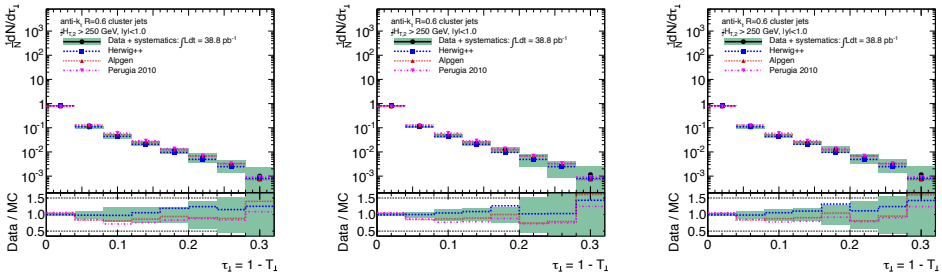

(a) $\tau_\perp$ using ALPGEN (b) $\tau_\perp$ using HERWIG++ (c) $\tau_\perp$ using PYTHIA Perugia 2010

Figure D.19: Unfolded hadron level measurements of $\tau_\perp$, where results are performed with and evaluated agains each MC generator.

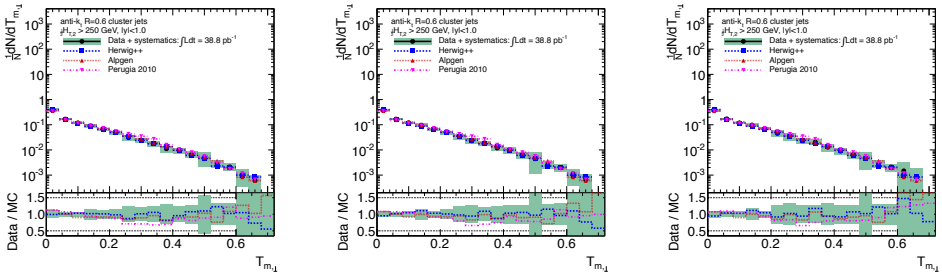

(a) $T_{m,\perp}$ using ALPGEN (b) $T_{m,\perp}$ using HERWIG++ (c) $T_{m,\perp}$ using PYTHIA (Perugia 2010)

Figure D.20: Unfolded hadron level measurements of $T_{m,\perp}$, where results are performed with and evaluated agains each MC generator.

Appendix E

Jet substructure systematics

E.1 Reconstruction of fat jets

Using the same method to define the purity with which calorimeter jets can be found and reconstructed in the data as in Section 5.4, track-jets constructed from charged particle tracks are used. Reconstruction purity is then defined as the fraction of calorimeter jets that can be matched to a reconstructed track-jet within a radius of $\Delta R < 0.3$ for jets with a nominal radius of $R = 0.6$. In this case, both calorimeter jets and track-jets are reconstructed with the same nominal jet radius. This definition of purity is shown as a function of calorimeter jet p_{T} and η in Figure E.1.

E.2 Calibration of fat jets

Figures E.2-E.5 show the equivalent jet-level calibration factors derived from the nominal Pythia MC10 sample for anti-k_t, $R = 1.0$ and and C/A, $R = 1.2$ (filtered) jets as those shown in the body of Chapter 8.

As discussed in the Section 8.1, the jet energy and mass scale uncertainties can be assessed in part by using the MC and detector simulation by varying parameters that are not constrained by data or test-beam studies. Samples are generated with a variety of generator-level and detector simulation conditions that attempt to bracket those of the nominal sample, Pythia. The calibration constants for these studies are

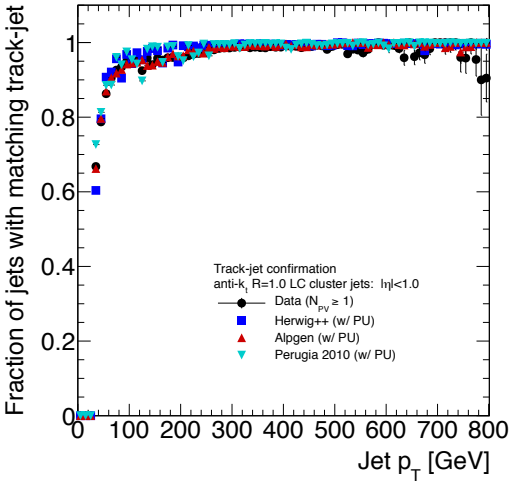

(a) anti-k_t, $R = 1.0$, p_{T}

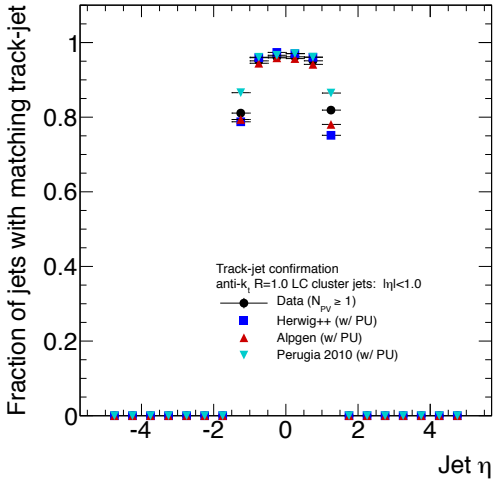

(b) anti-k_t, $R = 1.0$, η

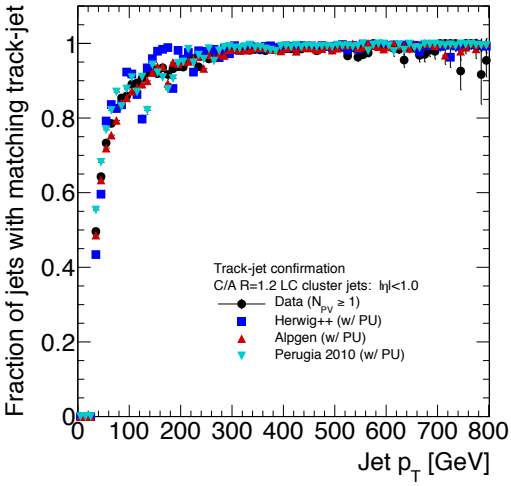

(c) anti-k_t, $R = 1.0$, p_{T}

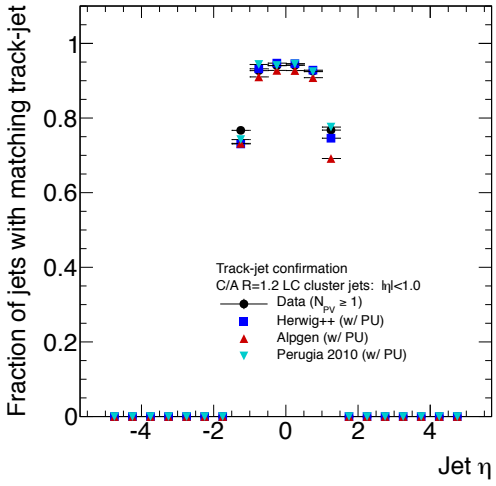

(d) anti-k_t, $R = 1.0$, η

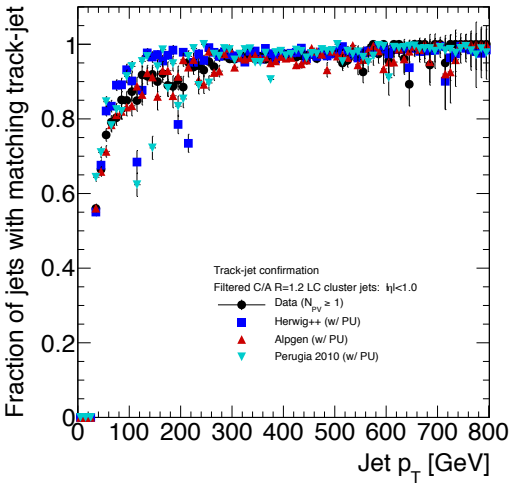

(e) C/A, $R = 1.2$ (filtered) , p_{T}

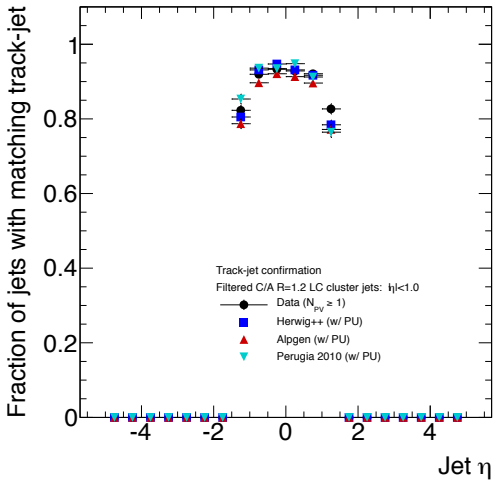

(f) C/A, $R = 1.2$ (filtered) , η

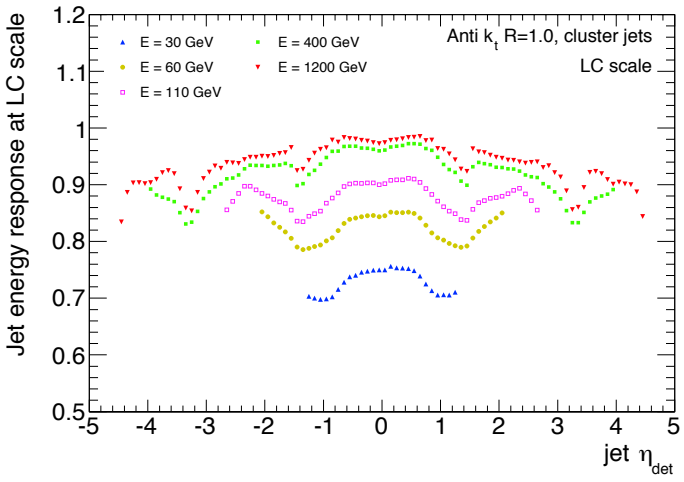

(a) anti-k_t, $R = 1.0$ energy response before calibration

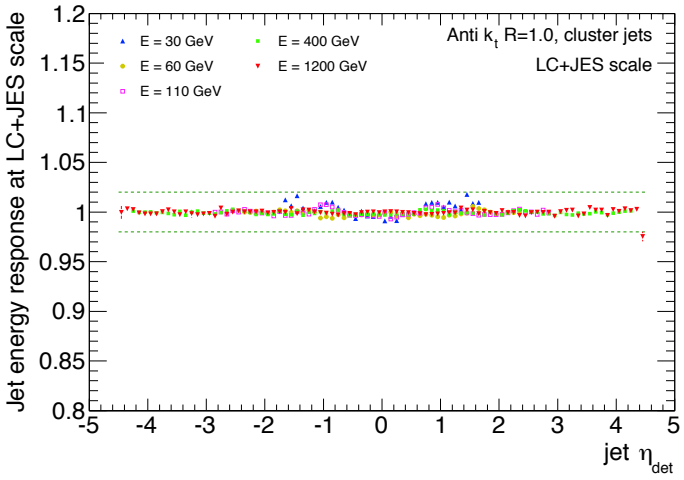

(b) anti-k_t, $R = 1.0$ energy response after calibration

Figure E.2: The MC based jet energy calibration procedure for anti-k_t, $R = 1.0$ jets to the LC+JES scale, showing the jet response before and after calibration as a function of η_{det}. (a) The uncorrected jet energy response showing the effect of the local cluster (LC) weighting factors. (b) The closure after the correction factors are applied as a function of E and η_{det}. The closure uncertainty is approximately 1.5% above 60 GeV.

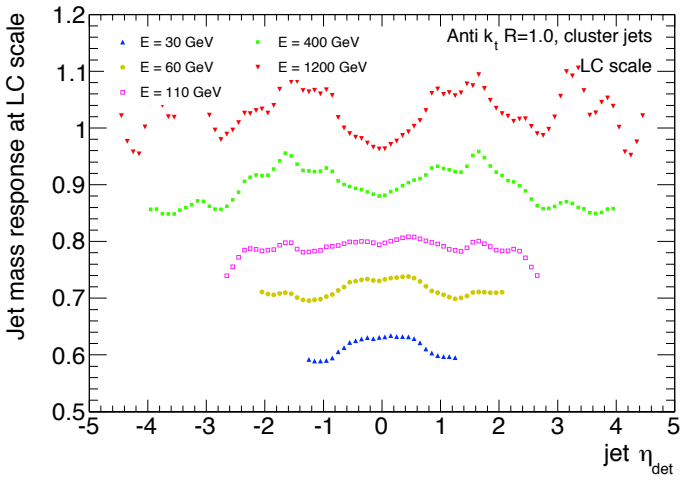

(a) anti-k_t, $R = 1.0$ mass response before calibration

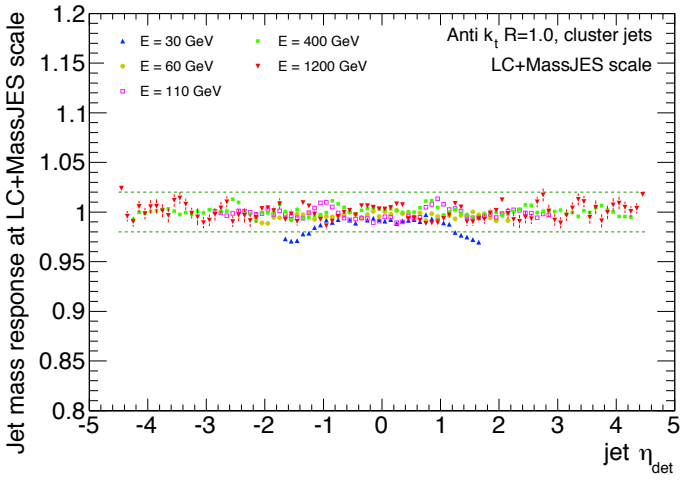

(b) anti-k_t, $R = 1.0$ mass response before calibration

Figure E.3: The MC based jet mass calibration procedure for anti-k_t, $R = 1.0$ jets to the LC+JES scale, showing the jet response before and after calibration as a function of η_{det}. (b) The uncorrected jet mass response showing wide variation prior to calibration. (a) The closure after the correction factors are applied as a function of E and η_{det}. The closure uncertainty is approximately 3% above 60 GeV.

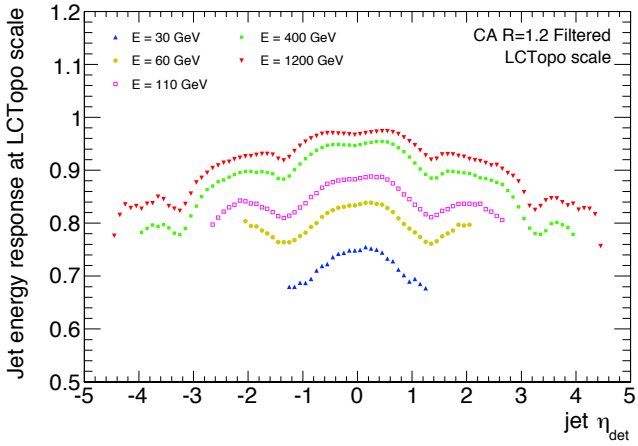

(a) C/A, $R = 1.2$ (filtered) energy response before calibration

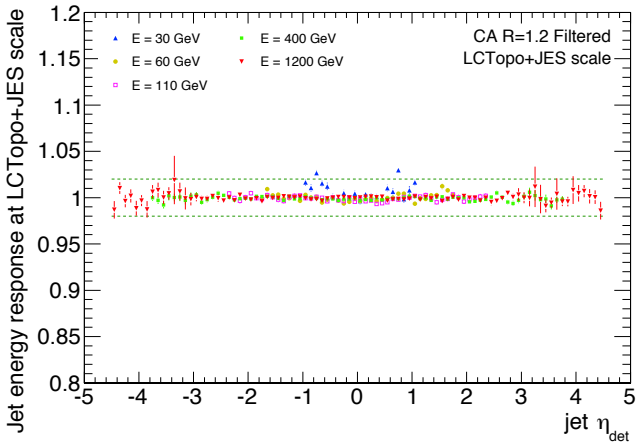

(b) C/A, $R = 1.2$ (filtered) energy response after calibration

Figure E.4: The MC based jet energy calibration procedure for C/A, $R = 1.2$ (filtered) jets to the LC+JES scale, showing the jet response before and after calibration as a function of η_{det}. (a) The uncorrected jet energy response showing the effect of the local cluster (LC) weighting factors. (b) The closure after the correction factors are applied as a function of E and η_{det}. The closure uncertainty is approximately 1.5% above 60 GeV.

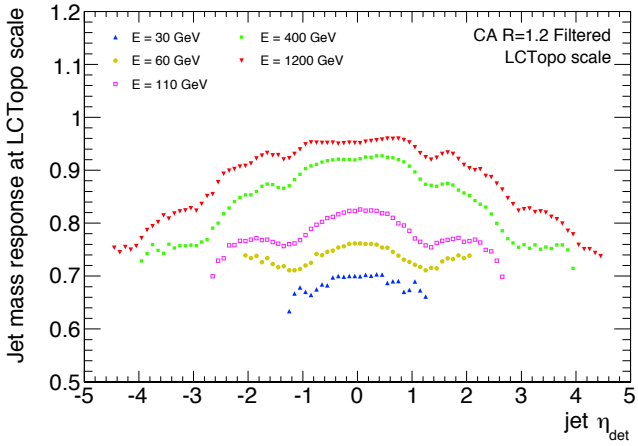

(a) C/A, $R = 1.2$ (filtered) mass response before calibration

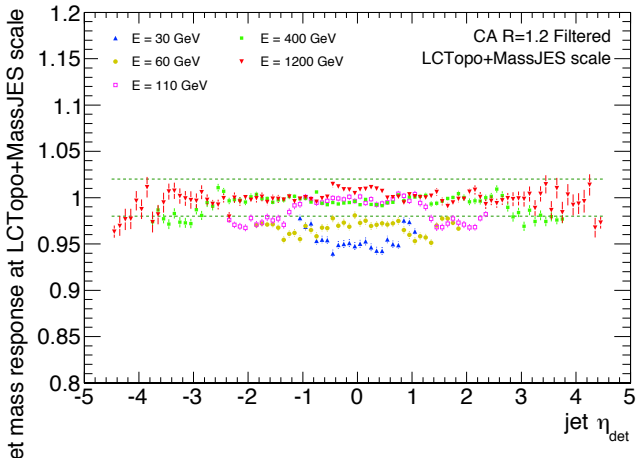

(b) C/A, $R = 1.2$ (filtered) mass response before calibration

Figure E.5: The MC based jet mass calibration procedure for C/A, $R = 1.2$ (filtered) jets to the LC+JES scale, showing the jet response before and after calibration as a function of η_{det}. (b) The uncorrected jet mass response showing wide variation prior to calibration. (a) The closure after the correction factors are applied as a function of E and η_{det}. The closure uncertainty is approximately 3% above 60 GeV.

described in Section 8.1 and are derived from the nominal Monte Carlo sample, as described in the previous section.

The primary contributions to the jet energy scale uncertainty were assessed among the following categories:

- **Dead Material:** A dedicated detector geometry is used in the GEANT4 simulation that modifies the amount of inactive material in the ATLAS detector, primarily within the cryostat and solenoid magnets. The distorted detector geometry has been simulated as follows:
  - An extra 0.05 radiation length (X_0) has been placed between the barrel pre-sampler and the calorimeter itself ($|\eta|| < 1.45$);
  - An extra 0.1 X_0 of dead material has been placed radially in the cryostat before the electromagnetic calorimeter ($|\eta|| < 1.5$);
  - An extra 0.1 X_0 has been placed in the cryostat after the barrel of the electromagnetic calorimeter;
  - extra material has also been placed in the in barrel-endcap transition region in the electromagnetic calorimeter ($1.37 < |\eta|| < 1.52$).
- **Hadronic shower model:** The hadronic shower model used will influence the shape and the size of the energy deposits and therefore, the jet energy scale and jet mass scale. This uncertainty is evaluated using two Monte Carlo samples:
  - **QGSP**, which defines a set of parameters for hadronic interactions in the detector follows the QGSP_BERT details used for the nominal sample, but with the Bertini nucleon cascades not simulated.
  - **FTFP_BERT**, where the Quark Gluon String fragmentation model from QGSP_BERT is substituted with the Fritiof model.
- **Monte Carlo event generator:** The contributions to the uncertainty from the fragmentation and underlying event model of the Monte Carlo used are obtained using the following samples:

- **Alpgen+Herwig+Jimmy:** This is used to test the effects of a different matrix-element, fragmentation and underlying event models.
- **Pythia MC10 tune with Perugia fragmentation:** This set of parameters for the PYTHIA generator uses a different underlying-event model with respect to the nominal sample.

Figure E.6 presents a nearly identical study to that in Figure 8.6 in Chapter 8 but the very restrictive $N_{\mathrm{PV}} = 1$ selection has been removed to demonstrate that the rise a high $p_{\mathrm{T}}^{\mathrm{jet}}$ is an artifact of statistical fluctuations due to the the low efficiency of the selection. If pile-up were related to this rise, the expectation is that it would increase and not decrease when this selection is removed.

Figures E.7 and E.8 show the ratios $r^{p_T}_{\mathrm{track-jet}}$, $r^{m}_{\mathrm{track-jet}}$ and double ratios $R^{p_T}_{r\mathrm{track-jet}}$, $R^{m}_{r\mathrm{track-jet}}$ as a function of both p_{T} and m^{jet} for each of the three fat jet types as well as the standard anti-k_t, $R = 0.6$ jets. The result is nearly identical to that shown in Chapter 8

The JVF distributions for each jet type in both data and MC simulated with pile-up are shown in Figure E.9.

E.3 Jet substructure observables

In addition to the results presented in Section 8.2, a complete set of results for anti-k_t, $R = 1.0$, anti-k_t, $R = 1.0$, and C/A, $R = 1.2$ (filtered) are presented here for those cases where they were not included in the body of the thesis.

E.3.1 Subjet multiplicity and scales

E.3.2 Jet mass

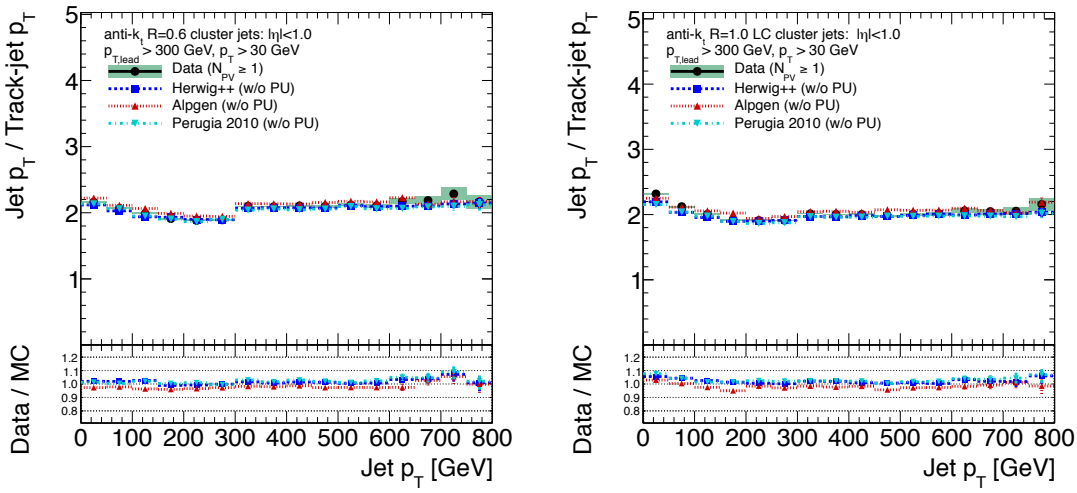

(a) anti-k_t, $R = 0.6$ (b) anti-k_t, $R = 1.0$

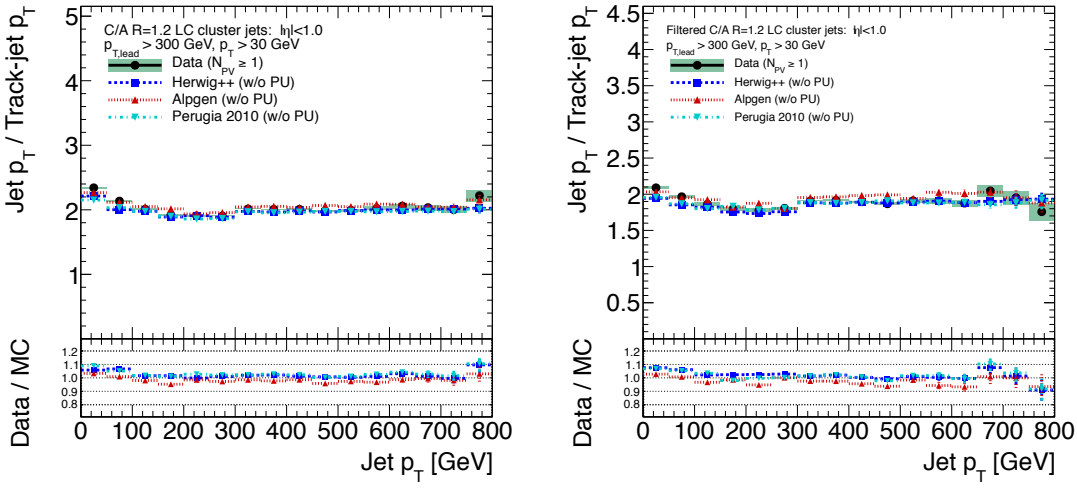

(c) anti-k_t, $R = 1.0$ (d) C/A, $R = 1.2$ (filtered)

Figure E.6: Distributions of $r^{p_T,\mathrm{data}}_{\mathrm{track-jet}}$ and $r^{p_T,\mathrm{MC}}_{\mathrm{track-jet}}$, as well as the double ratio, $R^{p_T}_{r\mathrm{track-jet}}$, versus $p_{\mathrm{T}}^{\mathrm{jet}}$ for jets reconstructed with the three algorithms considered as well as the standard anti-k_t, $R = 0.6$ jet algorithm. Events in the data are *not* required to have $N_{\mathrm{PV}} = 1$, contrary to those result shown in Figure 8.6, and the MC samples are simulated without pile-up overlaid.

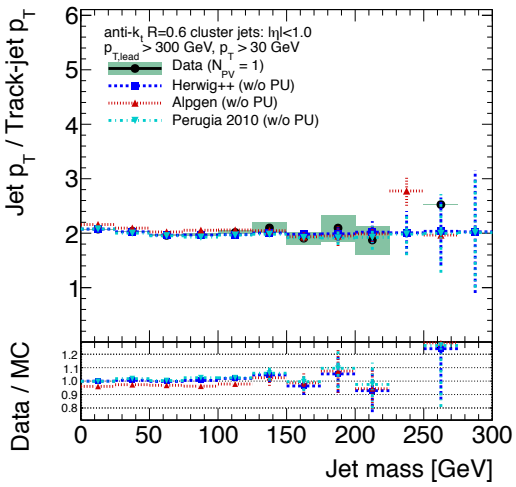

(a) anti-k_t, $R = 0.6$

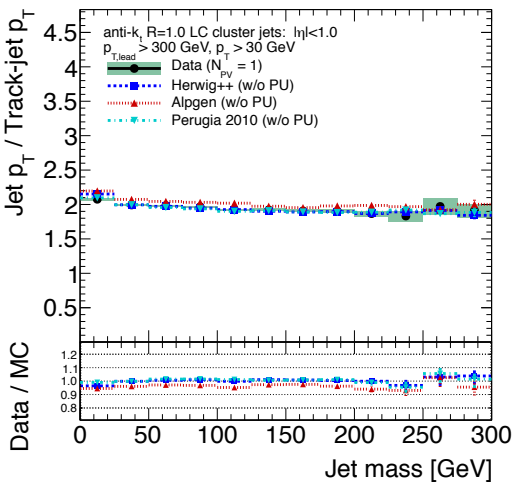

(b) anti-k_t, $R = 1.0$

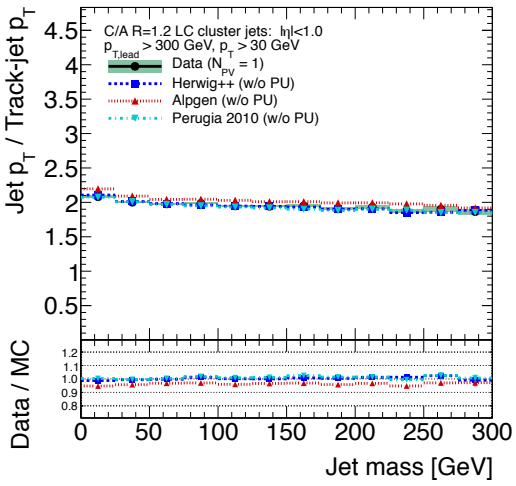

(c) C/A, $R = 1.2$

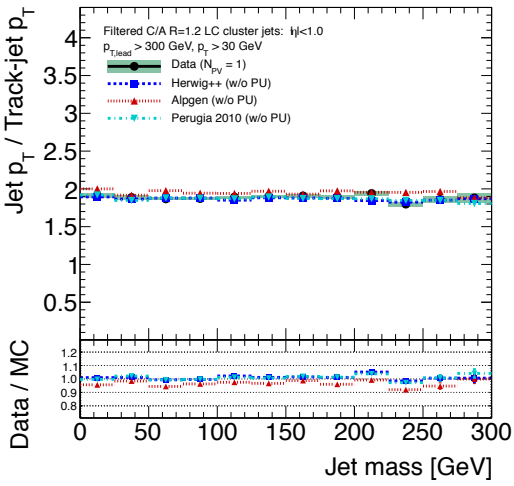

(d) C/A, $R = 1.2$ (filtered)

Figure E.7: Distributions of $r^{p_T,\mathrm{data}}_{\mathrm{track-jet}}$ and $r^{p_T,\mathrm{MC}}_{\mathrm{track-jet}}$, as well as the double ratio, $R^{p_T}_{r\mathrm{track-jet}}$, versus m^{jet} for jets reconstructed with the three algorithms considered as well as the standard anti-k_t, $R = 0.6$ jet algorithm. Events in the data are required to have $N_{\mathrm{PV}} = 1$ and the MC samples are simulated without pile-up overlaid.

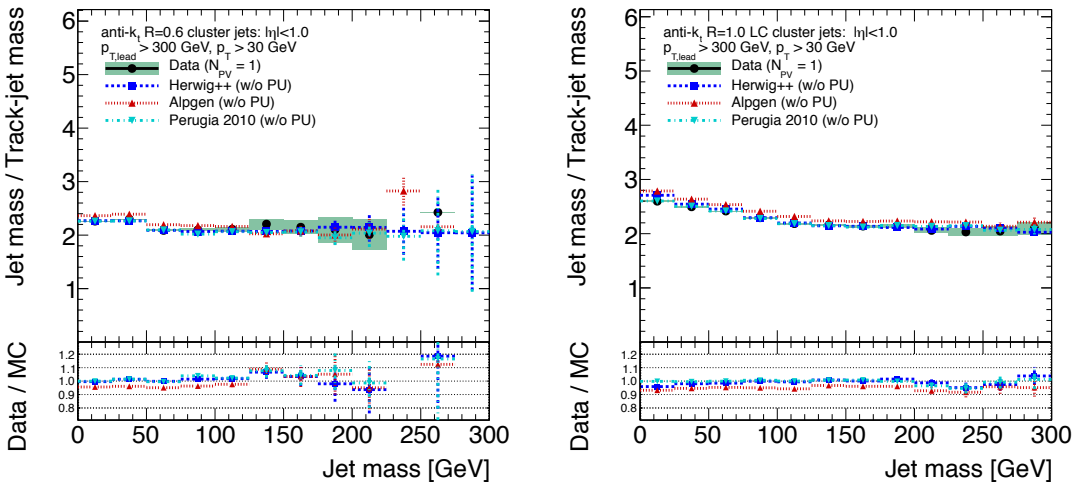

(a) anti-k_t, $R = 0.6$

(b) anti-k_t, $R = 1.0$

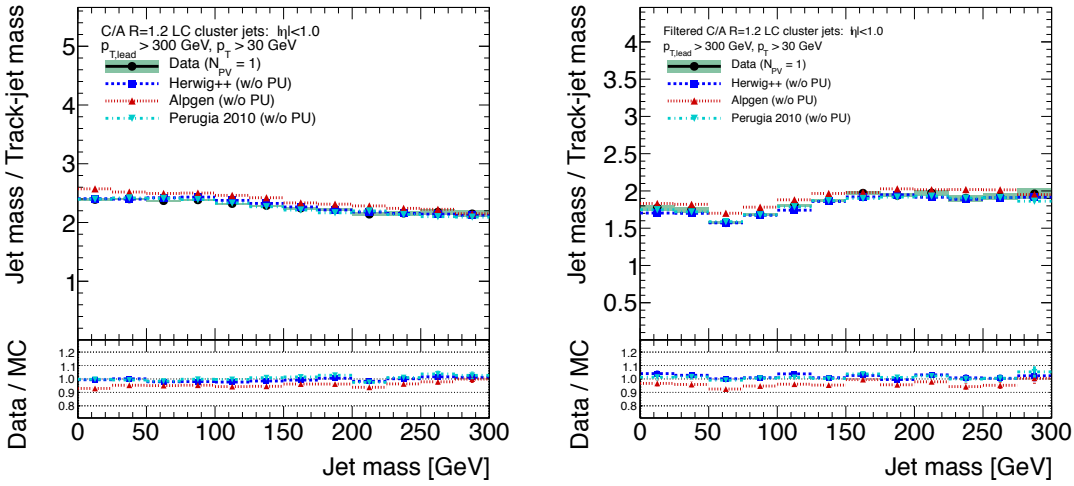

(c) C/A, $R = 1.2$

(d) C/A, $R = 1.2$ (filtered)

Figure E.8: Distributions of $r^{m,\mathrm{data}}_{\mathrm{track-jet}}$ and $r^{m,\mathrm{MC}}_{\mathrm{track-jet}}$, as well as the double ratio, $R^{m}_{r\mathrm{track-jet}}$, versus m^{jet} for jets reconstructed with the three algorithms considered as well as the standard anti-k_t, $R = 0.6$ jet algorithm. Events in the data are required to have $N_{\mathrm{PV}} = 1$ and the MC samples are simulated without pile-up overlaid.

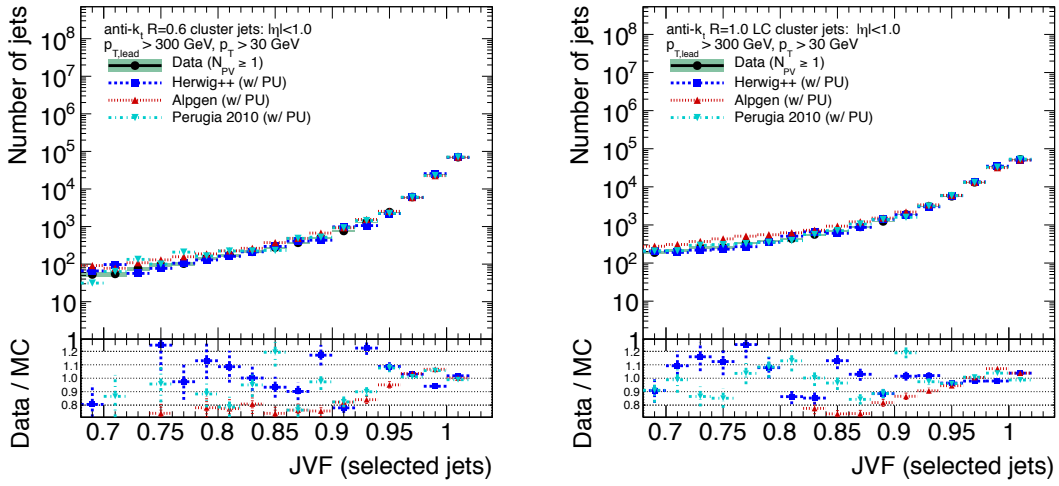

(a) anti-k_t, $R = 0.6$ (b) anti-k_t, $R = 1.0$

(c) C/A, $R = 1.2$ (d) C/A, $R = 1.2$ (filtered)

Figure E.9: Distributions of JVF for jets reconstructed with the three algorithms considered for substructure studies as well as the standard anti-k_t, $R = 0.6$ jet algorithm for comparison. The MC samples are each simulated with pile-up.

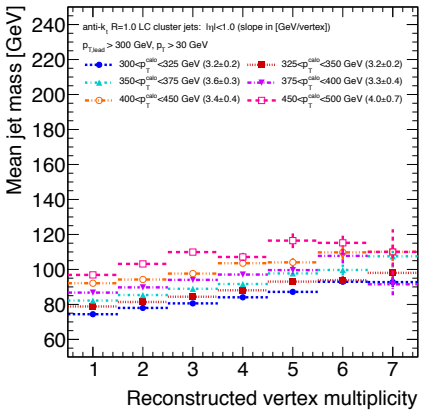

(a) anti-k_t, $R = 1.0$ (clusters)

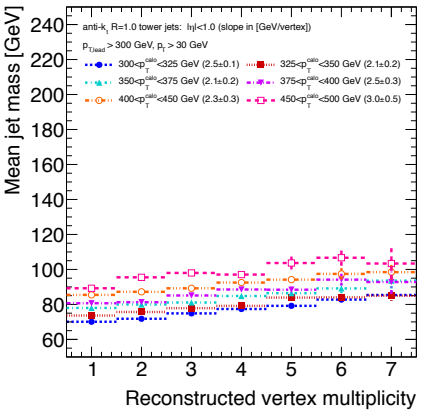

(b) anti-k_t, $R = 1.0$ (towers)

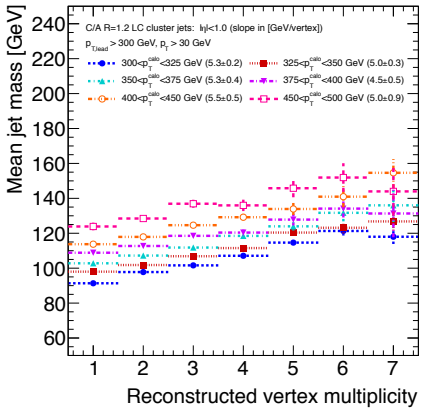

(c) C/A, $R = 1.2$ (clusters)

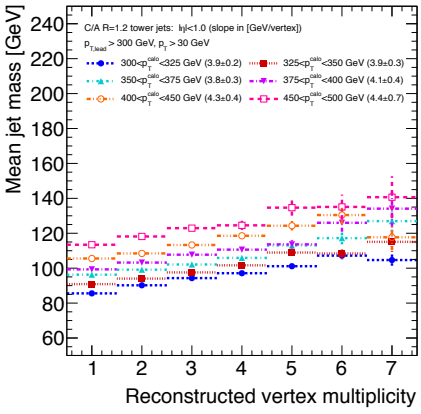

(d) C/A, $R = 1.2$ (towers)

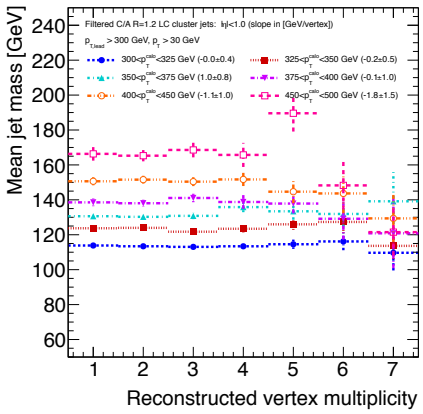

(e) Filtered C/A, $R = 1.2$ (clusters)

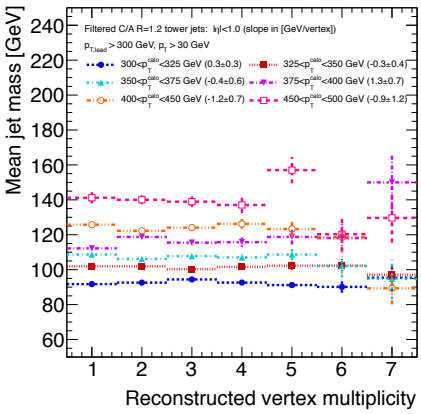

(f) Filtered C/A, $R = 1.2$ (towers)

Figure E.10: Differential jet mass increase as a function of the number of additional in-time pile-up interactions, as measured via the reconstructed primary vertex multiplicity.

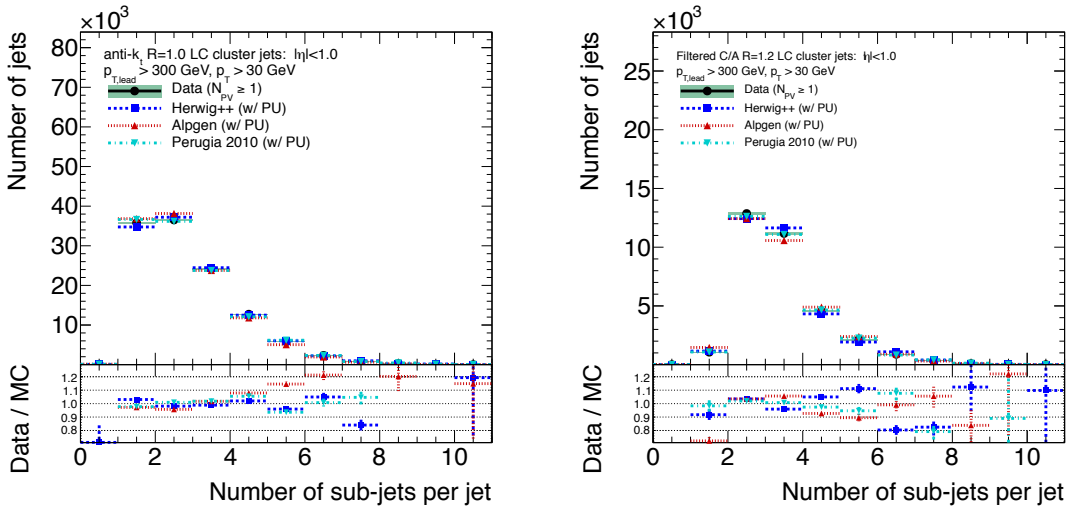

(a) anti-k_t, $R = 1.0$ (b) C/A, $R = 1.2$ (filtered)

Figure E.11: Subjet multiplicity in calorimeter jets for events in the data that include pile-up and for MC samples that have overlaid pile-up included.

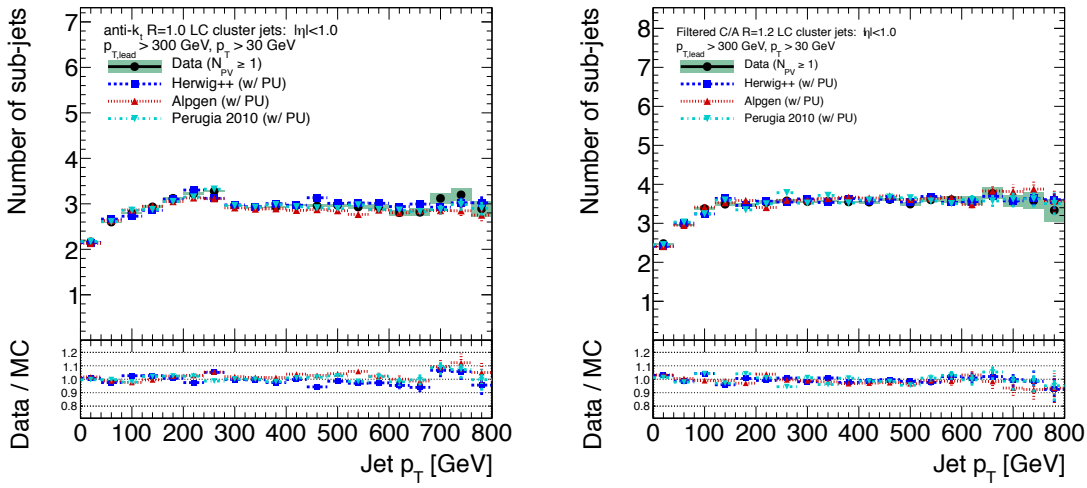

(a) anti-k_t, $R = 1.0$ (b) C/A, $R = 1.2$ (filtered)

Figure E.12: Subjet multiplicity in calorimeter jets as a function of the transverse momentum $p_{\mathrm{T}}^{\mathrm{jet}}$, of the parent jet for anti-k_t, $R = 1.0$ and C/A, $R = 1.2$ (filtered) parent jets.

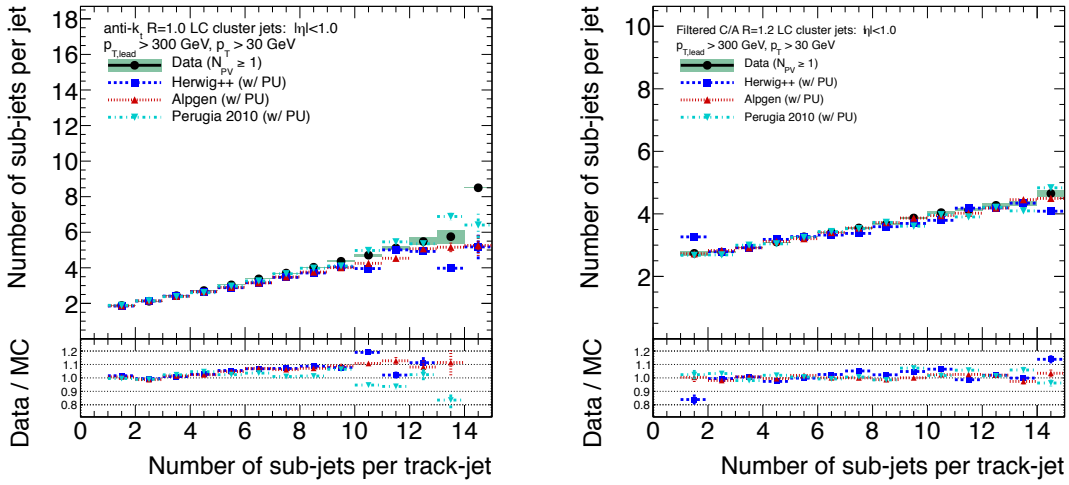

(a) anti-k_t, $R = 1.0$ (b) C/A, $R = 1.2$ (filtered)

Figure E.13: Subjet multiplicity in calorimeter jets as a function of the number of subjets observed in jets constructed from tracks originating in only the hard-scattering interaction. The track-jet is constructed using the same jet algorithm as the parent jet, but in the case of filtered calorimeter jets, no filtering is applied to the matched track-jet

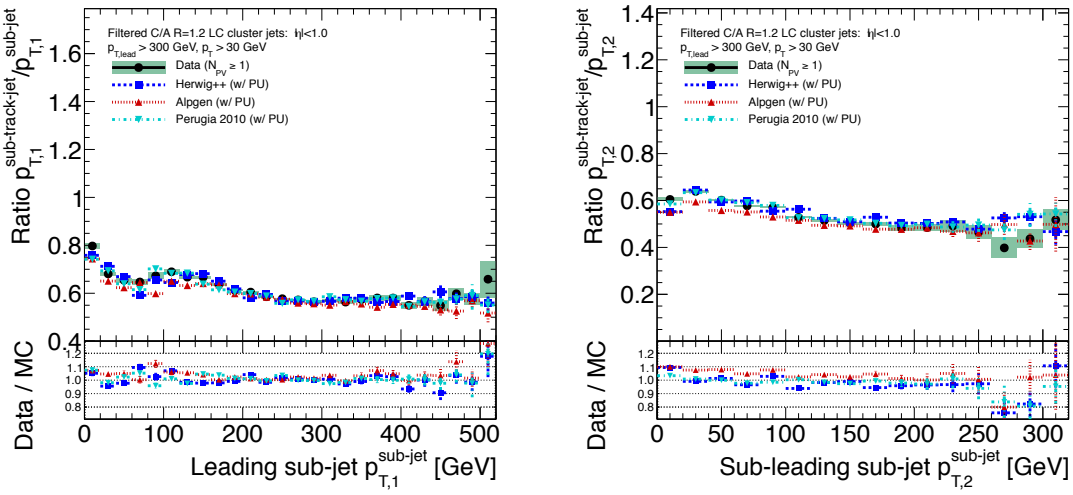

(a) Leading subjet, $j1$

(b) Sub-leading subjet, $j2$

Figure E.14: Ratio of sub-track-jet p_{T} to calorimeter subjet p_{T} using anti-k_t parent jets in order to assess the JES systematics. Both (a) leading, $j1$, and (b) sub-leading, $j2$, subjets exhibit very similar energy response in the data and the MC as compare to subjets within track-jets.

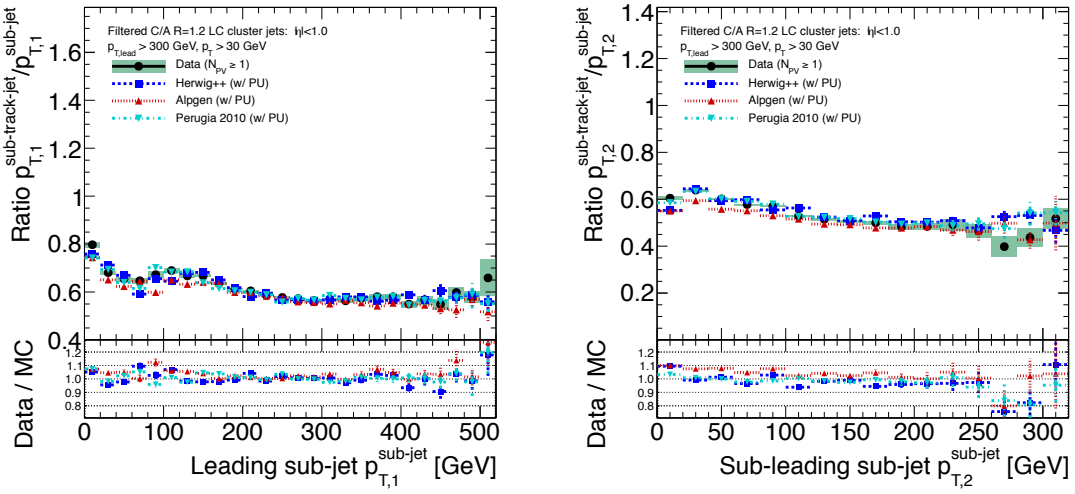

(a) Leading subjet, $j1$ (b) Sub-leading subjet, $j2$

Figure E.15: Ratio of sub-track-jet p_{T} to calorimeter subjet p_{T} using C/A, $R = 1.2$ (filtered) parent jets in order to assess the JES systematics. Both (a) leading, $j1$, and (b) sub-leading, $j2$, subjets exhibit very similar energy response in the data and the MC as compare to subjets within track-jets.

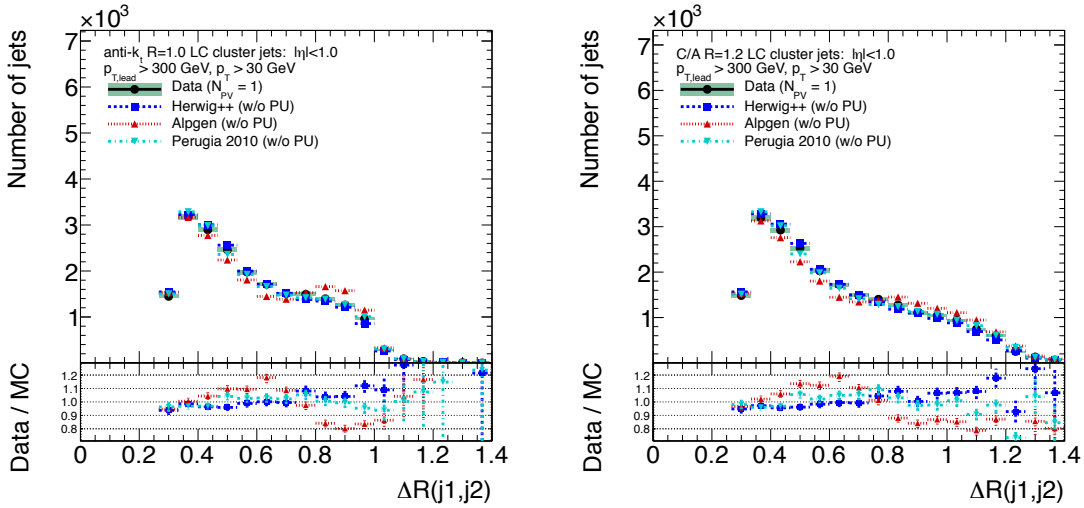

(a) anti-k_t (b) C/A

Figure E.16: Angular separation, ΔR, between the leading, $j1$, and sub-leading, $j2$, subjets within both (a) anti-k_t and (b) C/A parent jets. The MC samples include pile-up overlaid to match the data.

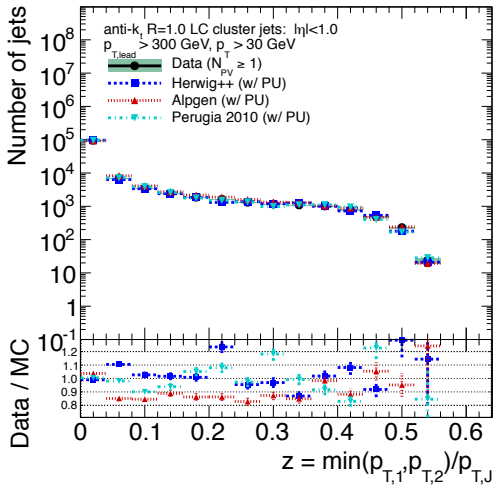

(a) anti-k_t, $R = 1.0$, z

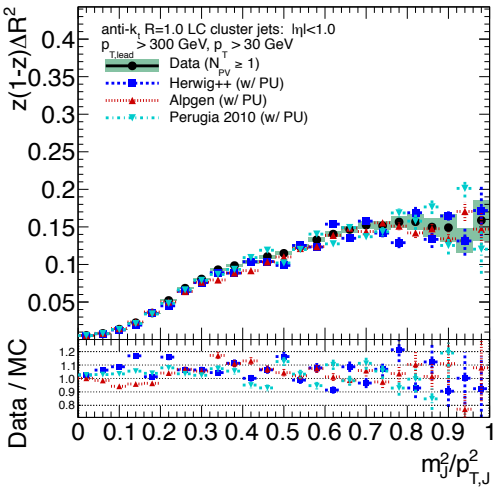

(b) anti-k_t, $R = 1.0$, x_J correlation

Figure E.17: In anti-k_t, $R = 1.0$ parent jets, the (a) subjet relative transverse momentum sharing characterized by $z = \frac{\min(p_{T,j1}, p_{T,j2})}{p_{T,J}}$ and (b) the correlation of $x_J = z(1-z)\Delta R^2_{j1,j2}$ with the relative mass, $\frac{m^2}{p_T^2}$ of the parent jet.

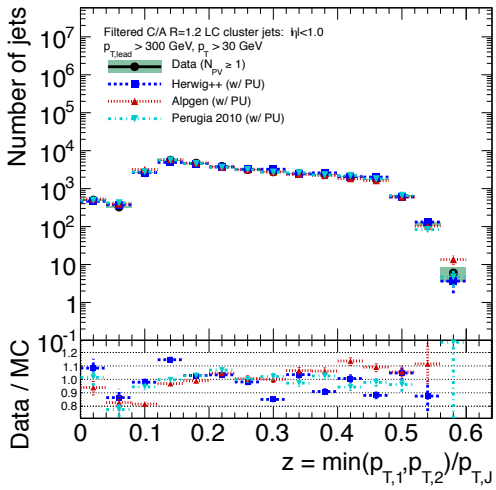

(a) C/A, $R = 1.2$ (filtered) , z

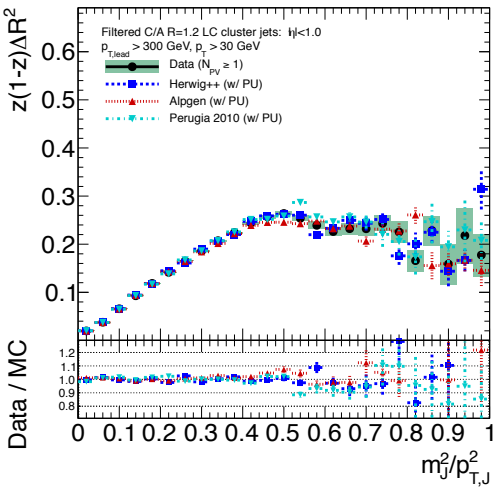

(b) C/A, $R = 1.2$ (filtered) , x_J correlation

Figure E.18: In C/A, $R = 1.2$ (filtered) parent jets, the (a) subjet relative transverse momentum sharing characterized by $z = \frac{\min(p_{T,j1}, p_{T,j2})}{p_{T,J}}$ and (b) the correlation of $x_J = z(1-z)\Delta R^2_{j1,j2}$ with the relative mass, $\frac{m^2}{p_T^2}$ of the parent jet.

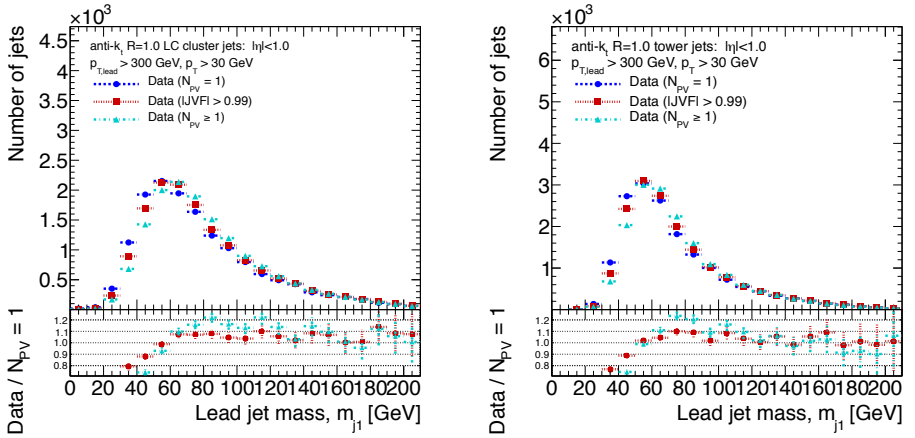

(a) anti-k_t, $R = 1.0$ (clusters) (b) anti-k_t, $R = 1.0$ (towers)

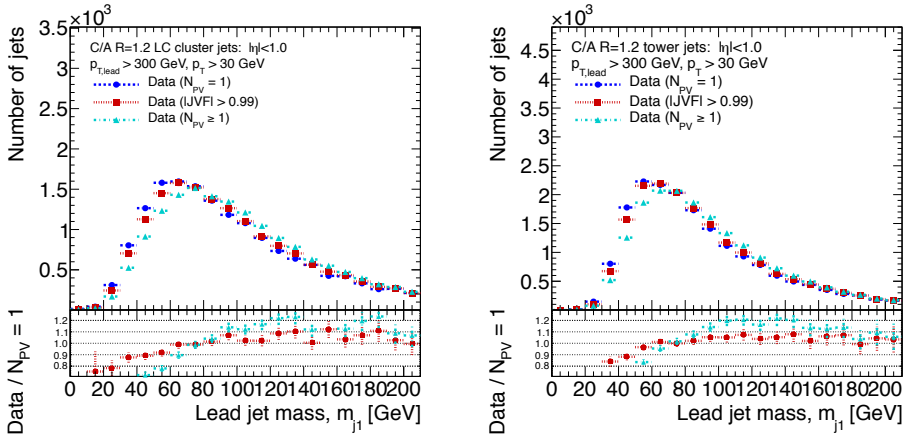

(c) C/A, $R = 1.2$ (clusters) (d) C/A, $R = 1.2$ (towers)

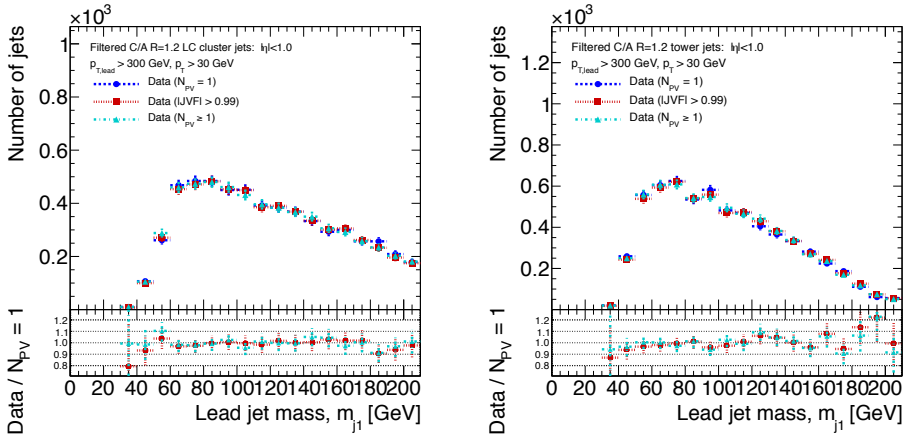

(e) Filtered C/A, $R = 1.2$ (clusters) (f) Filtered C/A, $R = 1.2$ (towers)

Figure E.19: Leading jet mass distributions in data for several selection criteria. Events with a single reconstructed primary vertex, $N_{\mathrm{PV}} = 1$ (dashed blue with circles), jets selected to have $|JVF| > 0.99$ and thus little to no impact from pile-up (dotted red with squares) and all events, including significant pile-up (dot-dashed cyan with triangles) are all compared.

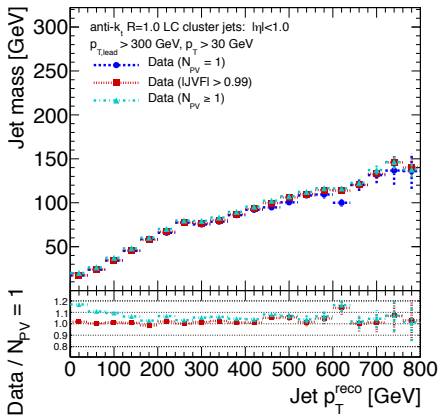

(a) anti-k_t, $R = 1.0$ (clusters)

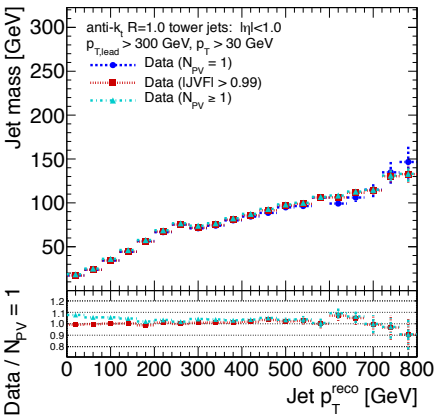

(b) anti-k_t, $R = 1.0$ (towers)

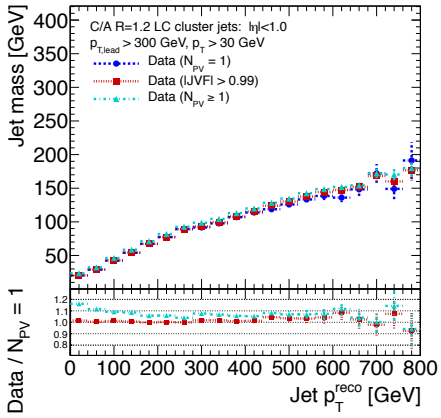

(c) C/A, $R = 1.2$ (clusters)

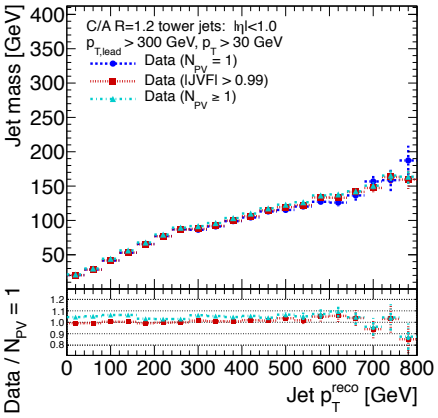

(d) C/A, $R = 1.2$ (towers)

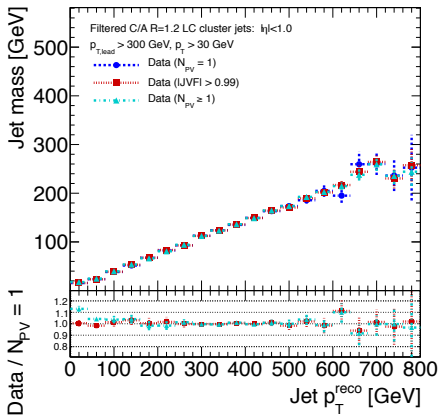

(e) Filtered C/A, $R = 1.2$ (clusters)

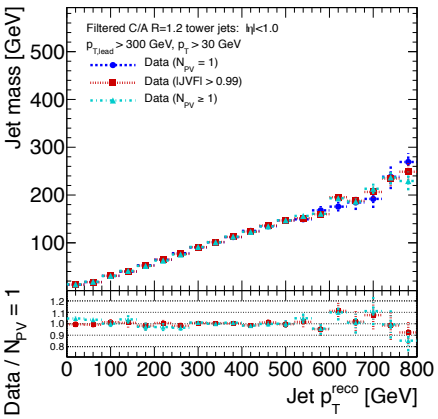

(f) Filtered C/A, $R = 1.2$ (towers)

Figure E.20: Mean jet mass versus $p_{\mathrm{T}}^{\mathrm{jet}}$ in data for several selection criteria. Events with a single reconstructed primary vertex, $N_{\mathrm{PV}} = 1$ (dashed blue with circles), jets selected to have $|JVF| > 0.99$ and thus little to no impact from pile-up (dotted red with squares) and all events, including significant pile-up (dot-dashed cyan with triangles) are all compared.

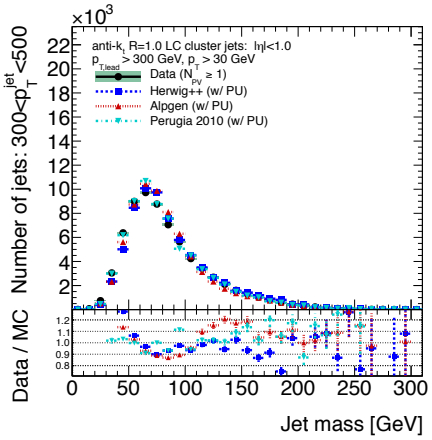

(a) anti-k_t, $R = 1.0$ (clusters)

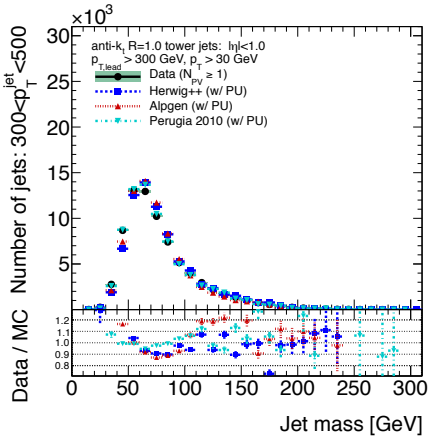

(b) anti-k_t, $R = 1.0$ (towers)

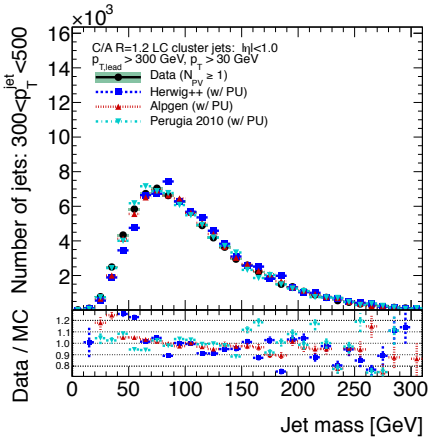

(c) anti-k_t, $R = 1.0$ (clusters)

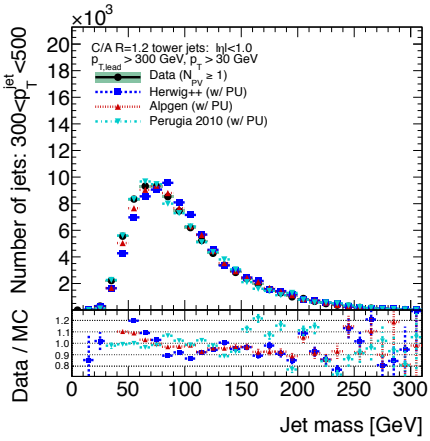

(d) anti-k_t, $R = 1.0$ (towers)

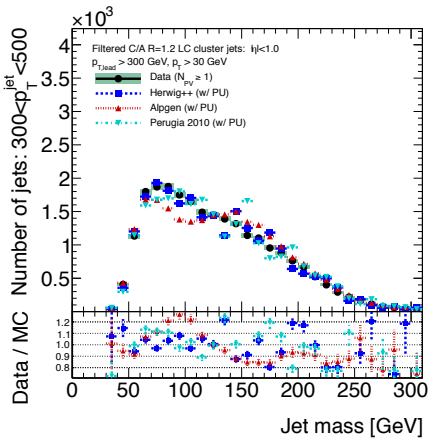

(e) Filtered anti-k_t, $R = 1.0$ (clusters)

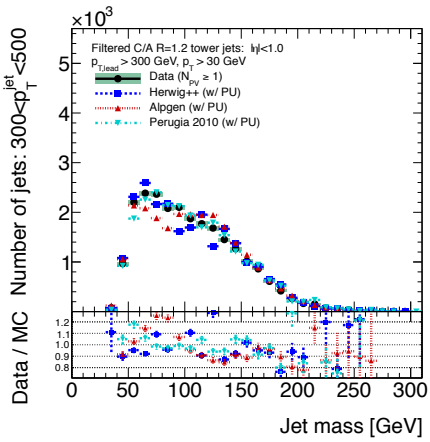

(f) Filtered anti-k_t, $R = 1.0$ (towers)

Figure E.21: Jet mass at the detector level for each jet algorithm and MC generator considered in the substructure analysis. Jets are selected to have 300 GeV $< p_{\mathrm{T}} <$ 500 GeV. The MC is simulated with additional pile-up interactions and the data contain multiple pp interactions.

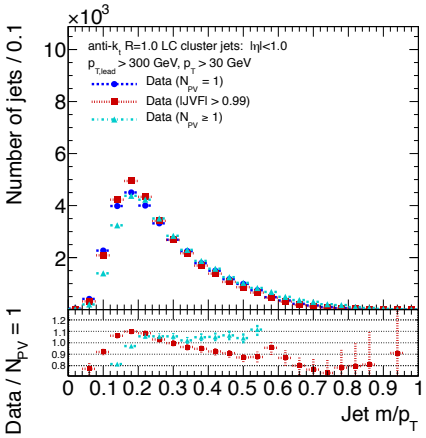

(a) anti-k_t, $R = 1.0$ (clusters)

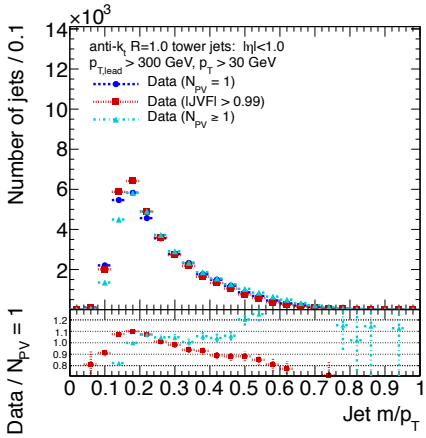

(b) anti-k_t, $R = 1.0$ (towers)

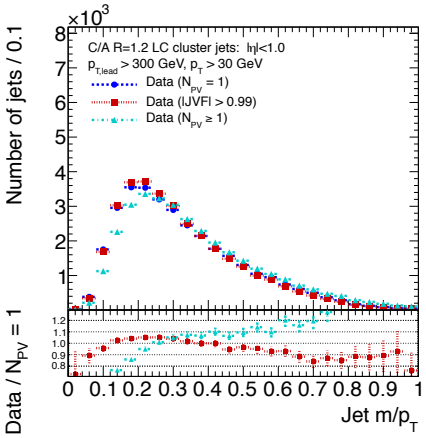

(c) C/A, $R = 1.2$ (clusters)

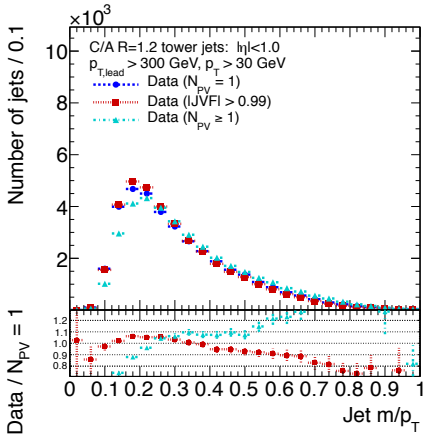

(d) C/A, $R = 1.2$ (towers)

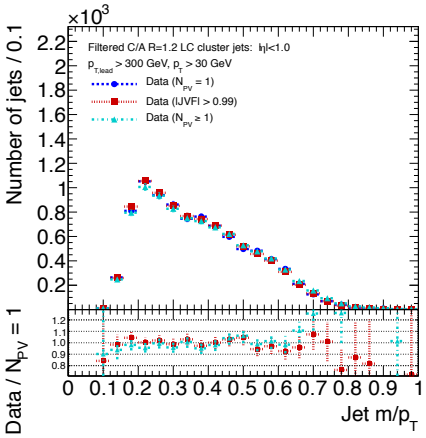

(e) Filtered C/A, $R = 1.2$ (clusters)

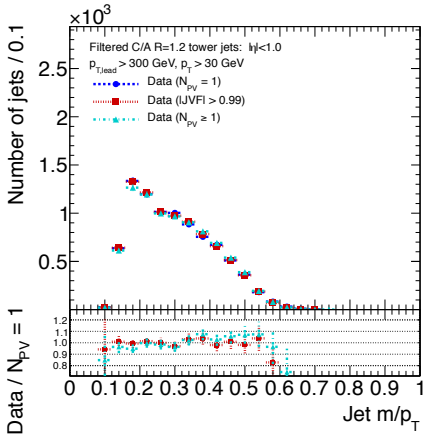

(f) Filtered C/A, $R = 1.2$ (towers)

Figure E.22: Inclusive jet $m^{\text{jet}}/p_{\text{T}}^{\text{jet}}$ distributions in data for several selection criteria. Events with a single reconstructed primary vertex, $N_{\text{PV}} = 1$ (dashed blue with circles), jets selected to have $|JVF| > 0.99$ and thus little to no impact from pile-up (dotted red with squares) and all events, including significant pile-up (dot-dashed cyan with triangles) are all compared.

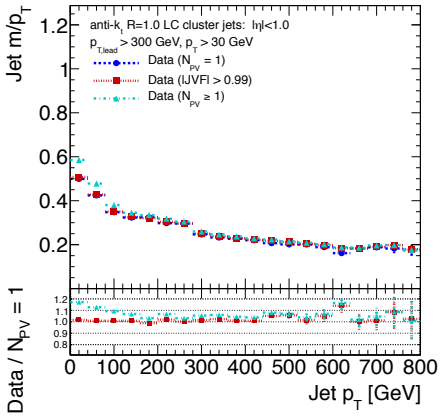

(a) anti-k_t, $R = 1.0$ (clusters)

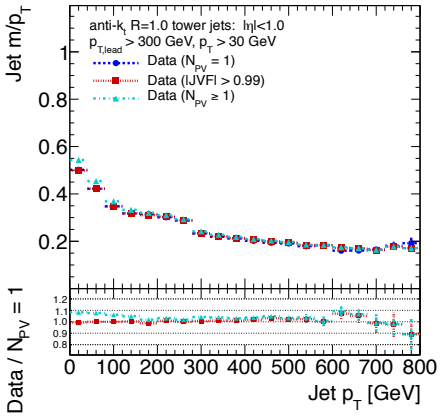

(b) anti-k_t, $R = 1.0$ (towers)

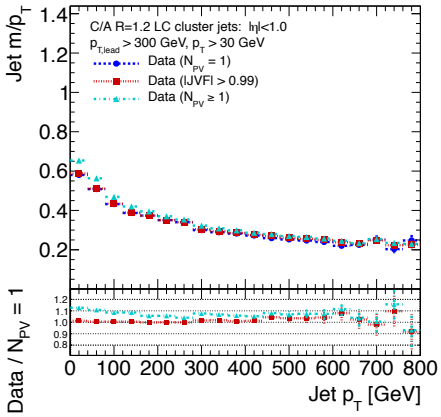

(c) C/A, $R = 1.2$ (clusters)

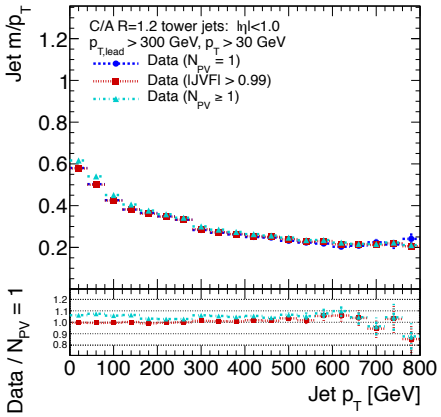

(d) C/A, $R = 1.2$ (towers)

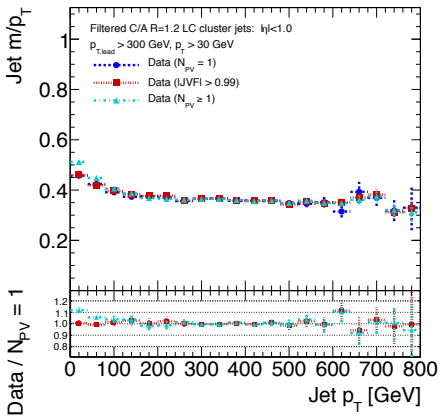

(e) Filtered C/A, $R = 1.2$ (clusters)

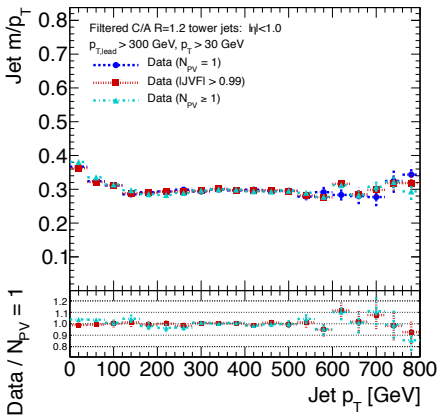

(f) Filtered C/A, $R = 1.2$ (towers)

Figure E.23: Mean jet $m^{\text{jet}}/p_{\text{T}}^{\text{jet}}$ versus $p_{\text{T}}^{\text{jet}}$ in data for several selection criteria. Events with a single reconstructed primary vertex, $N_{\text{PV}} = 1$ (dashed blue with circles), jets selected to have $|JVF| > 0.99$ and thus little to no impact from pile-up (dotted red with squares) and all events, including significant pile-up (dot-dashed cyan with triangles) are all compared.

E.3.3 Jet filtering

Figure E.25 shows the jet mass and p_{T} filtering ratios as a function of the jet mass.

Figure E.26 shows that as the opening angle between the two hardest tracks in the jet increases past the jet radius, the impact of filtering increases.

E.3.4 Color flow

Figure E.27 shows the dependence of the dipolarity on $\Delta R_{j1,j2}$ and z for the anti-k_t, $R = 1.0$ jet algorithm.

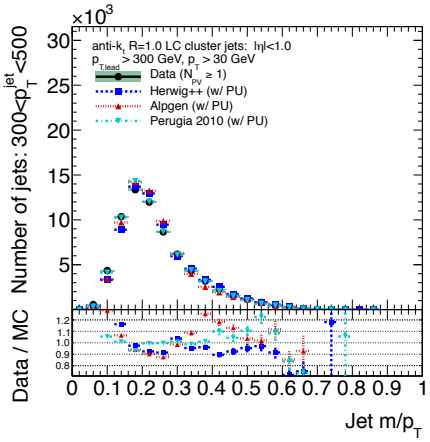

(a) anti-k_t, $R = 1.0$ (clusters)

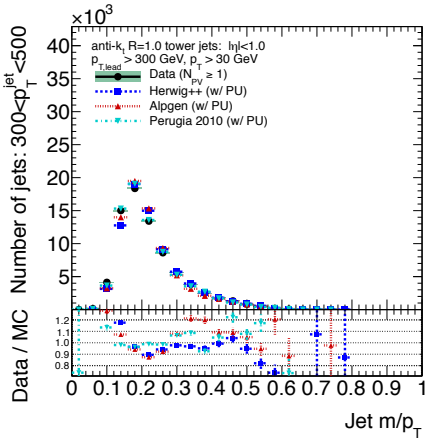

(b) anti-k_t, $R = 1.0$ (towers)

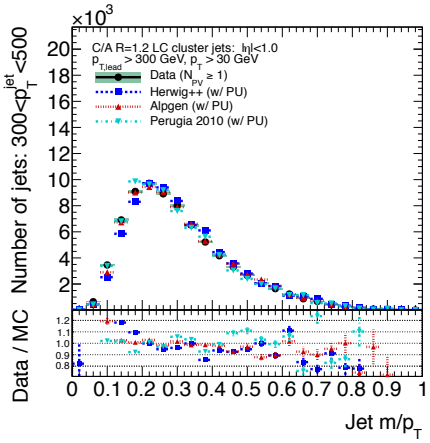

(c) C/A, $R = 1.2$ (clusters)

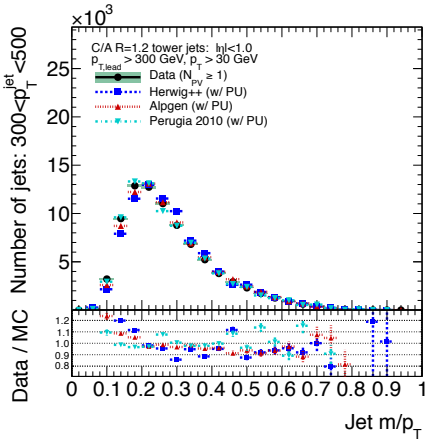

(d) C/A, $R = 1.2$ (towers)

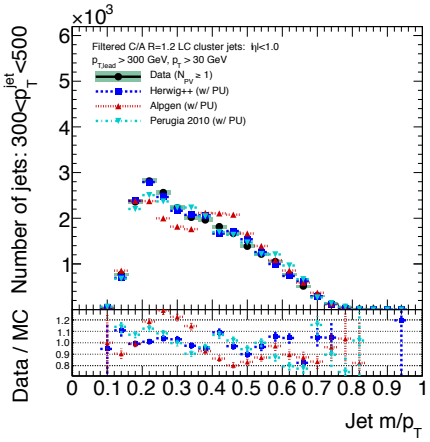

(e) Filtered C/A, $R = 1.2$ (clusters)

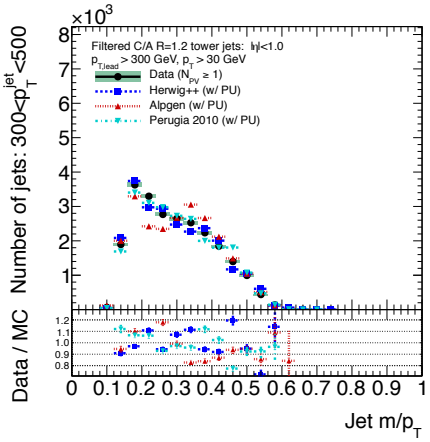

(f) Filtered C/A, $R = 1.2$ (towers)

Figure E.24: Jet $m^{\text{jet}}/p_{\text{T}}^{\text{jet}}$ at the detector level for each jet algorithm and MC generator considered in the substructure analysis. Jets are selected to have 300 GeV $< p_{\text{T}} <$ 500 GeV. The MC is simulated with additional pile-up interactions and the data contain multiple pp interactions.

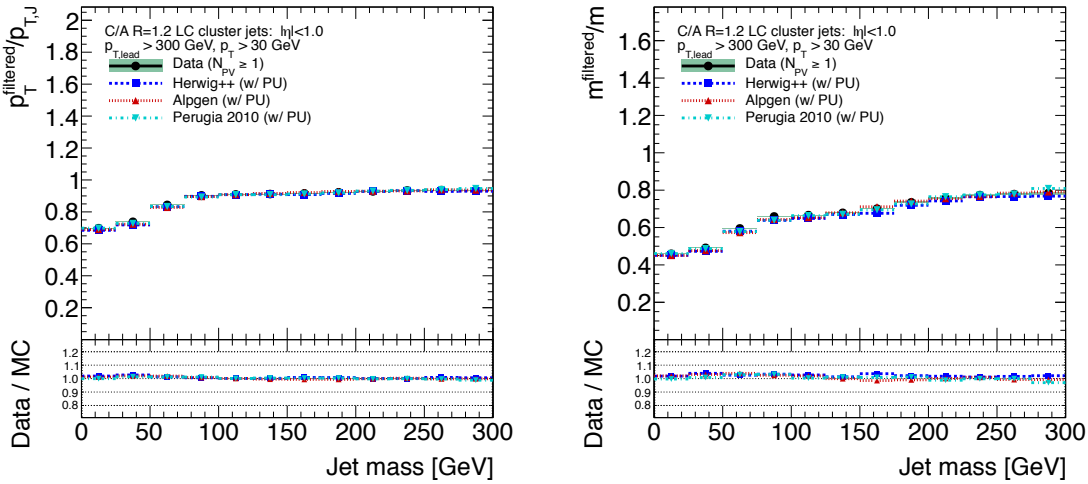

(a) p_{T} filtering ratio (b) Mass filtering ratio

Figure E.25: Ratios of jet mass and p_{T} filtering ratios as a function of the jet mass.

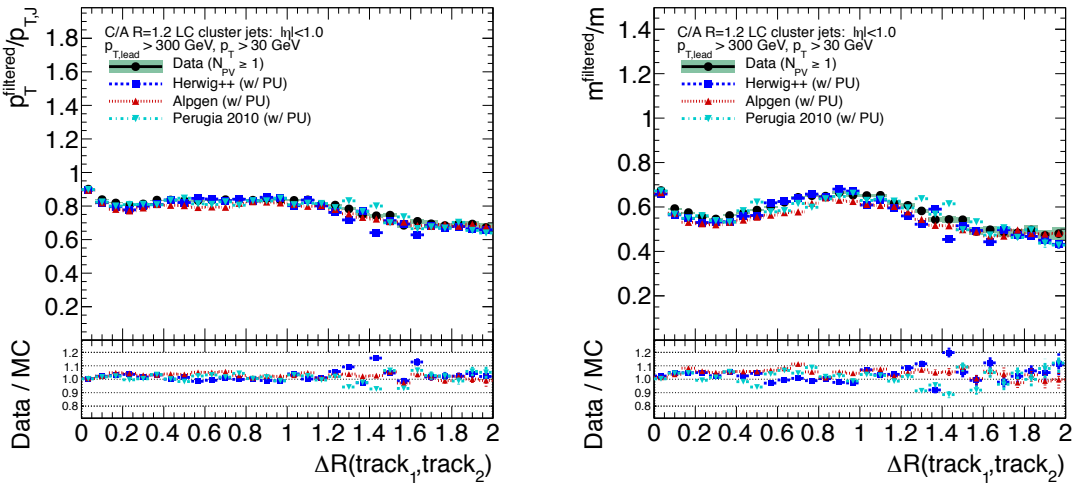

(a) p_{T} filtering ratio (b) Mass filtering ratio

Figure E.26: Ratios of jet mass and p_{T} filtering ratios as a function of the angle between the two hardest tracks found in the jet.

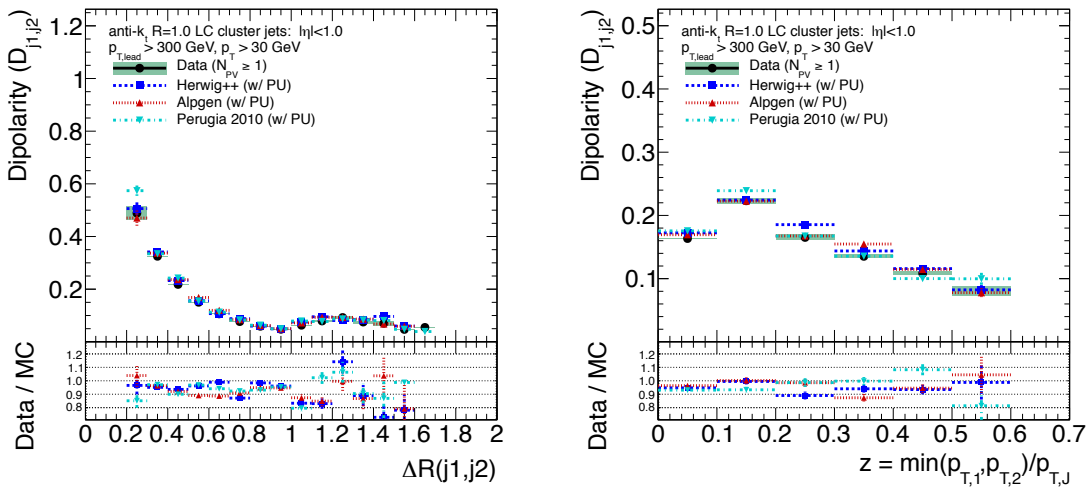

(a) $\mathcal{D}_{12}$ vs. $\Delta R_{j1,j2}$ (b) $\mathcal{D}_{12}$ vs. z

Figure E.27: Dipolarity, $\mathcal{D}_{12}$, for anti-k_t, $R = 1.0$ jets as a function of (a) $\Delta R_{j1,j2}$, where the subjets are defined using the inclusive $k_\perp$algorithm with $R = 0.3$ and (b) z, defined by Eq. 8.3 using the same inclusive subjet definition.

Bibliography

[1] S. Glashow. Partial-symmetries of weak interactions. *Nuclear Physics*, 22(4):579–588, February 1961.

[2] P. Higgs. Broken Symmetries and the Masses of Gauge Bosons. *Phys. Rev. Lett.*, 13(16):508–509, October 1964.

[3] D. A Dicus, E. W. Kolb, V. L. Teplitz, and R. V. Wagoner. Astrophysical bounds on the masses of axions and Higgs particles. *Phys. Rev. D*, 18:1829–1834, 1978.

[4] A. Stange, W. Marciano, and S. Willenbrock. Higgs bosons at the Fermilab Tevatron. *Phys. Rev. D*, 49(3):1354–1362, February 1994.

[5] G. Abbiendi. Search for the Standard Model Higgs boson at LEP. *Physics Letters B*, 565:61–75, July 2003.

[6] H. Georgi and S. Glashow. Unity of all elementary-particle forces. *Phys. Rev. Lett.*, 32(8):438–441, Feb 1974.

[7] G. Bertone, D. Hooper, and J. Silk. Particle Dark Matter: Evidence, Candidates and Constraints. *interactions*, page 144, April 2004.

[8] R. J. Gaitskell. Direct Detection of Dark Matter. *Annual Review of Nuclear and Particle Science*, 54(1):315–359, December 2004.

[9] D. Hooper, I. De La C. Perez, J. Silk, F. Ferrer, and S. Sarkar. Have Atmospheric Cerenkov Telescopes Observed Dark Matter? *Area*, page 19, April 2004.

[10] M. R. Buckley, D. Hooper, and T. M. P. Tait. Particle Physics Implications for CoGeNT, DAMA, and Fermi.

[11] Y. Bai and H.-C. Cheng. Identifying Dark Matter Event Topologies at the LHC.

[12] I. Affleck and M. Dine. A new mechanism for baryogenesis. *Nuclear Physics B*, 249(2):380–361, 1985.

[13] R. D. Peccei and H. R. Quinn. CP Conservation in the Presence of Pseudoparticles. *Phys. Rev. Lett.*, 38:1440–1443, June 1977.

[14] J. K. Kim. Weak-interaction singlet and strong CP invariance. *Phys. Rev. Lett.*, 2:103–107, 43.

[15] M. A. Shifman, A. I. Vainshtein, and V. I. Zakharov. Can confinement ensure natural *cp* invariance of the strong interactions? *nucpb*, 166:493–506, 1980.

[16] M. Dine, W. Fischler, and M. Srednicki. A simple solution to the strong CP problem with a harmless axion. *Phys. Lett. B*, 104:199–202, 1981.

[17] P. Sikivie. Dark matter axions '96. *Physics*, 32611(1):12, November 1996.

[18] J. E. Kim and H. P. Nilles. A Quintessential Axion.

[19] E. V. Bugaev. Matter-antimatter asymmetry. *Nuclear Physics B - Proceedings Supplements*, pages 98–108, 2003.

[20] G. Hanson et al. Evidence for Jet Structure in Hadron Production by e^+e^- Annihilation. *Phys. Rev. Lett.*, 35(24):1609–1612, December 1975.

[21] G. Hanson. Hadron production by e^+e^- annihilation at center-of-mass energies between 2.6 and 7.8 GeV. II. Jet structure and related inclusive distributions. *Phys. Rev. D*, 26(5):991 – 1012, 1982.

[22] W. Bartel et al. Experimental studies on multijet production in e^+e^- annihilation at PETRA energies. *Zeitschrift fur Physik C Particles and Fields*, 33(1):23–31, March 1986.

[23] S. Bethke et al. Experimental investigation of the energy dependence of the strong coupling strength. *Physics Letters B*, 213(2):235–241, October 1988.

[24] E. Torrence et al. Determination of Electroweak Parameters at the SLC.

[25] ALEPH Collaboration, CDF Collaboration, D0 Collaboration, DELPHI Collaboration, L3 Collaboration, OPAL Collaboration, SLD Collaboration, LEP Electroweak Working Group, Tevatron Electroweak Working Group, and SLD electroweak heavy flavour Groups. Precision Electroweak Measurements and Constraints on the Standard Model.

[26] M. Banner et al. Observation of very large transverse momentum jets at the CERN p collider. *Physics Letters B*, 118(1-3):203–210, December 1982.

[27] F. Pastore. Latest results on high-p_T jets in UA2. *CERN CDS*, CERN-EP-85, 1985.

[28] W. Kozanecki. The PEP-II B-factory: status and prospects*1.

[29] B. Aubert et al. The first year of the BABAR experiment at PEP-II. arXiv:0012042 [hep-ex].

[30] S. Kluth. Tests of quantum chromo dynamics at e^+e^- colliders. *Reports on Progress in Physics*, 69(6):1771–1846, June 2006.

[31] J. Drees. Review of Final LEP Results or A Tribute to LEP.

[32] H. Stenzel. Final QCD results from LEP.

[33] The OPAL Collaboration. Determination of α_s using OPAL hadronic event shapes at $\sqrt{s} = 91 - 209$ GeV and resummed NNLO calculations.

[34] F. Abe et al. Kinematic evidence for top quark pair production in W+multijet events in $p\bar{p}$ collisions at $\sqrt{s} = 1.8$ TeV. *Phys. Rev. D*, 51(9):4623–4637, May 1995.

[35] D. Toback. Cosmo-particle searches for supersymmetry at the Collider Detector at Fermilab. *Modern Physics Letters A*, 24(38):3063, November 2009.

[36] A. Bhatti and D. Lincoln. Jet Physics at the Tevatron.

[37] S. Eidelman et al. Review of Particle Physics. *Physics Letters B*, 592:1+, 2004.

[38] A. S. Kronfeld and C. Quigg. Resource Letter: Quantum Chromodynamics.

[39] M. Gell-Mann, M. Goldberger, N. Kroll, and F. Low. Amelioration of Divergence Difficulties in the Theory of Weak Interactions. *Physical Review*, 179(5):1518–1527, March 1969.

[40] H. Fritzsch, M. Gell-Mann, and H. Leutwyler. Advantages of the color octet gluon picture. *Physics Letters B*, 47(4):365–368, November 1973.

[41] K. Wilson. Confinement of quarks. *Phys. Rev. D*, 10(8):2445–2459, October 1974.

[42] G. Altarelli. Asymptotic freedom in parton language. *Nuclear Physics B*, 126(2):298–318, August 1977.

[43] G. Sterman. Jets from Quantum Chromodynamics. *Phys. Rev. Lett.*, 39(23):1436–1439, December 1977.

[44] E. Farhi. Quantum Chromodynamics Test for Jets. *Phys. Rev. Lett.*, 39(25):1587–1588, December 1977.

[45] A. Ali and G. Kramer. Jets and QCD.

[46] H. Politzer. Reliable Perturbative Results for Strong Interactions? *Phys. Rev. Lett.*, 30(26):1346–1349, June 1973.

[47] D. Gross and F. Wilczek. Ultraviolet Behavior of Non-Abelian Gauge Theories. *Phys. Rev. Lett.*, 30(26):1343–1346, June 1973.

[48] H. Nishino et al. Search for proton decay via $p \to e^+\pi^0$ and $p \to \mu^+\pi^0$ in a large water cherenkov detector. *Phys. Rev. Lett.*, 102(14):141801, Apr 2009.

[49] G. P. Salam. Elements of QCD for hadron colliders.

[50] M. Peskin and D. Schroeder. *Quantum field theory*. Addison-Wesley Advanced Book Program, 1996.

[51] M. Gemm-Mann. A schematic model of baryons and mesons. *Physics Letters*, 8(3):214–215, February 1964.

[52] R. Feynman. Very High-Energy Collisions of Hadrons. *Phys. Rev. Lett.*, 23(24):1415–1417, December 1969.

[53] G. Kalbfleisch et al. Observation of a Nonstrange Meson of Mass 959 MeV. *Phys. Rev. Lett.*, 12(18):527–530, May 1964.

[54] M. Goldberg, M. Gundzik, S. Lichtman, J. Leitner, M. Primer, P. Connolly, E. Hart, K. Lai, G. London, N. Samios, and S. Yamamoto. Existence of a New Meson of Mass 960 MeV. *Phys. Rev. Lett.*, 12(19):546–550, May 1964.

[55] G. Zweig. An $SU(3)$ model for strong interaction symmetry and its breaking, 1964.

[56] W. Bartel et al. Observation of four-jet structure in e^+e^- annihilation at $\sqrt{s} =$ 33 GeV. *Physics Letters B*, 115(4):338–344, September 1982.

[57] S. Kluth. $\alpha_s(M_Z)$ from Jade Event Shapes.

[58] D. Stump, J. Huston, J. Pumplin, W.-K. Tung, H.-L. Lai, S. Kuhlmann, and J. F. Owens. Inclusive jet production, parton distributions, and the search for new physics. *Journal of High Energy Physics*, 2003(10):046–046, October 2003.

[59] A. D. Martin, W. J. Stirling, R. S. Thorne, and G. Watt. Parton distributions for the LHC. *European Physical Journal C*, 63(2):189–285, July 2009.

[60] R. D. Ball, L. Del Debbio, S. Forte, A. Guffanti, J. I. Latorre, J. Rojo, and M. Ubiali. A first unbiased global NLO determination of parton distributions and their uncertainties.

[61] F. D. Aaron et al. Combined measurement and QCD analysis of the inclusive e p scattering cross sections at HERA. *Journal of High Energy Physics*, 2010(1):61, January 2010.

[62] D. Stump et al. Inclusive jet production, parton distributions, and the search for new physics. *JHEP*, 10:046, 2003, arXiv:hep-ph/0303013.

[63] A. Martin, W. Stirling, R. Thorne, and G. Watt. Parton distributions for the lhc. *The European Physical Journal C - Particles and Fields*, 63:189–285, 2009, arXiv:hep-ph/0901.0002. 10.1140/epjc/s10052-009-1072-5.

[64] G. T. J. Arnison et al. Experimental observation of lepton pairs of invariant mass around 95 GeV/c^2 at the CERN SPS collider. *Physics Letters B*, 126(5):398–410, 1983.

[65] M. L. Mangano, Mauro Moretti, F. Piccinini, R. Pittau, and A. D. Polosa. ALPGEN, a generator for hard multiparton processes in hadronic collisions. *JHEP*, 07:001, 2003, arXiv:hep-ph/0206293.

[66] E. Boos, V. Bunichev, M. Dubinin, L. Dudko, V. Edneral, V. Ilyin, A. Kryukov, V. Savrin, A. Semenov, and A. Sherstnev. CompHEP 4.4automatic computations from Lagrangians to events. *Nuclear Instruments and Methods in Research A*, 534(1-2):250–259, November 2004.

[67] J. Alwall, P. Demin, S. de Visscher, R. Frederix, M. Herquet, F. Maltoni, T. Plehn, D. L. Rainwater, and T. Stelzer. MadGraph/MadEvent v4: the new web generation. *Journal of High Energy Physics*, 2007(09):028–028, September 2007.

[68] S. Frixione, P. Nason, and C. Oleari. Matching NLO QCD computations with parton shower simulations: the POWHEG method. *Journal of High Energy Physics*, 2007(11):070–070, November 2007.

[69] S. Alioli, P. Nason, C. Oleari, and E. Re. A general framework for implementing NLO calculations in shower Monte Carlo programs: the POWHEG BOX. *Journal of High Energy Physics*, 2010(6):1–58–58, June 2010.

[70] A. Cafarella, C. G. Papadopoulos, and M. Worek. Helac-Phegas: A generator for all parton level processes. *Computer Physics Communications*, 180(10):1941–1955, October 2009.

[71] T. Gleisberg and S. Höche. Comix, a new matrix element generator. *Journal of High Energy Physics*, 2008(12):039–039, December 2008.

[72] G. Corcella, I. G. Knowles, G. Marchesini, S. Moretti, K. Odagiri, P. Richardson, M. H. Seymour, and B. R. Webber. HERWIG 6: an event generator for hadron emission reactions with interfering gluons (including supersymmetric processes). *Journal of High Energy Physics*, 2001(01):010–010, January 2001.

[73] J. M. Butterworth, J. R. Forshaw, and M. H. Seymour. Multiparton Interactions in Photoproduction at HERA. *Zeitschrift für Physik C Particles and Fields*, 72(4):21, January 1996, arXiv:9601371 [hep-ph].

[74] T. Sjöstrand. High-energy-physics event generation with PYTHIA6.1. *Computer Physics Communications*, 135(2):238–259, April 2001.

[75] P. Z. Skands. Tuning Monte Carlo Generators: The Perugia Tunes. *Phys. Rev. D*, 82:074018, 2010, arXiv:1005.3457 [hep-ph].

[76] M. Bähr, S. Gieseke, M. A. Gigg, D. Grellscheid, K. Hamilton, O. Latunde-Dada, S. Plätzer, P. Richardson, M. H. Seymour, A. Sherstnev, and B. R. Webber. Herwig++ physics and manual. *European Physical Journal C*, 58(4):639–707, November 2008.

[77] M. A. Dobbs et al. Les Houches Guidebook to Monte Carlo Generators for Hadron Collider Physics.

[78] M. L. Mangano and T. J. Stelzer. Tools for the simulation of hard hadronic collisions. *Annual Review of Nuclear and Particle Science*, 55(1):555–588, December 2005.

[79] T. Sjöstrand. Monte Carlo Tools.

[80] H Georgi. Effective Field Theory. *Annual Review of Nuclear and Particle Science*, 43(1):209–252, December 1993.

[81] G. Ecker. Effective field theories.

[82] C. P. Burgess. An Introduction to Effective Field Theory. *Annual Review of Nuclear and Particle Science*, 57(1):329–362, November 2007.

[83] J. C. Collins, D. E. Soper, and G. Sterman. *Perturbative Quantum Chromodynamics*. World Scientific, Singapore, 1989.

[84] G. Sterman. Partons, Factorization and Resummation, TASI95.

[85] C. W. Bauer, S. Fleming, and M. Luke. Summing Sudakov logarithms in B[over]X_{s}γ in effective field theory. *Phys. Rev. D*, 63(1):23, December 2000.

[86] C. W. Bauer, S. Fleming, D. Pirjol, and I. W. Stewart. An effective field theory for collinear and soft gluons: Heavy to light decays. *Phys. Rev. D*, 63(11):31, May 2001.

[87] C. Bauer. Invariant operators in collinear effective theory. *Physics Letters B*, 516(1-2):134–142, September 2001.

[88] C. W. Bauer, D. Pirjol, and I. W. Stewart. Soft-collinear factorization in effective field theory. *Phys. Rev. D*, 65(5):32, February 2002.

[89] C. W. Bauer, S. Fleming, D. Pirjol, I. Z. Rothstein, and I. W. Stewart. Hard scattering factorization from effective field theory. *Phys. Rev. D*, 66(1):35, July 2002.

[90] S. D. Ellis, A. Hornig, C. Lee, C. K. Vermilion, and J. R. Walsh. Jet Shapes and Jet Algorithms in SCET.

[91] S. D. Ellis, A. Hornig, C. Lee, C. K. Vermilion, and J. R. Walsh. Consistent factorization of jet observables in exclusive multijet cross sections. *Physics Letters B*, 689(2-3):82–89, May 2010.

[92] Iain W. Stewart, Frank J. Tackmann, and Wouter J. Waalewijn. Factorization at the LHC: From PDFs to Initial State Jets.

[93] S. Mantry and F. Petriello. Factorization and resummation of Higgs boson differential distributions in soft-collinear effective theory. *Phys. Rev. D*, 81(9):66, May 2010.

[94] T. Plehn. Lectures on LHC Physics. arXiv:0910.4182.

[95] G 't Hooft. Dimensional regularization and the renormalization group. *Nuclear Physics B*, 61:455–468, September 1973.

[96] S. Weinberg. New Approach to the Renormalization Group. *Phys. Rev. D*, 8(10):3497–3509, November 1973.

[97] R. K. Ellis, W. J. Stirling, and B. R. Webber. *QCD and Collider Physics*. Cambridge University Press, Cambridge, 1996.

[98] M. Dasgupta and G. P. Salam. Event shapes in e^+e^- annihilation and deep inelastic scattering. *Journal of Physics G: Nuclear and Particle Physics*, 30(5):R143–R181, May 2004.

[99] S. Catani, Yu. L. Dokshitzer, M. Olsson, G. Turnock, and B. R. Webber. New clustering algorithm for multijet cross sections in e^+e^- annihilation. *Physics Letters B*, 269(3-4):432–438, October 1991.

[100] S. D. Ellis. Successive combination jet algorithm for hadron collisions. *Phys. Rev. D*, 48(7):3160–3166, October 1993.

[101] S. Catani, Yu. L. Dokshitzer, M. H. Seymour, and B. R. Webber. Longitudinally-invariant k_t-clustering algorithms for hadron-hadron collisions. *Nuclear Physics B*, 406(1-2):187–224, September 1993.

[102] G. P. Salam. Towards Jetography.

[103] Y. L. Dokshitzer, G. D. Leder, S. Moretti, and B. R. Webber. Better Jet Clustering Algorithms. *JHEP*, 08:001, 1997, arXiv:hep-ph/9707323.

[104] M. Cacciari and G. P. Salam. Dispelling the N^3 myth for the k_t jet-finder. *Phys. Lett. B*, 641(1):57 – 61, 2006.

[105] M. Cacciari, G. P. Salam, and G. Soyez. The anti-k$_t$ jet clustering algorithm. *JHEP*, 04:063, 2008, arXiv:0802.1189 [hep-ph].

[106] L. Asquith et al. Performance of Jet Algorithms in the ATLAS Detector. *ATLAS Note*, ATL-PHYS-INT-2010-129, Dec 2010.

[107] M. Cacciari, G. P. Salam, and G. Soyez. FastJet.

[108] W. Bartel. Observation of planar three-jet events in e^+e^- annihilation and evidence for gluon bremsstrahlung. *Physics Letters B*, 91(1):142–147, March 1980.

[109] T. Kluge. alpha(s) Determinations from Jets and Scaling Violations at HERA.

[110] The OPAL Collaboration and G. Abbiendi. Measurement of alpha s with Radiative Hadronic Events.

[111] S. Kluth, P. A. M. Fernández, S. Bethke, C. Pahl, and P. Pfeifenschneider. A measurement of the QCD colour factors using event shape distributions at to 189 GeV. *European Physical Journal C*, 21(2):199 – 210, 2001.

[112] I. W. Stewart, F. J. Tackmann, and W. J. Waalewijn. N-Jettiness: An Inclusive Event Shape to Veto Jets.

[113] CMS Collaboration. First Measurement of Hadronic Event Shapes in *pp* Collisions at $\sqrt{s} = 7$ TeV.

[114] L. A. Anchordoqui, D. C. Dai, H. Goldberg, G. Landsberg, G. Shaughnessy, D. Stojkovic, and T. J. Weiler. Searching for the Layered Structure of Space at the LHC.

[115] J. Bjorken and S. Brodsky. Statistical Model for Electron-Positron Annihilation into Hadrons. *Phys. Rev. D*, 1(5):1416–1420, March 1970.

[116] S. Brandt, Ch. Peyrou, R. Sosnowski, and A. Wroblewski. The principal axis of jets an attempt to analyse high-energy collisions as two-body processes. *Physics Letters*, 12(1):57–61, September 1964.

[117] A. De Rújula. QCD predictions for hadronic final states in e^+e^- annihilation. *Nuclear Physics B*, 138(3):387–429, June 1978.

[118] E. Farhi. Quantum Chromodynamics Test for Jets. *Phys. Rev. Lett.*, 39(25):1587–1588, December 1977.

[119] A. Banfi, G. P. Salam, and G. Zanderighi. Phenomenology of event shapes at hadron colliders.

[120] M. Rubin, G. P. Salam, and S. Sapeta. Giant QCD K-factors beyond NLO.

[121] S. Ellis, C. Vermilion, and J. Walsh. Techniques for improved heavy particle searches with jet substructure. *Phys. Rev. D*, 80(5):051501, September 2009.

[122] J. M. Butterworth and A .R. Davison. Jet Substructure as a New Higgs-Search Channel at the Large Hadron Collider. *Phys. Rev. Lett.*, 100(24):4, June 2008.

[123] J. Thaler and L.-T. Wang. Strategies to identify boosted tops. *Journal of High Energy Physics*, 2008(07):092–092, July 2008.

[124] D. E. Kaplan, K. Rehermann, M. D. Schwartz, and B. Tweedie. Top Tagging: A Method for Identifying Boosted Hadronically Decaying Top Quarks. *Phys. Rev. Lett.*, 101(14):4, October 2008.

[125] L. Almeida, S. Lee, G. Perez, G. Sterman, I. Sung, and J. Virzi. Substructure of high-p_T jets at the LHC. *Phys. Rev. D*, 79(7):5, April 2009.

[126] S. D. Ellis, C. K. Vermilion, and J. R. Walsh. Recombination Algorithms and Jet Substructure: Pruning as a Tool for Heavy Particle Searches.

[127] J. Gallicchio and M. D. Schwartz. Seeing in Color: Jet Superstructure. *Phys. Rev. Lett.*, 105(2):022001, July 2010.

[128] Graham D. Kribs, Adam Martin, and Tuhin S. Roy. Higgs Discovery through Top-Partners using Jet Substructure.

[129] Y. Cui, Z. Han, and M. D. Schwartz. W-jet Tagging: Optimizing the Identification of Boosted Hadronically-Decaying W Bosons.

[130] J. Thaler and K. Van Tilburg. Identifying Boosted Objects with N-subjettiness.

[131] C. K. Vermilion. Jet Substructure at the Large Hadron Collider.

[132] G. Gur-Ari, M. Papucci, and G. Perez. Classification of Energy Flow Observables in Narrow Jets.

[133] CMS Collaboration. Jet Substructure Algorithms in CMS, 2011.

[134] Measurement of Jet Mass and Substructure for Inclusive Jets in $\sqrt{s} = 7$ TeV pp Collisions with the ATLAS Experiment. *ATLAS Note*, ATLAS-CONF-2011-073, May 2011.

[135] M. H. Seymour. Tagging a heavy Higgs boson. *Large Hadron Collider Workshop, Aachen ECFA Workshop 1990*, CAVENDISH-HEP-90-25, Nov 1990.

[136] L. G. Almeida, S. J. Lee, G. Perez, I. Sung, and J. Virzi. Top quark jets at the lhc. *Phys. Rev. D*, 79(7):074012, April 2009.

[137] S. Catani, Yu. L. Dokshitzer, F. Fiorani, and B. R. Webber. Average number of jets in e+e annihilation. *Nuclear Physics B*, 377(3):445–460, June 1992.

[138] S. Catani, Y. Dokshitzer, and B. Webber. The k-clustering algorithm for jets in deep inelastic scattering and hadron collisions. *Physics Letters B*, 285(3):291–299, July 1992.

[139] S. Catani, Yu. L. Dokshitzer, and B. R. Webber. Average number of jets in deep inelastic scattering. *Physics Letters B*, 322(3):263–269, February 1994.

[140] M. H. Seymour. Searches for new particles using cone and cluster jet algorithms: a comparative study. *Zeitschrift für Physik C Particles and Fields*, 62(1):127–138, March 1994.

[141] R. Snihur. Subjet multiplicity in quark and gluon jets at D0. *Nuclear Physics B - Proceedings Supplements*, 79(1-3):494–496, October 1999.

[142] J. R. Forshaw and M. H Seymour. Subjet rates in hadron collider jets. *Journal of High Energy Physics*, 1999(09):009–009, September 1999.

[143] Boost 2009, giving physics a new boost, SLAC National Accelerator Laboratory, 9-10 July, 2009.

[144] J. Abdessalam et al. Boosted objects as a probe of beyond the standard model physics. *J. Phys. G.*, 2010.

[145] A. Hook, M. Jankowiak, and J. G. Wacker. Jet Dipolarity: Top Tagging with Color Flow.

[146] J. Abraham, P. Abreu, M. Aglietta, E.J. Ahn, D. Allard, J. Allen, J. Alvarez-Muñiz, M. Ambrosio, L. Anchordoqui, and S. Andringa. Measurement of the energy spectrum of cosmic rays above 1018 eV using the Pierre Auger Observatory. *Physics Letters B*, 685(4-5):239–246, March 2010.

[147] G. Aad et al. The ATLAS Experiment at the CERN Large Hadron Collider. *JINST*, 3:S08003, 2008.

[148] R. Adolphi et al. The CMS experiment at the CERN LHC. *JINST*, 3:S08004, 2008.

[149] K. Aamodt et al. The ALICE experiment at the LHC. *JINST*, 3:S08002, 2008.

[150] A. A. Alves et al. The LHCb Detector at the LHC. *JINST*, 3:S08005, 2008.

[151] Georges Aad et al. Luminosity Determination in pp Collisions at $\sqrt{s} = 7$ TeV Using the ATLAS Detector at the LHC. *Eur.Phys.J.*, C71:1630, 2011, `arXiv:1101.2185 [hep-ex]`.

[152] M. Ferro-Luzzi. 2010 experiences and expectations for 2011. *The LHC Beam Operation workshop*, Workshop proceedings, Dec 2010.

[153] Cogging first beams: Cogging and RF signals report of Week1. *http://lhc-experiments-timing.web.cern.ch/lhc-experiments-timing/Coggingoperation.htm*, 2010.

[154] C. Ohm and T. Pauly. The ATLAS beam pick-up based timing system. *NIM A*, 2010, arXiv:0905.3648 [ins-det].

[155] O. S. Brüning, P. Collier, P. Lebrun, S. Myers, R. Ostojic, J. Poole, and P. Proudlock. *LHC Design Report*, volume CERN-2004-003-V-1. Geneva, 2004.

[156] M. (CERN) Ferro-Luzzi. LHC 2010 Operation - as viewed from the experiments. *Proceedings of the Chamonix 2011 LHC Performance Workshop*, page 9, 2010.

[157] G. Aad et al. Characterization of Interaction-Point Beam Parameters Using the *pp* Event-Vertex Distribution Reconstructed in the ATLAS Detector at the LHC. *ATLAS Note*, ATLAS-CONF-2010-027, Jul 2010.

[158] D. Cinabro, K. Korbiak, R. Ehrlich, S. Henderson, and Nari B. Mistry. Novel method of measuring electron positron colliding beam parameters. *NIM*, A481:29–35, 2002, arXiv:physics/0011075.

[159] J. Slaughter et al. Tevatron Run II Luminosity, Emittance and Collision Point.

[160] W. Kozanecki et al. Interaction-Point Phase-Space Characterization using Single-Beam and Luminous-Region Measurements at PEP-II. *Nuclear Instruments and Methods in Research A*, 607:293–321, 2009.

[161] S. van der Meer. Calibration of the effective beam height in the ISR.

[162] Updated Luminosity Determination in *pp* Collisions at $\sqrt{s} = 7$ TeV using the ATLAS Detector.

[163] G. Aad et al. Charged-particle multiplicities in *pp* interactions measured with the ATLAS detector at the LHC. *hep-ex/1012.5104, accepted by NJP*, 2011, arXiv:1012.5104 [hep-ex].

[164] I. Peric et al. The FEI3 readout chip for the ATLAS pixel detector. *Nuclear Instruments and Methods in Research A*, 565:178–187, 2006.

[165] G. Aad et al. The ATLAS Inner Detector commissioning and calibration. arXiv:physics.ins-det/1004.5293 [physics.ins-det].

[166] I. Ibragimov and D. W. Miller. Timing Behavior of the ATLAS Pixel Detector in Calibration and Cosmic-Ray Data. *ATLAS Note*, ATL-INDET-INT-2010-010, May 2010.

[167] F. Campabadal et al. Design and performance of the ABCD3TA ASIC for readout of silicon strip detectors in the ATLAS semiconductor tracker. *Nuclear Instruments and Methods in Research A*, A 552:292–328, 2005.

[168] E. Abat et al. The ATLAS TRT Barrel Detector. *JINST*, 3:P02014, 2008.

[169] E. Abat et al. The ATLAS TRT end-cap detectors. *JINST*, 3:P10003, 2008.

[170] E. Abat et al. The ATLAS TRT electronics. *JINST*, 3:P06007, 2008.

[171] ATLAS liquid-argon calorimeter: Technical Design Report. *Technical Design Report ATLAS*, ATLAS-TDR-002; CERN-LHCC-96-041, 1996.

[172] G. Aad et al. Drift Time Measurement in the ATLAS Liquid Argon Electromagnetic Calorimeter using Cosmic Muons. *European Physical Journal C*, 70(3):755–785, October 2010.

[173] E. Abat et al. Combined performance studies for electrons at the 2004 ATLAS combined test-beam. *JINST*, 5:P11006, 2010.

[174] M. Aharrouche et al. Measurement of the response of the ATLAS liquid argon barrel calorimeter to electrons at the 2004 combined test- beam. *Nuclear Instruments and Methods in Research A*, 614:400–432, 2010.

[175] J. Colas et al. Response Uniformity of the ATLAS Liquid Argon Electromagnetic Calorimeter. *Nuclear Instruments and Methods in Research A*, 582:429–455, 2007, arXiv:0709.1094 [physics.ins-det].

[176] M Aharrouche et al. Energy Linearity and Resolution of the ATLAS Electromagnetic Barrel Calorimeter in an Electron Test-beam. *Nuclear Instruments and Methods in Research A*, 568:601–623, 2006.

[177] P. Adragna et al. Testbeam studies of production modules of the ATLAS Tile calorimeter. *Nuclear Instruments and Methods in Research A*, 606:362–394, 2009.

[178] J. Pinfold et al. Performance of the ATLAS liquid argon endcap calorimeter in the pseudorapidity region $2.5 < |\eta| < 4.0$ in beam tests. *Nuclear Instruments and Methods in Research A*, 593:324–342, 2008.

[179] C. Cojocaru et al. Hadronic calibration of the atlas liquid argon end-cap calorimeter in the pseudorapidity region $1.6 < [\eta] < 1.8$ in beam tests. *Nuclear Instruments and Methods in Research A*, 531(3):481 – 514, 2004.

[180] M. Aharrouche et al. Study of the response of ATLAS electromagnetic liquid argon calorimeters to muons. *Nuclear Instruments and Methods in Research A*, 606:419–431, 2009.

[181] Readiness of the ATLAS Tile Calorimeter for LHC collisions. *Eur. Phys. J. C*, 70:1193–1236, 2010, arXiv:1007.5423 [physics.ins-det].

[182] G. Aad et al. Commissioning of the ATLAS Muon Spectrometer with cosmic rays. *European Physical Journal C*, 70(3):875–916, October 2010.

[183] G. Aad et al. Expected performance of the atlas experiment detector, trigger, physics. *ATLAS Note*, CERN-OPEN-2008-020. ISBN978-92-9083-321-5, Sep 2008, arXiv:0901.0512 [hep-ex].

[184] G. Aad et al. Performance of the ATLAS Inner Detector Trigger algorithms in *pp* collisions at $\sqrt{s} = 900$ GeV.

[185] Performance of the ATLAS Jet Trigger in the Early $\sqrt{s} = 7$ TeV Data. *ATLAS Note*, ATLAS-CONF-2010-094, October 2010.

[186] Properties of Jets and Inputs to Jet Reconstruction and Calibration with the ATLAS Detector Using Proton-Proton Collisions at $\sqrt{s} = 7$ TeV. *ATLAS Note*, ATLAS-CONF-2010-053, Jul 2010.

[187] Determination of the Absolute Jet Energy Scale in the DZERO Calorimeters. *NIM*, A424:352–394, 1999.

[188] A. Bhatti et al. Determination of the Jet Energy Scale at the Collider Detector at Fermilab. *NIM*, 566:A375, 2006.

[189] W. Lampl et al. Calorimeter clustering algorithms: description and performance. *ATLAS Note*, ATL-LARG-PUB-2008-002, April 2008.

[190] Properties and internal structure of jets produced in proton-proton collisions at $\sqrt{s} = 900$ GeV. *ATLAS Note*, ATLAS-CONF-2010-018, April 2010.

[191] ATLAS Monte Carlo tunes for MC09. *ATLAS Note*, ATL-PHYS-PUB-2010-002, Mar 2010.

[192] Properties of tracks in jets in proton-proton collisions at $\sqrt{s} = 7$ TeV in the ATLAS detector. *ATLAS Note*, ATLAS-CONF-2010-061, Jul 2010.

[193] Measurement of differential cross section and fragmentation of jets from tracks in proton-proton collisions at center-of-mass energy $\sqrt{s} = 7$ TeV with the ATLAS detector. *ATLAS Note*, ATLAS-CONF-2010-049, Jul 2010.

[194] Jet energy scale and its systematic uncertainty for jets produced in proton-proton collisions at $\sqrt{s} = 7$ TeV and measured with the ATLAS detector.

[195] Light-quark and gluon jets in atlas.

[196] F. Bordry. Status of the large hadron collider (lhc). *LHC Project Report*, CERN-LHC-PROJECT-Report-1130, September 2008.

[197] M. Cacciari and G. P. Salam. Pileup subtraction using jet areas. *Physics Letters B*, 659(1-2):119 – 126, 2008.

[198] Update on the jet energy scale systematic uncertainty for jets produced in proton-proton collisions at $\sqrt{s} = 7$ TeV measured with the ATLAS detector.

[199] Z. L Marshall. *A Measurement of Jet Shapes in Proton-Proton Collisions at 7.0 TeV Center-of-Mass Energy with the ATLAS Detector at the Large Hadron Collider*. *CERN-THESIS-2010-142*. PhD thesis, Pasadena, CA, USA, California Institute of Technology, 2010. Presented on 09 Nov 2010.

[200] G. Aad et al. Study of Jet Shapes in Inclusive Jet Production in pp Collisions at $\sqrt{s} = 7$ TeV using the ATLAS Detector. *Phys. Rev. D*, 83(5):052003, Mar 2011, arXiv:1101.0070 [hep-ex].

[201] D. Acosta et al. Study of jet shapes in g jet production in $p\overline{p}$ collisions at $\sqrt{s} = 1.96$ tev. *Phys. Rev. D*, 71(11):112002, Jun 2005.

[202] S. D. Ellis, C. K. Vermilion, and J. R. Walsh. Techniques for improved heavy particle searches with jet substructure. *Phys. Rev. D*, 80(5):051501, Sep 2009.

[203] M. Cacciari, G. P. Salam, and G. Soyez. The anti-k_t jet clustering algorithm. *JHEP*, 04:063, 2008, arXiv:0802.1189 [hep-ph].

[204] In-situ jet energy scale and jet shape corrections for multiple interactions in the first ATLAS data at the LHC $\sqrt{s} = 7$ TeV", institution = "CERN. *ATLAS Note*, ATLAS-CONF-2011-030, 2011.

[205] ATLAS jet energy scale uncertainties using tracks in proton proton collisions at $\sqrt{s}$ =7 TeV.

[206] Jet energy resolution and reconstruction efficiencies from in-situ techniques with the ATLAS Detector Using Proton-Proton Collisions at a Center of Mass Energy $\sqrt{s} = 7$ TeV. *ATLAS Note*, ATLAS-CONF-2010-054, 2010.

[207] M. Dasgupta, L. Magnea, and G. P. Salam. Non-perturbative QCD effects in jets at hadron colliders. *JHEP*, 02:055, 2008, arXiv:0712.3014 [hep-ph].

[208] V. M. Abazov et al. Subjet multiplicity of gluon and quark jets reconstructed with the k_T algorithm in $p\bar{p}$ collisions. *Phys. Rev. D*, 65:052008, 2002.

[209] S. Chekanov et al. Measurement of subjet multiplicities in neutral current deep inelastic scattering at HERA and determination of α_s. *Phys. Lett. B*, 558:41, 2003.

[210] S. Chekanov et al. Substructure dependence of jet cross sections at HERA and determination of α_s. *Nuclear Physics B*, 700:3, 2004.

[211] C. Glasman. Event shapes and subjet distributions at HERA.

[212] D. Acosta et al. Study of Jet Shapes in Inclusive Jet Production in $p\bar{p}$ Collisions at $\sqrt{s} = 1.96$ TeV. *Phys. Rev. D*, 71:112002, 2005.

[213] S. Chekanov et al. Subjet Distributions in Deep Inelastic Scattering at HERA. *Eur. Phys. J*, 63:527, 2009.

[214] T. Aaltonen et al. The Substructure of High Transverse Momentum Jets Observed by CDF II. *CDF Note*, 10199, 2010.

[215] T. Aaltonen et al. Preliminary Results of a Search for Boosted Top Quarks by CDF II. *CDF Note*, 10234, 2010.

[216] J. M. Butterworth, A. R. Davison, M. Rubin, and G. P. Salam. Jet substructure as a new Higgs search channel at the LHC. *Phys. Rev. Lett.*, 100:242001, 2008, arXiv:0802.2470 [hep-ph].

[217] G. Aad et al. Measurement of the top quark-pair production cross section with ATLAS in pp collisions at $\sqrt{s} = 7$ TeV. *European Physical Journal C*, 71, 2011, arXiv:1012.1792v2.

[218] A Search for New High-Mass Phenomena Producing Top Quarks with the ATLAS Experiment.

[219] Observation of top mono-jets (high p_T top quarks reconstructed as a single jet).

[220] G. Aad et al. Performance of the ATLAS Inner Detector Trigger algorithms in pp collisions at $\sqrt{s} = 900$ GeV. *ATLAS Note*, ATLAS-CONF-2010-014, 2010.

[221] D. Emeliyanov. A Fast Vertex Fitting Algorithm for ATLAS Level 2 Trigger.

[222] D. Emeliyanov. A fast vertex fitter for ATLAS level 2 trigger. *PoS*, ACAT:058, 2007.

[223] H. Burkhardt and P. Grafström. Absolute Luminosity from Machine Parameters.

[224] M. Lamont, R. Alemany-Fernandez, H. Burkhardt, and S. White. Luminosity Optimization and Calibration in the LHC.

[225] W. Lampl, S. Laplace, D. Lelas, P. Loch, H. Ma, S. Menke, S. Rajagopalan, D Rousseau, S. Snyder, and G. Unal. Calorimeter Clustering Algorithms: Description and Performance.

[226] The ATLAS Simulation Infrastructure. *European Physical Journal C*, 70:823–874, 2010.

[227] D. Sampsonidis, A. Krepouri, Ch. Petridou, M. Manolopoulou, A. Liolios, and S. Dedousis. Study of the response of the atlas monitored drift tubes to heavily ionizing particles and of their performance with cosmic rays. *Nuclear Instruments and Methods in Research A*, 535(1-2):260 – 264, 2004. Proceedings of the 10th International Vienna Conference on Instrumentation.

I certify that I have read this dissertation and that, in my opinion, it is fully adequate in scope and quality as a dissertation for the degree of Doctor of Philosophy.

(Su Dong) Principal Adviser

I certify that I have read this dissertation and that, in my opinion, it is fully adequate in scope and quality as a dissertation for the degree of Doctor of Philosophy.

(John Jaros)

I certify that I have read this dissertation and that, in my opinion, it is fully adequate in scope and quality as a dissertation for the degree of Doctor of Philosophy.

(Michael Peskin)

Approved for the University Committee on Graduate Studies